Development of a CFD time scheme for indoor airflow applications

Hector Galante Amino

École des Ponts ParisTech

THÈSE DE DOCTORAT

de l'École des Ponts ParisTech

Développement d'un schéma en temps pour des simulations CFD appliquées à l'aéraulique du bâtiment

Development of a CFD time scheme for indoor airflow applications

École doctorale N^o531, Ecole Doctorale - Sciences, Ingénierie et Environnement (SIE)

Spécialité : Mécanique des fluides

Thèse préparée au sein du laboratoire CEREA, et du département Mécanique des fluides, Energie et Environnement d'EDF R&D

Version jury pour la soutenance du 24 novembre 2022, par

Hector GALANTE AMINO

Composition du jury:

Patrick, LE QUERE Directeur de recherche, CNRS	*Président du jury*
Anne, SERGENT Maitre de conférences, Sorbonne Université	*Rapporteur*
Jean-Claude, LATCHE Directeur de recherche, IRSN	*Rapporteur*
Frédéric, KUZNIK Professeur, Cethil, INSA Lyon	*Examinateur*
Christian, INARD Professeur, Université de la Rochelle	*Examinateur*
Bertrand, CARISSIMO Maître de conférences, CEREA ENPC	*Directeur de thèse*
Martin, FERRAND Maître de conférences, EDF R&D, CEREA ENPC	*Co-encadrant de thèse*
Cédric, FLAGEUL Maître de conférences, Institut Pprime, Université de Poitiers	*Co-encadrant de thèse*

Remerciements

Cette thèse est l'accomplissement de trois années de travail entre le laboratoire CEREA et EDF R&D. Elle a été marquée par de nombreuses surprises, entrecoupée de confinements et couvre-feux, ponctuée par des hauts comme des bas, mais surtout chargée de rencontres et discussions où j'ai pu apprendre énormément.

J'aimerais tout d'abord remercier les membres du jury pour avoir évalué mes travaux ainsi que pour les divers échanges que nous avons eus. Merci en particulier à Anne Sergent et Jean-Claude Latché davoir accepté d'être rapporteurs de cette thèse, pour votre temps et vos remarques constructives.ă

Je souhaite remercier mon directeur de thèse, Bertrand Carissimo, pour m'avoir donné l'opportunité de réaliser cette thèse, ainsi que pour le suivi de mon travail et les nombreuses discussions que nous avons eu. Ses conseils, son expérience et sa rigueur scientifique mont beaucoup appris. J'adresse également tous mes remerciements à mon encadrant Cédric Flageul, qui dans les moments stressants, ma permis de prendre le recul scientifique nécessaire, indispensable pour réaliser cette thèse.ă Toute ma gratitude à Martin Ferrand, pour son encadrement et son implication dans cette thèse. Je le remercie pour son investissement, sa passion et son dynamisme qui m'inspirent beaucoup ainsi que pour son expertise technique et scientifique. C'est un plaisir de pouvoir continuer de travailler avec lui.

Merci, à vous trois, pour votre confiance et votre bienveillance qui comptent beaucoup pour moiă!

J'adresse également mes remerciements à l'ensemble du personnel du CEREA et du département MFEE d'EDF R&D que j'ai eu le plaisir de rencontrer et avec qui jai pu échanger. Merci à l'équipe de développement code_saturne qui a toujours été ouverte aux discussions ainsi que pour votre aide.ă Merci à Jean-Marc Hérard pour sa bienveillance, sa rigueur et le temps quil a consacré à mes travaux. Merci également à Sofiane Benhamadouche pour toutes les discussions intéressantes autour de mes cas de validation et au sujet de la turbulence.
Je remercie aussi les personnes qui mont aidé à rapidement assimiler le fonctionnement de lentreprise : Anne Peure, Pietro Bernardara et Nicolas Dos Santos. Une pensée à toutes les rencontres et amitiés faites pendant ces trois années: Léa, Luc, Guilhem, Elisa, et beaucoup d'autres. Vous êtes en grande partie responsables des bons souvenirs que je garderai avec moi sur cette période de trois ans.
Je ne saurais oublier mes anciens professeurs, du collège jusqu'à l'université, un grand merci. Votre inspiration a été clef dans mon parcours professionnel et personnel. Une pensée particulière à Monsieur Steinmetz, Anca Belme, Jean-Camille Chassaing et Hélène Dumontet, qui ont su croire en moi et m'ont guidé.ă

Merci à tous mes amis proches. J'ai beaucoup de chance de vous avoir. Merci au Menu, aux CG, pour tous les moments passés, votre soutien et amitié. Cette thèse ne se serait pas faite sans vous.

Enfin, merci à toute ma famille. Merci pour votre amour, sans lequel je ne serai pas là aujourd'hui. A tous ceux de l'autre côté de l'océan Atlantique, je ne vous oublie pas

Contents

List of Figures

List of Tables

Nomenclature

Superscripts

k	Current inner iteration
l	Current iteration related to the Newton method
n	Current time step

Subscripts

0	Reference value
c	Considered cell
$\widetilde{c}$	Neighbour cell separated by the face f
f	Face separating c and $\widetilde{c}$
a	Dry air
in	Inlet value
L	Left state
l	Liquid water
l	Shock left state
R	Right state
r	Shock right state
v	Water vapor
w	Total water

Abbreviations

RH	Relative humidity
AHU	Air handling unit
AI	Artificial intelligence

CAD Computer-aided design

CFD Computational fluid dynamics

CFL Courant Friedrichs Levy

CO_2 Carbon dioxide

CPC Compressible pressure correction

div Divergence

DNS Direct numerical simulation

DRSM Differential Reynolds stress model

DSS Double symmetric shock

EDF Electricité de France

EOS Equation of state

EVM Eddy viscosity model

GHG Greenhouse gases

HVAC Heat ventilation and air conditioning

IAQ Indoor air quality

IC Isentropic compressible

IPC Incompressible pressure correction

LES Large eddy simulation

PM10 Particle matter 10

PMV Predicted mean vote

RANS Reynolds averaged Navier–Stokes

SGDH Simple gradient diffusion hypothesis

SOLU Second order linear upwind

SSG Speziale-Sarkar-Gatski

UCD Unsteady contact discontinuity

VOC Volatile organic components

Greek symbols

α Thermal diffusivity

α_f Weighting factor

α_i Mass fraction $i = a, w, v, l$

α_i Volume fraction $i = a, w, v, l$.

β	Dilatation coefficient
$\Delta\underline{x}$	Spatial step
ΔT	Temperature variation
Δt	Time step
ϵ_m	Water and air molar masses ratio
η_s	Kolmogorov turbulent scale
Γ	Mass source term
γ	Heat capacity
$\Gamma_c^{u^2/2}$	Internal energy source term based on the kinetic energy
Γ_E	Total energy source term
Γ_s	Entropy source term
Γ_Y	Scalar source term
$\hat{\rho}$	Dimensionless density
κ	Wavelength
κ_q	Volume viscosity
λ	Heat conductivity
λ_i	Eigenvalues $i = 1, 2, 3, 4$
λ_s	Taylor turbulent scale
μ	Dynamic viscosity
ν	Kinematic viscosity
ν_T	Turbulent viscosity
Ω	Domain
ω	Specific dissipation
Ω_c	Cell volume
Ω_{tot}	System total volume
ϕ^k	Pressure increment
Φ_i	Normalised pressure variable $i = 1, 2$
Π	Porosity
ρ	Density
ρ_r	Characteristic density
σ	Shock speed

τ_η Kolmogorov turbulent scale characteristic time

τ_λ Taylor turbulent scale characteristic time

τ_L Integral turbulent scale characteristic time

$\underline{\underline{\omega}}$ Rotation tensor

$\underline{\underline{\Phi}}^*$ Reynolds stress velocity-pressure gradient correlation term

$\underline{\underline{\sigma}}$ Stress tensor

$\underline{\underline{\tau}}$ Viscous stress tensor

$\underline{\underline{\tau}}^{sgs}$ Subgrid stress tensor

$\underline{\underline{\varepsilon}}_R$ Reynolds stress dissipation tensor

θ Theta scheme numerical parameter

$\Theta((.)^n, (.)^{n+1})$ Time interpolation operator

θ_p Potential temperature

ε Turbulent kinetic energy dissipation rate

ε_{e0} Newton method error threshold

ε_{piso_0} Sub-iterative process error threshold

ε_{piso}^k Sub-iterative process error

$\widetilde{\rho}$ Predicted density

Roman symbols

$()''$ Instantaneous field component (Favre average framework)

$(.)'$ Instantaneous field component (Reynolds average framework)

$(.)_c$ Mean space value over a cell c

$(.)_f$ Mean space value over a face f

$\underline{\hat{u}}$ Dimensionless velocity

$\hat{e}$ Dimensionless internal energy

$\hat{p}$ Dimensionless pressure

$\hat{T}$ Dimensionless temperature

$\hat{x}$ Dimensionless x coordinate

$\dot{M}_f$ Face mass flux

$\overline{(.)}$ Reynolds average operator

ϕ_i Riemann invariants $i = 1, 2, 3, 4$

$\underline{\underline{\mathbb{P}}}_R$ Reynolds stress production term

$\underline{\underline{a}}$	Dimensionless anisotropy tensor
$\underline{\underline{d}}$	Reynolds stress diffusive term
$\underline{\underline{d}}^{\mu}$	Reynolds stress molecular diffusive term
$\underline{\underline{d}}^{p}$	Reynolds stress pressure diffusive term
$\underline{\underline{d}}^{t}$	Reynolds stress turbulent diffusive term
$\underline{\underline{G}}$	Reynolds stress gravity production term
$\underline{\underline{I}}$	Identity tensor
$\underline{\underline{R}}$	Reynolds stress tensor
$\underline{f}$	Field of source terms
$\underline{g}$	Gravity acceleration
$\underline{q}$	Momentum
$\underline{Q}_c$	Cell momentum
$\underline{r}_i$	Eigenvectors $i = 1, 2, 3, 4$
$\underline{S}_f$	Face normal surface vector
$\underline{u}$	Velocity
$\underline{u}^k$	Predicted velocity
$\underline{u}^{in}$	Injected momentum
$\underline{x}$	Spatial coordinates vector (x, y, z)
$\underline{x}_c$	Cell c barycentre
$\underline{x}_f$	Face f barycentre
$\widetilde{(.)}$	Favre average operator
c_p	Isobaric heat capacity
c_v	Isochoric heat capacity
C_{PM}	PM10 concentration
c_{vm}	Mixture isochoric heat capacity
$d_{\widetilde{cc}}$	Distance used for the gradient computing
E	Total energy
e	Internal energy
Fo	Fourier number
h	Air heat transfer coefficient
h	Enthalpy

K	Scalar molecular diffusivity
k	Turbulent kinetic energy
L	Characteristic length
l_m	Mixing length
L_s	Integral turbulent scale
L_{00}	Water latent heat related to the reference temperature
M_c	Cell mass
M_a	Dry air molar mass
p	Total pressure
p_s	Water vapour pressure at saturation
P_{AHU}	Air handling unit power
Pr_T	Turbulent Prandtl number
Q	Heat exchange per unit of mass
Q_i	Heat flux
R_a	Dry air specific gas constant
R_v	Water vapour gas constant
s	Entropy
ST_ε	Turbulent kinetic energy dissipation rate source term
ST_k	Turbulent kinetic energy source term
T	Temperature
t	time
T_∞	Bulk temperature
T_c	Cold temperature
T_h	Hot temperature
T_r	Characteristic temperature
T_w	Wall temperature
U	Characteristic velocity
W	Work per unit of mass
x_s	Absolute humidity ratio
Y	Scalar mass fraction
y_s	Water vapour mass fraction at saturation

z_i	Normalised density variable $i = 1, 2$
$\mathcal{G}$	Turbulent kinetic energy gravity production term
$\mathcal{P}$	Turbulent kinetic energy shear stress production term
t^+	Dimensionless time
c	Speed of sound
Fr	Froud number
KH	Kelvin Helmholtz
Ma	Mach number
Re	Reynolds number
Sc	Schmidt number

Résumé

La caractérisation d'écoulements d'air intérieur est un enjeu d'importance dans un contexte social et réglementaire visant à optimiser la consommation énergétique et le confort thermique dans le bâtiment. Parallèlement, la qualité de l'air intérieur est responsable de milliers de décès dans le monde et suscite l'intérêt croissant de la communauté scientifique et des institutions; la crise épidémique liée au virus SARS-COVID 19 souligne l'utilité des études en milieu confiné. Dans ce but, la simulation est un outil efficace pouvant reproduire de manière fiable l'écoulement considéré et de manière moins coûteuse comparée à l'expérimental. Cette thèse se focalise sur le développement d'un outil numérique pour les simulations aérauliques à l'échelle locale (computational fluid dynamics, CFD). Ce dernier a pour but d'être appliqué dans des études de milieux intérieurs allant du domaine résidentiel (aide à la maîtrise d'oeuvre, étude de la qualité d'air intérieur) à l'industriel et tertiaire (sûreté des centrales nucléaires, ventilation d'enceintes sportives). Après avoir posé le contexte et les enjeux liés à l'aéraulique dans le premier chapitre, l'identification des phénomènes physiques caractérisant les écoulements d'air intérieurs et le choix des équations à utiliser sont présentés dans le second. Au troisième chapitre, pour répondre aux enjeux de modélisation ciblés, un schéma volumes finis d'ordre 2 en temps pour les écoulements à densité variable est proposé, pour des solutions régulières et discontinues. Développé pour l'air sec tout d'abord, le schéma est implémenté dans le logiciel CFD sous licence libre code_saturne. Ce dernier rentre dans la famille des theta-schémas de type prédiction correction. Le second ordre en temps est atteint grâce à une localisation de variables décalées. De plus, l'énergie totale est conservée grâce à la résolution de l'équation de l'énergie interne complétée par un terme source dérivé de l'équation discrète de l'énergie cinétique. Enfin, la variation de pression est prise en compte en linéarisant l'équation d'état, ce qui conduit à la formulation d'une équation d'Helmholtz à résoudre pour la pression. Les termes liés à cette linéarisation sont implicités, menant à des calculs plus rapides tout en évitant toute contrainte sur le pas de temps liée aux ondes acoustiques. Après une analyse numérique menant à des nouvelles contraintes de stabilité, le schéma en temps est vérifié et validé à l'aide de cas allant de zéro à trois dimensions et du régime incompressible au compressible, représentatifs des enjeux de modélisation aérauliques. Des simulations d'écoulements turbulents (RANS, LES) sont également réalisées. Le quatrième chapitre présente des développements complémentaires permettant d'étendre le schéma à l'air humide avec changement de phase. L'équilibre thermodynamique est considéré et la fraction massique d'eau totale, sous forme gazeuse et liquide, est transportée. Dans le but d'utiliser les équations choisies auparavant, le changement de phase est traité en utilisant la méthode de Newton à partir de l'énergie interne résolue. À nouveau, une analyse numérique et des vérifications sont réalisées. De nouvelles conditions CFL sont ainsi présentées. Enfin, dans le cinquième chapitre, l'outil numérique est appliqué pour caractériser l'écoulement d'air intérieur au sein du Stade Pierre de Coubertin, dans le cadre des jeux olympiques 2024 de Paris. Le maillage numérique est créé à partir d'un nuage de points issu de mesures scanners 3D. Les premières simulations mènent à l'identification de zones d'intérêt dynamiques et thermiques et à l'élaboration d'un protocole expérimental pour une campagne de mesures. S'en suit une validation du schéma dans le but de reproduire l'évolution de la concentration de particules lors de la finale de la ligue de Handball française, lors de laquelle un pic de PM10 (fumigènes) a été mesuré.

Les travaux de cette thèse ont mené à la publication d'un article dans la revue "International Journal of Numerical methods in fluids" en 2022 intitulé "A time-staggered second order conservative time scheme for variable density flow" (Hector Amino, Cédric Flageul, Sofiane Benhamadouche, Iztok Tiselj, Bertrand Carissimo et Martin Ferrand).

Deux articles de conférence ont été également publiés en 2022, le premier étant "A second order conservative time scheme for variable density flow" (Hector Amino, Cédric Flageul, Sofiane Benhamadouche, Iztok Tiselj, Bertrand Carissimo et Martin Ferrand), à la 17th UK Heat Transfer Conference (UKHTC2021) et le deuxième intitulé "A time-staggered second order scheme for moist air variable density flow" (Hector Amino, Cédric Flageul, Jean-Marc Hérard, Bertrand Carissimo, Martin Ferrand) à la conférence ECCOMAS 2022.

Mots clefs : aéraulique, CFD, schéma numérique, flottabilité, turbulence, compressible, incompressible, changement de phase

Abstract

Characterising indoor airflow is an important stake in a reglementary and social context of energy and thermal comfort optimisation of buildings. Concomitantly, the indoor air quality is responsible for a consequent number of deaths world-wide and arouses a growing interest of the scientific community. The important number of studies related to the COVID virus propagation emphasises the importance of studying such environments. In this purpose, numerical simulations are a powerful tool to predict the indoor physical phenomena while being cost-less compared to experimental measurements. This thesis focuses on the development of a local scale simulation (computational fluid dynamics, CFD) scheme for indoor airflow in order to perform residential (indoor air quality and environment design) and industrial (nuclear safety, sport facilities ventilation) thermoaeraulic studies. After presenting the aforementioned context in the first chapter, an identification of the main physical phenomena driving the indoor airflow is made in the second one. Some existing models are presented and a choice of the governing equations to be used is made. In the third chapter, to meet the modelling challenges presented, a second order conservative time scheme for variable density flow is proposed, for smooth and singular solutions. First written for dry air, the time scheme is implemented in the CFD open source solver code_saturne. The latter falls within the class of theta pressure correction schemes. The second order time convergence is reached by a time staggered variable arrangement. Moreover, the total energy is conserved thanks to the solving of the internal energy equation completed with a source term based on the kinetic energy discrete equation. Finally, the pressure variation is taken into account by linearizing the equation of state, leading to an Helmholtz equation for the pressure correction. Some pressure related terms are implicited, leading to faster calculations and avoiding any stability condition related to acoustic waves. An analysis on the positivity of the thermodynamic variables is made, leading to new stability conditions which are studied as well in the manuscript. The scheme is verified and validated on test cases going from zero to three dimensions, for incompressible and compressible flows, chosen to represent the different indoor modelling stakes. Furthermore, it is verified that the scheme is compatible with first and second order turbulent approaches (RANS, LES). In the fourth chapter, the dry air time scheme is extended to moist air applications, including variable properties, another equation of state and phase change. The thermodynamic equilibrium is considered and the total water mass fraction (in liquid and vapor states) is transported as a scalar. In order to use the set of equations chosen previously, the phase change is taken into account using the Newton method related to the solved internal energy. A numerical analysis, verification and validation are made as well. Finally, in the fifth chapter, the numerical tool is applied on the study of the Pierre de Coubertin handball stadium, in the context of the Paris 2024 Olympic Games. The numerical mesh is generated from a three dimensional cloud of points, created from laser measurements. First simulations are performed to identify the stadium dynamic and thermal interest zones and a protocol is proposed for an upcoming experimental campaign. Then, a numerical validation is made on the evolution of particles concentration during the french league handball final, where fog sources were ignited outside the stadium, promoting a concentration peak inside arena.

This thesis work led to a journal paper entitled "A time-staggered second order conservative time scheme for variable density flow" (Hector Amino, Cédric Flageul, Sofiane Benhamadouche, Iztok Tiselj, Bertrand Carissimo et Martin Ferrand), published in the "International Journal of Numerical methods in fluids". Additionally, two conferences papers were published. The first one entitled "A second order conservative time scheme for variable density flow" (Hector Amino, Cédric Flageul, Sofiane Benhamadouche, Iztok Tiselj, Bertrand Carissimo et Martin Ferrand), presented at the 17th UK Heat Transfer Conference (UKHTC2021) and the second one entitled "A time-staggered second order scheme for moist air variable density flow" (Hector Amino, Cédric Flageul, Jean-Marc Hérard, Bertrand Carissimo, Martin Ferrand), presented at the ECCOMAS 2022 congress.

Key words : indoor air flow, CFD, numerical scheme, finite volumes, buoyancy, turbulence, compressible flow, incompressible flow, phase change

CHAPTER 1

Introduction

Résumé

Dans ce chapitre sont introduits le contexte global de ce manuscrit et son objectif principal, qui est de développer un schéma numérique pour des simulations aérauliques à l'échelle locale. Les motivations sont nombreuses, allant de l'optimisation thermique d'environnements intérieurs, la qualité d'air et enfin les études industrielles, comme la sûreté au sein de centrales nucléaires. La méthodologie globale de la thèse est enfin décrite ainsi que le plan de ce manuscrit.

1.1 Context and motivation

Since the 70's, the world population has importantly grown to reach 7.8 billion people in 2021. Predictions (Buettner, 2020) forecast a 12% additional increase by 2030. At the same time, the urban population grows. By 2050, 6.4 billions citizens are expected in cities (UNO, 2018), compared to 4.35 billions today. In parallel, the energy and natural resources consumption will increase directly linked with the population raise.

Humans are thus very likely to spend more and more of their time in enclosed environments (residential buildings, industrial facilities, transports, schools). Thermal comfort and recently indoor air quality (IAQ) are important concerns in the current society. These stakes depends on parameters such as the air temperature, its humidity rate, the environment ventilation, among others. Their comprehension is crucial to insure the aforementioned stakes.

Today in France, buildings consume 43% of the primary energy (ADEME, 2018), partially due to heat, ventilation and air conditioning (HVAC) systems (see Figure 1.1 for the final consumption of energy in France in 2019/2020, note that the building consumption is part of the residential and tertiary sectors here), placing it on the top of the final energy consumption sector.

This percentage might grow every year with the increase of the usage of electrical devices and the change of the weather conditions.

Moreover, the residential/tertiary sector represents 22% and 7.8% of France CO_2 and green house gas (GHG) emissions as well (ADEME, 2018).

In that way, several laws and guidance have been set from the national institutions concerning the existing and new buildings energy consumption and IAQ. To illustrate this, in France, the renovation of all existing buildings to become low consumption before 2050 (Ministère de la Transition Ecologique et Solidaire, 2018) and the reduction of 60% of energy consumption related to 2010 of all buildings as well (Assemblée Nationale Française, 2018).

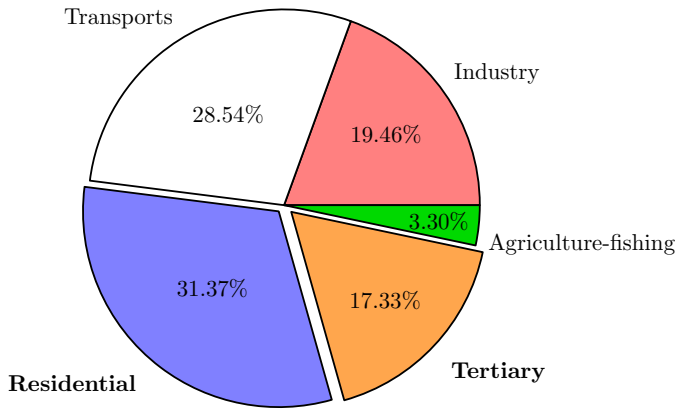

Figure 1.1: Pie chart of the relative final energy consumption in France in 2019/2020 by sector.

From these major stakes, optimising the indoor environment appears to be essential to reduce the GHG emissions, energy consumption and to respect the institutions guidance.

In addition, IAQ plays a major role from a public health point of view, causing close to 4 millions deaths around the world per year (WHO, 2021). Generated largely by inefficient and poorly ventilated stoves burning biomass fuels, an optimised environment would prevent many life losses. In France, for instance, formaldehyde's concentrations (cancerous, inflammable and allergic species) in indoor environments are actually ten times higher than in the outdoor ambient environment (Ramalho and Kirchner, 2007).

Finally, in the last Sars-COVID crisis context, it was shown that ensuring a proper ventilation reduces the virus contamination in indoor environments, by dispersing the particles containing virus and consequently, its concentration (Bhagat et al., 2020; Sun and Zhai, 2020; Meng et al., 2020).
From an industrial point of view, understanding the indoor airflow is crucial for safety studies, such as the conception of optimised ventilation systems in rooms with thermal sources (Hassan et al. (2013), Figure 1.2, right) or the dispersion of flammable species in an enclosed system (e.g. hydrogen in a nuclear plant, see Hoyes and Ivings (2016), Figure 1.2, left). An *a priori* comprehension of the indoor airflow is useful as well when designing residential and tertiary buildings, regarding the system energy consumption (Norton et al., 2010; Bustamante et al., 2013; Yang et al., 2014; Cuce et al., 2019) , thermal comfort (Kwong et al., 2014)and IAQ (Spengler and Chen, 2000; Tong et al., 2016)(see Shree et al. (2019)for a review of IAQ CFD applications).
Regardless of any particular strategy related to energy reduction, industrial safety, air comfort or air quality, the key within this optimisation process is the accurate understanding of the physics governing the given system.
To do so, either experiments or numerical simulations can be made. The first leads to results close to reality but are complex to set up and can be expensive, in particular when looking for reproductibility in complex environments. The second depends on experimental data and reference results for validation, but is financially more affordable. Additionally, with the growing computational power context, simulations are more and more used in both industrial and academic fields. Therefore, a good combination of both may lead to a better understanding of the phenomena.

Figure 1.2: Consequences of a bad design, monitoring or exploitation of industrial buildings. (Left) Fukushima accident in 2011 caused by an hydrogen explosion after the endomagement of the primary cooling cycle by an earthquake (credits: Fukushima Central Television). (Right) Fire at a data centre in Strasbourg in 2021 (credits: Sapeurs Pompiers du Bas Rhin), due to an overheat of two inverters. Moreover, given the building design, the firefighter could not have a proper access to the burning devices. Additionally, the centre architecture (which used a free cooling ventilation strategy) accelerated the fire dispersion (Lawrance, 2020).

Yet, the indoor environment can be very difficult to properly reproduce numerically. First, the studied system can be very complex: many geometries are very often connected by the HVAC system or by any opening; from furniture to occupants and possible heat and pollutant sources, the complexity increases rapidly. Simultaneously, the indoor flow can be driven by numerous physical influences, such as natural convection, a differential of pressure and jets. Given this difficulty, very often the problem is simplified by the application of models and large scale numerical methods.
Indeed, following the context and the goal of the simulation, a modeller may use different numerical techniques. Among them, the most popular are the nodal, multi zones and local scale methods (Chen, 2009), represented in Figure 1.3.

The nodal zone model studies the building at a macroscopic scale. It considers the system characteristics (temperature, pressure...) to be spatially uniform over the node (Kusuda, 1976). Nevertheless, it has been shown that for studies where mass and heat transfer are coupled (such as natural ventilation or in presence of natural convection), this type of simulation is too simple (Mora, 2003). The multi zone modelling appeared then, where a building would be divided in different spatial zones linked by airflow resistances. This allows particular conditions following the studied environment (corresponding to a zone) to be imposed. A detailed description of the theory related to multi zones modelling can be found in Axley (2007). Examples of using multi zones to model the indoor environment can be cited: Allard and Inard (1992); Inard et al. (1996); Musy et al. (2002); Teshome and F. Haghighat (2004); Foucquier et al. (2013). Moreover, this type of method is fast, allowing long time simulations (of one or several months, for instance) to be performed. However, it may not account any local heterogeneous behaviour, such as thermal stratification (Wang and Chen, 2008), which, according to the situation, has a strong impact on the flow.
Various multi zone softwares and libraries exist and are widely used to analyse HVAC systems (CONTAM (Walton et al., 2006), COMIS (Feustel, 1999) , BuildSysPro (Plessis et al., 2014), TRNSYS/Energy plus).
The last method is the local scale simulation, also known as computational fluid dynamics (CFD), which takes into account the local fields by solving conservation equations on a highly discretised domain. Yet, while multi zone simulations can cover a year of prediction, CFD will focus on smaller time periods. A coupling between these techniques can also be interesting; the CFD simulation can provide local information for a larger scale model (Wang and Chen, 2007) and the latter can be used during a CFD simulation to accelerate the computation time (Bellivier, 2004) . Also, CFD can be coupled to multi zone models to perform simulations covering the flow of a single room to the local urban micro-climate scale (Malys et al., 2015) . Still, CFD is widely used for indoor airflow studies due to its capacity to predict both spatial and temporal fields (Nielsen, 2015) . Among its distinct applications, one may highlight, related to indoor environments, studies on site planning (Zhai, 2006) , human body impact on the flow (see Gao and Niu (2005) for a review) , personalised ventilation (Zhai et al., 2002; Shen et al., 2013; Liu et al., 2019) , pollution dispersion and control (Zhai et al., 2003; Kassomenos et al., 2008; Rui et al., 2008) and thermal comfort (Zhang and Chen, 2007; Catalina et al., 2009).

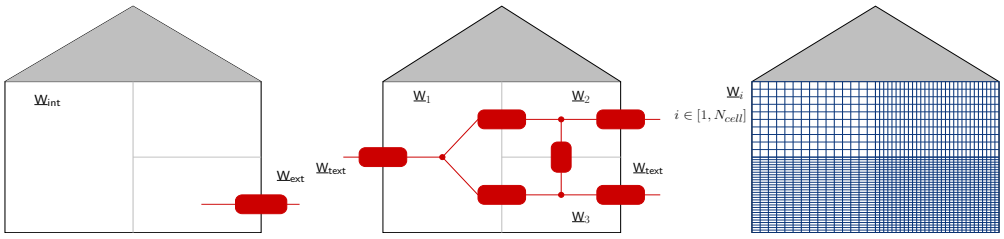

Figure 1.3: Different scales when modelling a building. (Left) Nodal model. (Center) Multi zone model. (Right) CFD. $\underline{W}$ is the variables array. N_{cell} is the number of cells of the CFD simulation.

Note that local simulations do not always provide accurate results. The verification and validation processes, where the numerical results are compared to analytical, reference or experimental data are crucial (Chen and Srebric, 2002) when designing any tool. While the verification verifies that one is solving the equations correctly, the validation confirms that the system of equations, including the choice of models, initial and boundary conditions is in agreement with the studied physics.
This thesis focuses essentially on the local scale of simulation. Indeed, the main goal is to properly reproduce the indoor air-flow complexity that can be characterised by different coexistent processes, which is ideal for CFD simulations.
To conclude, a focus on the indoor environment modelling stakes to reproduce at the local scale shall lead to a better understanding on the indoor airflow physics. With the new numerical tool, an easier indoor

space design optimisation may be made, inducing a reduction of the building energy consumption, GHG emissions and occupants negative health impact.
Among the different under license and open source CFD solvers (Jasak, 2009; Popinet, 2003) , all the numerical implementations and studies in this thesis are made with code_saturne (Archambeau et al., 2004) , used extensively in the industry, see for example nuclear thermal-hydraulic applications (Flageul et al., 2019; Gauffre et al., 2020) , atmospheric modelling (Milliez and Carissimo, 2007; Defforge et al., 2021) , ventilation, waves interactions (Ferrand and Harris, 2021) , and combustion (Han and Morgans, 2015) .

1.2 Problem formulation

The aim of this thesis is to develop a new numerical scheme to simulate indoor air-flow. In order to reproduce the thermal stratification and recirculation zones, the local simulation scale is chosen.
More precisely, this manuscript focuses on answering the following question:

Can one accurately simulate the physics of indoor airflow in a local scale while preserving an affordable computation time?

The expected outcome of the present work is a robust and accurate numerical tool for indoor airflow local scale simulations. The latter should also be easy to use. Furthermore, an additional care is provided to the simulations computation time, which is one of the criteria for the numerical choices while designing the scheme.

1.3 Methodology and thesis plan

To achieve this goal, the methodology combines a numerical and a physical approaches, whose main steps are represented on Figure 1.4. First, from a physical point of view, an identification is made regarding the main physical phenomena that should be accounted for an indoor airflow CFD simulation. This is done thanks to a literature review. Also, this step is useful to identify test cases for the tool verification and validation. This physical step is followed by the choice concerning the equations and models to be used. The next step is to propose a space and time discretised numerical scheme related to this set of equations, to be implemented in code_saturne. Then, a numerical analysis is performed on the numerical scheme properties and stability, followed by the verification and validation processes. Finally, the numerical tool is tested on a more complex configuration: an enclosed stadium. Physical insights are provided for a better understanding of the airflow patterns, illustrating and emphasising the presented time scheme type of application.
Realised between EDF's R&D Fluid Mechanics, Energy and Environment department (MFEE) and the Center of Research and Teaching in Atmospheric Flow (CEREA) at the Ecole des Ponts ParisTech, this thesis main achievements are:

- The development and validation (on relatively simple test cases) of a novel numerical time scheme for variable density dry airflow, able to handle pressure variations while preserving the total energy, with no time step restriction related to sound waves, and compatible with first and second order turbulent simulations.
- Its extension to moist air with phase change using an homogeneous model.
- The application of the numerical tool on a complex 3D configuration, the Pierre de Coubertin stadium.

Thus, the outline of the manuscript is the following:

- Chapter 2 focuses on the physical aspect of the problem. The continuous governing equations are presented and the main modelling stakes are identified. Then, models are presented followed by a final choice of equations.
- Chapter 3 presents the time scheme developed for indoor dry airflow. Both space and time discretisations are detailed, followed by a numerical analysis and the scheme verification and validation.
- Chapter 4 describes the extension of the dry air scheme from the previous chapter to moist airflow. After the presentation of the new set of equations and its discretisation, the scheme verification and analysis is performed.
- Finally, chapter 5 focuses on the study of the Pierre de Coubertin stadium. The problem parameters are detailed and different cases and applications are discussed.

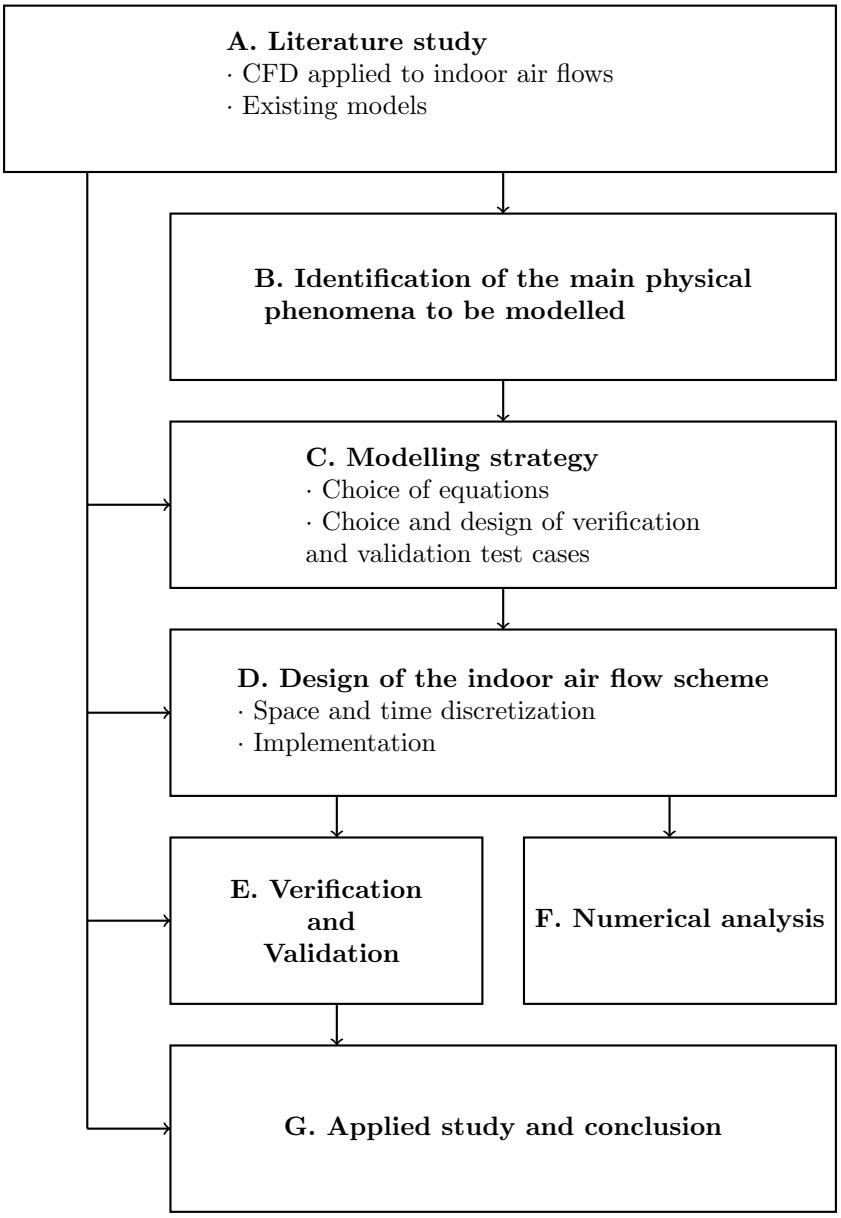

Figure 1.4: Summary of the thesis methodology.

CHAPTER 2

Physical background and governing equations

Résumé

Dans ce chapitre, les équations continues de Navier–Stokes compressibles sont présentées, ainsi que les équations thermiques. Ensuite, une identification des phénomènes physiques ayant un impact sur l'écoulement intérieur est réalisée. Des modèles existant dans la littérature sont décrits, notamment ceux liés à la turbulence et au filtrage des ondes acoustiques. A partir des enjeux de modélisation et simplifications présentés, un choix sur le système d'équations à discrétiser est enfin réalisé.

2.1 Continuous equations

Consider a domain Ω (usually bounded). Fluid motion, when studied with the continuum hypothesis can be described by the conservative laws – mass, momentum and energy conservation – supplemented with an equations of state (EOS). This set of equations is called the Navier–Stokes equations.
The application of the mass conservation on a local volume leads to the continuity equation:

$$\frac{\partial \rho}{\partial t} + \text{div}\left(\underline{q}\right) = \Gamma, \tag{2.1}$$

where ρ represents the fluid density and $\underline{q} = \rho \underline{u}$ its momentum, with $\underline{u}$ the fluid velocity. Γ is a possible mass source term.
In terms of physical interpretation, the first term represents the rate of density variation inside the volume and the second is the rate of mass flux passing in its surfaces. The Newton's second law applied to the fluid at the same volume leads to the momentum $\underline{q}$ conservation equation:

$$\frac{\partial \underline{q}}{\partial t} + \underline{\text{div}}\left(\underline{u} \otimes \underline{q}\right) = \underline{\text{div}}\left(\underline{\underline{\sigma}}\right) + \underline{f} + \Gamma \underline{u}^{in}. \tag{2.2}$$

$\underline{\underline{\sigma}}$ is the stress tensor, $\underline{f}$ is a field of source terms (*e.g.*, gravity, Coriolis, additional head losses), and $\underline{u}^{in}$ the value of the corresponding injected momentum. For sake of simplicity, Γ will be set to zero hereafter.
The stress tensor $\underline{\underline{\sigma}}$ is decomposed, for the so called Newtonian fluids (where the stress at a point varies linearly with the rate of the fluid deformation), into an isotropic component, called the pressure p, and the deviatoric component, called the viscous stress tensor, $\underline{\underline{\tau}}$:

$$\underline{\underline{\sigma}} = -p\underline{\underline{I}} + \underline{\underline{\tau}}, \tag{2.3}$$

where:

$$\underline{\underline{\tau}}\left(\underline{u}\right) = \mu\left(\underline{\underline{\nabla}}\,\underline{u} + \underline{\underline{\nabla}}\,\underline{u}^{T}\right) + \left(\kappa_q - \frac{2}{3}\mu\right)\text{div}\left(\underline{u}\right)\underline{\underline{I}}. \tag{2.4}$$

μ is the molecular viscosity and κ_q the volume viscosity, usually neglected for fluids and therefore omitted hereafter. Similarly to the continuity equation, Equation (2.2) first term describes the variation of momentum per unit of volume. The second is a convection term of the momentum fluxes over surfaces.

Remark 2.1.1. Equations (3.1) and (2.2) are written in their conservative form: all terms are written as space or time divergence. When dealing with singular solutions, those are mandatory. Otherwise, the non conservative form is equivalent and reads for these equations:

$$\begin{cases} \dfrac{\partial \rho}{\partial t} + \underline{\nabla}\rho \cdot \underline{u} = -\rho \text{div}\left(\underline{u}\right), \\ \rho\left(\dfrac{\partial \underline{u}}{\partial t} + \underline{\underline{\nabla}}\,\underline{u} \cdot \underline{u}\right) = \underline{\text{div}}\left(\underline{\underline{\sigma}}\right) + \underline{f}. \end{cases} \tag{2.5}$$

When studying the transport of a variable ψ, two point of views can be adopted. The Eulerian one looks at $\frac{\partial}{\partial t}\psi(\underline{x}, t)$, where the space variable $\underline{x}$ is fixed.
The Lagrangian point of view looks at the variable evolution following the fluid particles, so the space variable $\underline{x}(t)$ is time dependent. The variable evolution can then be defined by its Lagrangian derivative, also called particle derivative:

$$\frac{\mathrm{d}\psi(\underline{x}(t), t)}{\mathrm{d}t} = \frac{\partial \psi(\underline{x}(t), t)}{\partial t} + \underline{\nabla}\psi \cdot \underline{u}.$$

2.1.1 Energy equations

This subsection presents the different energy equations that can be solved for the fluid. The latter is considered as an ideal gas. Its equation of state linking the density, pressure and energy reads:

$$p = \rho R_a T = (\gamma - 1)\rho\, e, \tag{2.6}$$

with T the fluid temperature, e its internal energy (per unit of mass), $R_a = 287.058\,\mathrm{J\,kg^{-1}\,K^{-1}}$ the specific gas constant and $\gamma = \dfrac{c_p}{c_v} = 1.4$ the dry air heat capacity ratio. Let's now derive the different energy equations. Applying the first law of thermodynamics to a control volume yields to the total energy (per unit of mass) E equation:

$$\frac{\partial\left(\rho E\right)}{\partial t} + \mathrm{div}\,\left(\rho E \underline{u}\right) = -\mathrm{div}\left(\underline{q}_E\right) + \rho \underline{f} \cdot \underline{u} + \mathrm{div}\,\left(\underline{\underline{\sigma}} \cdot \underline{u}\right) + \Gamma_E, \tag{2.7}$$

where $E = e + \dfrac{|\underline{u}|^2}{2}$ is the sum of the internal e and kinetic energy.

> **Remark 2.1.2.** It is considered that the total energy is only composed of the internal and kinetic energy, since the present manuscript focuses mainly on studies with negligible variation of potential energy.

Equation (2.7) right-hand-side first term is the heat transfer rate by conduction through the volume surfaces, modelled by the Fourier et al. (1822) [↗]law:

$$\underline{q}_E = -\lambda \underline{\nabla} T, \tag{2.8}$$

where λ is the fluid thermal conductivity. The second term is the work done on the volume by the external forces. The third is the work done by the surface forces and Γ_E is a source term. One can see the analogy to the first law of Thermodynamics, where the evolution of the volume energy is equal to the sum of heat transfer and work done on it.
Equation (2.7) can be used for derive the transport equation of other thermal quantities. By applying the scalar product of the momentum equation (Equation (2.2), without the mass source term) and the velocity $\underline{u}$, one obtains:

$$\underline{u} \cdot \frac{\partial(\rho \underline{u})}{\partial t} + \underline{u} \cdot \underline{\mathrm{div}}\,\left(\underline{u} \otimes \rho\, \underline{u}\right) = \underline{u} \cdot \underline{\mathrm{div}}\,\left(\underline{\underline{\sigma}}\right) + \underline{u} \cdot \rho \underline{f}. \tag{2.9}$$

which can be rewritten as:

$$\frac{\partial\left(\rho \dfrac{|\underline{u}|^2}{2}\right)}{\partial t} + \mathrm{div}\,\left(\rho \frac{|\underline{u}|^2}{2} \underline{u}\right) = -\underline{u} \cdot \underline{\nabla} p + \underline{u} \cdot \underline{\mathrm{div}}\,\left(\underline{\underline{\tau}}\right) + \underline{u} \cdot \rho \underline{f}. \tag{2.10}$$

Subtracting the kinetic energy transport equation (Equation (2.10)) to the total energy equation (Equation (2.7)) yields to the internal energy equation:

$$\frac{\partial\left(\rho e\right)}{\partial t} + \mathrm{div}\,\left(\rho e \underline{u}\right) = -p\mathrm{div}\,\left(\underline{u}\right) + \underline{\underline{\tau}} : \underline{\underline{\nabla}}\,\underline{u} + \mathrm{div}\,\left(\lambda \underline{\nabla} T\right) + \Gamma_E. \tag{2.11}$$

Note that $-p\mathrm{div}\,\left(\underline{u}\right) = \mathrm{div}\,\left(p\underline{u}\right) - \underline{u} \cdot \underline{\nabla} p$ and $\underline{\underline{\tau}} : \underline{\underline{\nabla}}\,\underline{u} = \underline{\mathrm{div}}\,\left(\underline{\underline{\tau}} \cdot \underline{u}\right) - \underline{u} \cdot \underline{\mathrm{div}}\,\left(\underline{\underline{\tau}}\right)$. The latter term is called the dissipation function related to the deformation of the fluid due to the molecular viscosity.

Remark 2.1.3. In the ideal gas scope, this equation can also be rewritten using the temperature. The Maxwell's relation states that:

$$\mathrm{d}e = c_v \mathrm{d}T + \left(T \frac{\partial p}{\partial T}\bigg|_{\rho} \right) \mathrm{d}v, \quad \text{so} \quad e = c_v T,$$

where c_v is the fluid heat capacity, considered constant here. The internal energy equation reads then:

$$c_v \left(\frac{\partial (\rho T)}{\partial t} + \mathrm{div}\,(T \underline{u} \rho) \right) = -p \mathrm{div}\,(\underline{u}) + \underline{\underline{\tau}} : \underline{\underline{\nabla u}} + \mathrm{div}\,(\lambda \underline{\nabla} T) + \Gamma_E, \tag{2.12}$$

To go further, the fluid enthalpy can be defined as $h = e + \frac{p}{\rho}$. Since $\frac{\mathrm{d}}{\mathrm{d}t}\left(\frac{p}{\rho}\right) = \frac{1}{\rho}\frac{\mathrm{d}p}{\mathrm{d}t} - \frac{p}{\rho^2}\frac{\mathrm{d}\rho}{\mathrm{d}t}$ and $\frac{\mathrm{d}\rho}{\mathrm{d}t} = -\rho \mathrm{div}\,(\underline{u})$, the enthalpy expression can be injected in the Equation (2.11) leading to:

$$\frac{\partial (\rho h)}{\partial t} + \mathrm{div}\,(\rho h \underline{u}) = \frac{\mathrm{d}p}{\mathrm{d}t} + \underline{\underline{\tau}} : \underline{\underline{\nabla u}} + \mathrm{div}\,(\lambda \underline{\nabla} T) + \Gamma_E. \tag{2.13}$$

Remark 2.1.4. In the ideal gas scope, this equation can also be rewritten using the temperature. The Maxwell's relation states that:

$$\mathrm{d}h = c_p \mathrm{d}T + \frac{1}{\rho}(1 - \beta T)\mathrm{d}p, \quad \text{so} \quad h = c_p T.$$

With β the fluid dilation coefficient, defined as:

$$\beta = \rho \frac{\partial \rho^{-1}}{\partial T}\bigg|_{p} = \frac{1}{T}, \quad \text{for ideal gases.}$$

The enthalpy equation reads then:

$$c_p \left(\frac{\partial (\rho T)}{\partial t} + \mathrm{div}\,(\rho T \underline{u}) \right) = \frac{\mathrm{d}p}{\mathrm{d}t} + \underline{\underline{\tau}} : \underline{\underline{\nabla u}} + \mathrm{div}\,(\lambda \underline{\nabla} T) + \Gamma_E. \tag{2.14}$$

The first and second thermodynamic laws state that $\mathrm{d}e = \delta Q + \delta W$, where Q and W are the heat exchange and work (per unit of mass) done over the system, and that $\mathrm{d}s = \frac{\delta Q}{T}$ (for a reversible process), with s the fluid entropy. Combining both laws leads to the fundamental thermodynamic relation, used to the derivation of other known thermodynamic laws such as the Maxwell relations:

$$\mathrm{d}e = T\mathrm{d}s - p\mathrm{d}\left(\frac{1}{\rho}\right), \tag{2.15}$$

where chemical reactions were not considered. The latter equation is written as:

$$\rho T \frac{\mathrm{d}s}{\mathrm{d}t} = \rho \frac{\mathrm{d}e}{\mathrm{d}t} - \frac{p}{\rho}\frac{\mathrm{d}\rho}{\mathrm{d}t}. \tag{2.16}$$

Notice that the right hand side second term is (using the continuity equation) equal to $-p\mathrm{div}\,(\underline{u})$. Injecting Equation (2.16) into Equation (2.11) leads to the fluid entropy transport equation:

$$\begin{aligned} \frac{\partial (\rho s)}{\partial t} + \mathrm{div}\,(\rho s \underline{u}) &= \frac{1}{T}\underline{\underline{\tau}} : \underline{\underline{\nabla u}} + \frac{1}{T}\mathrm{div}\,(\lambda \underline{\nabla} T) + \Gamma_s. \\ &= \frac{1}{T}\underline{\underline{\tau}} : \underline{\underline{\nabla u}} + \mathrm{div}\left(\lambda \frac{\underline{\nabla} T}{T}\right) - \lambda \frac{\underline{\nabla}^2 T}{T^2} + \Gamma_s. \end{aligned} \tag{2.17}$$

Remark 2.1.5. For outdoor atmospheric applications, the potential temperature θ_p is defined using the entropy. This thermal variable is conserved during isentropic displacements through the atmosphere i.e.:

$$\frac{c_p}{\theta_p}\frac{\mathrm{d}\theta_p}{\mathrm{d}t} = \frac{\mathrm{d}s}{\mathrm{d}t}. \tag{2.18}$$

The potential temperature can be interpreted as the temperature that a volume would have if it travels isentropically from a height z to the surface. Its expression, by integrating Equation (2.18), is:

$$\theta_p = T\left(\frac{p_0}{p}\right)^{\frac{R_a}{c_p}}. \tag{2.19}$$

This variable is used in code_saturne's atmospheric module by solving the following equation:

$$c_p\frac{\partial(\rho\theta_p)}{\partial t} + c_p\mathrm{div}\ (\rho\theta_p\underline{u}) = \mathrm{div}\ (\lambda\underline{\nabla}\theta_p) + \Gamma_E\left(\frac{p}{p_0}\right)^{\frac{R_a}{c_p}}.$$

To summarise, the different thermal equations that can be solved are:

$$\begin{aligned}
&(E) \quad \frac{\partial(\rho E)}{\partial t} + \mathrm{div}\ (\rho E\underline{u}) = -\mathrm{div}\,(\underline{q}) + \rho\underline{f}\cdot\underline{u} + \mathrm{div}\ \left(\underline{\underline{\sigma}}\cdot\underline{u}\right) + \Gamma_E,\\
&(e) \quad \frac{\partial(\rho e)}{\partial t} + \mathrm{div}\,(\rho e\underline{u}) = -p\mathrm{div}\,(\underline{u}) + \underline{\underline{\tau}} : \underline{\underline{\nabla u}} + \mathrm{div}\,(\lambda\underline{\nabla}T) + \Gamma_E,\\
&(h) \quad \frac{\partial(\rho h)}{\partial t} + \mathrm{div}\ (\rho h\underline{u}) = \frac{dp}{dt} + \underline{\underline{\tau}} : \underline{\underline{\nabla u}} + \mathrm{div}\,(\lambda\underline{\nabla}T) + \Gamma_E.\\
&(s) \quad \frac{\partial(\rho s)}{\partial t} + \mathrm{div}\,(\rho s\underline{u}) = \frac{1}{T}\underline{\underline{\tau}} : \underline{\underline{\nabla u}} + \mathrm{div}\ \left(\lambda\frac{\nabla T}{T}\right) - \lambda\frac{\nabla^2 T}{T^2} + \Gamma_s.
\end{aligned} \tag{2.20}$$

Any additional scalar transport equation, such as chemical species, reads:

$$\frac{\partial(\rho Y)}{\partial t} + \mathrm{div}\ (Y\rho\underline{u}) = \mathrm{div}\ (K\underline{\nabla}Y) + \Gamma_Y. \tag{2.21}$$

where Γ_Y is a scalar source term, and K is the molecular diffusivity of the scalar.

2.1.2 Non dimensional compressible Navier–Stokes equations

Non dimensional variables related to the ones used in the Navier–Stokes equations are defined: $x \coloneqq \hat{x}L$, $\rho \coloneqq \hat{\rho}\rho_r$, $p \coloneqq \hat{p}R_a\rho_r T_r$, $t \coloneqq t^+L/U$, $\underline{u} \coloneqq U\underline{\hat{u}}$, $T \coloneqq \hat{T}T_r$ and $e \coloneqq \hat{e}c_v T_r$. The equations presented in the section above are rewritten using these new variables for an ideal gas. The mass conservation Equation (3.1) reads:

$$\frac{\rho_r U}{L}\frac{\partial\hat{\rho}}{\partial t^+} + \frac{\rho_r U}{L}\widehat{\mathrm{div}}\,(\hat{\rho}\underline{\hat{u}}) = 0 \Leftrightarrow \frac{\partial\hat{\rho}}{\partial t^+} + \widehat{\mathrm{div}}\ \left(\underline{\hat{q}}\right) = 0. \tag{2.22}$$

The momentum Equation (2.2) can be rewritten (considering the viscosity constant) after some rearrangement as:

$$\frac{\partial(\hat{\rho}\underline{\hat{u}})}{\partial t^+} + \widehat{\underline{\mathrm{div}}}\,(\underline{\hat{u}}\otimes\hat{\rho}\,\underline{\hat{u}}) = -\frac{R_a T_r}{U^2}\widehat{\underline{\nabla}}\hat{p} + \frac{\mu}{LU\rho_r}\widehat{\underline{\mathrm{div}}}\left((\widehat{\underline{\underline{\nabla}}}\underline{\hat{u}} + \widehat{\underline{\underline{\nabla}}}\underline{\hat{u}}^T) - \frac{2}{3}\widehat{\mathrm{div}}\,(\underline{\hat{u}})\underline{\underline{I}}\right) + \frac{L}{U^2}\hat{\rho}\underline{g}. \tag{2.23}$$

Introducing the Mach number,

$$\mathrm{Ma} \coloneqq \frac{U}{c}, \tag{2.24}$$

the speed of sound for ideal gases,

$$c = \sqrt{\gamma R_a T_r}, \tag{2.25}$$

the Reynolds number

$$Re \coloneqq \frac{UL\rho}{\mu}, \tag{2.26}$$

and the Froude number

$$Fr \coloneqq \frac{U}{\sqrt{gL}}, \tag{2.27}$$

leads to the final non dimensional form of the momentum equation:

$$\frac{\partial(\hat{\rho}\underline{\hat{u}})}{\partial t^+} + \widehat{\mathrm{div}}\,(\underline{\hat{u}} \otimes \hat{\rho}\,\underline{\hat{u}}) = -\frac{1}{\gamma \mathrm{Ma}^2}\widehat{\underline{\nabla}}\hat{p} + \frac{1}{Re}\widehat{\mathrm{div}}\left((\underline{\underline{\widehat{\nabla}}}\underline{\hat{u}} + \underline{\underline{\widehat{\nabla}}}\underline{\hat{u}}^T) - \frac{2}{3}\widehat{\mathrm{div}}\,(\underline{\hat{u}})\underline{\underline{I}}\right) + \frac{1}{Fr^2}\hat{\rho}\underline{e}_z. \tag{2.28}$$

Note that the Reynolds number is the ratio of inertial forces to viscous forces within the fluid. The Froude number is the ratio of the flow inertia to the external field (here the gravity).

Remark 2.1.6. Non dimensional equations are useful when studying a particular type of flow. For instance, for high speed flows, the Mach number is also high, which leads to the vanishment of the first right hand term of the Equation (2.28).

The internal energy equation, which is the thermal equation used in this work, is rewritten in its non dimensional form. Details on the choice of this equation are given later in the manuscript. Disconsidering additional source terms, the modified Equation (2.12) reads:

$$\frac{\rho_r c_v T_r U}{L}\left(\frac{\partial \hat{\rho}\hat{T}}{\partial t^+} + \widehat{\mathrm{div}}\,(T\underline{\hat{u}}\hat{\rho})\right) = -\frac{R_a T_r \rho_r}{L}\hat{p}\widehat{\mathrm{div}}\,(\underline{\hat{u}}) + \frac{\mu U}{L}\underline{\underline{\tau}} : \underline{\underline{\widehat{\nabla}}}\underline{\hat{u}} + \frac{T_r}{L^2}\widehat{\mathrm{div}}\,(\lambda\underline{\widehat{\nabla}}\hat{T}). \tag{2.29}$$

In the ideal gas framework, $R_a = c_p - c_v$. Equation (2.12) is then multiplied by $\dfrac{L}{\rho_r c_v T_r U}$:

$$\frac{\partial \hat{\rho}\hat{T}}{\partial t^+} + \widehat{\mathrm{div}}\,(T\underline{\hat{u}}\hat{\rho}) = -\frac{R_a}{c_v}\hat{p}\widehat{\mathrm{div}}\,(\underline{\hat{u}}) + \frac{U\nu}{Lc_v T_r}\frac{U}{U}\underline{\underline{\tau}} : \underline{\underline{\widehat{\nabla}}}\underline{\hat{u}} + \frac{\lambda}{Lc_v\rho_r U}\frac{\mu c_p}{\mu c_p}\widehat{\mathrm{div}}\,(\underline{\widehat{\nabla}}\hat{T}). \tag{2.30}$$

After defining the Prandtl number as the ratio of the momentum diffusivity to the thermal diffusivity, the latter equation is written in its final form:

$$\frac{\partial \hat{\rho}\hat{T}}{\partial t^+} + \widehat{\mathrm{div}}\,(T\underline{\hat{u}}\hat{\rho}) = -(\gamma-1)\hat{p}\widehat{\mathrm{div}}\,(\underline{\hat{u}}) + (\gamma-1)\frac{\gamma \mathrm{Ma}^2}{Re}\underline{\underline{\tau}} : \underline{\underline{\widehat{\nabla}}}\underline{\hat{u}} + \frac{\gamma}{Pr\ Re}\widehat{\mathrm{div}}\,(\underline{\widehat{\nabla}}\hat{T}). \tag{2.31}$$

Lastly, the scalar equation and ideal gas equation of state read:

$$\frac{\partial \hat{\rho}Y}{\partial t^+} + \widehat{\mathrm{div}}\,(Y\hat{\rho}\underline{\hat{u}}) = \frac{1}{Re\ Sc}\widehat{\mathrm{div}}\left(\underline{\widehat{\nabla}}Y\right), \qquad p = \rho_r T_r \rho R_a T. \tag{2.32}$$

Where $Sc = \dfrac{\nu}{K}$, the ratio of the kinematic viscosity $\nu = \mu/\rho$ and the scalar molecular viscosity, is the Schmidt number. A summary of other non dimensional number useful for the indoor environment, used to characterised its different physics is presented in Table 2.1.
To conclude on this subsection, the non dimensional equations are often used as basis to simplify the Navier–Stokes set of equations depending on the type of application.

Name		Ratio	Formula	Used in
Prandtl	Pr	Dynamic x heat diffusion	$\frac{\mu C_p}{\lambda}$	Diffusion
Nusselt	Nu	Convection x conduction	$\frac{hL}{\lambda}$	Heat transfers
Reynolds	Re	Inertia x viscous forces	$\frac{\rho U L}{\mu}$	Turbulence description
Rayleigh	Ra		$\frac{g\beta\Delta T L^3}{\alpha\nu}$	Turbulence description
Grashoff	Gr	Buoyant x viscous forces	$\frac{g\beta(T_w - T_\infty)L^3}{\nu^2}$	Natural convection
Richardson	Ri	Natural x forced convection	$\frac{g\beta(T_w - T_\infty)L}{U^2}$	Convection

Table 2.1: Adimensional numbers often used in thermal-aeraulics. $\alpha = \lambda/(\rho c_p)$ is the thermal diffusivity, L is a characteristic length, g is the gravitational acceleration constant, h is the convection heat transfer coefficient, U is a characteristic velocity, T_w is a surface temperature and T_∞ the bulk temperature.

2.2 Phenomenological background

The indoor airflow can be characterised by different physical phenomena. In the following, some identified important flow drivers are presented.

2.2.1 Fluid composition

One may define in the first place which kind of fluid is simulated. Indeed, taking into account every single mixture component is usually more binding than useful. In case of a reactive flow, considering some particular species is primordial. However, all chemical reaction is left to further investigation and is beyond the scope of the present manuscript (since it usually leads to very small species concentration); thus, the problem will be simplified. The major fluid component is the dry air, modelled as a mixture of oxygen and nitrogen with a molar mass equal to $M_a = 0.028\,96\,\mathrm{kg\,mol^{-1}}$. Another important component is the water, in both its liquid and gaseous phases, which needs to be considered. Its presence affects the mixture properties such as the density and thermal coefficients. In some cases, a phase change may occur and cannot be neglected. The latter phenomena complicates considerably the numerical resolution method.
A high humidity level in a given set up can affect the occupants well being; it also facilitates the microbes growth and expansion. Moreover, a low humidity may lead to a respiratory system infection and eventually electrostatic shocks (Toftum et al. (1998); Fountain et al. (1999) , see Arens and Baughman (1996) for a review of the humidity effects on health as addressed in indoor ventilation and environmental standards). Some CFD studies related to the humidity in indoor systems can be highlighted (Steeman et al., 2009; Teodosiu et al., 2003; You et al., 2017) .

2.2.2 Pressure variation

In indoor environments, a small pressure variation relative to the atmospheric one can induce flow. It is thus important to consider such variations. In addition, pressure can be a quantity of interest to reproduce correct thermal exchanges in presence of natural convection.

To illustrate this phenomena, the pressure variation created by the opening of two windows which are not in the same building facade is likely to create a draught. Similarly, if an indoor zone is exposed to any source of power, its temperature will rise creating thermal and pressure gradients and thus mass transfer.

2.2.3 Total energy conservation

Besides the importance of preserving the mass and momentum of the system, it is important as well to preserve its total energy. This is particularly relevant to correctly reproduce singular solutions (Archambeau et al., 2009; Amino et al., 2022) . The reader may ask himself, in the given indoor context, if focusing on the correct shock reproduction is of importance. Indeed, this would be doubtlessly true in the aerospace's context for instance, where the flow is at high velocity, with the possible propagation of pressure shock waves. Nevertheless, one may illustrate the importance of being consistent (see the definition in Chapter 3) related to singular solutions when a fluid, at a given state (density, pressure, velocity), enters in contact through an interface with another state (the opening of a door or windows for example). This is a singular problem in a smaller scale, but not negligible since a small pressure difference is able to impact the flow (see Figure 2.1 for an illustration).

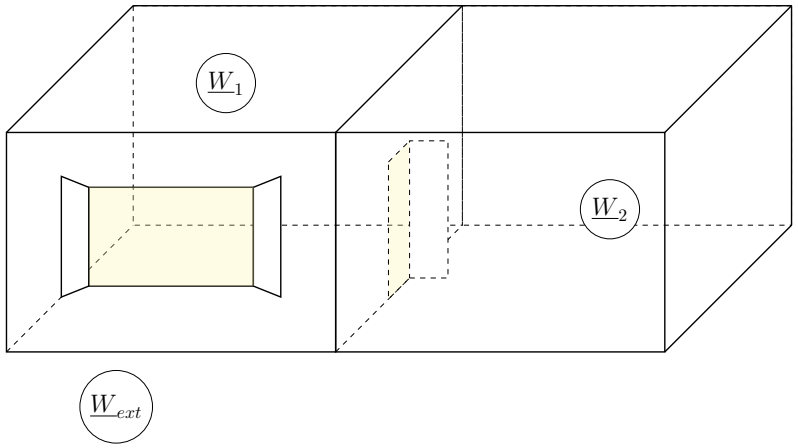

Figure 2.1: Example of configuration with three distinct initial states that may enter in contact at a given time. Here, two pieces indoor system enter in contact between themselves and with the outdoor conditions through the opening of a window.

Another example of the importance of taking account of the pressure variation and preserving the total energy is to properly perform simulations of laboratories or hospital rooms under safety conditions. CFD is notably cited as an useful tool for designing such configurations ventilation systems (norm NF-EN-ISO-14644-16). Indeed, for rooms where no contamination is wanted, a differential of pressure of 15 ± 5 Pa is mandatory in France (norm NF-S90-351). In this context, in case of contact between two rooms, a pressure (and possibly other variables) discontinuity needs to be considered.

2.2.4 Buoyancy effects

Buoyancy effects are a crucial physical stake to correctly reproduce the thermal impacts on the flow. Directly linked to the density, this phenomena is a consequence of artificial and natural sources of power such as a convector, the presence of humans in the given room and the sun radiation. Such sources create a thermal plume which drives the local flow. Buoyant effects are also used to design natural ventilated systems (see Linden (1999) for more details about natural ventilation). Many studies focused on this phenomena using CFD (Alsaad and Voelker; Zukowska et al., 2007; Choi and Kim, 2012; Teodosiu et al., 2014) , notably with some guidance for buoyancy driven flows (Cook and Lomas, 1997) .

In case of human presence in the system, a correct treatment of possible thermal sources has to be made. Indeed, thermal plumes can be created with presences of humans (Murakami et al., 2000b; Liu et al., 2015) ; this is also directly linked to the buoyancy forces effects on the flow (see Figure 2.3, left). Occupants can be as well source of pollution in some enclosed spaces. For further information, experimental (Zukowska et al., 2007, 2012) and numerical studies (Sørensen and Voigt, 2003; Srebric et al., 2008; Gupta et al., 2011) are available in the literature. Natural convection flow can also be turbulent, which makes it even harder to simulate (Salat et al., 2004) . Experimental data concerning thermal plumes, useful for validation purposes, are also available for different source geometries (Kofoed, 1991; Bouzinaoui et al., 2007; Blaise, 2008) .

2.2.5 Turbulence

In both indoor and outdoor environments, the majority of flows are turbulent; this phenomena is chaotic by itself. This term is used to characterise random fluctuations appearing in a given flow when its speed is important or when its scale is large. This phenomena is present in atmospheric, rivers, ocean and indoor flows. In the industrial context, flows around any solid shape such as cars, planes and trains are affected by turbulence as well (see Figure 2.2 for some examples of turbulent flows).
To describe its origin, one may focus on the non dimensional momentum equation (Equation (2.28)). The momentum may be transported by both diffusive and convective effects. Their interaction is useful to describe the flow turbulence. Indeed, in the diffusive term of the non dimensional equation, the Reynolds number appears. This number is defined as the ratio between the inertial and viscous flow effects. It can be interpreted as the ratio between characteristic times of both physical phenomena aforementioned.
If the inertia effects are more important than the viscous ones, then the Reynolds number is greater than unity and the flow is turbulent. Otherwise, the flow is laminar and the diffusive effects prevail.
An important concept related to turbulent flows which needs to be accounted for in simulations is the energy cascade, mentioned first by Lewis Fry Richardson (1922) . The latter stated that a given turbulent flow is composed of several structures of different scales. The Reynolds number for those with a larger length scale is important. Thus, the viscous effects, less important, are not able to dissipate the structure kinetic energy into heat. These eddies are also less stable, and tend to vanish with time to smaller structures. Similarly, these structures will be divided into even smaller eddies at their turn until their length scale is small enough so the viscous effects related to the inertial ones are not small anymore: the energy is finally dissipated into heat. Kolmogorov (1941b,a) studied at his turn the turbulent cascade and proposed a definition of this dissipation scale where $Re = 1$, named after his name. The Kolmogorov scale, also known as the dissipation scale has the particularity of dissipating the structures kinetic energy into heat. However, turbulence is a complex problem, and is not completely described by the aforementioned sketch. It remains an open fundamental research area, in particular when looking at advanced statistical properties such as intermittency (Yasuda and Vassilicos, 2018) .
In the indoor environment framework, turbulence models and approaches were widely tested on experimental configurations or in conception and optimisation studies. Zhai et al. (2007) and Chen (1995) compared several turbulence models, showing that different average models (later presented in Subsection 2.3.2) have correct accuracy on the mean indoor flow quantities but are not able to reproduce turbulent ones. Other comparisons were made in the last decades (Posner et al., 2003; Kuznik et al., 2007; Blocken, 2018) . Recently, more and more research on indoor airflow is made by combining both averaged and unsteady approaches (Jiang et al., 2002; Chang et al., 2006; Sajjadi et al., 2017) .
Note that more details on the different turbulence modelling are provided in the next section.

2.2.6 Radiation

The most impacting radiations in the indoor environment are the solar and infrared (emissions of low temperature bodies) ones. They can impact the thermal behaviour of a given system (Sadrizadeh and

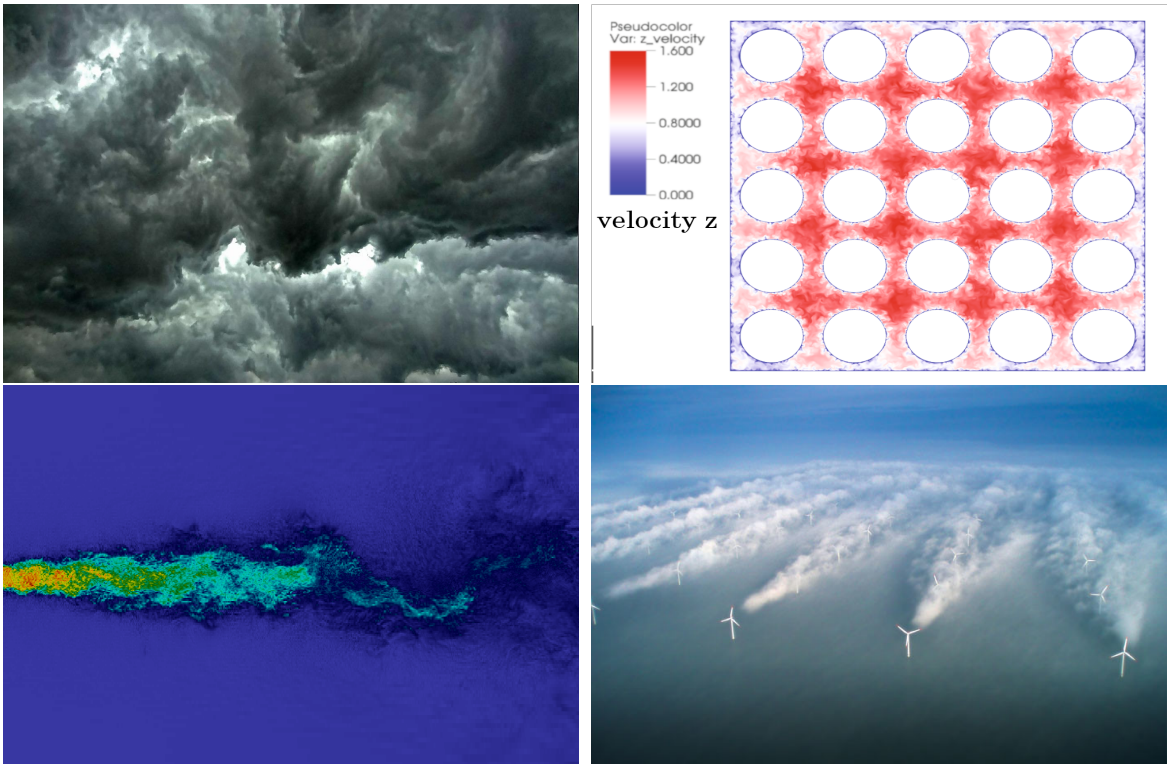

Figure 2.2: Examples of turbulent flows. (Top left) Photo. Turbulence in an atmospheric flow. (Top right) Simulations. Instantaneous stream-wise velocity for a 5x5 square rod bundle configuration (Kraus et al., 2021). (Bottom left) Simulation. Velocity field of an axisymmetric jet. (Bottom right) Photo. Offshore wind farm picture, credit: Christian Steiness/Vattenfall.

Holmberg, 2015). A good example is the greenhouse effects of a room under the sun radiation (sketched in Figure 2.3, right), where the room thermal conditions would vary in a non negligent time. However, a good setting of the thermal boundary conditions, such as treating the radiation effects as source terms and taking into account possible emissions may be sufficient in some cases to correctly reproduce the flow. Sometimes, a radiation model shall be used as well, since a little difference in the temperature distribution over the environment can lead to an incorrect airflow pattern and thus impact any type of study.
This topic is left to further investigations given its complexity.

2.2.7 Jets

Jets are common in indoor environments, usually used for ventilation. A velocity shear is created between the entering and ambient fluids and may lead to an important amount of turbulence.
A jet can be classified as plane, round, axial or three-dimensional. Depending on the thermal environment conditions, it can also be classified as isothermal or anisothermal, where its behaviour will depend on buoyant forces. Each jet can be characterised by its Reynolds number based on the initial jet speed, the inlet length d, the fluid viscosity and density. Above $Re = 2.10^3$, the jet is considered turbulent (Lee et al., 2003) and a good account of this phenomena is necessary.
Different jet zones exist (Pope, 2000). The first is the potential core, where the jet maximum velocity U_m is equal to the injection velocity U_{in}, followed by the characteristic zone, where $\frac{U_m}{U_{in}} = \frac{1}{y^n}$, y being the axial coordinate. This zone is negligible for axisymmetric jets (Kuznik, 2005). The axisymmetric zone or developing zone (Kaushik et al., 2015) describes the majority of the jet heat and mass transfer.

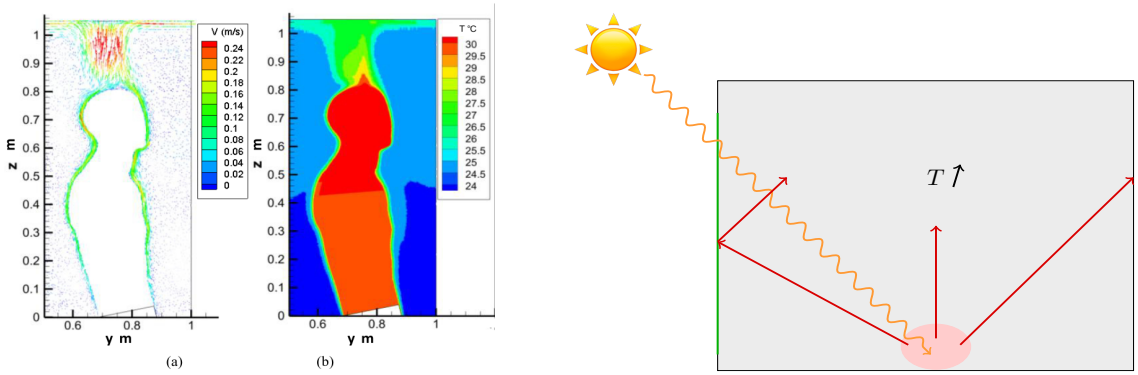

Figure 2.3: (Left) Time average flow field from Liu et al. (2015) numerical results, (a) velocity (b) temperature. (Right) Greenhouse effect illustration, which can affect the indoor environment thermal state. Solar waves are in orange, infrared in red.

In this zone, $\frac{U_m}{U_{in}} = \frac{1}{y}$. Finally, the terminal zone, also called fully-developed zone, contains the less important jet velocities with a consequent jet diffusion.
Kelvin-Helmholtz (KH) instabilities, which comes from shear stresses, are commonly present in jets. They are created by the velocity difference in the interface between two different fluids. For instance, ocean waves or vortices created behind trains or planes are typically result from KH instabilities (Figure 2.4). This type of instability contributes to vortices in the jet and other fluid interfaces, whose size gets

Figure 2.4: KH instabilities. (Left) Sky instabilities. Credits: Alec Kownacki. (Right) KH instabilities represented by Van Gogh.

more important while distancing the jet inlet. Thus, in presence of jets, a good reproduction of these instabilities is important.

2.2.8 Summary

The main physical processes to be accounted for have been presented in this section. From the buoyant forces to the pressure variation, the present work shall focus as well on the possible variable fluid properties and if possible, on all the other processes.
Given the number of physical phenomena of interest and their complexity, not all are considered in this thesis. More particularly, the radiation effects and the human presence impact on the flow are left for further scientific investigations (see Figure 2.5 for a summary of the aimed stakes).

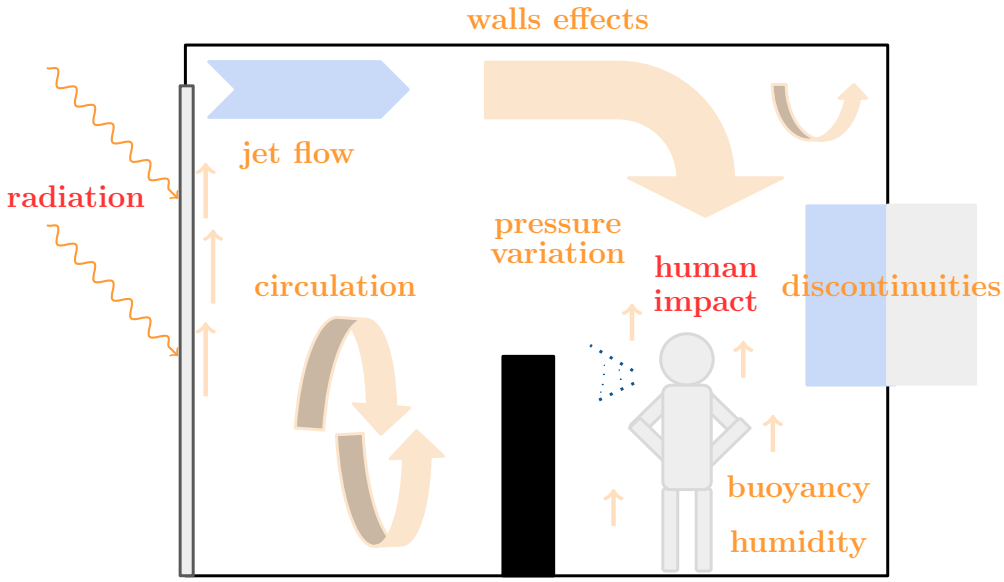

Figure 2.5: Aforementioned indoor physics to be accounted for an indoor airflow simulation. In orange, the physical processes to be focused while designing the numerical scheme.

2.3 Modelling the indoor physics

In a CFD simulation, models are used to simplify or close the complex system of equations to be solved. Moreover, the numerical results are dependent on the way one discretises the time and space and also on how the mathematical problem is solved. In this section are presented the different modelling strategies related to some physical phenomena aforementioned. Note that the numerical discretisation details are left for the next chapter.

2.3.1 Acoustic waves and buoyancy

To better understand the motivations of the following simplifications, one needs to define the Courant Friedrichs and Lewy number (CFL), a classical stability conditions related to numerical schemes in fluid mechanics. It is defined as the ratio of the distance travelled by the flow at speed u during a given time step by the volume spatial step i.e.:

$$\text{CFL} = u\,\Delta t/\Delta x.$$

In order to capture the flow information in this case, the simulation time step must be inferior to the ratio of the spatial step and the velocity u. If one wants to take the macro speed u and also the pressure waves speed c on a simulation, the condition on the time step reads:

$$\Delta t < \frac{\Delta x}{u + c}$$

For flows with low speed, taking into account the sound pressure waves can be thus computationally more expensive than it could be without accounting for the celerity (for important Mach number flows, the simulation would automatically considerate the acoustic effects). In cases where the acoustic have little impact on the physical simulated phenomena, it is efficient to get rid of it in the Navier–Stokes equations. To do so, several methods which apply an asymptotic expansion on the governing equations variables exist and are detailed hereafter. Generally, the problem stated is how to accurately reproduce the flow while saving as much as possible computational time of simulation.

The "simplest" and very popular approximation of the Navier–Stokes equation is the incompressible flow hypothesis, often used when the flow Mach number $u/c << 1$. In that case, the density along the line of the flow is considered constant, that is $\frac{\mathrm{d}\rho}{\mathrm{d}t} = 0$. The mass equation becomes then:

$$\mathrm{div}\,(\underline{u}) = 0.$$

The density and pressure waves are disconsidered and the incompressible momentum equation reads:

$$\frac{\partial(\rho\underline{u})}{\partial t} + \underline{\mathrm{div}}\,(\underline{u} \otimes \rho\,\underline{u}) = -\underline{\nabla}(p) + \underline{\mathrm{div}}\,(\mu\underline{\underline{\nabla}}\underline{u}) + \rho\underline{g}.$$

Similarly, the velocity non divergence affects the thermal equations as well, but this will not be further discussed here since this thesis aims to take into account both pressure and density variations.
Another model uses the so called Boussinesq (1903) approximation, which is based on a linearisation of the initial set of equations with respect to the thermodynamic variables. It is widely used, assuming that density variations have no effect on the flow, except for the buoyancy forces (i.e. on the momentum equation). In more practical terms, this approximation is typically used to model liquids around a constant temperature or natural ventilation. A reference state is introduced corresponding to a steady horizontal motion under adiabatic and non viscous conditions, satisfying a thermodynamic hydrostatic and adiabatic equilibrium (Chassaing et al., 2002) , leading to simplified Navier–Stokes equations. For instance, the mass equation reads:

$$\mathrm{div}\,(\underline{u}) = 0,$$

which is identical to the incompressible model mass equation. As previously mentioned, the Boussinesq approximation states that the density variation is only present in the momentum equation buoyant term and is considered constant in the rest of the equation, resulting in:

$$\rho_0\left(\frac{\partial\underline{u}}{\partial t} + \underline{\mathrm{div}}\,(\underline{u} \otimes \underline{u})\right) = -\underline{\nabla}(p) + \underline{\mathrm{div}}\,(\mu\underline{\underline{\nabla}}\underline{u}) + \rho\underline{g},$$

where:

$$\rho = \rho_0 - \beta\rho_0(T - T_0).$$

In this approximation, the density is considered to vary linearly with the temperature: pressure effects are not accounted, once again, restraining this type of model application field.
The anelastic approximation, widely used in the simulation of atmospheric flows, was first proposed by Ogura and Phillips (1962) to filter the acoustic waves by decomposing the Navier–Stokes equations variables. For instance, the density is written as

$$\rho(x,y,z,t) = \rho^{(0)}(z) + \gamma\mathrm{Ma}^2\rho^{(1)}(x,y,z,t) + ...$$

Other thermodynamic fields are decomposed similarly, and the velocity reads

$$\underline{u}(x,y,z,t) = \underline{u}^{(0)}(x,y,z,t) + \gamma\mathrm{Ma}^2\underline{u}^{(1)}(x,y,z,t) + ...$$

Then, the non dimensional Navier–Stokes equations (see 2.1.2) are rewritten using the anelastic decomposition at the order $(\gamma\mathrm{Ma}^2)^0$ for the velocity and density (except for the buoyant term in the momentum equation) and at the first order for the temperature and pressure. This takes into account a possible pressure and density variation; the momentum equation reads in this case:

$$\left(\frac{\partial}{\partial t}(\rho^{(0)}\underline{u}^{(0)}) + \underline{\mathrm{div}}\,(\underline{u}^{(0)} \otimes \rho^{(0)}\underline{u}^{(0)})\right) = -\underline{\nabla}p^{(1)} + \frac{1}{Re}\underline{\mathrm{div}}\left(\underline{\underline{\tau}}^{(0)}\right) + \frac{\gamma\mathrm{Ma}^2}{Fr}\rho^{(1)}\underline{g}.$$

The density is no more considered constant, but only depends on the vertical coordinate z, based on an adiabatic reference state. To this approximation the isobaric one is added: the variables are once again decomposed but differently. The pressure first term $p^{(0)}$ is time dependent. The other variables first term are both spatial and time dependent i.e. $\psi^{(0)} = \psi^{(0)}(x, y, z, t)$.
To better understand the differences between the aforementioned approximations, Schneider (2015) proposed to study which Kovasznay (1953) modes each model is able to reproduce.

Remark 2.3.1. Kovasnay modes are used to describe random fluctuations in a supersonic flow, which can be decomposed into three distinct modes: vorticity, sound and entropy. The modes follow separate linear differential equations if the fluctuations are weak. Otherwise, they have moderate interaction.
If the disturbances are not negligible, the effect of heat transfer and viscosity can be neglected regarding the short time history of disturbances. The velocity, temperature and pressure fluctuations are divided into these modes.
The velocity is split into a non divergent and an irrotational field. The first contributes to the vorticity mode and the last one to the acoustic. Pressure variations contribute to the acoustic modes and finally, the temperature variation is divided into an isentropic and a anisentropic fluctuations. The first belongs to the acoustic modes and the second to the entropy ones.

What can be already seen from the previous equations, is that the pressure variation is not completely accounted in all approximations. This is confirmed by Schneider (2015) where none of the previous approximations take into account the acoustic modes (see Table 2.2).

Model	Continuity	Vorticity modes	Entropy modes	Acoustic modes
Incompressible	$\text{div}\,(\underline{u}) = 0$	no	no	no
Boussinesq	$\text{div}\,(\underline{u}) = 0$	yes	no	no
Isobaric	$\frac{\partial \rho^{(0)}}{\partial t} + \text{div}\,(\rho^{(0)}\underline{u}) = 0$	yes	partial	no
Anelastic	$\text{div}\,(\rho^{(0)}\underline{u}) = 0$	yes	yes	no
Compressible	$\frac{\partial \rho}{\partial t} + \text{div}\,(\rho\underline{u}) = 0$	yes	yes	yes

Table 2.2: Comparison between the different approximations related to the Kovasnay modes (from Schneider (2015)).

2.3.2 Turbulence modelling

When simulating high Reynolds number flows, the latter are no longer laminar and a complex phenomena, turbulence, introduced previously as an important physical stake, needs to be accounted for. When it comes to turbulent flows, one may distinguish several approaches.
Usually the more details one wants to get in the flow, the more computationally expensive the simulation is. Indeed, a major problem is that both space and time turbulent scales can be very small, so the number of spatial grid points and the time step needed to solve them are respectively increased and reduced.
Among the wide range of length and time scales related to turbulent flows, some are important to highlight. These are useful when setting up a turbulent simulation. One may choose which spatial scale the simulation should take into account for instance. Here are presented the four main scales in a turbulent flow (note that other scales related to heat transfer and combustion exist (Echekki, 2009)) .

First, the largest scale which is dependent on the problem geometry. Then, the integral scale (L_s) often taken as $1/5$ of the large scale, followed by the Taylor microscale (λ_s), corresponding to the inertial subrange and finally, the Kolmogorov scale (η_s), the smallest one. These scales can be compared and characterised by their wavenumbers κ (Figure 2.6). Note that when the Reynolds number decreases, the inertial subrange decreases as well.

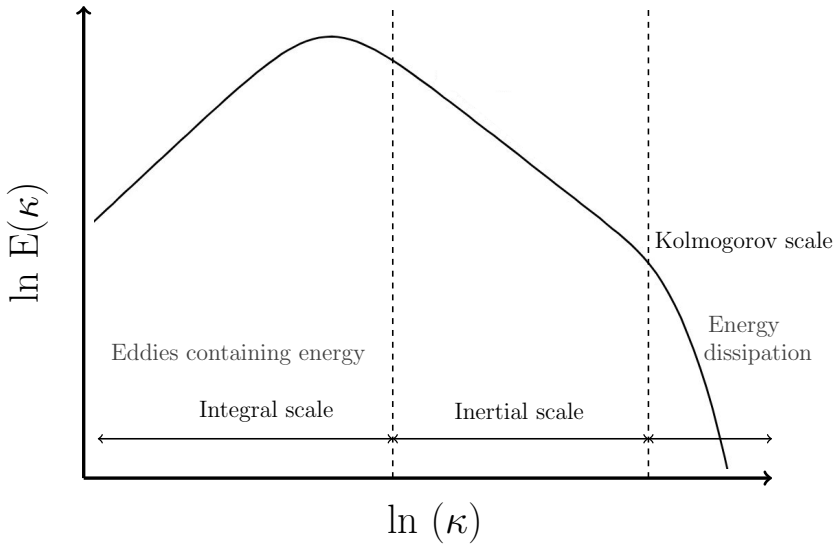

Figure 2.6: Turbulence energy wavenumber spectrum. The viscous subrange is also called dissipation scale. The maximum y-axis point is the integral scale. Between lies the inertial scale.

These scales can be written according to the flow variables (Sagaut et al., 2013) and are presented in Table 2.3.

Scale	Integral	Taylor	Kolmogorov
Space	$L_s = \frac{k^{3/2}}{\varepsilon}$	$\lambda_s = (\frac{10k\nu}{\varepsilon})^{0.5}$	$\eta_s = (\frac{\nu^3}{\varepsilon})^{1/4}$
Time	$\tau_L = \frac{k}{\varepsilon}$	$\tau_\lambda = \sqrt{\frac{15\nu}{\varepsilon}}$	$\tau_\eta = \sqrt{\frac{\nu}{\varepsilon}}$
Turbulent Reynolds number	$Re_L = \frac{k^2}{\nu\varepsilon}$	$Re_\lambda = \sqrt{\frac{20}{3}}\frac{k}{\sqrt{\nu\varepsilon}}$	$Re_\eta = 1$

Table 2.3: Different turbulence scales definition Sagaut et al. (2013).

Note that the turbulent time scales can be very useful in order to correctly perform time averages during a simulation.
The most accurate numerical technique, called direct numerical simulation (DNS) is to solve the complete set of equations with no special treatment. Even with the computational growing power context, the DNS is not often used in industrial applications due to its computational cost. One effective way to reduce the calculation time while conserving a numerical accuracy is to either proceed with a statistical average on the governing equations or to apply a spatial filter in order to control which turbulent scales are modelled and which are solved (Figure 2.7).
The first method is the Reynolds averaged Navier–Stokes equations (RANS) which decomposes the fluid variables into a mean and a fluctuating part using the Reynolds average operator $\overline{(.)}$. Each variable ψ is written as $\psi = \bar{\psi} + \psi'$. For compressible and low compressible flow, the density weighted Favre average operator is used instead (i.e. $\tilde{\psi} = \overline{\rho\psi}/\overline{\rho}$, $\psi = \tilde{\psi} + \psi''$). The second approach is the large

eddy simulation (LES), where a spatial filter is applied on the Navier–Stokes equations; one part of the turbulence spectrum is solved whereas the other is modelled. ψ being a variable, the filtering operation $\overline{\psi}$ is defined as $\overline{\psi} = \int_{-\infty}^{\infty} G(x-\xi)\psi(\xi)d\xi$, where G is the LES filter function (considered homogeneous). Similar to the RANS method, the Favre filter is defined as $\tilde{\psi} = \overline{\rho\psi}/\overline{\rho}$. For both turbulent approaches, the averaged Navier–Stokes equations (using the internal energy equation) read:

$$
\begin{aligned}
&(a) \qquad \frac{\partial \overline{\rho}}{\partial t} + \text{div}\left(\overline{\underline{q}}\right) = 0, \\
&(b) \qquad \frac{\partial \overline{\underline{q}}}{\partial t} + \underline{\text{div}}\left(\tilde{\underline{u}} \otimes \overline{\underline{q}}\right) = -\underline{\nabla}\overline{p} + \underline{\text{div}}\left(\mu\left[\underline{\underline{\nabla}}\tilde{\underline{u}} + \underline{\underline{\nabla}}\tilde{\underline{u}}^T - \frac{2}{3}\text{div}\,\tilde{\underline{u}}\,\underline{\underline{I}}\right]\right) - \underline{\text{div}}\left(\underline{\underline{\tau}}_T\right) + \overline{\underline{f}}, \\
&(c) \qquad \frac{\partial\left(\overline{\rho}\,\widetilde{e}\right)}{\partial t} + \text{div}\left(\widetilde{e} \otimes \overline{\underline{q}}\right) = -\overline{p}\text{div}\left(\tilde{\underline{u}}\right) + \text{div}\left(\lambda\underline{\nabla}\widetilde{T}\right) + \underbrace{\text{div}\left(\lambda\underline{\nabla}\overline{T''}\right)}_{(1*)} \\
&\qquad\qquad - c_v\text{div}\left(\overline{\rho}\overline{\underline{u}''T''}\right) + \tilde{\underline{\underline{\tau}}} : \underline{\underline{\nabla}}\tilde{\underline{u}} + \underbrace{\overline{\underline{\underline{\tau}} : \underline{\underline{\nabla}}\underline{u}''}}_{(2*)} + \underbrace{\overline{\underline{\underline{\tau}}'' : \underline{\underline{\nabla}}\tilde{\underline{u}}}}_{(3*)}, \\
&(d) \qquad \frac{\partial\left(\overline{\rho}\,\widetilde{Y}\right)}{\partial t} + \text{div}\left(\widetilde{Y} \otimes \overline{\underline{q}}\right) = \text{div}\left(K\underline{\nabla}\widetilde{Y}\right) + \text{div}\left(K\underline{\nabla}\overline{Y''}\right) - \text{div}\left(\overline{\rho}\overline{\underline{u}''Y''}\right), \\
&(e) \qquad \overline{p} = \overline{\rho}R_a\widetilde{T},
\end{aligned}
\tag{2.33}
$$

where $\overline{\underline{q}} = \overline{\rho}\tilde{\underline{u}}$ and $\overline{\underline{f}}$ is the source term. The term (1*) can be neglected considering $\Delta\widetilde{T} >> \Delta T''$, which is usually the case for non reactive flows. The same hypothesis is considered for the scalar transport equation. Terms (2*) and (3*) can also be neglected by assuming a flow below the hypersonic regime and that $|\tilde{\underline{\underline{\tau}}}| >> |\underline{\underline{\tau}}''|$. The tensor $\underline{\underline{\tau}}_T$ is defined according to the operator applied to the balance equations. For the RANS approach, $\underline{\underline{\tau}}_T = \overline{\rho}\underline{\underline{R}}$, with $\underline{\underline{R}} = \overline{\rho u_i'' u_j''}/\overline{\rho}$ being the Reynolds stress tensor. If the filter operator is used, $\underline{\underline{\tau}}_T$ is the subgrid stress tensor defined as $\underline{\underline{\tau}}^{sgs} := \overline{\rho}(\widetilde{u_i u_j} - \widetilde{u}_i\widetilde{u}_j)$.
In both RANS and LES simulations, a closure for $\underline{\underline{\tau}}_T$ is required. The averaged internal energy and scalar equations also present a new term corresponding to the turbulent flux $\overline{\underline{u}''T''}$ and $\overline{\underline{u}''Y''}$ which also require a closure. The simple gradient diffusion hypothesis (SGDH) is used in the present work, which is an eddy viscous model (EVM). For instance for the internal energy equation:

$$
\overline{\underline{u}''T''} = -\frac{\nu_T}{Pr_T}\underline{\nabla}T, \tag{2.34}
$$

where Pr_T is the turbulent Prandtl number, set as 0.9. Such model adds no additional transport equation to the simulation. Other more complex model exist for the turbulent thermal flux but are beyond the scope of this manuscript.

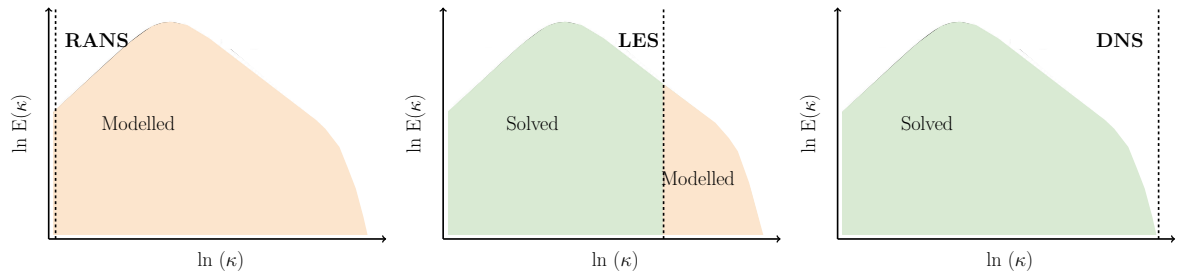

Figure 2.7: Comparison of the different turbulent approaches related to the modelling of the turbulent energy spectrum.

RANS closures

Numerous RANS closures exist, from algebraic models to the resolution of a single or several additional transport equations related to the turbulent quantities.
The first class of models are the eddy viscosity models. The second one solves the Reynolds stress tensor transport equations, called the differential Reynolds stress model (DRSM).
The EVM relies on the Boussinesq (1903) closure which states that the Reynolds stresses tensor is based on the viscous stress tensor:

$$-\overline{\rho}\underline{\underline{R}} = \mu_T \left(\underline{\underline{\nabla}}\tilde{\underline{u}} + \underline{\underline{\nabla}}\tilde{\underline{u}}^T - \frac{2}{3}\text{div}\,\tilde{\underline{u}}\,\underline{\underline{I}} \right) - \frac{2}{3}\overline{\rho}k\underline{\underline{I}}. \tag{2.35}$$

The whole point here is to model the turbulent viscosity μ_T. The simplest models are the algebraic ones (Smith and Cebeci, 1967; Baldwin and Lomax, 1978) . For instance, Prandtl (1925) proposes the following expression for the turbulent viscosity :

$$\mu_T = l_m^2 \left| \frac{\partial \tilde{\underline{u}}}{\partial y} \right|, \tag{2.36}$$

where l_m^2 is the mixing length, which depends on the nature of the studied flow and is generally space dependent.
Then, come the one equation models, where a single turbulent transport equation is added to the system, usually being the turbulent kinetic energy k. These methods, which are not used in the presented simulations, are widely referenced (Baldwin and Barth, 1991; Spalart and Allmaras, 1992) and are beyond the scope of this thesis.
Two equations models are the most popular turbulent method. The turbulent viscosity is defined following two quantities. The popular $k-\varepsilon$ model, first introduced by Launder and Sharma (1974b) , uses turbulent kinetic energy k and its dissipation rate ε:

$$\mu_T = C_\mu \overline{\rho}\frac{k^2}{\varepsilon}, \qquad \text{with} \qquad C_\mu = 0.09.$$

The standard closure is supplemented by two transport equations for both quantities:

$$\frac{\partial(\overline{\rho}k)}{\partial t} + \text{div}\,(k\tilde{\underline{u}}\overline{\rho}) = \text{div}\left(\left[\mu + \frac{\mu_T}{\sigma_k} \right] \underline{\nabla} k \right) + \overline{\rho}(\mathcal{P} + \mathcal{G}) + ST_k - \overline{\rho}\varepsilon, \tag{2.37}$$

$$\frac{\partial(\overline{\rho}\varepsilon)}{\partial t} + \text{div}\,(\tilde{\underline{u}}\overline{\rho}\varepsilon) = \text{div}\left(\left[\mu + \frac{\mu_T}{\sigma_\varepsilon} \right] \underline{\nabla}\varepsilon \right) + \overline{\rho}C_{\varepsilon 1}\frac{\varepsilon}{k}[\mathcal{P} + (1 - C_{\varepsilon 3})\mathcal{G}] + ST_\varepsilon - \overline{\rho}C_{\varepsilon 2}\frac{\varepsilon^2}{k}, \tag{2.38}$$

$$\mathcal{P} = -\underline{\underline{R}} : \underline{\underline{\nabla}}\tilde{\underline{u}}, \qquad \mathcal{G} = -\frac{\mu_T}{\sigma_T}\underline{\nabla}\overline{\rho} \cdot \underline{g}.$$

$\mathcal{P}$ is the shear stress production term, $\mathcal{G}$ is the gravity production term and ST are source terms. $\sigma_k = 1$, $\sigma_\varepsilon = 1.3$, $C_{\varepsilon 1} = 1.44$, $C_{\varepsilon 2} = 1.92$ and $C_{\varepsilon 3} = 1.0$ are constants based on Launder and Sharma (1974a) . The standard model is essentially used for high Reynolds numbers. Other versions of the $k-\varepsilon$ model exist as well such as the realisable $k-\varepsilon$ model or the RNG $k-\varepsilon$ model (Yakhot et al., 1992) . In this work, the $k-\varepsilon$ with a linearised turbulent production is used (Guimet and Laurence, 2002) . A second type of two equations model is the $k-\omega$, which is also commonly used, where ω is the specific dissipation (Menter, 1994) . The latter is not detailed here since it is not used in the present simulations.

For the Differential Reynolds Stress Models (DRSM), the Reynolds stress tensor $\underline{\underline{R}}$ is calculated by solving its transport equations rather than modelling it:

$$\frac{\partial(\overline{\rho}\underline{\underline{R}})}{\partial t} + \underline{\underline{\text{div}}}\,(\underline{\underline{R}} \otimes \overline{\rho}\tilde{\underline{u}}) = \overline{\rho}\underline{\underline{\mathbb{P}}}_R + \underline{\underline{d}} + \underline{\underline{\Phi}}^* - \underline{\underline{\varepsilon}}_R + \underline{\underline{G}}. \tag{2.39}$$

$\underline{\underline{\mathbb{P}}}_R$ is the Reynolds stresses production term:

$$\underline{\underline{\mathbb{P}}}_R = \underline{\underline{R}} \cdot \underline{\underline{\nabla}}(\tilde{\underline{u}}) + \underline{\underline{R}} \cdot \underline{\underline{\nabla}}(\tilde{\underline{u}})^T. \tag{2.40}$$

$\underline{\underline{G}}$ is the gravity production term:

$$\underline{\underline{G}} = -\beta\Big((\underline{g} \otimes \overline{\underline{u}''T''}) + (\overline{\underline{u}''T''} \otimes \underline{g})\Big). \tag{2.41}$$

$\underline{\underline{\Phi}}^*$ is the velocity-pressure gradient correlation:

$$\underline{\underline{\Phi}}^* = \overline{p''(\underline{\underline{\nabla}}\underline{u}'' + \underline{\underline{\nabla}}\underline{u}''^T)}, \tag{2.42}$$

which is divided in three tensors. The first is linked to the instantaneous velocities, the second is calculated with the velocity gradient and the third is linked to the buoyant effects:

$$\underline{\underline{\Phi}}^* = \underline{\underline{\Phi}}^{(1)} + \underline{\underline{\Phi}}^{(2)} + \underline{\underline{\Phi}}^{(3)}.$$

In this manuscript simulations, each tensor is modelled using the SSG (Speziale et al., 1991) closure (other models exist) . $\underline{\underline{\Phi}}^{(1)}$ reads:

$$\underline{\underline{\Phi}}^{(1)} = -C_1\frac{\varepsilon}{k}\underline{\underline{a}} + C_1'\frac{\varepsilon}{k^2}(\underline{\underline{a}} \cdot \underline{\underline{a}} - \frac{1}{3}\text{tr}(\underline{\underline{a}}^2)\underline{\underline{I}}), \tag{2.43}$$

where $\underline{\underline{a}}$ is the dimensionless anisotropy tensor:

$$\underline{\underline{a}} = \frac{\overline{\underline{u}' \otimes \underline{u}'}}{k} - \frac{2}{3}\underline{\underline{I}},$$

and $\underline{\underline{\Phi}}^{(2)}$ is given by:

$$\underline{\underline{\Phi}}^{(2)} = -C_2'\frac{1}{2k}\text{tr}(\underline{\underline{\mathbb{P}}}_R)\underline{\underline{a}} + (C_3 - C_3'\sqrt{\text{tr}(\underline{\underline{a}}^2)})k\underline{\underline{S}} + C_4(\underline{\underline{a}} \cdot \underline{\underline{S}} + \underline{\underline{S}} \cdot \underline{\underline{a}} - \frac{2}{3}\text{tr}(\underline{\underline{a}} \cdot \underline{\underline{S}})\underline{\underline{I}}) \tag{2.44}$$
$$+C_5k(\underline{\underline{a}} \cdot \underline{\underline{\omega}} - \underline{\underline{\omega}} \cdot \underline{\underline{a}}),$$

where $\underline{\underline{\omega}} = \frac{1}{2}(\underline{\underline{\nabla}}(\underline{u}) - \underline{\underline{\nabla}}(\underline{u})^T)$ is the rotation tensor. The last correlation tensor reads:

$$\underline{\underline{\Phi}}^{(3)} = -C_6(\underline{\underline{G}} - \frac{1}{3}\text{tr}(\underline{\underline{G}})\underline{\underline{I}}). \tag{2.45}$$

The constants are represented in Table 2.4.

C_1	C_1'	C_2'	C_3	C_3'	C_4	C_5	C_6
1.7	-1.05	0.9	0.8	0.65	0.625	0.2	0.55

Table 2.4: SSG Constants (Speziale et al., 1991).

$\underline{\underline{d}}$ is the diffusive term which is divided in a molecular, pressure and turbulent diffusion:

$$\underline{\underline{d}} = \underline{\underline{d}}^{\mu} + \underline{\underline{d}}^{p} + \underline{\underline{d}}^{t} = \underline{\underline{\text{div}}}\left(\mu\underline{\underline{\nabla}}(\underline{\underline{R}}) - \overline{p'\left(\underline{u}'' \otimes \underline{\underline{I}} + \underline{\underline{I}} \otimes \underline{u}''\right)} - \overline{\rho}\overline{\underline{u}'' \otimes \underline{u}'' \otimes \underline{u}''}\right). \tag{2.46}$$

While the molecular diffusion does not require a closure, the turbulent and pressure diffusive diffusive terms

$$\underline{\underline{d}}^T = -\underline{\underline{\text{div}}}\left(\overline{p'\left(\underline{u}'' \otimes \underline{\underline{I}} + \underline{\underline{I}} \otimes \underline{u}''\right)} + \overline{\rho}\overline{\underline{u}'' \otimes \underline{u}'' \otimes \underline{u}''}\right),$$

can be closed using either the Shir (1973)

$$\underline{\underline{d}}^p + \underline{\underline{d}}^T = C_s \underline{\underline{\mathrm{div}}} \left(\frac{\rho k^2}{\varepsilon} \underline{\underline{\nabla}}(\underline{\underline{R}}) \right). \tag{2.47}$$

or the Daly and Harlow (1970)

$$\underline{\underline{d}}^p + \underline{\underline{d}}^T = C_s \underline{\underline{\mathrm{div}}} \left(\rho \frac{k}{\varepsilon} \underline{\underline{R}} \cdot \underline{\underline{\nabla R}} \right). \tag{2.48}$$

models, where $C_s = 0.22$. The dissipation tensor $\underline{\underline{\varepsilon}}_R$ is assumed to be isotropic:

$$\underline{\underline{\varepsilon}}_R = \frac{2}{3} \varepsilon \underline{\underline{I}}. \tag{2.49}$$

An additional transport equation is solved for ε.
The DRSM approach has a larger scope of validity than the first order approaches but needs consequently more computational effort due to the many new equations to be solved. For further theoretical information the reader is invited to consult Dehoux (2012).

LES closure

As for the RANS equations, many models exist for the LES closure. The dynamic Smagorinsky model, which relies on an EVM hypothesis, is used in the current work. The subgrid stress tensor is written as:

$$\underline{\underline{\tau}}^{sgs} = \mu_{sgs} \left(\underline{\underline{\nabla}} \tilde{\underline{u}} + \underline{\underline{\nabla}} \tilde{\underline{u}}^T - \frac{2}{3} \mathrm{div}\, \tilde{\underline{u}}\, \underline{\underline{I}} \right) - \frac{2}{3} \mathrm{tr}(\underline{\underline{\tau}}^{sgs}) \underline{\underline{I}}.$$

The Smagorinsky (1963) formula for the subgrid scale is used

$$\mu_{sgs} = \overline{\rho} C_s \Delta^2 \sqrt{2 \tilde{\underline{\underline{S}}} : \tilde{\underline{\underline{S}}}},$$

where Δ is the local grid spacing and $\tilde{\underline{\underline{S}}} = \frac{1}{2}(\underline{\underline{\nabla}} \tilde{\underline{u}} + \underline{\underline{\nabla}} \tilde{\underline{u}}^T)$. The dynamic model uses a test filter, $\hat{\Delta}$, usually taken as $\hat{\Delta} = 2\Delta$ which generates a second set of filtered fields. Using the Germano (1992) identity, the resolved stress tensor:

$$\underline{\underline{L}} = \underline{\underline{T}} - \underline{\underline{\tau}}^{sgs}.$$

Where $\underline{\underline{T}} = \overline{\tilde{\underline{u}} \otimes \tilde{\underline{u}}} - \overline{\tilde{\underline{u}}} \otimes \overline{\tilde{\underline{u}}}$ is the test filter subgrid stress tensor. Using the Smagorinsky model, the resolved stress tensor expression becomes:

$$\underline{\underline{L}} = (C_s^{\Delta})^2 \underline{\underline{M}} + \frac{1}{3} \mathrm{tr}(\underline{\underline{L}}) \underline{\underline{I}},$$

where $\underline{\underline{M}} = 2\Delta^2 \overline{|\tilde{\underline{\underline{S}}}|\, \tilde{\underline{\underline{S}}}} - 2\hat{\Delta}^2 |\overline{\tilde{\underline{\underline{S}}}}|\, \overline{\tilde{\underline{\underline{S}}}}$. In order to evaluate C_s^{δ}, Lilly (1992) proposed a minimisation resolution by a least square method which gives:

$$(C_s^{\Delta})^2 = \max \left(\frac{\underline{\underline{M}} : \underline{\underline{L}}}{\underline{\underline{M}} : \underline{\underline{M}}}, 0 \right).$$

For the sake of simplicity, the governing equations are written without the average and filter operators from now on.

2.4 Summary

Section 2.2 presented the main physics of indoor air flow. The objective of this chapter is to select the most important ones to take into account in simulations and to chose a system of equations accordingly. It is recalled (Section 1.1) that the main guidance and objectives related to buildings are the stakes related to occupants i.e. the thermal comfort, indoor air quality, ventilation systems, but also related to industrial safety.
However, it is difficult to separate each stake independently with a particular physic introduced previously. Indeed, for instance, to perform a study related to a system thermal comfort, one needs to consider buoyant effects, the present humidity, pressure variation, turbulence in the ventilation jets... Thus, the main goal will be to develop a numerical scheme able to account for the most number of the presented phenomena.

Remark 2.4.1. Note that the radiation and human presence effects on the flow, which may not be neglected in some cases, are left to further investigations.

From Section 2.3, the choice of using the compressible Navier–Stokes equations is made. Indeed, the different approximations presented are less likely to properly reproduce temporal and spatial pressure variations.
Regarding turbulence, no particular approach is brought to the front. Yet, let's keep in mind that RANS simulations may be interesting for steady problems, while LES should be performed when trying to have a more detailed flow characterisation, notably for transient simulations.
In the next chapters, the numerical strategy to discretise the chosen equations are detailed to take into account the latter physical stakes.

CHAPTER 3

A time-staggered second order conservative time scheme for variable density flow

Résumé

Ce chapitre détaille le schéma en temps numérique développé pour des simulations aérauliques d'air sec. Ce dernier a été développé dans le but de répondre aux enjeux physiques de modélisation présentés auparavant. Après la présentation du contexte et des objectifs numériques du schéma, la stratégie de discrétisation en espace et en temps est introduite, suivie de la présentation de certaines propriétés numériques, dont des nouvelles conditions de stabilité pour préserver la positivité des variables thermodynamiques. Enfin, les propriétés et la précision du schéma en temps sont testées sur des cas tests de vérification et de validation, allant du régime incompressible au compressible.

This chapter presents in details the development of a numerical scheme for indoor dry airflow simulations. After a description of the numerical stakes and the scheme novelties related to the literature, the set of the continuous equations and turbulence models used are introduced. The discrete spatial and temporal schemes are then described and a numerical analysis to ensure the thermodynamic fields positivity is performed. Finally, the proposed scheme properties are verified on analytical test cases and their numerical results are compared with the existing code_saturne incompressible second-order variable density time scheme for reactive flow, by Ma et al. (2019) (denoted incompressible pressure correction, IPC, scheme and detailed in Appendix 3.C) and compressible scheme (Colas et al., 2019), which uses an isentropic pressure step (denoted isentropic compressible, IC scheme and detailed in Appendix 3.D). This is first done with a pressure-cooker-like system, showing that the scheme takes into account the correct pressure variation while preserving the systems global mass, and then by transporting a scalar through an one-dimensional tube in order to verify both mass and momentum conservation and the time scheme convergence order. Its consistency related to irregular solutions is also tested with a shock tube configuration. Finally, the scheme is validated on a natural convection, gravity flow, jet and a ventilation case, emphasising its ability and robustness to provide accurate results in an industrial context.

3.1 Numerical motivations and strategy

The numerical strategy adopted goes with the identification of indoor physics to be taken into account during the simulation.

3.1.1 Numerical goals

From a numerical point of view, different stakes related to the schemes and models (Ferziger et al., 2002) exist and are summarised in the next paragraph.

The first one is the consistency of a numerical scheme, related to the spatial discretisation error, also called truncation error. For a numerical method to be consistent, the truncation error must become zero when the mesh spacing and the time step tend to zero. In case of consistency, this error is usually proportional to a power of the grid spacing or time step: this is why one may cite "high order" spatial and time schemes; in such cases, the given scheme is called of n^{th} order approximation. Note that even if the approximation is consistent, it does not necessarily insure that the solution of the discretised system of equations will be the exact solution of the problem in the limit of small step size.

The second important numerical property is the scheme stability, which insures that the possible numerical errors which appear during the resolution process are not amplified. One known method for studying a scheme stability is the Von Neumann's analysis (Isaacson and Keller, 2012).

Moreover, the set of equations to be simulated are conservation equations: the numerical scheme should thus conserve these quantities. For instance, without considering any diffusive or source terms and by assuming a steady state, the flow entering and leaving a given system should be the same. If the conservation of mass, momentum and total energy are insured, the error can only improperly distribute

these quantities over the solution domain. In opposition, non conservative schemes can produce artificial sources, changing the local and global balances. Still, these types of schemes can be consistent and stable in the limit of fine grids. These errors due to non conservation are in most cases noticeable for coarse grids; the problem is the difficulty to accurately know on which grid refinement they become small enough. Therefore, conservative schemes are preferred.
Finally, a numerical scheme should have solutions within proper bounds. A negative temperature (in Kelvin) or total pressure magnitude has no physical sense in the indoor environment framework. Another example is that any volume, mass or concentration fraction must lie between 0 and 1. These constraints should be inherited by the numerical approximation. Boundedness may be difficult to guarantee and leads sometimes to numerical constraints. The consistency, stability, conservation and boundedness are thus very important to keep in mind while designing any numerical scheme or model.

3.1.2 Literature and numerical strategy

Simulating variable density flow at all Mach numbers is an active field of research and can be useful in many additional industrial domains such as combustion (Huang et al., 2003), power generation (Douce et al., 2003; Archambeau et al., 2009; Kraus et al., 2021) among others. When the flow Mach number tends to zero, the compressible Navier–Stokes equations converge toward the incompressible ones (Klainerman and Majda, 1981). This is not easily achieved in numerical simulations as an incompressible formulation of the equations does not reproduce correctly compressible effects and compressible solvers can perform poorly when the Mach number decreases (Guillard and Viozat, 1999).
In the latter context, the low-Mach set of the Navier–Stokes equations is often used to describe flow motion, where the acoustic waves propagate at an infinite speed and are not considered in the simulation. Nevertheless, if one wants to consider its effects on the flow, the compressible Navier–Stokes equations are used. In this case, an additional numerical constraint appears, limiting the simulation time step related to sound celerity. This can be very inconvenient for slow-speed flow simulations. Thus, significant attention was given to designing time schemes for CFD able to cover both regimes, while compromising the preservation of accurate numerical results and reducing the total computational calculation time. In that scope, one solution is the use of implicit time integrators, which may not be simple to implement due to the complexity of the system to solve. An alternative method related to different time scale problems is the implicit treatment of some terms of the system while keeping the remaining explicit. This semi implicit (or implicit explicit) approach allows the development of stabler schemes by reducing the time step constraint related to the fast time scale.
In the context of incompressible and compressible flow, different all speed semi-implicit schemes based on the asymptotic preserving method have been proposed in the last decades (Park and Munz, 2005; Degond and Tang, 2011; Haack et al., 2012; Cordier et al., 2012; Herbin et al., 2012; Boscheri et al., 2020), which inspired some features of this work, notably the incompressible limit of the pressure equation, which is later detailed in this chapter.
Moreover, the present scheme belongs to the pressure correction methods, which are time marching techniques widely used in CFD. First introduced in the late 60's (Chorin, 1968; Temam, 1969) for incompressible flow (see Guermond et al. (2006) for a review of the different variants), they were extended for compressible flow (Harlow and Amsden, 1968, 1971; Gallouët et al., 2008) followed by many numerical schemes (including diphasic flow Kheriji et al. (2013)), mostly using finite volume methods. Among them, one can highlight the essentially implicit (Van Doormaal et al., 1987; Demirdžić et al., 1993; Politis and Giannakoglou, 1997; Moukalled and Darwish, 2001) algorithms which differ from the semi-implicit ones (such as the SIMPLE (Karki and Patankar, 1989) method) where a prediction of the momentum is first performed, followed by a correction step for the pressure, momentum, and velocity (Issa, 1986b,a; Colella and Pao, 1999; van der Heul et al., 2003; Herbin et al., 2020).

Furthermore, recent work addressed a strategy of using high-order schemes to capture unsteady turbulent flow phenomena. Harlow and Welch (1965) introduced a staggered grid arrangement for a second order finite difference scheme for incompressible flow using the Crank and Nicolson (1947) method. Pierce and Moin (2004) extended the previous scheme to variable-density flow using the low Mach assumption. A similar version of this algorithm was proposed by the same authors (Wall et al., 2002) , where an Helmholtz equation was used instead of a Poisson equation in the correction step, avoiding the acoustic Courant–Friedrichs–Lewy (CFL) number limitation. The latter used the enthalpy equation to compute the temperature and was specially designed for low speed flow, with no presence of shocks. Solving an Helmholtz equation to correct the pressure was also shown to be relevant for an atmospheric flow solver by Benacchio and Klein (2019) and for a low Mach number kinetic energy conservation scheme by Moureau et al. (2007) . High-order low and all Mach number schemes remain very popular. Desjardins et al. (2008) proposed a high order version of Pierce's low Mach finite difference staggered time-stepping, using the Poisson equation in the correction step. The combination of semi-implicit asymptotic preserving and Runge–Kutta methods (Ascher et al., 1997; Pareschi and Russo, 2005; Bispen et al., 2017) led also to high-order all Mach number schemes (Boscheri et al., 2020; Boscheri and Pareschi, 2021) .

Note that boundary conditions, especially in incompressible pressure correction methods, can affect its time convergence order (Guermond et al., 2006) . This is beyond the scope of the current study.

This chapter presents a conservative second-order time scheme for variable density flow using the compressible Navier–Stokes equations. The finite difference scheme introduced by Pierce and Moin (2004) with a staggered variable arrangement in time is extended on different grounds using the collocated finite-volume discretisation (Versteeg and Malalasekera, 2007) for regular and discontinuous solutions. The staggered arrangement should allow the scheme to be of first and second time order; making it compatible with both steady and unsteady turbulent approaches.

Three major features of the new scheme are highlighted. First, it includes the effect of the thermodynamic pressure in the correction step by solving an Helmholtz equation (thanks to the linearisation of the EOS). Therefore, the acoustic waves are treated implicitly and are thus separated from advection, which removes the acoustic CFL restriction on the time step.

Moreover, the internal energy equation is used to compute the temperature. First introduced by Herbin et al. (2020) for an Euler pressure correction scheme, this choice of equation allows the third feature, a numerical analysis, to be made, ensuring the temperature, pressure and density positivity under certain constraints detailed later. Since computing shock solutions using the internal energy equation yields an incorrect velocity field (Archambeau et al., 2009; Toro, 2013) , a correction term based on the discrete kinetic energy equation similar to the one used by Herbin et al. (2020) is added to the internal energy equation. This term, derived here for the sub-iterative time-staggered scheme, preserves the sum of the internal and kinetic energy to ensure the conservation of the total energy, thus implying a good reproducibility of the numerical shock velocities.

Table 3.1 summarises each modelling stake introduced in the last chapter and the corresponding numerical objective and strategy deployed.

Note that the humidity and phase change numerical treatments are detailed and discussed in Chapter 4.

The proposed algorithm, from now on called compressible pressure correction (CPC) scheme, is implemented in the open-source CFD solver code_saturne, verified and validated on a wide range of zero to three dimensions test cases.

Modelling stake	**Numerical objetive**	**Corresponding numerical approach**
Pressure variation	Density dependence on both the pressure and temperature i.e. $\rho(T, p)$	• Equation of state linearisation • Solve of Helmholtz equation for the pressure
Buoyant effects	Density variation $\frac{\partial \rho}{\partial t} \neq 0$	Use of the compressible Navier–Stokes equations
Wall effects	Take into account the dynamic and thermal walls effects	Use of wall functions
Compatibility with turbulent approaches	• Possibility of first and second order time convergence rate • Be compatible with the existing turbulent approaches of code_saturne	Time variables staggered arrangement
Regular and singular solutions	Conservation of the mass, momentum and total energy	Solve of the internal energy with a corrective source term related to the kinetic energy dissipation
Acoustic waves	No time step constraint related to the celerity	Implicitation of the sources related to the pressure
Humidity	Phase change and properties variation consideration	• Transport of the water mass fraction • Change of the equation of state • Newton method on the phase change

Table 3.1: Summary of the physical modelling stakes, the related numerical target and the proposed numerical approach.

3.2 Set of equations

The Navier–Stokes compressible conservative equations supplemented with scalars Y transport equation and an equation of state were chosen in Chapter 2 to be discretised.
As a reminder, for a fluid considered as a perfect gas of density ρ, velocity $\underline{u}$, momentum $\underline{q} = \rho\underline{u}$, internal energy e, temperature T, viscosity μ, heat capacities c_v and c_p; thermal conductivity λ, and scalar diffusion coefficient K, the final set of equations reads:

$$
\begin{aligned}
&(a)\ \frac{\partial \rho}{\partial t} + \text{div}\left(\underline{q}\right) = 0, \\
&(b)\ \frac{\partial \underline{q}}{\partial t} + \underline{\text{div}}\left(\underline{u} \otimes \underline{q}\right) = -\underline{\nabla} p + \underline{\text{div}}\left(\underline{\underline{\tau}}\right) + \underline{f}, \\
&(c)\ \frac{\partial \left(\rho e\right)}{\partial t} + \text{div}\left(e\underline{q}\right) = -p\text{div}\left(\underline{u}\right) + \underline{\underline{\tau}} : \underline{\underline{\nabla u}} + \text{div}\left(\lambda \underline{\nabla} T\right), \\
&(d)\ \frac{\partial \left(\rho Y\right)}{\partial t} + \text{div}\left(Y\underline{q}\right) = \text{div}\left(K\underline{\nabla} Y\right), \\
&(e)\ T = \mathcal{T}(\rho, e) = \frac{\gamma - 1}{R_a}\, e, \qquad p = \mathcal{P}(\rho, e) = \rho R_a T.
\end{aligned}
\tag{3.1}
$$

(a) is the mass conservation equation (b) is the momentum conservation equation. (c) is the internal energy equation, which is not conserved. (d) is the scalar transport equation and (e) is the equation of state. The other equations terms are presented in Chapter 2, Section 2.1. In the perfect gas context, the internal energy is linked to the fluid temperature through $e = c_v\, T$. Possible additional source terms were not considered in the aforementioned equations.

3.3 Space and time discretisation notations

The space domain Ω is meshed with a collection of polyhedral cells c of volume Ω_c. Two neighbouring cells c and $\widetilde{c}$ share a polygonal face f of normal surface vector $\underline{S}_f$ oriented from c to $\widetilde{c}$, as shown in Figure 3.1.

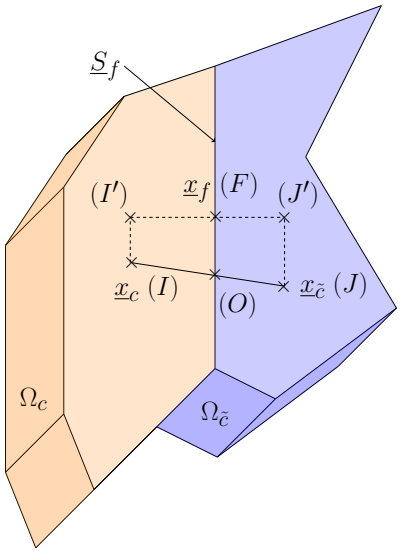

Figure 3.1: Labelling information used for a mesh. $\underline{x}_c$ and $\underline{x}_{\widetilde{c}}$ are the barycentres of cells c and $\widetilde{c}$, respectively. $\underline{x}_f$ is the barycentre of the face f separating the two cells.

Mean space values over a cell c and averaged values over a face f of a quantity $(.)$ are denoted by:

$$(.)_c \coloneqq \frac{1}{\Omega_c}\int_c (.)\mathrm{d}\Omega, \qquad (.)_f \coloneqq \frac{1}{S_f}\int_f (.)\mathrm{d}S. \tag{3.2}$$

S_f is the cells face surface. Note that face values are computed using spatial schemes presented in Section 3.5. The mean time value over the time interval $[t^n,\, t^{n+1}[$ is denoted by

$$(.)|_n^{n+1} \coloneqq \frac{1}{\Delta t}\int_{t^n}^{t^{n+1}} (.)\mathrm{d}t, \tag{3.3}$$

where $\Delta t = t^{n+1} - t^n$ is the interval measure. Moreover, the time values at time t^n and t^{n+1} are written with the superscript $(.)^n$ and $(.)^{n+1}$, respectively.
In the present numerical scheme, the time stepping is defined by the parameter θ, bounded in $[0, 1]$ (theta-scheme). We consider the cases where $\theta = 1$ (implicit Euler, 1^{st} order time interpolation of $(.)|_n^{n+1}$) and $\theta = 1/2$ (Crank Nicolson, 2^{nd} order time interpolation of $(.)|_n^{n+1}$). A field ψ time interpolation $\Theta\left(\psi^n,\, \psi^{n+1}\right)$ between times n and $n+1$ is defined as:

$$\Theta\left(\psi^n,\, \psi^{n+1}\right) \coloneqq (1-\theta)\,\psi^n + \theta\psi^{n+1}.$$

The dual time interval around time n is denoted by $[n-1+\theta, n+\theta]$, and is of length:

$$\Delta t|_{n-1+\theta}^{n+\theta} \coloneqq \Theta\left(\Delta t|_{n-1}^{n},\, \Delta t|_n^{n+1}\right),$$

From the above expressions, the extensive quantities such as the cell mass M_c, cell momentum $\underline{Q}_c$ and face mass flux $\dot{M}_f$ are defined as follows:

$$M_c \coloneqq \int_c \rho\mathrm{d}\Omega, \qquad \underline{Q}_c \coloneqq \int_c \rho\underline{u}\mathrm{d}\Omega, \qquad \dot{M}_f \coloneqq \int_f \underline{q}\cdot\underline{\mathrm{d}S} = \underline{q}_f\cdot\underline{S}_f.$$

Finally, discrete spatial operators (denoted by capital letters) are defined. The discrete operator divergence of a face-averaged field $\underline{\psi}_f$ is written as follows:

$$\mathrm{Div}_c\left(\underline{\psi}_f\right) \coloneqq \frac{1}{\Omega_c}\sum_{f\in\mathcal{F}_c}\underline{\psi}_f\cdot\underline{S}_f = \left(\mathrm{div}\left(\underline{\psi}\right)\right)_c, \tag{3.4}$$

where $\mathcal{F}_c$ is the ensemble of all the planar polygonal faces of the cell c, and $\underline{S}_f$ is the outward surface vector. The discrete cell gradient operator of a field ψ is also defined as the divergence of the tensor $\psi\underline{\underline{I}}$:

$$\underline{\mathrm{Grad}}_c\left(\psi_f\right) \coloneqq \frac{1}{\Omega_c}\sum_{f\in\mathcal{F}_c}\psi_f\underline{S}_f = \left(\underline{\mathrm{div}}\left(\psi\underline{\underline{I}}\right)\right)_c. \tag{3.5}$$

Finally, the discrete Laplacian operator of a given scalar ψ with coefficient of diffusion K uses the two points flux approximation (TPFA) (see Eymard et al. (2014) and Ferrand et al. (2014) for more details) and is defined as:

$$\mathrm{Lap}_c\left(K,\, \psi\right) \coloneqq \frac{1}{\Omega_c}\sum_{f\in\mathcal{F}_c}K\underline{\nabla}_f\psi\cdot\underline{S}_f, \qquad \underline{\nabla}_f\psi = \frac{\psi_{\widetilde{c}} - \psi_c}{d_{c\widetilde{c}}}. \tag{3.6}$$

Remark 3.3.1. The mass balance is performed between time steps n and $n+1$. Therefore, since they are linked by the equation of state, scalar mass fractions Y, temperature T, total pressure p and density ρ are stored in the same space and time locations. The mass balance implies that the mass fluxes denoted by $\underline{q}_f\cdot\underline{S}_f$ are stored in the time interval $[n, n+1]$ and on the mesh faces. Note that the time interval $[n, n+1]$ is the dual space of time $n+\frac{1}{2}$. Therefore, the momentum equation is solved between times $n-\frac{1}{2}$ and $n+\frac{1}{2}$ when $\theta = 1/2$. Figure 3.2 shows the time locations of the different

scheme variables. When $\theta = 1/2$, the velocity location is at the centre of the time interval $[n, n+1]$, whereas other fields are evaluated at times n and $n+1$, respectively.

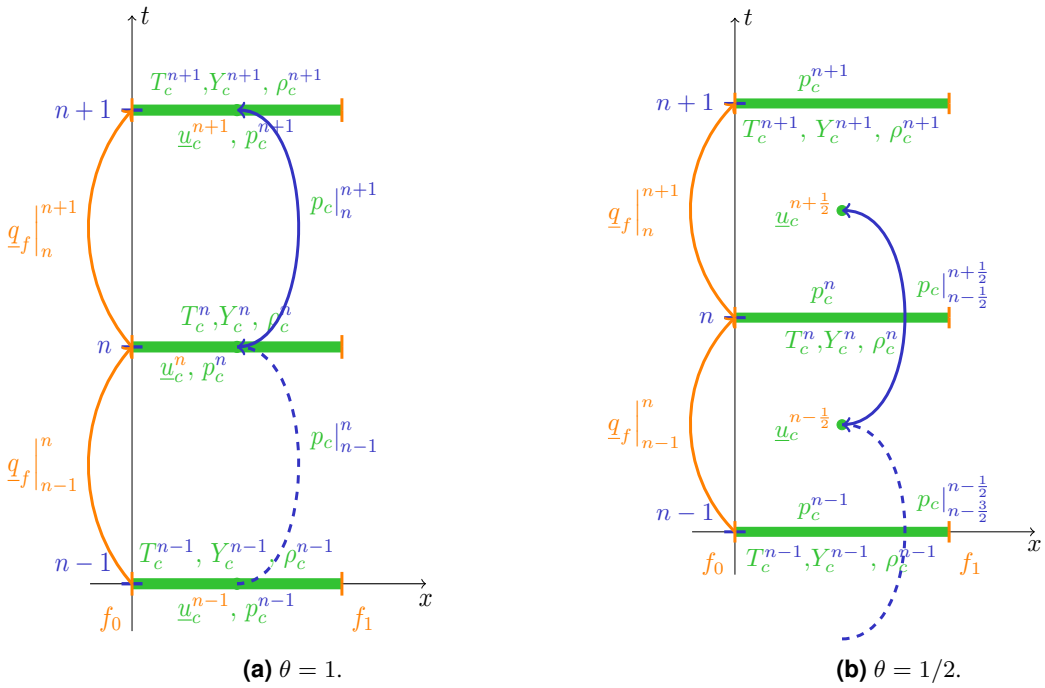

(a) $\theta = 1$. **(b)** $\theta = 1/2$.

Figure 3.2: Time variables localisation for the two θ values.

3.4 Time discretisation

The CPC scheme assumes that numerical fluxes are evaluated by considering one mean variable value ψ_c^n at a given cell of volume Ω_c^n and at the time $t = n\Delta t$ presented in Figure 3.2, according to the theta-scheme parameter θ. Each time stepping is divided in a sub-iterative process, with inner iterations characterised by the subscript k (PISO method (Barton, 1998)). The latter stops either if a maximum sub iteration or local error is reached. The reader may distinguish two different pressures. The total thermodynamic pressure, denoted p^{n+1} at the time t^{n+1}, which is located with other thermodynamic variables, can be differentiated from the mechanical pressure $p|_{n-1+\theta}^{n+\theta}$, which applies a force on the momentum equation during the time interval $[n-1+\theta, n+\theta]$. More explicitly, the total pressure expression reads:

$$p^{n+1,k} = p_0 + \frac{1}{\theta} p|_{n-1+\theta}^{n+\theta,k} - 2\left[1-\theta\right] p|_{n-2+\theta}^{n-1+\theta}, \tag{3.7}$$

where variables with the subscript 0 are reference values.
Figure 3.3 shows the time scheme main steps. First, an initialisation is made for the given time iteration. As mentioned in this chapter motivations, the presented work belongs to the pressure-correction class of CFD schemes. The transport equations of the internal energy and scalars are then solved leading to the internal energy $e^{n+1,k}$ and to $Y^{n+1,k}$. After deduction of the temperature from the internal energy, an intermediate predicted density $\tilde{\rho}^k$. The prediction step uses the momentum conservation equation to estimate a predicted velocity denoted $\tilde{\underline{u}}^k$. Finally, a combination of the mass and momentum equation is used to solve an Helmholtz equation for the pressure increment, denoted $\phi^k = p|_{n-1+\theta}^{n+\theta,k} - p|_{n-1+\theta}^{n+\theta,k-1}$. The thermodynamical pressure $p^{n+1,k}$, the mechanic pressure $p|_{n-1+\theta}^{n+\theta,k}$, the velocity $\underline{u}^{n+\theta,k}$ and the density

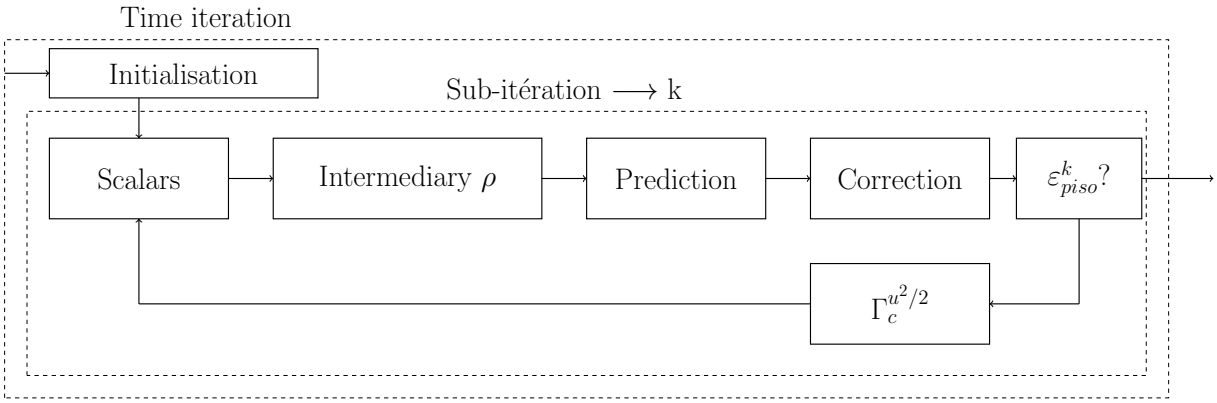

Figure 3.3: Sub-iterative scheme main steps.

$\rho^{n+1,k}$ are then updated. The last elements are used to compute, if needed, the discrete kinetic energy source term $\Gamma_c^{u^2/2}\Big|_n^{n+1,k-1}$ that is injected in the next step internal energy equation.

Remark 3.4.1. Three conditions are considered while designing the proposed scheme.

- At each inner step, the instantaneous density must be in coherence with the convective mass flux.
- To maintain the scheme conservation property, when adding the prediction and correction Equations (3.13) and (3.14), the unsteady terms of the predicted velocity $\widetilde{\underline{u}}^k$ should disappear.
- The densities of the prediction and correction step are centred at the time step n when $\theta = 1/2$.

For a sake of clarity, the time step Δt is supposed constant in this section. The reader may find the scheme equations for a variable time step in Appendix 3.B.
In the following, each main step of the system of equations time discretisation is detailed.

3.4.1 Initialisation

The first inner step within a time step is the variables initialisation regarding the sub iterative process. Thus, for $k = 1$, the different variables at $k-1$ are initialised as following:

$$\rho_c^{n,0} = \rho_c^{n-1}, \quad \rho_c^{n+1,0} = \rho_c^n, \quad \underline{q}_f\Big|_n^{n+1,0} \cdot \underline{S}_f = \underline{q}_f\Big|_{n-1}^{n} \cdot \underline{S}_f, \quad p|_{n-1+\theta}^{n+\theta,0} = p^n.$$

As a side note, at any sub-iteration, the mass flux should verify the following mass balance equation:

$$\mathrm{Div}_c\left(\underline{q}_f\Big|_n^{n+1,k}\right) = -\frac{\left(\rho_c^{n+1,k} - \rho_c^{n,k}\right)}{\Delta t}.$$

3.4.2 Scalars step

Buoyant scalars $Y^{n+1,k}$, which for dry air do not contribute to the density variation, are computed by solving each scalar transport equation in $[n, n+1]$:

$$\frac{\rho_c^{n+1,k-1}Y_c^{n+1,k} - \rho_c^{n,k-1}Y_c^n}{\Delta t} + \mathrm{Div}_c\left(\left\langle\Theta\left(Y^n,\, Y^{n+1,k}\right)\right\rangle_f \underline{q}_f\Big|_n^{n+1,k-1}\right) = \mathrm{Lap}_c\left(K, \Theta\left(Y^n,\, Y^{n+1,k}\right)\right). \tag{3.8}$$

Note that for the first sub-iteration, $\rho^{n,k-1}$ is ρ^{n-1} and $\rho^{n+1,k-1}$ is ρ^{n}; thus, the density variation $(\rho^{n} - \rho^{n-1})$ is balanced by the mass flux $\underline{q}_f\Big|_{n-1}^{n}$ term, as stated in the first of the three conditions presented in this section introduction.
As for the internal energy, its equations is solved using the variable $T^{n+1,k}$ in $[n, n+1]$:

$$c_v \left[\frac{\rho_c^{n+1,k-1} T_c^{n+1,k} - \rho_c^{n,k-1} T_c^{n}}{\Delta t} + \mathrm{Div}_c \left(\left\langle \Theta \left(T^n,\, T^{n+1,k} \right) \right\rangle_f \underline{q}_f \Big|_n^{n+1,k-1} \right) \right] = \mu(S_c^2)^{n+\theta,k-1} + \Gamma_c^{u^2/2}\Big|_n^{n+1,k-1}$$
$$+ \mathrm{Lap}_c \left(\lambda, \Theta \left(T^n,\, T^{n+1,k} \right) \right) - \mathrm{Div}_c \left(\left\langle \Theta \left(p^n,\, p^{n+1,k-1} \right) \underline{u}^{n+\theta,k-1} \right\rangle_f \right) + \underline{u}_c^{n+\theta,k-1} \cdot \underline{\nabla}_c p |_{n-1+\theta}^{n+\theta,k-1}. \tag{3.9}$$

The term $-p\ \mathrm{div}\ (\underline{u})$ is computed here as $-\mathrm{div}\ (p\underline{u}) + \underline{u} \cdot \underline{\nabla} p$ due to the ease of implementation that the pressure gradient is already computed in the previous prediction step $(k-1)$ and that all faces values are computed as well. Thus, the user has the choice on the spatial discretisation (later detailed) of the term $\mathrm{div}\ (p\underline{u})$. $\mu(S_c^2)$ is the dissipation term and reads:

$$\mu(S_c^2) = \mu \Bigg[2 \left(\frac{\partial u}{\partial x} \right)^2 + 2 \left(\frac{\partial v}{\partial y} \right)^2 + 2 \left(\frac{\partial w}{\partial z} \right)^2 + \left(\frac{\partial v}{\partial x} + \frac{\partial u}{\partial y} \right)^2 + \left(\frac{\partial w}{\partial y} + \frac{\partial v}{\partial z} \right)^2 + \left(\frac{\partial u}{\partial z} + \frac{\partial w}{\partial x} \right)^2$$
$$- \frac{2}{3} \left(\frac{\partial u}{\partial x} + \frac{\partial v}{\partial y} + \frac{\partial w}{\partial z} \right)^2 \Bigg], \tag{3.10}$$

where u, v and w are the different components of the velocity vector. Inspired by Herbin et al. (2020), the internal energy equation is supplemented with $\Gamma_c^{u^2/2}\Big|_n^{n+1,k-1}$, a corrective source term derived from the discrete kinetic energy equation. Its expression reads:

$$\Gamma_c^{u^2/2}\Big|_n^{n+1,k-1} = \frac{\Theta \left(\rho_c^n,\, \rho_c^{n+1,k-2} \right)}{\Theta \left(\rho_c^n,\, \rho_c^{n+1,k-1} \right)} \Theta \left(\rho_c^{n-1},\, \rho_c^n \right) \frac{\left[|\widetilde{\underline{u}}_c^{k-1} - \underline{u}_c^{n-1+\theta}|^2 \right]}{2\Delta t}$$
$$+ \left[1 - \frac{\Theta \left(\rho_c^n,\, \rho_c^{n+1,k-2} \right)}{\Theta \left(\rho_c^n,\, \rho_c^{n+1,k-1} \right)} \right] \left[\Theta \left(\rho_c^{n-1},\, \rho_c^n \right) \frac{|\underline{u}_c^{n-1+\theta}|^2}{2\Delta t} - \mathrm{Div}_c \left(\frac{\left| \left\langle \Theta \left(\underline{u}^{n-1+\theta},\, \widetilde{\underline{u}}^{k-1} \right) \right\rangle_f \right|^2}{2} \underline{q}_f \Big|_{n-1+\theta}^{n+\theta,k-2} \right) \right]$$
$$- \frac{\Theta \left(\rho_c^n,\, \rho_c^{n+1,k-2} \right)}{\Theta \left(\rho_c^n,\, \rho_c^{n+1,k-1} \right)} \mathrm{Div}_c \left(\frac{\left| \left\langle \Theta \left(\underline{u}^{n-1+\theta},\, \widetilde{\underline{u}}^{k-1} \right) \right\rangle_f - \widetilde{\underline{u}}_c^{k-1} \right|^2}{2} \underline{q}_f \Big|_{n-1+\theta}^{n+\theta,k-2} \right). \tag{3.11}$$

This corrective term allows the total energy to be conserved in the given interval, leading to consistent solutions even in the presence of irregularities. Note that this term is computed in the previous inner iteration. The reason is related to its derivation, detailed in Appendix 3.A.
The new temperature is used to predict an intermediary density value through the equation of state:

$$\tilde{\rho}_c^k = \frac{p_c^{n+1,k-1}}{R_a T_c^{n+1,k}} \tag{3.12}$$

This new density is not balanced by any mass flux. The mass conservation is insured in the correction step.

3.4.3 Prediction step

The momentum equation is integrated over the time interval $[n-1+\theta, n+\theta]$ to compute the predicted velocity $\underline{\widetilde{u}}^k$:

$$\begin{aligned}&\frac{\Theta\left(\rho_c^n,\, \rho_c^{n+1,k-1}\right)\underline{\widetilde{u}}_c^k - \Theta\left(\rho_c^{n-1},\, \rho_c^{n,k-1}\right)\underline{u}_c^{n-1+\theta}}{\Delta t} + \mathrm{Div}_c\left(\left\langle\Theta\left(\underline{u}^{n-1+\theta},\, \underline{\widetilde{u}}^k\right)\right\rangle_f \otimes \underline{q}_f\Big|_{n-1+\theta}^{n+\theta,k-1}\right)\\ &= -\underline{\mathrm{Grad}}_c\left(\left\langle p\big|_{n-1+\theta}^{n+\theta,k-1}\right\rangle_f\right) + \underline{\mathrm{Div}}_c\left(\underline{\tau}_f\Big|_{n-1+\theta}^{k}\right) + \underline{f}_c\Big|_{n-1+\theta}^{n+\theta,k-1}.\end{aligned} \tag{3.13}$$

The mass flux $\underline{q}\big|_{n-1+\theta}^{n+\theta,k-1}{}_f$ is defined by:

$$\underline{q}_f\Big|_{n-1+\theta}^{n+\theta,k-1} = \Theta\left(\underline{q}_f\Big|_{n-1}^{n},\, \underline{q}_f\Big|_{n}^{n+1,k-1}\right).$$

Note that the cell pressure gradient and external volume force are taken at the same time interval; if they are in a partial balance, no parasite velocities are created.

3.4.4 Correction step

During this stage, the pressure increment $\phi^k = p\big|_{n-1+\theta}^{n+\theta,k} - p\big|_{n-1+\theta}^{n+\theta,k-1}$ is computed and used to correct the velocity $\underline{u}^{n+\theta,k}$. The following system is solved on $[n, n+1]$:

$$\begin{cases}\dfrac{\Theta\left(\rho_c^n,\, \rho_c^{n+1,k}\right)\underline{u}_c^{n+\theta,k} - \Theta\left(\rho_c^n,\, \rho_c^{n+1,k-1}\right)\underline{\widetilde{u}}_c^k}{\Delta t} + \underline{\nabla}_c\phi^k = \delta\underline{f}_c^k,\\ \mathrm{Div}_c\left(\underline{q}_f\Big|_{n}^{n+1,k}\right) + \dfrac{\rho_c^{n+1,k} - \rho_c^n}{\Delta t} = 0,\end{cases} \tag{3.14}$$

with

$$\delta\underline{f}_c^k = \underline{f}_c\Big|_{n-1+\theta}^{n+\theta,k} - \underline{f}_c\Big|_{n-1+\theta}^{n+\theta,k-1}$$

and where, by definition:

$$\underline{q}_f\Big|_{n}^{n+1,k} = \left\langle\Theta\left(\rho^n,\, \rho^{n+1,k}\right)\underline{u}^{n+\theta,k}\right\rangle_f = \left\langle\Theta\left(\rho^n,\, \rho^{n+1,k-1}\right)\underline{\widetilde{u}}^k\right\rangle_f - \Delta t\left(\underline{\nabla}_f\phi^k - \delta\underline{f}_c^k\right), \tag{3.15}$$

which verifies the mass balance with $\dfrac{\rho_c^{n+1,k} - \rho_c^n}{\Delta t}$, and whose field face values are calculated using a centred scheme. Combining the equations in (3.14) and using the Rhie and Chow (1983) filter leads to an Helmholtz equation for the cell thermodynamic pressure $p_c^{n+1,k}$, solved for ϕ^k:

$$\begin{aligned}\frac{\rho_c^{n+1,k} - \rho_c^n}{\Delta t} - \theta\mathrm{Lap}_c\left(\Delta t, p^{n+1,k}\right) = &-\mathrm{Div}_c\left(\left\langle\Theta\left(\rho^n,\, \rho^{n+1,k-1}\right)\underline{\widetilde{u}}^k + \Delta t\left(\underline{\nabla}p\big|_{n-1+\theta}^{n+\theta,k-1} + \delta\underline{f}^k\right)\right\rangle_f\right)\\ &+ (1-\theta)\mathrm{Lap}_c\left(\Delta t, p\big|_{n-2+\theta}^{n-1+\theta}\right),\end{aligned} \tag{3.16}$$

where, alternatively to Equation (3.7), the total pressure $p^{n+1,k}$ is linked to ϕ^k through:

$$\phi^k = \Theta\left(p\big|_{n-2+\theta}^{n-1+\theta},\, p^{n+1,k}\right) - p\big|_{n-1+\theta}^{n+\theta,k-1}. \tag{3.17}$$

The density $\rho_c^{n+1,k}$ is written as:

$$\rho_c^{n+1,k} = \widetilde{\rho_c}^k + \left(p_c^{n+1,k} - p_c^{n+1,k-1}\right)\left(\left.\frac{\partial\rho}{\partial p}\right|_T \left(T_c^{n+1,k}, p_c^{n+1,k-1}\right)\right). \tag{3.18}$$

Note that for ideal gases, the density $\rho^{n+1,k}$ expression (Equation (3.18)) reduces to the ideal gas equation of state since $\left.\frac{\partial\rho}{\partial p}\right|_T = \frac{1}{R_a T}$.
This density update makes the scheme conservative in space and time for mass, which is an important property, especially for non-regular solutions. From a generic point of view, the density $\rho^{n+1,k}$ in Equation (3.16) might not satisfy the equation of state (contrary to what was done in step 6 of Wall et al. (2002) ↗).

Remark 3.4.2. As mentioned, Equation (3.16) is solved for the pressure increment ϕ^k as following:

$$\begin{aligned}
&\frac{(3-2\theta)}{\Delta t}\left.\frac{\partial\rho}{\partial p}\right|_T (p_c^{n+1,k-1}, T_c^{n+1,k})\phi^k - \theta \mathrm{Lap}_c\left(\Delta t, \phi^k\right) = (1-\theta)\mathrm{Lap}_c\left(\Delta t, p|_{n-2+\theta}^{n-1+\theta}\right) \\
&- \mathrm{Div}_c\left(\left\langle \Theta\left(\rho^n, \rho^{n+1,k-1}\right)\underline{\widetilde{u}}^k + \Delta t\left(\underline{\nabla} p|_{n-2+\theta}^{n-1+\theta} + \delta\underline{f}^k\right)\right\rangle_f\right) - \frac{\widetilde{\rho_c}^k - \rho_c^n}{\Delta t} \\
&- \frac{(2-2\theta)\, p_c|_{n-1+\theta}^{n+\theta,k-1} - p_c|_{n-2+\theta}^{n-1+\theta}}{\Delta t}\left.\frac{\partial\rho}{\partial p}\right|_T (p_c^{n+1,k-1}, T_c^{n+1,k}).
\end{aligned}$$

The sub-iterative process for the time step ends when the error:

$$\varepsilon_{piso}^k = \sqrt{\sum_{c=1}^{N_{cell}} \Omega_c |\underline{u}_c^{n+\theta,k} - \underline{u}_c^{n+\theta,k-1}|^2}$$

is below a fixed value ε_{piso_0} or when a maximal number of inner iterations is reached.
The scheme main steps, showing the primary variables solved and their related equations are summarised in Algorithm 1.

3.5 Spatial discretisation

The time scheme is integrated in the open source solver code_saturne, which uses a collocated finite volume method. Based on the notations introduced in Section 3.3, the time integrated equations are integrated over a control volume. In their spatially discretised form, they involve many faces values. Thus, in this section the convective schemes used in the different numerical simulations are presented. Concerning the spatial cells notations, the reader is invited to use Figure 3.1 as reference.

3.5.1 Convective schemes

As a reminder, a faces mass flux, denoted $\dot{M}_f$ is defined as:

$$\dot{M}_f = \underline{q}_f \cdot \underline{S}_f.$$

The first convective scheme is the first order upwind scheme, where the face field ψ value reads:

$$\psi_f = \begin{cases} \psi_c, \text{ if } \dot{M}_f \geq 0, \\ \psi_{\widetilde{c}}, \text{ if } \dot{M}_f < 0. \end{cases} \tag{3.19}$$

Algorithm 1 Time scheme main steps

First time step initialisation,
Time loop
for `n = 0, N-1` **do**
  Initialisation of variables at the first sub-iteration $k = 1$
  for `k = 1, M` **do**
    Compute scalars and temperature $Y_c^{n+1,k}, T_c^{n+1,k}$, ▷ Equation (3.9)
    Update of the density $\widetilde{\rho}_c^k$ with $T_c^{n+1,k}$, ▷ Equation (3.12)
    Compute the predicted velocity $\underline{\widetilde{u}}_c^k$, ▷ Equation (3.13)
    Correction step: compute $\phi^k \rightarrow p_c|_{n-1+\theta}^{n+\theta,k}$, ▷ Equation (3.16)
    Correct the thermodynamic pressure $p_c^{n+1,k}$, ▷ Equation (4.27)
    Correct the density $\rho_c^{n+1,k}$, ▷ Equation (3.18)
    Correct the velocity $\underline{u}_c^{n+\theta,k}$, ▷ Equation (3.15)
    if $\epsilon_{piso}^k \leq \epsilon_{piso_0}$ **then**
      Break the for loop,
    else
      Compute the kinetic energy source term $\Gamma_c^{u^2/2}\Big|_n^{n+1}$, ▷ Equation (3.11)
    end if
  end for
end for

Then, for a centred scheme, one has:

$$\psi_f = \alpha_f \psi_c + (1-\alpha_f)\psi_{\widetilde{c}} + \frac{1}{2}\left[\underline{\nabla}_c\psi + \underline{\nabla}_{\widetilde{c}}\psi\right] \cdot \underline{OF}. \tag{3.20}$$

α_f is a weighting factor defined to measure the distance of the cell center I to the face f relative to the neighbour cell $\widetilde{c}$, written as following:

$$\alpha_f = \frac{d_{f\widetilde{c}'}}{d_{c'\widetilde{c}}}, \tag{3.21}$$

with the distances:

$$d_{c'\widetilde{c}} = \frac{\underline{I'J'} \cdot \underline{S}_f}{|\underline{S}_f|}, \qquad d_{f\widetilde{c}'} = \frac{\underline{FJ'} \cdot \underline{S}_f}{|\underline{S}_f|}. \tag{3.22}$$

This scheme ensures a second order space discretization for the given variable (see Saturne (2019) for further details).

Remark 3.5.1. code_saturne's strategy for computing the numerical cell gradient can be found in Archambeau et al. (2004) and is beyond the scope of this manuscript.

The second order linear upwind (SOLU) scheme is used as well (Fromm, 1968) . In that case, the field face value reads:

$$\psi_f = \begin{cases} \psi_c + \underline{\nabla}_c\psi.\underline{IF} & \text{if} \quad \dot{M}_f \geq 0 \\ \psi_{\widetilde{c}} + \underline{\nabla}_{\widetilde{c}}\psi.\underline{IF} & \text{if} \quad \dot{M}_f < 0 \end{cases} \tag{3.23}$$

For the boundary face value,

$$\psi_f = \begin{cases} \psi_c + \underline{\nabla_c \psi}.\underline{IF} & \text{if} \quad \dot{M}_f \geq 0 \\ A^g_{f_b} + B^g_{f_b}\psi_c & \text{if} \quad \dot{M}_f < 0 \end{cases} \tag{3.24}$$

Remark 3.5.2. A slope test can switch from the centred and SOLU scheme to the upwind one. Also it is possible to compute the field face value as a weighted average between the upwind and centred face value.

Remark 3.5.3. The coefficients $A^g_{f_b}$ and $B^g_{f_b}$ are presented in the boundary conditions Section 3.6.

3.5.2 Diffusive terms

The scalar ψ diffusive term div $(K\underline{\nabla}\psi)$ is written as a sum of numerical fluxes $D_f(K_f, \psi)$ discretised as following: if the field ψ is non reconstructed, the flux reads:

$$D_f(K_f, \psi) = -\frac{K_f|\underline{S}_f|}{d_{c'\widetilde{c'}}}\left(\psi_c - \psi_{\widetilde{c}}\right), \tag{3.25}$$

where

$$K_f = \frac{K_c K_{\widetilde{c}}}{\alpha_f K_c + (1-\alpha_f)K_{\widetilde{c}}}. \tag{3.26}$$

In case of reconstruction, the diffusive flux reads:

$$D_f(K_f, \psi) = -\frac{K_f|\underline{S}_f|}{d_{c'\widetilde{c'}}}\left(\psi_c - \psi_{\widetilde{c}}\right) - \frac{K_f|\underline{S}_f|}{d_{c'\widetilde{c'}}}\frac{1}{2}\left(\underline{\nabla_c \psi} + \underline{\nabla_{\widetilde{c}}\psi}\right)\cdot\left(\underline{II'} - \underline{JJ'}\right). \tag{3.27}$$

This reconstruction ensures the second order discretisation in space for ψ.

3.6 Boundary conditions

As any numerical scheme, a specific treatment related to boundary conditions is made. The latter can be either an imposed flux, also called Neumann condition, an imposed field variable value, known as Dirichlet condition, and a mix of the two previous conditions, called Robin condition.
These conditions are translated into implicit and explicit contributions entering the linear system to be solved. More precisely, within the code_saturne solver, for a given variable ψ, two families of coefficient exist. The first one, denoted A^g_{fb} and B^g_{fb} respectively, is used by the gradient and advection operators through the calculation of the boundary field variable face value ψ_{fb}:

$$\psi_{fb} = A^g_{fb} + B^g_{fb}\psi_{I'}.$$

The other type of coefficients, denoted A^f_{cb} and B^f_{cb}, are used for the diffusive flux calculation as mentioned in the last Subsection.
A particular boundary condition is assigned to a boundary face following its type.
For example, inlet faces are assigned Dirichlet condition for scalar fields except for the pressure, where an homogeneous Neumann condition is imposed.

For outlet faces, an homogeneous Neumann conditions is assigned for all variables, excepting the pressure whose conditions is:

$$\frac{\partial^2 p}{\partial \eta \partial \tau} = 0,$$

for any vector $\underline{\tau}$ parallel to the face. This condition means that the pressure profile does not vary in the normal direction of the face outlet.

Remark 3.6.1. In case of a negative boundary face mass flux, a clipping to 0 concerning the flux is performed to respect the outlet face condition.

Remark 3.6.2. The pressure is also defined as the constant reference pressure p_0 defined by the user.

A combination of inlet and outlet conditions, called free inlet outlet exists as well. In that case, a standard outlet condition is set when the flow is outgoing. In the other case, an inlet condition is set. To couple both velocity and pressure at these free inlet faces, the Bernoulli relationship is used to derive a boundary condition on the pressure increment.
For symmetry faces, an homogeneous Neumann condition is assigned for scalar fields. For vectors such as the velocity, a null Dirichlet value is set for the normal component and an homogeneous Neumann condition for the tangential components.
The conditions for tensors are beyond the scope of this Section. Further details can be found in Saturne (2019).
For walls, the boundary condition treatment depends on the variable. For the velocity, a Dirichlet condition on the wall is transformed into a Neumann condition where the wall shear stress is accounted. This is done using the so called wall functions. Similarly, the same strategy is used for the scalar fields. For the pressure field, an homogeneous Neumann condition is set by default.

Remark 3.6.3. If the numerical mesh is enough refined to capture the variations of the variables near the wall, wall functions are no longer needed and thus a Dirichlet condition is assigned to the variables.

For the velocity, one or two friction velocity scales wall functions can be used. More information about those can be found in Appendix 3.E.

3.7 Properties of the scheme

3.7.1 Positivity of the thermodynamical variables

This sub-section focuses on the new numerical constraints related to the positivity of the internal energy (consequently, the temperature), the pressure and the density. To do so, the concerned equations are written in their space and time discretised form (from section 3.5). Note that this numerical analysis is made using an upwind spatial discretisation for the convective terms.
The discretised internal energy (Equation (3.9)) written using the temperature variable, for $k > 1$, reads:

$$\begin{aligned} & c_v \left[M_c^n \frac{T_c^{n+1,k} - T_c^n}{\Delta t} + \sum_{f \in \mathcal{F}_c} \left(\left\langle \Theta \left(T^n, T^{n+1,k} \right) \right\rangle_f - T_c^{n+1,k} \right) \dot{M}_f \Big|_n^{n+1,k-1} \right] \\ & + \sum_{f \in \mathcal{F}_c} \lambda |\underline{S}_f| \frac{\Theta \left(T_c^n, T_c^{n+1,k} \right) - \Theta \left(T_{\widetilde{c}}^n, T_{\widetilde{c}}^{n+1,k} \right)}{d_{c\widetilde{c}}} = \Omega_c \mu (S_c^2)^{n+\theta} + \Gamma_c^{u^2/2} \Big|_n^{n+1,k-1} \\ & - \sum_{f \in \mathcal{F}_c} \left\langle \Theta \left(p^n, p^{n+1,k-1} \right) \underline{u}^{n+\theta,k-1} \right\rangle_f \cdot \underline{S}_f + \Omega_c \underline{u}_c^{n+\theta,k-1} \cdot \underline{\nabla}_c p \Big|_{n-1+\theta}^{n+\theta,k-1}. \end{aligned} \tag{3.28}$$

Equation (4.34) yields a linear system $\underline{\underline{A}}\underline{X} = \underline{B}$, where $\underline{X} = (T_c^{n+1,k})_{c\in\{1,..,N_{cell}\}}$.
The diagonal matrix $\underline{\underline{A}}$ coefficients are, $\forall c \in \{1, ..., N_{cell}\}$:

$$A_{cc} = c_v \frac{M_c^n}{\Delta t} + c_v \left[\sum_{f\in\mathcal{F}_c} \theta \dot{M}_f^+ \Big|_n^{n+1,k-1} - \dot{M}_f \Big|_n^{n+1,k-1} \right] + \left[\sum_{f\in\mathcal{F}_c} \theta \frac{|\underline{S}_f|\lambda_c}{d_{c\widetilde{c}}} \right], \tag{3.29}$$

where, $\dot{M}_f^+ \Big|_n^{n+1} = \max\left(0, \dot{M}_f \Big|_n^{n+1}\right)$ is the positive contribution of the face f mass flux. To ensure that these terms are positive, the following sufficient CFL-like condition is defined:

$$\text{Max}_c(\text{CFL}_{T_1}^+)_c < 1, \tag{3.30}$$

where:

$$(\text{CFL}_{T_1}^+)_c \coloneqq (1-\theta)\frac{\Delta t}{M_c^n} \sum_{f\in\mathcal{F}_c} \dot{M}_f^+ \Big|_n^{n+1,k-1}. \tag{3.31}$$

$\forall c, \widetilde{c}, \in \{1, ..., N_{cell}\}$ with $c \neq \widetilde{c}$, the off-diagonal coefficients are

$$A_{c\widetilde{c}} = \theta \dot{M}_f^- \Big|_n^{n+1,k-1}. \tag{3.32}$$

$\dot{M}_f^- \Big|_n^{n+1,k-1} = \min\left(0, \dot{M}_f \Big|_n^{n+1}\right)$ is the negative contribution of the face f mass flux.

Remark 3.7.1. If the initial temperatures for all cells are positive, $d_{c\widetilde{c}} > 0$, c_v, λ, R_a, and Δt are positive and the condition (3.30) is respected, all diagonal terms of the matrix $\underline{\underline{A}}$ are strictly positive. Moreover, all off-diagonal coefficients are negative or null. The diagonal terms are strictly larger than the sum of the modulus of off-diagonal terms. Therefore, A is diagonal dominant and a M-matrix.

The internal energy equation right hand side coefficients are (without the kinetic energy source term):

$$\begin{aligned} B_c = {} & c_v \frac{M_c^n T_c^n}{\Delta t} + \mu_c \Omega_c^n (S_c^2)^{n+1} - \sum_{f\in\mathcal{F}_c} c_v (1-\theta) T_f^n \dot{M}_f \Big|_n^{n+1,k-1} \\ & + \Omega_c \underline{u}_c^{n+\theta,k-1} \cdot \underline{\nabla}_c p \big|_{n-1+\theta}^{n+\theta,k-1} - \sum_{f\in\mathcal{F}_c} \left[|\underline{S}_f|\lambda_c (1-\theta) \frac{(T_c^n - T_{\widetilde{c}}^n)}{d_{c\widetilde{c}}} \right] \\ & - R_a \sum_{f\in\mathcal{F}_c} \left[\Theta\left(T_c^n, T_c^{n+1,k-1}\right) \dot{M}_f^+ \Big|_n^{n+1,k-1} + \Theta\left(T_{\widetilde{c}}^n, T_{\widetilde{c}}^{n+1,k-1}\right) \dot{M}_f^- \Big|_n^{n+1,k-1} \right]. \end{aligned}$$

We seek for a sufficient condition insuring that $B_c > 0\ \forall c$. Thus, the positive contributions related to the mass flux are discarded and the convective and diffusive right hand side terms are treated separately. Each case leads to a new condition to keep B_c positive.
The first, related to the convective term, is a CFL-like condition:

$$\text{Max}_c(\text{CFL}_{T_2}^+)_c < 1, \tag{3.33}$$

where:

$$\begin{aligned} (\text{CFL}_{T_2}^+)_c \coloneqq {} & \frac{\Delta t}{M_c^n} \sum_{f\in\mathcal{F}_c} \left[\theta(\gamma-1)\frac{T_c^{n+1,k-1}}{T_c^n} + (1-\theta)\gamma \right] \dot{M}_f^+ \Big|_n^{n+1,k-1} \\ & - \frac{\Delta t(\gamma-1)\underline{u}_c^{n+\theta,k-1} \cdot \underline{\nabla}_c p \big|_{n-1+\theta}^{n+\theta,k-1}}{p_c^n}. \end{aligned} \tag{3.34}$$

The second, related to the diffusion term, is a Fourier-like condition:

$$\text{Max}_c(Fo_T^+)_c < 1, \tag{3.35}$$

where:

$$(Fo_T^+)_c \coloneqq \frac{\lambda_c(1-\theta)\Delta t}{c_v M_c^n} \sum_{f\in\mathcal{F}_c} |\underline{S}_f| \frac{T_c^n - T_{\widetilde{c}}^n}{T_c^n d_{c\widetilde{c}}}. \tag{3.36}$$

Property 3.7.1. If the initial temperatures for all cells are positive, $d_{c\widetilde{c}} > 0$, c_v, λ, R_a, and Δt are positive and the conditions (3.30), (3.34) and (3.35) are respected, $\underline{\underline{A}}$ is a M-matrix and $B_c > 0$. The solution of the linear system is thus positive.

Now, the same methodology is applied to the pressure (Equation (3.16)):

$$\begin{aligned}
&\frac{\Omega_c p_c^{n+1,k}}{\Delta t R_a T_c^{n+1,k}} - \theta\Delta t \sum_{f\in\mathcal{F}_c} \underline{\nabla}_f p_c^{n+1,k} \cdot \underline{S}_f = \frac{(\rho_c^n - \widetilde{\rho}_c)\Omega_c^n}{\Delta t} \\
&- \sum_{f\in\mathcal{F}_c} \left\langle \Theta\left(\rho^n,\, \rho^{n+1,k-1}\right) \underline{\widetilde{u}}^k + \Delta t \underline{\nabla}_c p|_{n-1+\theta}^{n+\theta,k-1} \right\rangle_f \cdot \underline{S}_f \\
&+ (1-\theta)\Delta t \sum_{f\in\mathcal{F}_c} \underline{\nabla}_f p|_{n-2+\theta}^{n-1+\theta} \cdot \underline{S}_f + \frac{\Omega_c p_c^{n+1,k-1}}{\Delta t R_a T_c^{n+1,k}}.
\end{aligned} \tag{3.37}$$

Equation (4.43) yields a linear system $\underline{\underline{A}}\underline{X} = \underline{B}$, where $\underline{X} = (p_c^{n+1,k})_{c\in\{1,..,N_{cell}\}}$.
The diagonal matrix A coefficients are, $\forall c \in \{1, ..., N_{cell}\}$:

$$A_{cc} = \frac{\Omega_c}{\Delta t R_a T_c^{n+1,k}} + \theta\Delta t \sum_{f\in\mathcal{F}_c} \frac{|\underline{S}_f|}{d_{c\widetilde{c}}}. \tag{3.38}$$

$\forall c, \widetilde{c}, \in \{1, ..., N_{cell}\}$ with $c \neq \widetilde{c}$, the off-diagonal coefficients are

$$A_{c\widetilde{c}} = -\theta\ \Delta t \frac{|\underline{S}_f|}{d_{c\widetilde{c}}}. \tag{3.39}$$

Remark 3.7.2. If the initial temperature for all cells is positive, $d_{c\widetilde{c}} > 0$, c_v, λ, R_a, and Δt are positive, all the diagonal terms of the matrix $\underline{\underline{A}}$ are strictly positive. Moreover, all off-diagonal coefficients are negative or null. Moreover, the diagonal terms are strictly larger than the sum of the modulus of off-diagonal terms. Therefore, A is diagonal dominant and a M-matrix.

The right hand side terms B_c are strictly positive if:

$$\frac{\rho_c^n \Omega_c^n}{\Delta t} - \sum_{f\in\mathcal{F}_c} \left\langle \Theta\left(\rho^n,\, \rho^{n+1,k-1}\right) \underline{\widetilde{u}}^k + \Delta t \underline{\nabla} p|_{n-1+\theta}^{n+\theta,k-1} \right\rangle_f \cdot \underline{S}_f + (1-\theta)\Delta t \sum_{f\in\mathcal{F}_c} \underline{\nabla}_f p|_{n-2+\theta}^{n-1+\theta} \cdot \underline{S}_f > 0, \tag{3.40}$$

i.e. if:

$$\text{Max}_c(\text{CFL}_p^+)_c < 1, \tag{3.41}$$

$$(\text{CFL}_p^+)_c \coloneqq \frac{\Delta t}{\rho_c^n \Omega_c^n} \sum_{f\in\mathcal{F}_c} a_f^\phi, \tag{3.42}$$

and

$$a_f^\phi = \left\langle \Theta\left(\rho^n,\, \rho^{n+1,k-1}\right) \underline{\widetilde{u}}^k + \Delta t \underline{\nabla} p|_{n-1+\theta}^{n+\theta,k-1} \right\rangle_f \cdot \underline{S}_f - (1-\theta)\Delta t \underline{\nabla}_f p|_{n-2+\theta}^{n-1+\theta} \cdot \underline{S}_f.$$

Property 3.7.2. If the initial temperature for all cells is positive, $d_{c\widetilde{c}} > 0$, c_v, λ, R_a, and Δt are positive and the condition (3.41) is respected, then $\underline{\underline{A}}$ is a M-matrix and $B_c > 0 \; \forall c$. Thus, the solution to the linear system is strictly positive.

Remark 3.7.3. If both the cell temperature and pressure are positive, then its density is positive as well thanks to the equation of state.

Remark 3.7.4. The new presented conditions are compared to the classical material velocity based CFL number in the next section.

3.7.2 Low Mach number limit

By defining the sound speed $\dfrac{1}{c^2} = \left.\dfrac{\partial \rho}{\partial p}\right|_s \approx \left.\dfrac{\partial \rho}{\partial p}\right|_T$, the Helmholtz Equation (3.16) can be rewritten as

$$\begin{aligned}\frac{p_c^{n+1,k} - p_c^{n+1,k-1}}{c^2\,\Delta t} - \theta \mathrm{Lap}_c\left(\Delta t, p^{n+1,k}\right) = -\frac{\widetilde{\rho}_c^k - \rho_c^n}{\Delta t} + (1-\theta)\mathrm{Lap}_c\left(\Delta t, p|_{n-2+\theta}^{n-1+\theta}\right) \\ - \mathrm{Div}_c\left(\left\langle \Theta\left(\rho^n, \rho^{n+1,k-1}\right)\underline{\widetilde{u}}^k + \Delta t\left(\underline{\nabla} p|_{n-1+\theta}^{n+\theta,k-1} + \delta \underline{f}^k\right)\right\rangle_f\right).\end{aligned} \tag{3.43}$$

By introducing the Mach number $\mathrm{Ma} = \dfrac{U}{c}$ with U a characteristic velocity, the order of magnitude of the first term on the left-hand side is

$$\mathrm{Ma}^2 \frac{\Delta p}{\rho_r U^2} \frac{\rho_r}{\Delta t}.$$

In the limit of the zero-Mach number, this term is negligible compared with the first term on the right-hand side. The Helmholtz equation becomes a Poisson equation, similar to the one used for incompressible flow with variable density (IPC scheme, see Appendix 3.C).

3.7.3 Local total energy balance

The total energy balance is performed in the interval $[n; n+1, k]$. The discrete kinetic energy equation related to the source term injected in the internal energy equation is recalled (Appendix 3.A):

$$\begin{aligned}&\frac{\Theta\left(\rho_c^n, \rho_c^{n+1,k-1}\right)|\underline{u}_c^{n+\theta,k-1}|^2 - \Theta\left(\rho_c^{n-1}, \rho_c^{n,k-1}\right)|\underline{u}_c^{n-1+\theta}|^2}{2\Delta t} + \mathrm{Div}_c\left(\frac{|\Theta\left(\underline{u}_f^{n-1+\theta}, \widetilde{\underline{u}}_f^{k-1}\right)|^2}{2}\underline{q}_f\Big|_{n-1+\theta}^{n+\theta,k-2}\right) \\ &+ \underline{\mathrm{Grad}}_c\left(\left\langle p|_{n-1+\theta}^{n+\theta,k-1}\right\rangle_f\right)\cdot \underline{u}_c^{n+\theta,k-1} = -\Gamma_c^p|_{n-1+\theta}^{n+\theta,k-1} - \Gamma_c^{u^2/2}\Big|_n^{n+1,k-1},\end{aligned} \tag{3.44}$$

where

$$\Gamma_c^p|_{n-1+\theta}^{n+\theta,k-1} = \frac{\Delta t}{2\Theta\left(\rho_c^n, \rho_c^{n+1,k-1}\right)}\left[\left|\underline{\mathrm{Grad}}_c\left(\left\langle p|_{n-1+\theta}^{n+\theta,k-1}\right\rangle_f\right)\right|^2 - \left|\underline{\mathrm{Grad}}_c\left(\left\langle p|_{n-1+\theta}^{n+\theta,k-2}\right\rangle_f\right)\right|^2\right]. \tag{3.45}$$

Summing the internal and kinetic energies equations ((3.44) and (3.9)) for $k \geq 1$ leads to the local total energy balance between $[n; n+1, k]$:

$$\frac{\rho_c^{n+1,k-1}\left(e_c^{n+1,k}+\theta\frac{|\underline{u}_c^{n+\theta,k-1}|^2}{2}\right)-\rho_c^n\left(e_c^n+\theta\frac{|\underline{u}_c^{n-1+\theta}|}{2}\right)}{\Delta t}+(1-\theta)\frac{\rho_c^n|\underline{u}_c^{n+\theta,k-1}|^2-\rho_c^{n-1}|\underline{u}_c^{n-1+\theta}|^2}{2\Delta t}$$

$$\mathrm{Div}_c\left(\frac{|\Theta\left(\underline{u}_f^{n-1+\theta},\,\widetilde{\underline{u}}_f^{k-1}\right)|^2}{2}\underline{q}_f\Big|_{n-1+\theta}^{n+\theta,k-2}\right)+\mathrm{Div}_c\left(\left\langle\Theta\left(e^n,\,e^{n+1,k}\right)\right\rangle_f\underline{q}_f\Big|_n^{n+1,k-1}\right)=$$

$$\mathrm{Div}_c\left(\left\langle\Theta\left(p^n,\,p^{n+1,k-1}\right)\underline{u}^{n+\theta,k-1}\right\rangle_f\right)-\Gamma_c^p|_{n-1+\theta}^{n+\theta,k-1}+\mu(S_c^2)^{n+\theta,k-1}+\mathrm{Lap}_c\left(\lambda,\Theta\left(T^n,\,T^{n+1,k}\right)\right).$$

3.8 Verification and Validation

The CPC scheme is verified and validated on different analytical and experimental test cases. Each numerical study was chosen in order to verify the scheme accuracy and properties related to the indoor air-flow context. To illustrate this, Table 3.2 shows the different cases used during this important process. For each study, the reader may find in this section all the information concerning the numerical mesh, the boundary conditions and other parameters used to perform the simulation. Inner iterations are performed following an error threshold ε_{piso_0}, that may variate following the test case. Note that this errors differs from the solver precision, which is related for each solved equation in the sub-iterative process.

Verification case	**Physical phenomena/property**
0-D pressure cooker like system	Pressure variation, Mass conservation, Time convergence order
1-D convective flow	Mass and Momentum conservation, Spatial schemes compatibility, Time convergence order
Shock tube	Discontinuous solutions, Time convergence order, Total energy conservation
Atmosphere column	Reproduction of the pressure variation related to the height
Validation case	**Physical phenomena/property**
Axisymmetric jet	3-D isothermal jet reproduction
Le Queré Cavity	Natural laminar convection, Pressure variation
Minibat	3-D turbulent jet reproduction, Buoyant effects, Turbulence
Lock exchange configuration	Gravity flow, Incompressible scheme limit

Table 3.2: Different test cases used for the verification and validation related to their represented physical phenomena and/or properties.

Note that the various verification and validation problems can be classified between the incompressible to the compressible flow, represented in Figure 3.4. Other flow characteristics (laminar or turbulent, steady or unsteady) can be found in the figure as well.
The numerical results presented in this section are compared, according to the type of case, to exact, reference or experimental solutions. For some simulations, an additional comparison between the CPC scheme and code_saturne's IPC or IC schemes is made.
In the following simulations, the time step was kept constant and only hexahedral meshes were used. Moreover, test cases are ran using a constant CFL number; in case of mesh refinement, the time step is divided as well, according to the latter.

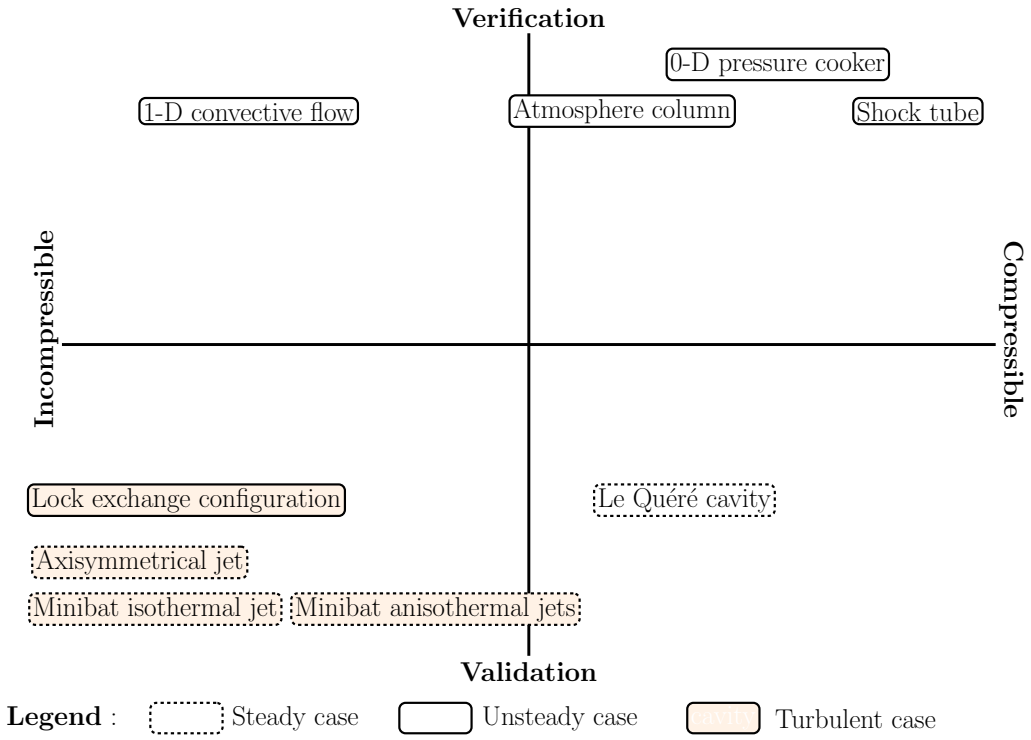

Figure 3.4: Classification of the studied verification and validation test cases.

3.8.1 Pressure cooker like system

This first verification case is designed to test the time scheme ability to take into account a correct pressure variation while conserving the system total mass. Physically, this test is based on a pressure cooker (in the indoor context, the reproduction of the greenhouse effect for instance).

Motivations 3.8.1. This test case is interesting since incompressible pressure correction schemes which solve a Poisson equation for the pressure usually are not able to reproduce an accurate pressure and density variation.

The system is composed of a single $[1 \times 1 \times 1]\mathrm{m}^3$ cell, represented in Figure 3.6. The enclosed cell is heated through its lateral walls while other walls are considered adiabatic i.e. with no heat exchange with the exterior. Two cases are considered, where the lateral walls boundary condition changes. First, a constant flux Neumann boundary condition is imposed, allowing to verify the scheme correct reproduction of the pressure while preserving the system mass. Then, a Dirichlet condition is imposed and the scheme time convergence rate is studied at a given time and for the two θ values.
For both cases, the initial conditions are $T_0 = 300\,\mathrm{K}$ and $\rho_0 = 1.177\,\mathrm{kg\,m^{-3}}$. Thanks to the simplicity of the problem, an analytical expression is derived from the energy balance for the temperature, pressure and density. For the Neumann (N) case, the temperature expression reads:

$$T_{\mathrm{N}}(t) = T_0 \left(1 + \frac{t}{\tau_1}\right), \qquad \tau_1 = \frac{\Omega_{tot}\ \rho_0\ c_v\ T_0}{S\ Q_i}, \tag{3.46}$$

where Ω_{tot} is the total cell volume, c_v is the fluid heat capacity, and S is the total heated wall surface. Q_i is the lateral walls heat flux, equal to $100\,\mathrm{W\,m^{-2}}$. The temperature expression for the Dirichlet (D) case reads:

$$T_{\mathrm{D}}(t) = (T_0 - T_w)\ e^{-\frac{t}{\tau_2}} + T_w, \qquad \tau_2 = \frac{\Omega_{tot}\ \rho_0\ c_v}{S\ h}, \tag{3.47}$$

where $T_w = 313\,\mathrm{K}$ denotes the wall temperature. The interior air heat transfer coefficient $h = 30\,\mathrm{W\,m^{-2}\,K^{-1}}$ remains constant. Since the density for both cases is expected to stay constant, the exact pressure value p_i can be expressed as well using the EOS:

$$p_i = \rho_0 R_a T_i. \tag{3.48}$$

For a field ψ, the numerical ψ_c results are compared to their analytical ψ_{ex} solution through the L_2 relative error norm:

$$L_2^{\mathrm{err}}(\psi) := \sqrt{\frac{\frac{1}{\Omega_{tot}}\sum_c (\psi_c - \psi_{ex})^2 \Omega_c}{\frac{1}{\Omega_{tot}}\sum_c \psi_0^2 \Omega_c}}. \tag{3.49}$$

For all simulations, the time step is set to $\Delta t = 1\,\mathrm{s}$, with a single inner iteration ($\varepsilon_{piso_0} = 10^{-6}$, but note that since the zero dimensional system and the absence of velocity, the inner iterations error ε^k_{piso} is zero). The Neumann simulation is ran during $1000\,\mathrm{s}$ and the Dirichlet during $0.8\tau_2$ s.
Figure 3.5 shows the density, temperature and pressure errors over time for both CPC and IPC scheme for the Neumann test case.

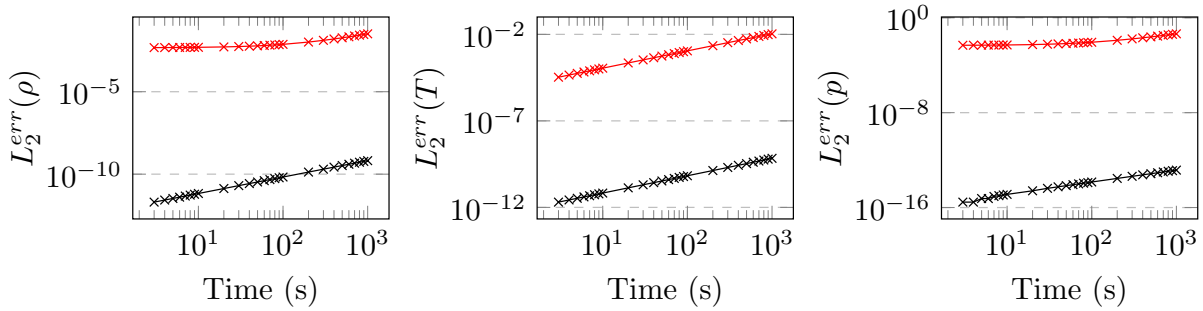

Figure 3.5: L_2 error norm of the density, temperature and pressure for the Neumann boundary condition case. (–) IPC scheme. (–) CPC scheme.

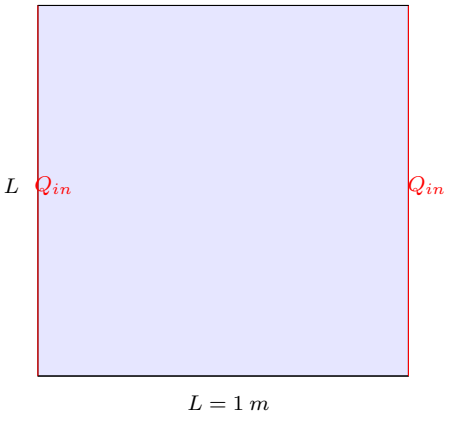

Figure 3.6: Sketch of the system.

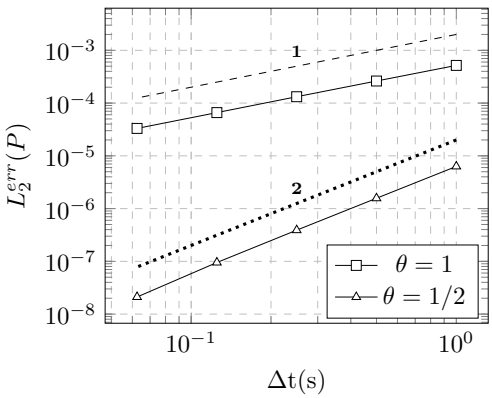

Figure 3.7: Dirichlet boundary condition case. L_2 error norm for the pressure at $t = 0.8\tau_2$ s for a first-order implicit Euler ($\theta = 1$) and Crank Nicolson ($\theta = 1/2$) time scheme.

It is shown that the presented algorithm takes into account the pressure variation while the cell is heated (Fig 3.5, black lines) whereas the IPC scheme leads to more important and increasing errors (red lines). This is an expected result: solving the Helmholtz equation allows the simulation to take into account the

correct pressure variation. Moreover, the errors are below the solver precision for all variables, fixed as 10^{-8}. Note that the increasing behaviour of all errors can be explained as an accumulation of numerical truncation errors. For a 0-D case, the scheme was thus able to catch correctly the thermodynamical variables evolution with negligible density variation.
Figure 3.7 shows the pressure L_2 error at $t = 0.8\tau_2$ s for the Dirichlet boundary condition study. It is verified that the first and second order time convergence rates are obtained when $\theta = 1$ and $1/2$, respectively.

3.8.2 1-D Convection verification case

Motivations 3.8.2. This verification case is designed to first verify the scheme mass and momentum conservation over time and its time convergence order when using the different code_saturne spatial schemes.

In this case, two studies are made. The domain is a 1-D tube of length L ($L = 40\,\mathrm{m}$ for the first and $20\,\mathrm{m}$ for the second), represented in Figure 3.8. For all simulations, viscous terms are disabled turning the problem fully convective.

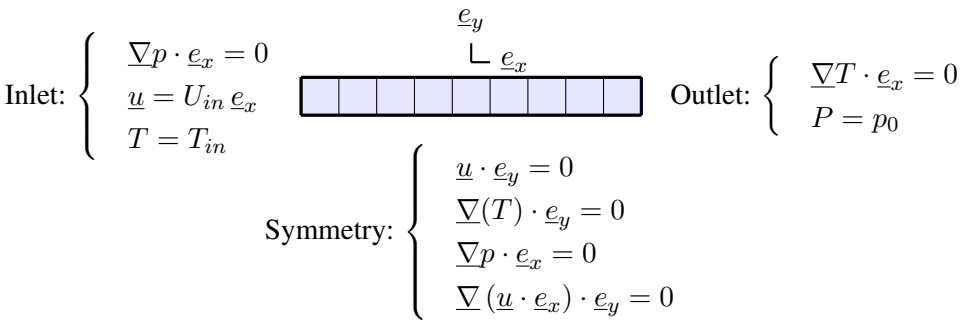

Figure 3.8: Sketch of the system with the boundary conditions used.

A first study is made to verify the mass and momentum conservation, using a mesh composed of 40 hexahedral cells. In this context, the temperature inlet boundary condition varies over time as follows:

$$T_{in} = 473\,\mathrm{K} \quad \text{if } t \in [10, 20[, \quad T_{in} = 300\,\mathrm{K} \quad \text{otherwise.}$$

The outlet pressure is set to a reference value p_0 and all other walls are considered as symmetries. A constant inlet velocity $U_{in} = 1\,\mathrm{m\,s^{-1}}$ and an initial density of $\rho_0 = 1.177\,\mathrm{kg\,m^{-3}}$ are set. Mass and momentum balances are then performed over the entire system and normalised by their initial values during $100\,\mathrm{s}$ as follows:

$$I_\rho = \frac{\displaystyle\int_\Omega \rho^n \mathrm{d}\Omega + \int_{t=0}^{t^n} \int_{\partial\Omega} \rho u \mathrm{d}S_x \mathrm{d}t}{\displaystyle\int_\Omega \rho_0 \mathrm{d}\Omega}, \tag{3.50}$$

$$I_q = \frac{\displaystyle\int_\Omega (\rho u)^{n-\theta} \mathrm{d}\Omega + \int_{t=0}^{t^{n-\theta}} \int_{\partial\Omega} (\rho u u + p)\, \mathrm{d}S_x \mathrm{d}t}{\displaystyle\int_\Omega \rho_0 U_{in} \mathrm{d}\Omega}. \tag{3.51}$$

The conservation of both quantities is tested for $\theta = 1$ and $\theta = 1/2$.

For each time step, set as $\Delta t = 0.3\,\mathrm{s}$, five inner-iterations are performed ($\varepsilon_{piso_0} = 10^{-7}$). The results of this study (Figure 3.9, Figure 3.10) show that the variation of mass and momentum relative to their initial values are negligible for both simulations, validating their conservation. Note that slight variations are observed when the inlet scalar condition changes; yet, they can still be neglected given their amplitude.

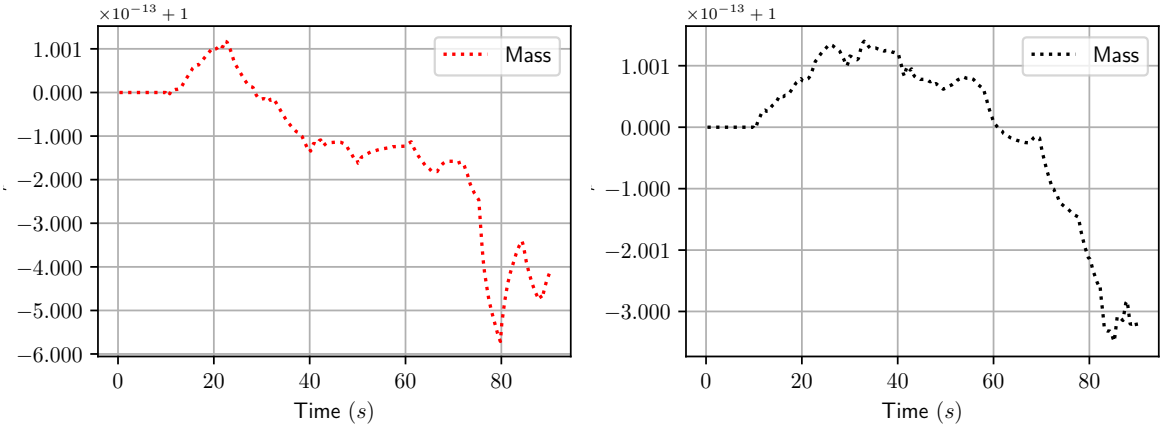

Figure 3.9: Mass conservation for the (left) Euler implicit scheme ($\theta = 1$) and the (right) Crank Nicolson scheme ($\theta = 1/2$).

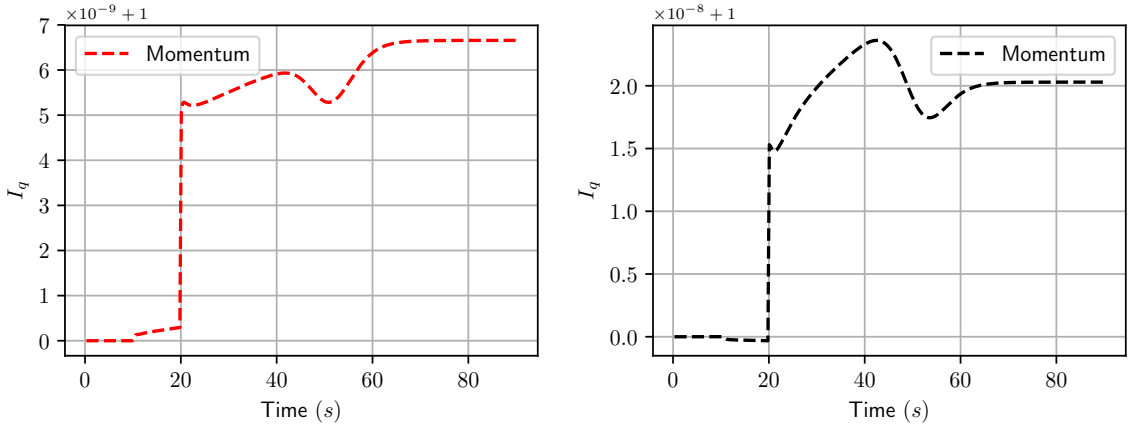

Figure 3.10: Momentum conservation for the (left) Euler implicit scheme ($\theta = 1$) and the (right) Crank Nicolson scheme ($\theta = 1/2$).

The second study consists on verifying the CPC scheme time convergence rate while transporting a passive scalar for different convective schemes. The scalar is initialised following two different profiles:

$$Y(x,0) = Y_0 \exp(-(x/L - 5)^2) \qquad \text{and} \qquad Y(x,0) = Y_0 \tanh(x/L - 5),$$

where $Y_0 = 1$ denotes an initial constant. The source and diffusive terms being disabled, an exact solution can be derived from its transport Equation (3.52) and compared to the numerical solution through the L_2 error norm:

$$\frac{\partial Y}{\partial t} + U_{in}\frac{\partial Y}{\partial x} = 0 \longrightarrow Y(x,t) = Y(x - U_{in}t, 0). \tag{3.52}$$

The inlet velocity U_{in} is set to $0.1\,\mathrm{m\,s^{-1}}$.
Several mesh refinements are used to study the scheme time convergence rate. The time step is adjusted so the CFL number is equal to 0.05 and four inner iterations are performed ($\varepsilon_{piso_0} = 10^{-7}$). Table 3.3 summarises the three different types of spatial discretisations for its face value Y_f that are tested.

Name	Formula	Notation
First Order Upwind	$Y_f \coloneqq \begin{cases} Y_c \; if \; \dot{M}_f \geq 0 \\ Y_{\widetilde{c}} \; else \end{cases}$	Upwind
Second Order Linear Upwind	$Y_f \coloneqq \begin{cases} Y_c + \underline{\nabla_c Y} \cdot \underline{IF} \text{ if } \dot{M}_f \geq 0 \\ Y_{\widetilde{c}} + \underline{\nabla_{\widetilde{c}} Y} \cdot \underline{JF} \text{ else} \end{cases}$	SOLU
Centered	$Y_f \coloneqq \alpha_{c\widetilde{c}} Y_c + (1 - \alpha_{c\widetilde{c}}) Y_{\widetilde{c}}$	Centered

Table 3.3: Different convective space schemes used to compute Y_f.

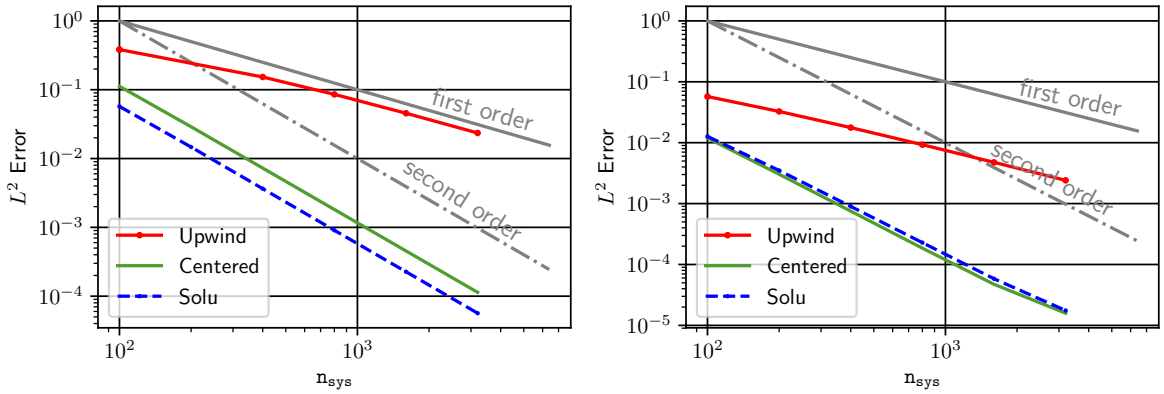

Figure 3.11: Scalar L_2 error norm following the grid refinement for three different convective schemes for the (left) Gaussian scalar initialisation and (right) tanh scalar initialisation.

At the time $t = 45\,\mathrm{s}$, the scalar error L_2 norm is studied over the spatial grid refinement. Results (Figure 3.11) show that the scheme converges to the first order when using the upwind scheme for both initial scalar profiles. When using the centered and SOLU convective schemes, a second order convergence rate is reached. The scalar profiles over the x axis at the final time are represented in Figure 3.12; one can see that the upwind simulations led to a more important error that can be explained by the convective numerical diffusion. This can be observed as well in the errors Figure 3.11.
This 1-D convection setup provided results showing that the scheme is able to verify the conservation of mass and momentum by the CPC scheme. Its convergence rate while transporting a scalar was also verified through two scalar profiles and different spatial convective schemes, compatible with the time scheme.

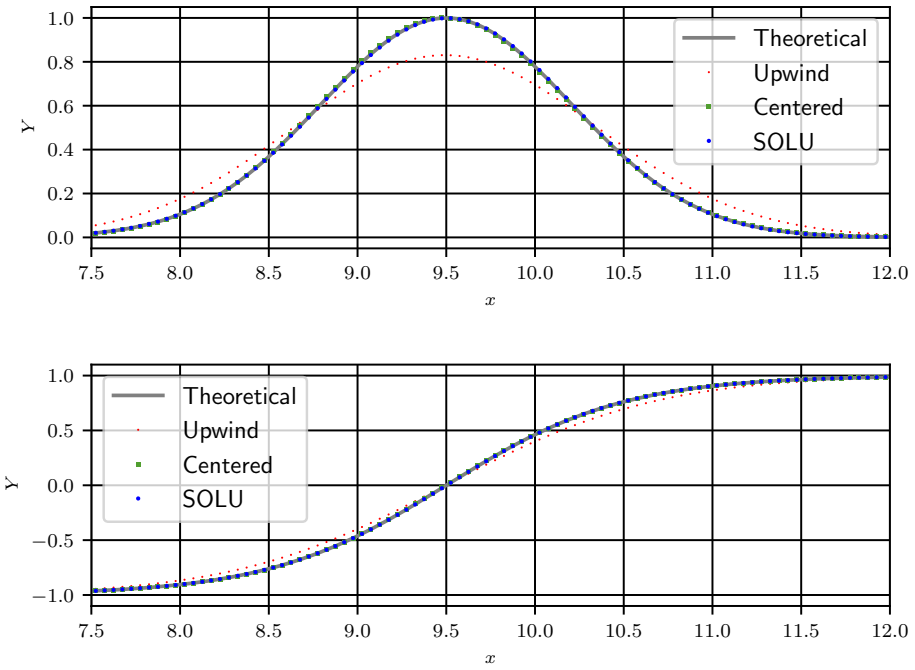

Figure 3.12: Scalar profiles at $t = 45\,\mathrm{s}$. (Top) Gaussian profile. (Bottom) tanh profile.

3.8.3 Shock tube

Motivations 3.8.3. The aim of this test case is to verify the accuracy and consistency of the scheme for regular and singular solutions which confirms as well the scheme preservation in fine of the total energy, which is one of its numerical goals.

Two one-dimensional Riemann problems are considered to verify the scheme accuracy for flows with shock and rarefaction waves. First, a double symmetric rarefaction wave expansion (Dse) is studied and then a more irregular configuration (Sod (1978) shock tube).
The computational domain is a tube of length $L = 400\,\mathrm{m}$ extending from $x = -L/2$ to $x = L/2$, the interface being located at $x = 0$.
Simulations are carried out on grids with $2^m \times 800$ cells, $0 \leq m \leq 6$. The initial conditions are given in Table 3.4; note that a membrane in the middle of the system separates two different fluid states. Symmetry conditions are imposed on all boundary faces of the computational domain except at the two end faces of the tube, which are set to be outlets. For each case, the fields L_1 error norm (related to the Riemann problem exact solution ψ_e (Smoller, 2012), Equation (4.115)) time convergence rate $\alpha(L_1^{err}(\psi))$ is studied for both θ values and for two fluid-velocity based CFL numbers (CFL = 0.04 and CFL = 1.00).
The convergence rate $\alpha(L_1^{err}(\psi))$ is calculated using Equation (3.53) applied on the data from the two most refined meshes simulations for each configuration. Independently of the time step, results are achieved with 3 inner-iterations ($\varepsilon_{piso_0} = 10^{-7}$).

$$L_1^{err}(\psi) = \frac{\sum_{c=1}^{N_c} |\Omega_c| \, |\psi_e(x_c) - \psi_c|}{\sum_{c=1}^{N_c} |\Omega_c| \, |\psi_e(x_c)|}, \qquad \alpha(L_1^{err}(\psi)) = \frac{\left| L_1^{err}(\psi)\big|_{m=6} - L_1^{err}(\psi)\big|_{m=5} \right|}{25600}. \tag{3.53}$$

The profiles of the density, temperature, pressure and velocity magnitude are qualitatively studied as well.

Test	$\rho_L[\mathrm{kg\,m^{-3}}]$	$u_L[\mathrm{m\,s^{-1}}]$	$p_L[\mathrm{Pa}]$	$\rho_R[\mathrm{kg\,m^{-3}}]$	$u_R[\mathrm{m\,s^{-1}}]$	$p_R[\mathrm{Pa}]$
Dse	1	-100	100,000	1	100	100,000
Sod	1	0	100,000	0.125	0	10,000

Table 3.4: Initial states for the two one-dimensional Riemann problems used.

Double Symmetric Expansion

Numerical results show that for all fields, the simulation convergence rates are close to 0.8 for CFL $=$ 0.04 (Figure 3.13, and Table 3.5). A slight improvement is observed when $\theta = 1/2$.
For the cases with CFL $= 1.00$, the theta value has a more important impact on the numerical results: the convergence rates are higher (close to 1) when using the time staggered scheme.
Figure 3.14 shows the simulation fields at $t = 0.3\,\mathrm{s}$ so all waves are visible in the computational domain, for a mesh composed of 3200 cells. The different fields are in agreement with the analytical solution, confirming the scheme accuracy related to regular solutions.

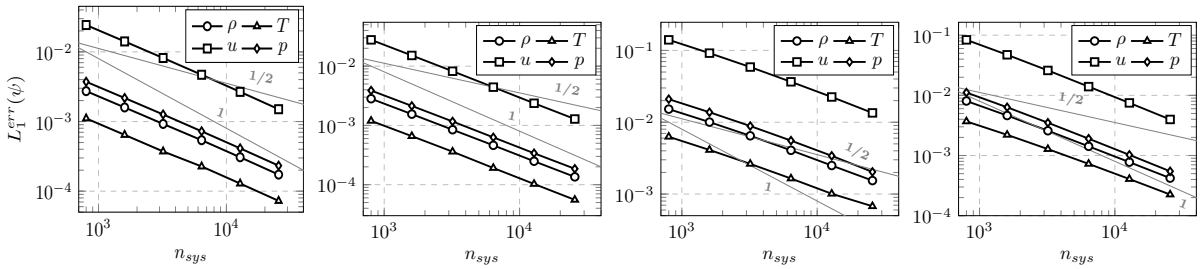

(a) CFL $= 0.04$, $\theta = 1$. **(b)** CFL $= 0.04$, $\theta = 1/2$. **(c)** CFL $= 1.0$, $\theta = 1$. **(d)** CFL $= 1.0$, $\theta = 1/2$.

Figure 3.13: L_1 error convergence for the Dse case using an upwind convective scheme for two values of CFL and θ.

CFL	θ	ρ rate	$\underline{u}$ rate	p rate	T rate
0.04	1.00	0.83	0.83	0.83	0.83
0.04	0.50	0.88	0.88	0.87	0.89
1.00	1.00	0.49	0.73	0.74	0.58
1.00	0.50	0.88	0.91	0.91	0.85

Table 3.5: L_1 convergence rates for the Dse case.

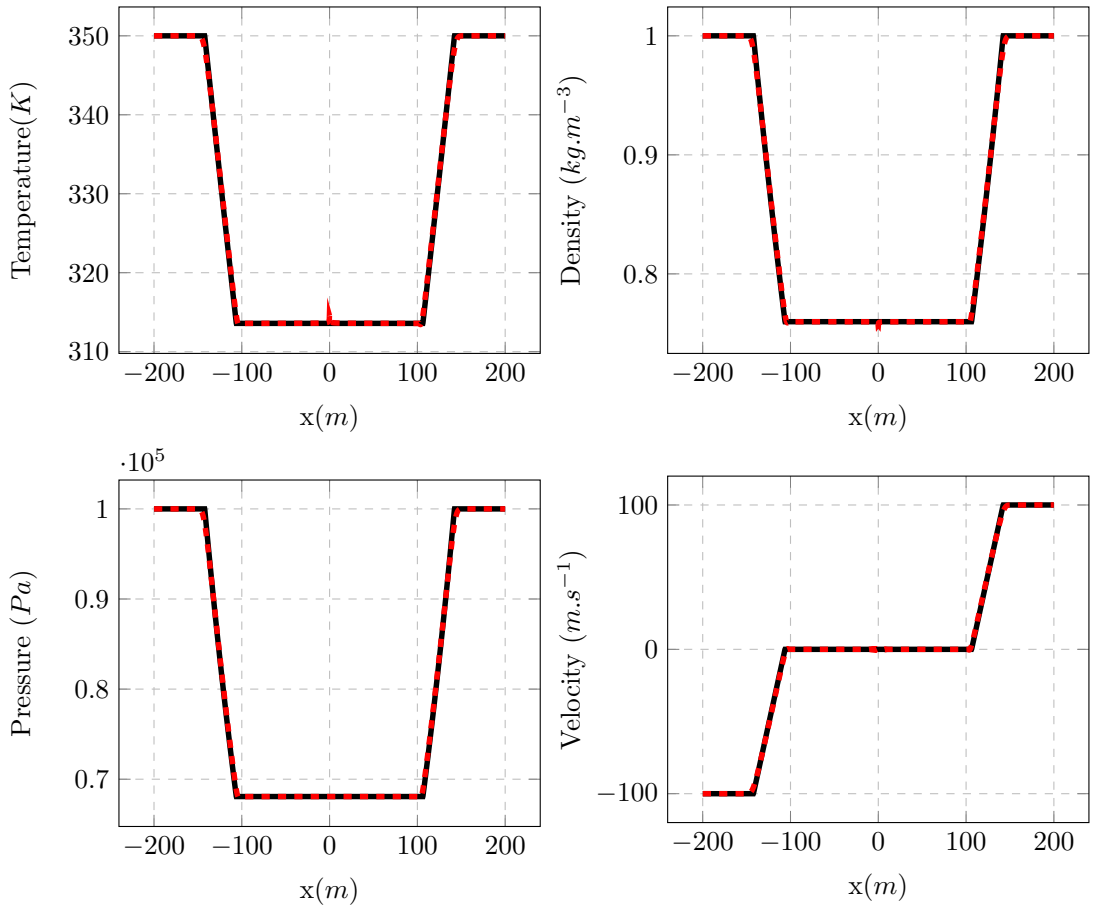

Figure 3.14: Double symmetric expansion wave results at $t = 0.3\,\mathrm{s}$ using a 3200 cells mesh and with $\theta = 1$ (–) exact solution (–) simulation.

Sod case

This test case is used to show the importance of adding the source term $\Gamma^{u^2/2}$ to the internal energy equation. Based on the qualitative numerical results (Figure 3.17), one can notice that without the source term, even if the pressure, velocity and density values are close to the exact solution, the correct temperature plateau value is incorrect (Figure 3.17, blue lines). When using the source term (Figure 3.17, red lines), the temperature plateau value is well reached by the simulation, leading to consistent numerical results.

Table 3.6 shows the fields L_1 error convergence rate that are represented in Figures 3.15 and 3.16. For irregular solutions, it is known that even second order schemes used for compressible flows do not exhibit second order accuracy. The convergence rates are around 0.5 for the density and temperature and around 1.0 for the pressure and velocity. They can be actually comparable and are in agreement with the convergence rates available in the literature for compressible flow solvers (Archambeau et al., 2009; Colas et al., 2019; Herbin et al., 2020) [][][]. Similarly to the previous case, when using the staggered scheme ($\theta = 1/2$), the overall L_1 error for all fields is less important than the one obtained with $\theta = 1$.

Finally, Figure 3.18 shows that for the Sod configuration, the CFL like conditions presented in Section 3.7 are respected and below the speed-based CFL number for both calculations CFL simulations ($\theta = 1$). This is a good point, where for important velocity and pressure jumps, both conditions are less constraining than the classical one.

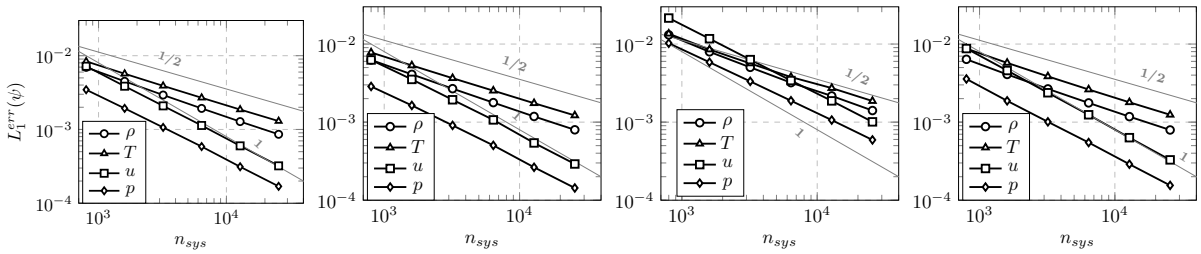

(a) CFL $= 0.04$, $\theta = 1$. **(b)** CFL $= 0.04$, $\theta = 1/2$. **(c)** CFL $= 1.0$, $\theta = 1$. **(d)** CFL $= 1.0$, $\theta = 1/2$.

Figure 3.15: L_1 error convergence for the Sod case using an upwind convective scheme for two values of CFL and θ.

CFL	θ	Convective scheme	ρ rate	$\underline{u}$ rate	p rate	T rate
0.04	1	Upwind	0.60	0.88	0.86	0.54
0.04	0.5	Upwind	0.59	0.86	0.85	0.53
1.00	1	Upwind	0.65	0.89	0.82	0.54
1.00	0.5	Upwind	0.59	0.90	0.85	0.53
0.04	1	Centered	0.61	0.96	0.92	0.53
0.04	0.5	Centered	0.60	0.95	0.95	0.54
1.00	1	Centered	0.64	0.89	0.82	0.56
1.00	0.5	Centered	0.56	0.90	0.89	0.51

Table 3.6: Convergence rates for the Sod case.

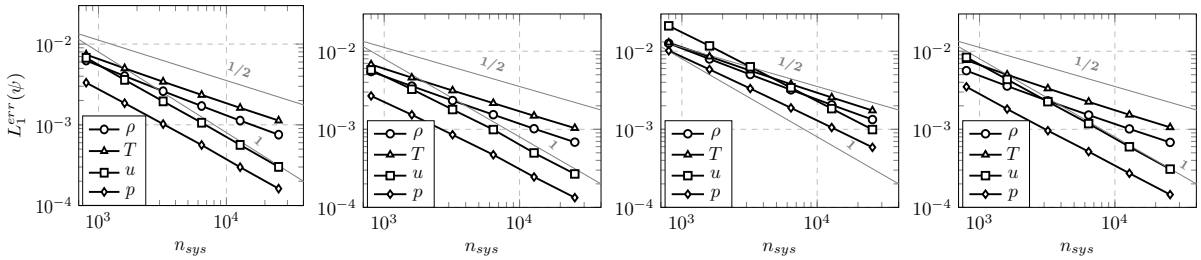

(a) CFL $= 0.04$, $\theta = 1$. **(b)** CFL $= 0.04$, $\theta = 1/2$. **(c)** CFL $= 1.0$, $\theta = 1$. **(d)** CFL $= 1.0$, $\theta = 1/2$.

Figure 3.16: L_1 error convergence for the Sod case using a centered convective scheme for two values of CFL and θ.

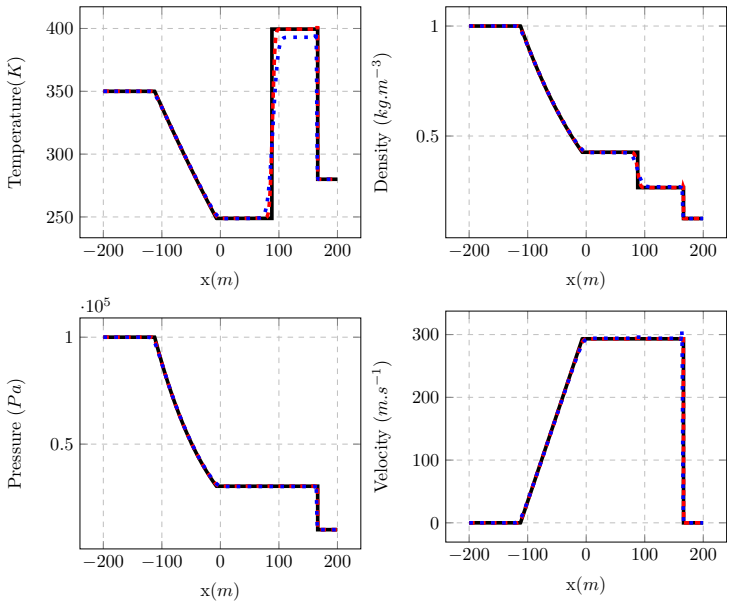

Figure 3.17: Sod case results at $t = 0.3\,\mathrm{s}$ for $\theta = 1$ using a 3200 cells mesh (–) exact solution (- -) simulation using the source term $\Gamma^{u^2/2}$ (- -) simulation without the source term $\Gamma^{u^2/2}$.

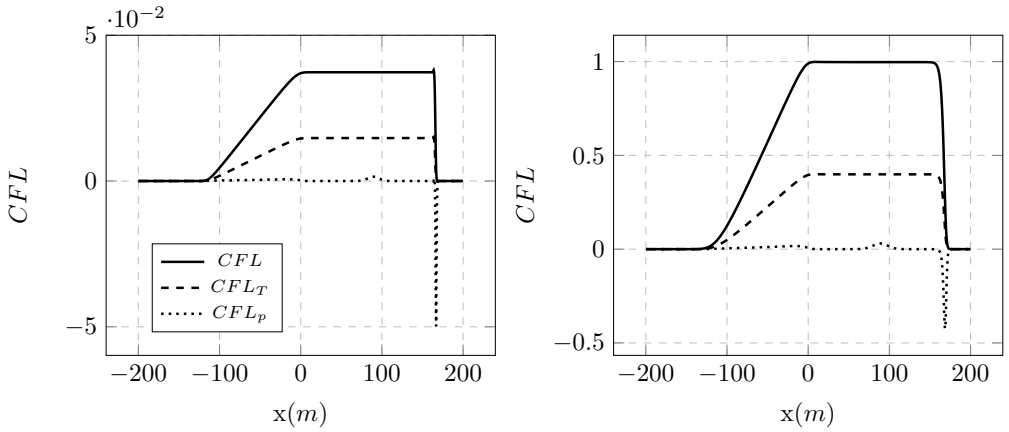

Figure 3.18: New CFL conditions related to the CPC scheme time discretisation for the Sod case and for two different velocity based CFL simulations, with $\theta = 1$. (Left) CFL = 0.04. (Right) CFL = 1.0.

Remark 3.8.1. This test case could correctly be reproduced by the IC scheme, but an incompressible scheme wouldn't be able to correctly simulate the singular solution.

3.8.4 Atmospheric column

Motivations 3.8.4. This test emphasises the potential of coupling indoor and outdoor airflow simulations using the CPC time scheme. For instance, a good reproduction of the thermodynamical variables evolution in an atmospheric context is interesting for a micro urban scale simulation.

This case represents an one-dimensional atmospheric column of $100\,\mathrm{m}$ height. The numerical reproduction of the system pressure, temperature and density variation while increasing the altitude is

tested here. The expected thermodynamic fields expressions are:

$$
\begin{aligned}
T &= T_0 - \frac{g}{c_p} z, \\
\rho &= \rho_0 \left(1 - \frac{\gamma - 1}{\gamma} \frac{\rho_0 g z}{p_0}\right)^{\frac{1}{\gamma - 1}}, \text{ and} \\
p &= p_0 \left(1 - \frac{\gamma - 1}{\gamma} \frac{\rho_0 g z}{p_0}\right)^{\frac{\gamma}{\gamma - 1}}.
\end{aligned}
\tag{3.54}
$$

$T_0 = 300\,\mathrm{K}$, $p_0 = 10^5\mathrm{Pa}$ and $\rho_0 = p_0/(R_a T_0)$ are references values. The system initial fields values are set according to the expected profiles and the simulation is ran during $50\,\mathrm{s}$ with an initial time step (divided per two for each mesh refinement) equal to $\Delta t = 1\,\mathrm{s}$. The fields L_2 error norm (see Equation (3.49)) are plotted over time. Moreover, it is verified that no parasite velocities are created and that the potential temperature (Equation (2.19)) remains constant along the z axis.
Simulations are carried out on three different spatial grids (100, 200 and 400 cells). One inner iteration is performed ($\varepsilon_{piso_0} = 10^{-5}$). The bottom face is considered as a non-slip adiabatic wall and other faces are set as symmetries.
Figure 3.19 shows the L_2 error norm for the temperature, density and pressure at $t = 50\,\mathrm{s}$ following the z axis. First, it is observed that all variables error related to their exact solution are below the solver precision 10^{-8} (cells out of the boundaries). Some higher errors exist in the boundary zone.

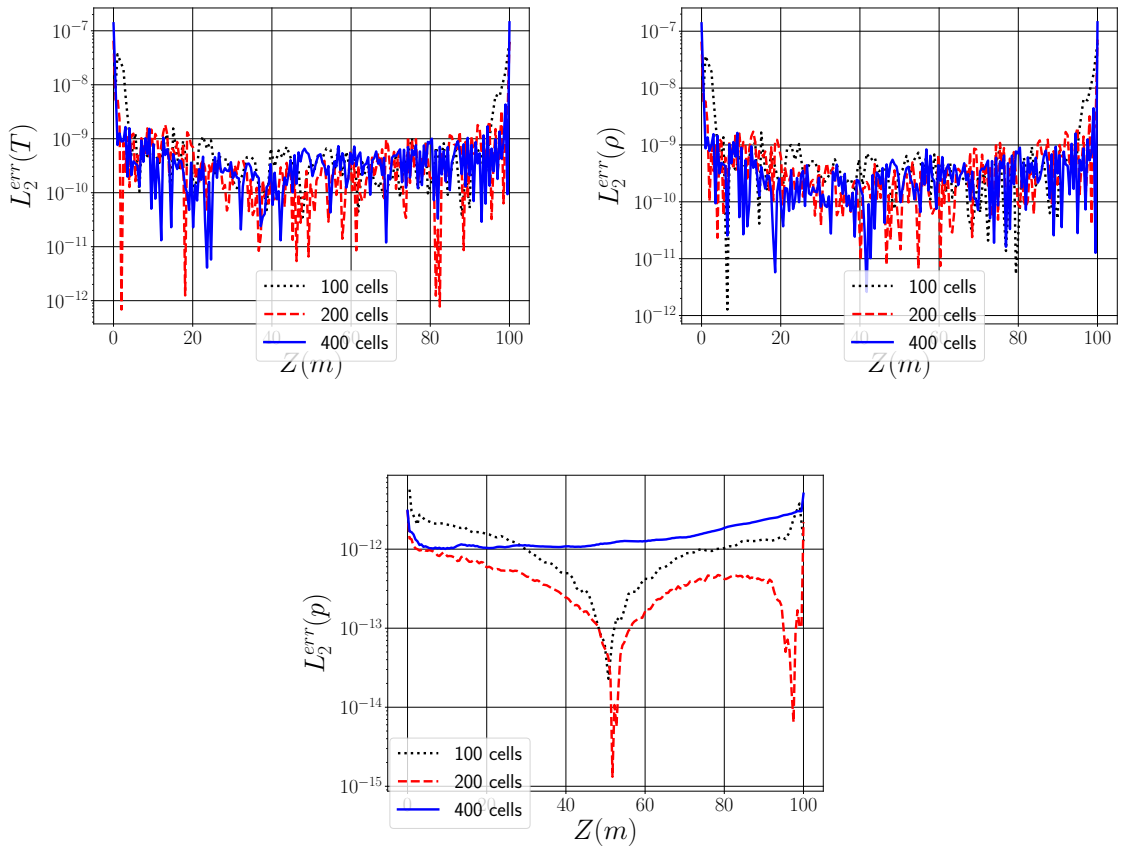

Figure 3.19: Fields L_2 error norm at $t = 50\,\mathrm{s}$ according to the height.

Finally, Figure 3.20 represents the potential temperature and the vertical velocity along z at the end of the

simulation. The left figure shows the correct conservation of the potential temperature over the height. The right one shows some parasite velocities for all different meshes, but that presents negligible values.

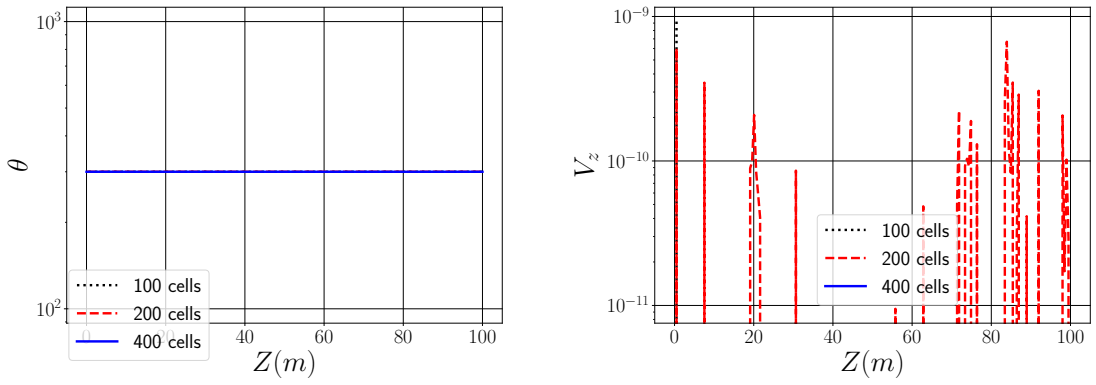

Figure 3.20: Potential temperature and vertical velocity at $t = 50\,\mathrm{s}$ according to the height.

3.8.5 Heated cavity - 2-D natural convection

Motivations 3.8.5. This validation case is of great importance since it represents a numerical benchmark case of natural convection, which is, as presented in the introduction, often present in indoor environments. Providing results in agreement with the reference emphasises the scheme application for such systems. A comparison between the IPC and CPC schemes is made.

This natural convection validation case presented in Le Quéré et al. (2005) and studied in Le Quéré et al. (1992); Vierendeels et al. (1999a); Becker et al. (1999); Darbandi and Hosseinizadeh (2006) focuses on the heat transfer in a steady flow driven by buoyancy effects.
The corresponding 2-D system of characteristic length $L = 0.4603\,\mathrm{m}$ is illustrated on Figure 3.24. The flow is driven by the lateral walls temperature difference, respectively at $T_h = 960\,\mathrm{K}$ and $T_c = 240\,\mathrm{K}$. In some situations, a small temperature difference may be modelled using the incompressible equations and the Boussinesq approximation. In case of a larger difference, the flow shall be considered as compressible. In this section, only the test case T1 of the reference paper is studied, with $Ra = 10^6$ (Equation (3.56)) and constant fluid properties.
The mean Nusselt number

$$\overline{Nu} = \frac{1}{L}\int_{y=0}^{y=L} Nu(y)\mathrm{d}y, \tag{3.55}$$

evaluated on the cold and hot walls are compared to their referenced values, with:

$$\begin{aligned} Nu(y) &= \frac{L}{(T_h - T_c)}\frac{\lambda}{\lambda_0}\frac{\partial T}{\partial x}\bigg|_w (y), \\ Ra &= Pr\frac{g\rho_0^2(T_h - T_c)L^3}{T_0\mu_0^2}. \end{aligned} \tag{3.56}$$

The flow dimensionless variables are:

$$\hat{p} := p/p_0, \quad \hat{u} := u/U, \quad \hat{v} := v/U, \quad \text{and } \hat{T} := (T - T_c)/(T_h - T_c),$$

where $U = \alpha_0/L$, with $\alpha_0 = \lambda_0/(\rho_0 C_p)$. The initial conditions are $p_0 = 10.1325 \times 10^4\,\mathrm{Pa}$ and $T_0 = 600\,\mathrm{K}$. Other walls are considered adiabatic. The following fluid properties are constant: $\mu_0 = 1.68 \times 10^{-5}\,\mathrm{kg\,m^{-1}\,s^{-1}}$ and $\lambda_0 = \mu_0 \gamma R_a/((1-\gamma)Pr)$, with $Pr = 0.71$ and $R_a = 287\,\mathrm{J\,kg^{-1}\,K^{-1}}$. All simulations are performed with $\theta = 1$ (steady solution) and 2 inner iterations ($\varepsilon_{piso_0} = 10^{-5}$).
First, a mesh sensitivity study is performed and shown in Figure 3.21 (b). Beyond 740×740 cells, the Nusselt number have negligible variation. Thus, only results obtained with this mesh (Figure 3.23, (b)) are discussed. The corresponding time step for the mesh is $\Delta t = 0.0025\,\mathrm{s}$. The steady state, represented in Figure 3.22, is reached after approximately $10\,\mathrm{s}$ of simulation (Figure 3.21, (a)). One can see that the wall temperature difference causes a non symmetric flow, with a consequent temperature gradient. Similarly to the first verification test case, the mean cavity density remains constant over time (Figure 3.21, left, continuous line), while the other thermodynamic fields converge to their steady solution.

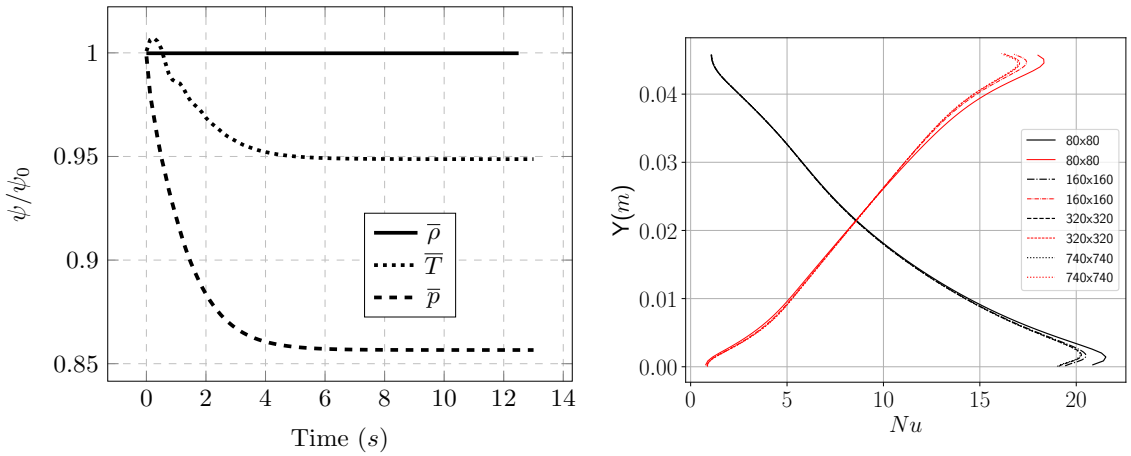

(a) Simulation convergence in time

(b) Mesh sensibility analysis

Figure 3.21: (a) Relative domain-averaged quantities ψ/ψ_0 over time (b) Nusselt number over the non adiabatic walls for different mesh refinements; the hot and cold walls are represented by red and black lines, respectively.

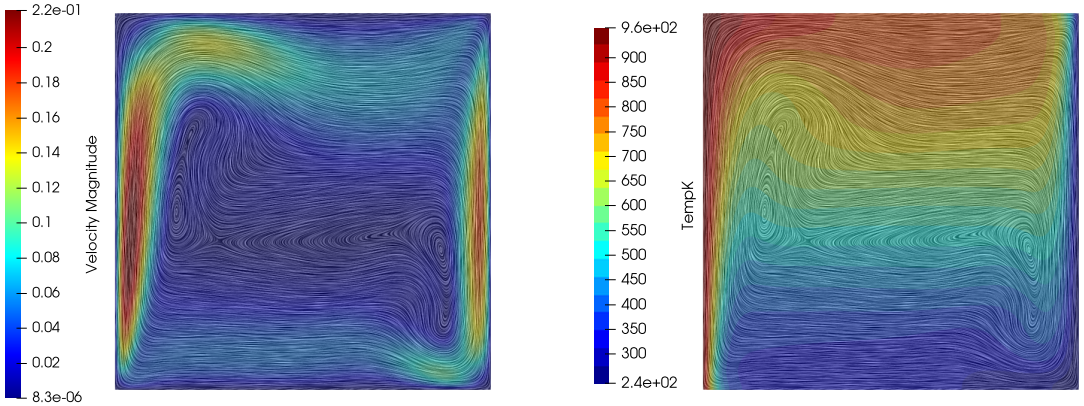

(a) Velocity

(b) Temperature

Figure 3.22: Steady fields at the final time of simulation for the 740×740 cells mesh.

Figure 3.24 compares some temperature iso-contours over the cavity for the presented algorithm to the reference results (Darbandi and Hosseinizadeh, 2006), which are very similar.

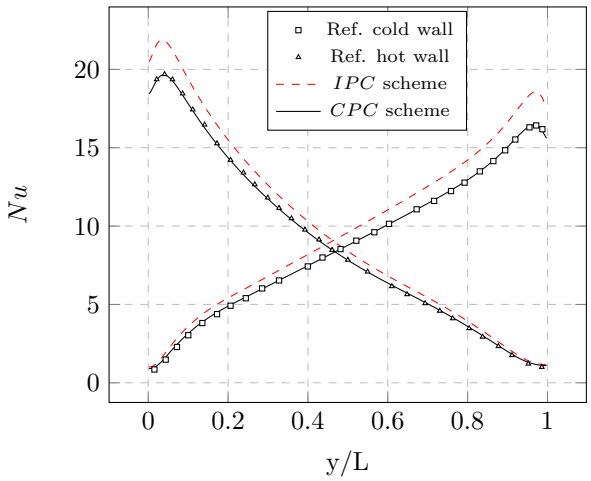

(a) Nusselt number over the walls

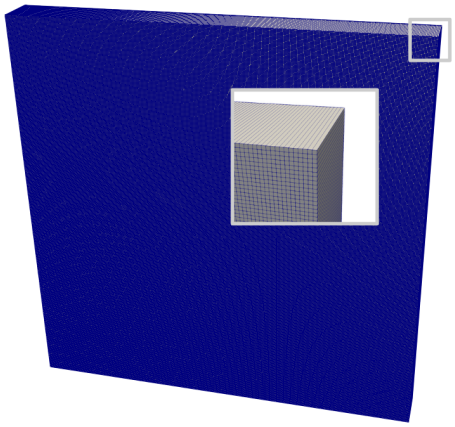

(b) Hexahedral mesh

Figure 3.23: (a) Nusselt number profiles for the hot and cold walls compared to the IPC scheme and the reference results (Darbandi and Hosseinizadeh, 2006). (b) 740×740 cells hexahedral mesh used for the presented results.

Table 3.7 compares the CPC and IPC schemes mean Nusselt number and mean pressure value against the reference ones (Le Quéré et al., 2005). The pressure variation is well reproduced by the CPC algorithm in the heated cavity, where its mean value reaches the expected reference value of 0.856. This is not the case for the IPC scheme due to the lack of pressure variation (and possibly a variation of density).
Moreover, the mean Nusselt numbers of both walls are in agreement with their expected values of 8.86 (see Figure 3.23 (a) for the Nusselt number profiles over the two given walls). This is directly linked to the correct shape of the vertical and horizontal velocity profiles over the cavity, as shown in Figure 3.25, and the steady problem behaviour.
As observed in the pressure cooker test case (3.8.1), the present comparison clearly shows that the thermodynamic pressure variation and wall heat fluxes are well reproduced and not negligible for natural convection.
To conclude on this case, the simulation results showed that the proposed scheme can be as accurate as other numerical methods (Le Quéré et al., 1992; Becker et al., 1999; Le Quéré et al., 2005; Vierendeels et al., 1999b), which are known to predict correct natural convection solutions. Additional comparisons are made in Table 3.8 between the CPC and the literature reference results.

	IPC scheme	CPC scheme	Ref (Le Quéré et al., 2005)
$\overline{Nu}_w$	9.689	8.859	8.860
$\hat{p}$	1.000	0.855	0.856

Table 3.7: Comparison between the mean Nusselt numbers and total pressure ratio with the reference values from Le Quéré et al. (2005). Results from the mesh simulation of a converged 740×740 cells for both CPC and IPC schemes.

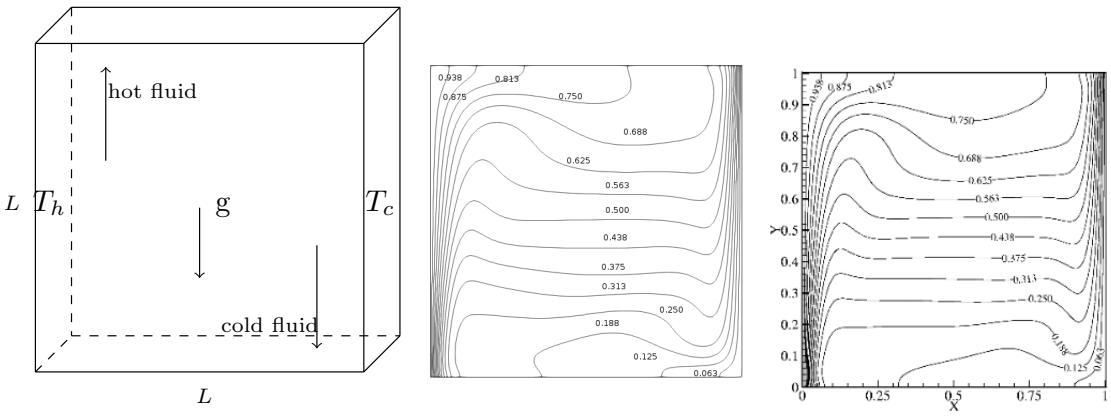

Figure 3.24: (Left) Sketch of the system. (Centre) Steady state dimensionless temperature $\hat{t}$ iso-contours. (Right) Steady state dimensionless temperature $\hat{T}$ iso-contours, reference from Darbandi and Hosseinizadeh (2006).

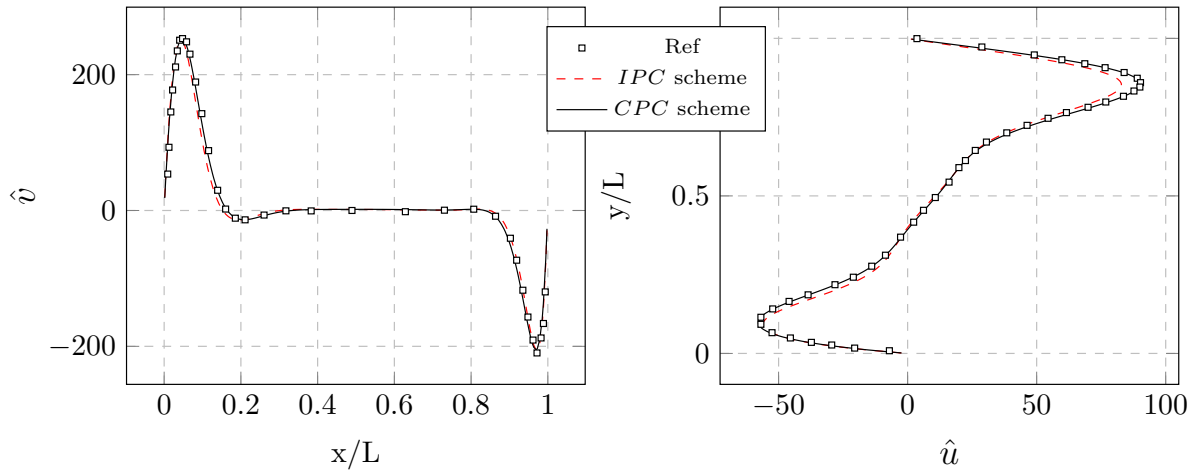

Figure 3.25: Distribution of the velocity on the centrelines of the convective cavity compared to the reference (Darbandi and Hosseinizadeh, 2006).

	Vierendeels	Dabbene	Beccantini	Studer	Kloczko	Heuveline	Darbandi	CPC	Ref
$\overline{Nu}$ (h)	8.860	8.864	8.860	8.860	8.862	8.860	8.880	8.860	8.860
$\overline{Nu}$ (c)	8.860	8.864	8.860	8.860	8.862	8.860	8.88	8.85978	8.86
Nu (y=0.5)(h)	7.819	7.822	7.820	N.A.	7.820	N.A.	N.A.	7.824	N.A.
Nu (y=0.5)(c)	8.796	8.817	8.796	N.A.	8.797	N.A.	N.A.	8.777	N.A.
Nu max (h)	19.596	19.626	19.595	19.595	19.611	19.596	N.A.	19.649	N.A.
Nu max(c)	16.362	16.352	16.363	16.361	16.375	16.362	16.463	16.463	N.A.
Type of mesh	2048 x 2048	320 x 320	296 x 296	80 x 80	240 x 240	2.10^5	300 x 300	740 x 740	N.A.

Table 3.8: Additional references results to the Le Quéré cavity (test 1) related to the Nusselt number over the cold and hot walls.

3.8.6 Lock exchange case

Motivations 3.8.6. Here we aim to validate the numerical scheme related to an incompressible test case, where the flow is only driven by the gravity. Numerical results are compared to reference results and to both IPC and IC schemes.

This case focuses on a two dimensional gravity current flow in a lock exchange configuration. The system is a rectangular cavity of height 2L and width 30L, with $L = 1\,\mathrm{m}$ the half-height of the cavity (see Figure 3.26 for the system sketch). The temperature difference $\Delta T = 2\,\mathrm{K}$ between the heavy and light fluids, respectively at T_c (on the right) and T_h (on the left), drives the flow. An adiabatic non slip condition is imposed to the top and bottom walls while others are treated as symmetries.

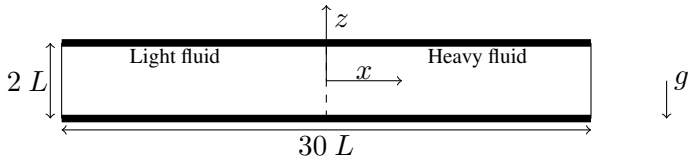

Figure 3.26: Sketch of the lock exchange system.

The Grashof number describing the flow is

$$Gr = \frac{g\beta\Delta T L^3}{\nu^2} = 1.25.10^6.$$

The dimensionless time is denoted by $t^+ = \frac{tU}{L}$, where $U = \sqrt{\beta\Delta T g L}$ and $\beta = 2/(T_h + T_c)$.
A LES simulation is performed using a mesh with 768×91 cells based on the reference paper (Härtel et al., 2000), with $\Delta t = 0.017\,\mathrm{s}$. 2 inner-iterations are performed by time-step ($\varepsilon_{piso_0} = 10^{-6}$) and $\theta = 1/2$ (we focus on a unsteady flow, thus using the staggered scheme is of interest).
The CPC simulation numerical density isolines (10 contours linearly separated from the minimum and maximum densities) at respectively $t^+ = 10$ and 20 are compared with the 2D DNS (Härtel et al., 2000) and LES (Ooi et al., 2007) reference results.
Moreover, both IC and IPC code_saturne algorithms are tested as well using the LES approach. Figure 3.27 shows the temperature evolution over time at the centre of the system for the CPC simulation. Symmetric structures can be observed induced by the buoyant flow effects.
The results presented in Figures 3.28 and 3.29 show the different density isolines, for the reference papers and code_saturne simulations at $t^+ = 10$ and 20.
One can observe that both IPC and CPC simulations led to similar density isolines compared to the references. As expected, due to its isentropic pressure step, the IC time scheme was not able to reproduce correctly the flow structures.
Such results emphasise the ability of the proposed algorithm to reproduce incompressible and compressible flows.

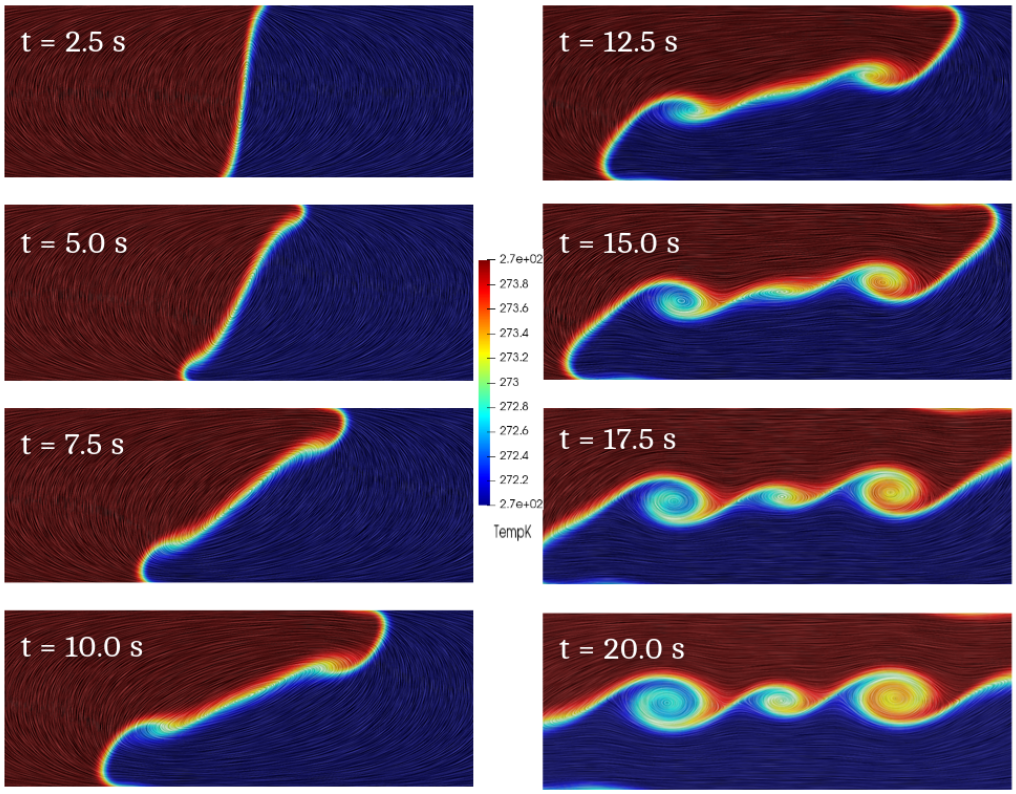

Figure 3.27: Zoom at the temperature evolution at the center of the system along time.

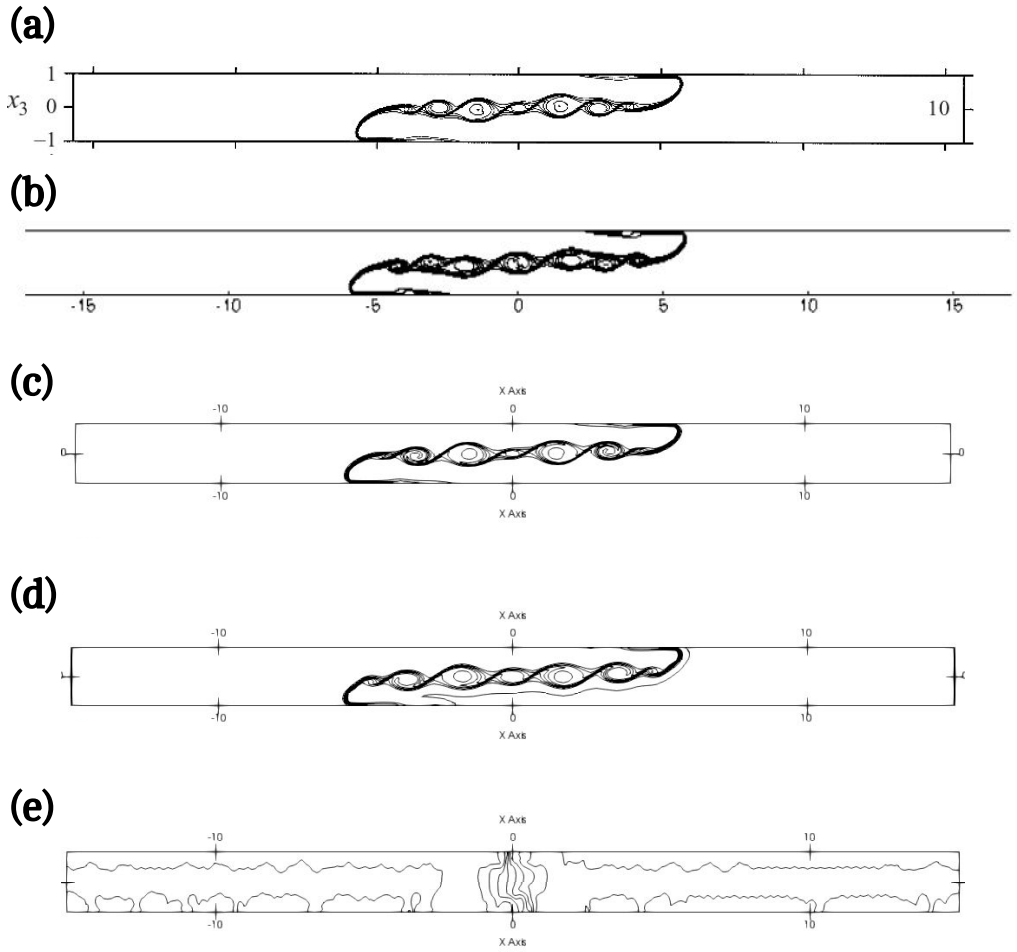

Figure 3.28: Density isolines at $t^+ = 10$. (a) Reference (Härtel et al., 2000), DNS simulation. (b) Reference (Ooi et al., 2007), LES simulation. (c) CPC scheme, LES simulation. (d) IPC algorithm, LES simulation. (e) IC algorithm, LES simulation.

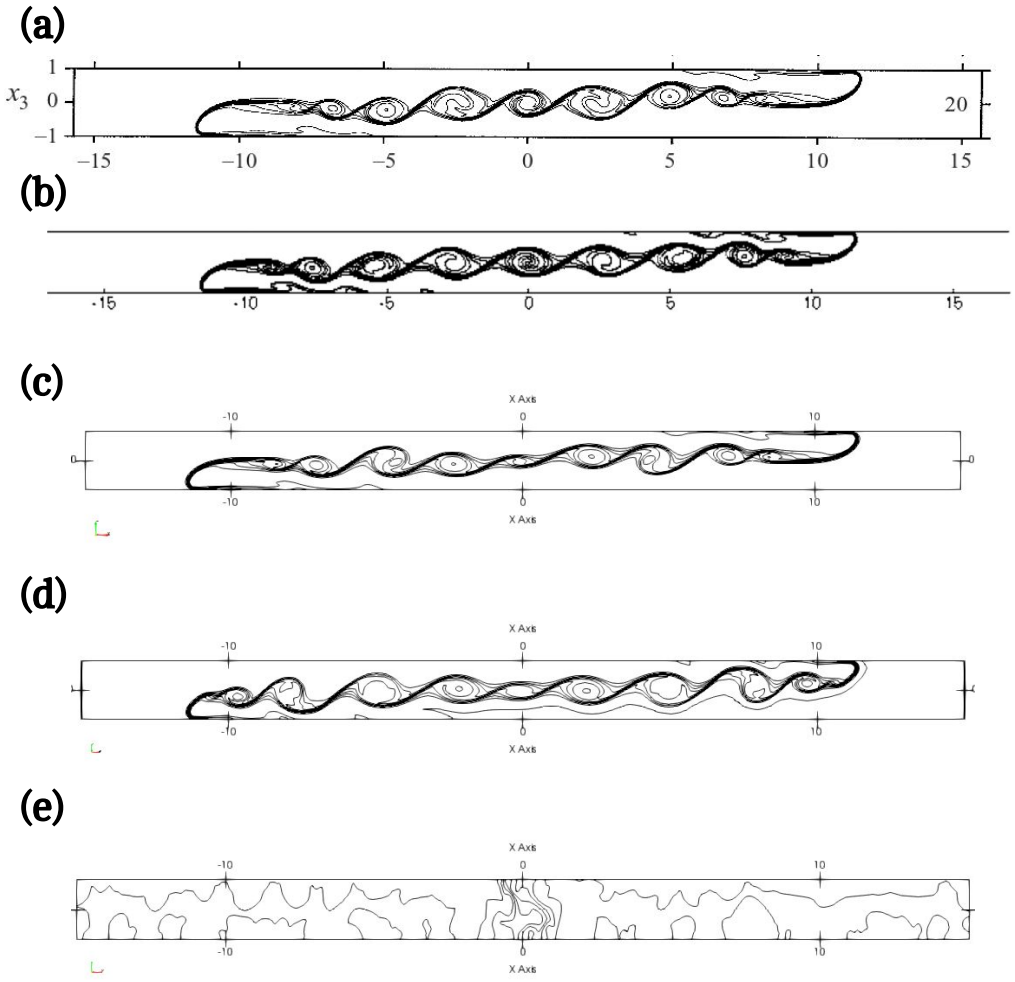

Figure 3.29: Density isolines at $t^+ = 20$. (a) Reference (Härtel et al., 2000), DNS simulation. (b) Reference (Ooi et al., 2007), LES simulation. (c) CPC scheme, LES simulation. (d) IPC algorithm, LES simulation. (e) IC algorithm, LES simulation.

3.8.7 Axisymmetric jet

Motivations 3.8.7. In order to perform LES simulations on a more complex ventilation validation case, a 3-D axisymmetric jet is studied and a mesh analysis is made. The goal is to determine, given the jet Reynolds number, the required mesh refinement to get accurate numerical results for an axisymmetric jet.

This case, based on Lee et al. (2003), focuses on reproducing the jet decay by studying the evolution of the centerline velocity u/U_{in}. $U_{in} = 1\,\mathrm{m\,s^{-1}}$ is the inlet (circle with a diameter of $D_{in} = 0.5\,\mathrm{m}$) velocity and u the maximal jet velocity given a vertical profile on the non dimensional axial coordinate x/D_{in}. The jet turbulent length scales are analysed in order to have an idea of the required mesh refinement on the more complex Minibat jet case that follows in this chapter. The fluid considered here is water

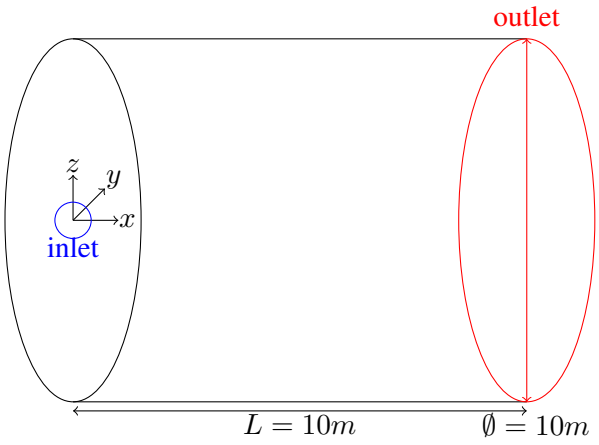

Figure 3.30: Setup sketch

and the jet Reynolds number is $Re = 5.62.10^4$ (close to the next case Reynolds number). The system, reproduced in Figure 3.30, is an extruded cylinder of length $L = 10\,\mathrm{m}$ and diameter of $10\,\mathrm{m}$, the outlet being the entire circle of diameter $10\,\mathrm{m}$ at $x = 10\,\mathrm{m}$. For all simulations, the time step is set so the CFL condition is equal to the unity related to the inlet velocity and two inner iterations are performed ($\varepsilon_{piso_0} = 10^{-6}$).
A first RANS $k - \varepsilon$ simulation is realised with a 7.6 10^5 cells mesh ($\Delta x = 10\,\mathrm{cm}$), to compute the flow turbulent spatial integral and Taylor length scales (Figure 3.31). The Kolmogorov scale could be represented as well but we assume that this scale should not be taken into account by the mesh refinement (due to computational costs). The mesh used for this case is represented in Figure 3.32, (a).
A mesh sensibility analysis is then made on u/U_{in} where a LES simulation is performed for three different meshes during $500\,\mathrm{s}$ ($\Delta x = 10\,\mathrm{cm}$, $\Delta x = 5\,\mathrm{cm}$ and $\Delta x = 2.5\,\mathrm{cm}$ corresponding respectively to 7.6 10^5, 6.1 10^6 and 4.8 10^6 cells), to achieve converged time averages (the 100 last seconds are averaged). A focus is made on the axial spatial step. Note that this jet is isothermal; no density variation is considered. Figure 3.33 presents for the different meshes the velocity decay when increasing the axial distance related to the inlet.

Remark 3.8.2. The numerical value of u/U_{in} is computed from a time averaged velocity profile (see Figure 3.34 to see the average velocity field).

Results show that for the most refined mesh, corresponding to the half (between the minimum and maximum values) of the Taylor turbulent length scale, the jet decay is close to the experimental one. This conclusion must be kept in mind while designing the next test case mesh.

Figure 3.35 shows the evolution of the jet diffusion over the system along time for the most refined mesh (i.e. $\Delta z = 0.025\,\mathrm{m}$, 32 10^6 cells). Figure 3.34 shows the average velocity magnitude at the final time of simulation. From the three figures, one can identify the different theoretical jet regions presented in Subsection 2.2.7. Close to the inlet, the centerline velocity remains equal to the initial one (plateau value in Figure 3.33), denoting the core jet region. Around $x/D_{in} = 5$, a decay region begins where the velocity starts decreasing, corresponding to the axisymmetric zone. The decay is proportional to the axial distance from the inlet, which is in agreement with jets similarity theory. Note that the study did not focus on the terminal zone, since no experimental data were available for larger x values.

(a) Integral scale

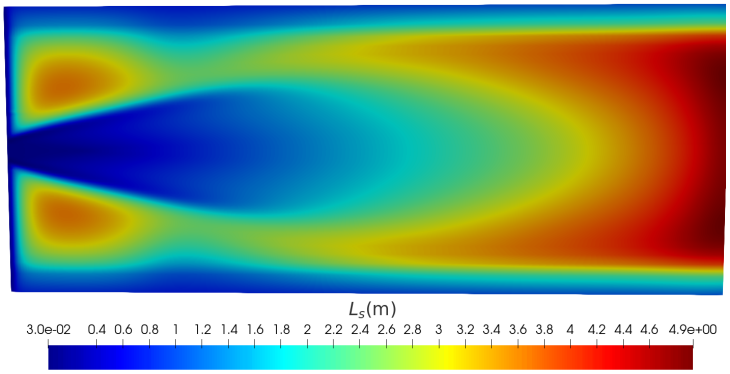

(b) Taylor scale

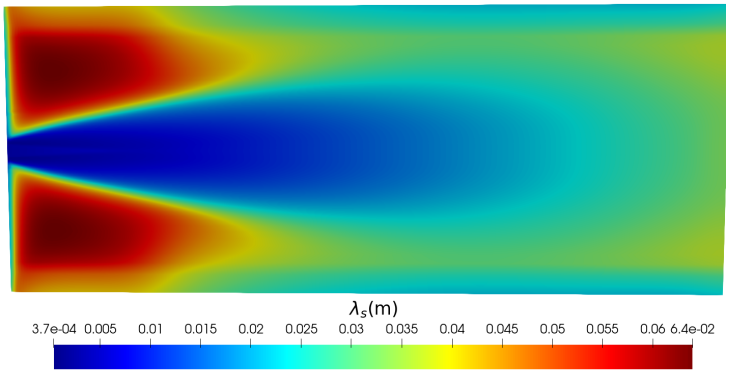

Figure 3.31: Jet turbulent length scales from the RANS simulation. (a) Integral scale (b) Taylor scale.

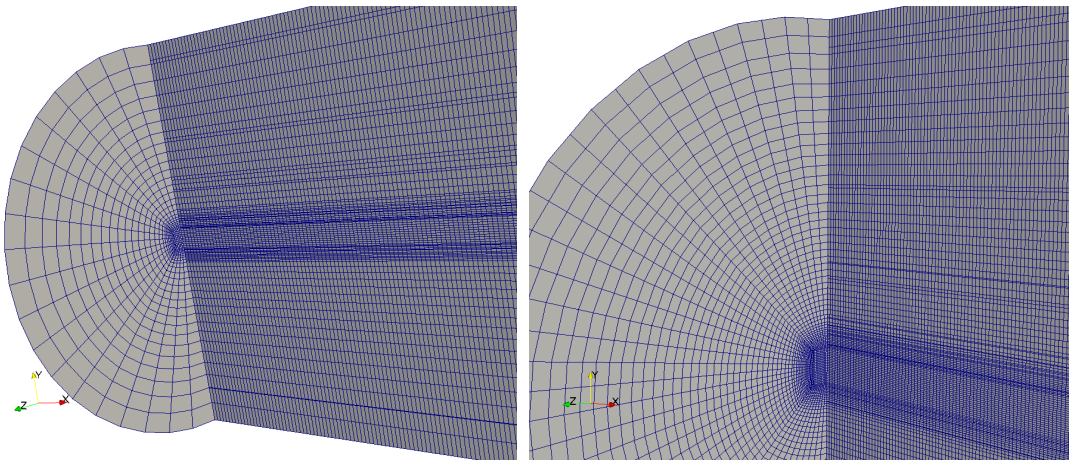

Figure 3.32: Different meshes used (a) 10 cm axial spatial step (b) 5 cm axial spatial step.

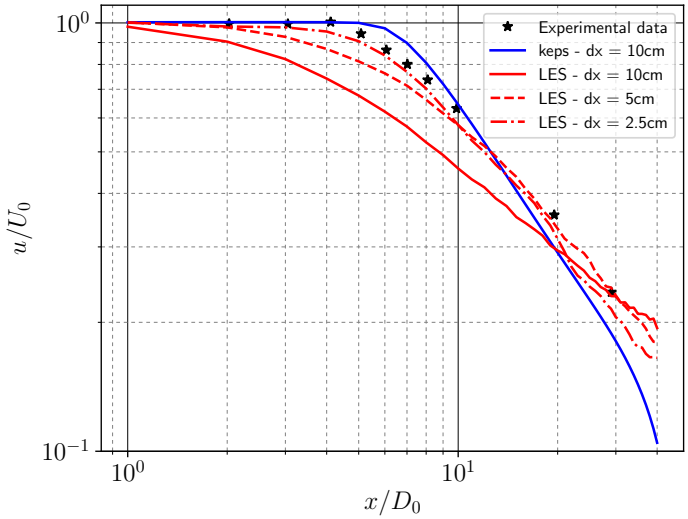

Figure 3.33: u/U_{in} along the axis x for the $k-\varepsilon$ and LES different mesh refinements.

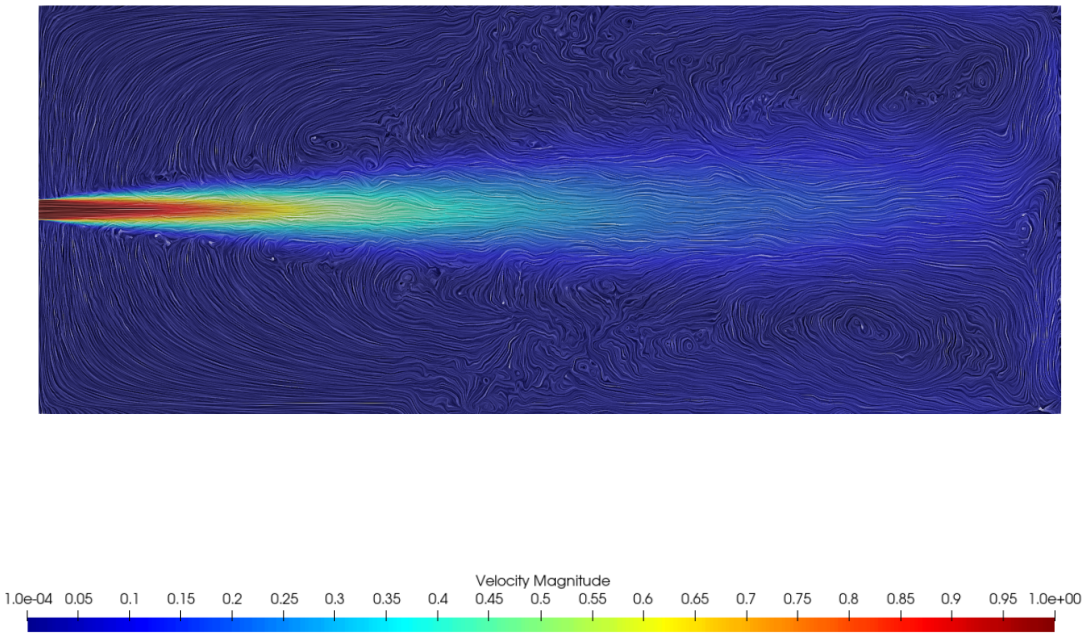

Figure 3.34: Time averaged velocity magnitude at $t = 500\,\mathrm{s}$ for the most refined mesh.

(t= 62.5 s)

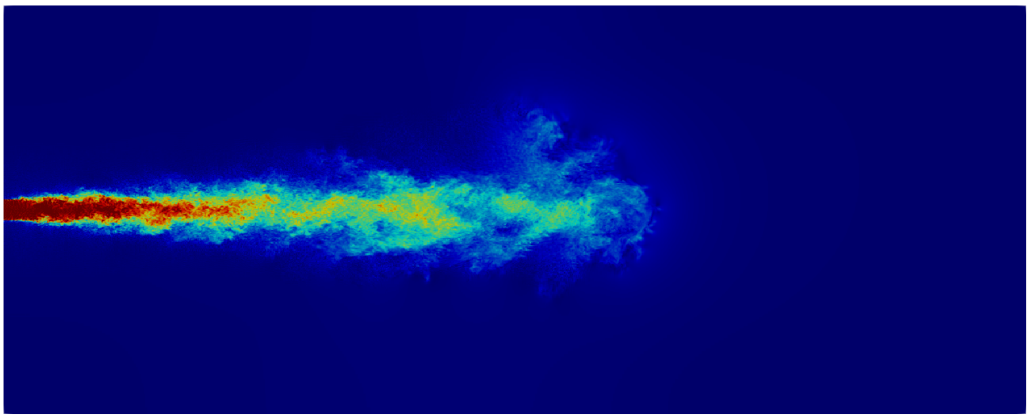

(t= 125.0 s)

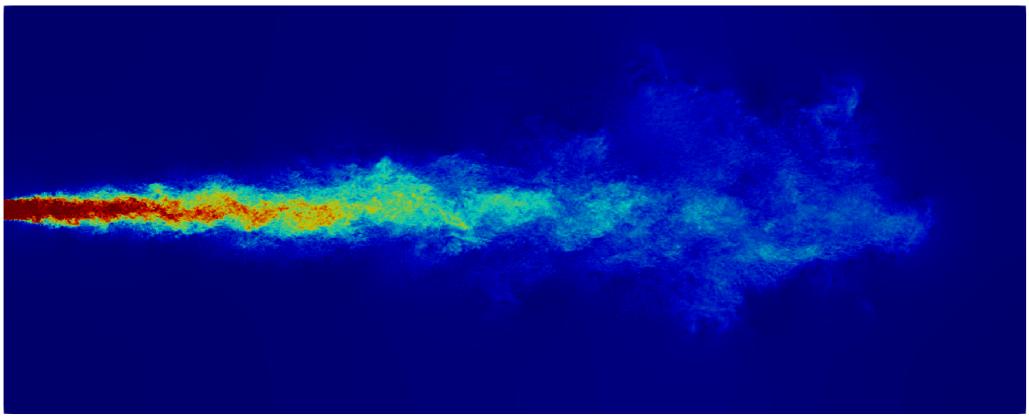

(t= 500.0 s)

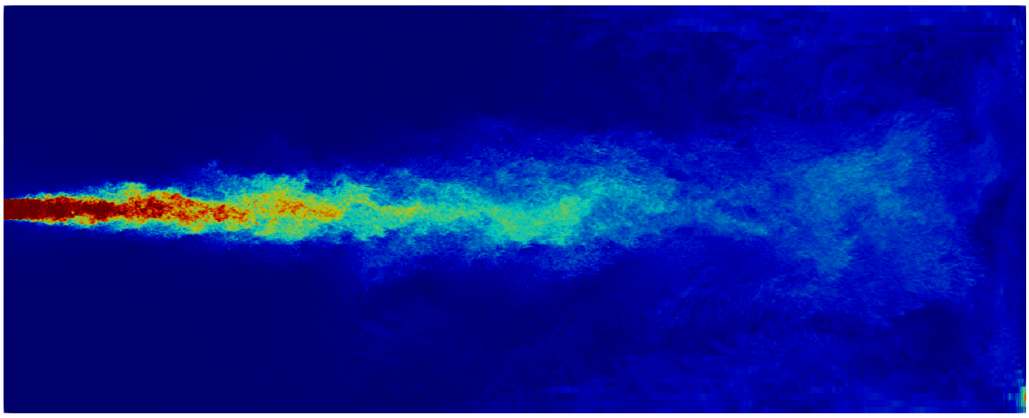

Figure 3.35: Velocity magnitude at different times for the most refined LES simulation.

3.8.8 Minibat: 3-D iso and anisothermal jets

Motivations 3.8.8. This is the last validation case related to the dry air scheme. Simulations are carried out on both isothermal and anisothermal ventilation jets in a studied room. We want to compare as well the accuracy of the different first and second order turbulent approaches.

This test case represents the most complex validation case for the dry air time scheme. The Minibat (Kuznik, 2005) experimental configuration represents something common in the real habitations, ventilation. The goal of this study is to compare dynamic and thermal numerical results to experimental data, presented by Gresse et al. (2020). Even if the system geometry (shown in Figure 3.37) appears simple, several studies have shown the difficulty in predicting the flow mean and instantaneous quantities (Kuznik et al., 2006, 2007). RANS simulations, using the $k-\varepsilon$ and $R_{ij}-\varepsilon$ approaches were compared to LES simulations; results showed an increasing difference between numerical and experimental results when studying more distant fields profiles to the jet inlet.
Our goal is to validate the CPC scheme related to three different jets. First, an isothermal (I) jet is studied, without the complexity related to the thermal buoyant effects. Then, a hot (H) and a cold (C) jets are studied.

Experimental setup

The following is based on Kuznik (2005).
The system is an enclosure of $[3.1 \times 3.1 \times 2.5]$ m, represented in the Figure 3.37. Five of its walls are thermally isolated. The south wall is in contact with a climatic chamber allowing its temperature to be set between 263 K and 313 K. The walls thermal isolation is made using an optimal air circulation. The ceiling is made of plaster and glass wool. The floor is made of aerated concrete and other walls are made of wood and plaster.
The inlet airflow is generated by a centrifugal ventilation fan. The inlet duct geometry (Figure 3.38, left) is chosen in order to generate an axisymmetrical jet, commonly found in ventilated rooms. The air extractor is located on the lower part of the east wall.
To do the boundary conditions measurements, nine thermocouples were placed on each wall (Figure 3.36). The inlet and outlet mass flow are measured with two flowmeters. The air thermal measures were made with three miniature Pt100 thermoprobes with a resolution of ± 0.2 K. A DANTEC 55R91 is used for the measurement of the three instantaneous velocity components. The uncertainty on the mean velocity measurements is of $0.5\,\mathrm{m\,s^{-1}}$.
Many mean quantity profiles were measured; the temperature ones were determined by averaging the measures over an acquisition time of 15 s and the mean velocity were calculated from a total of $1.5\ 10^5$ samples corresponding to an acquisition time of 30 s. Note that these acquisition times were in agreement with the physical characteristic times (Kuznik, 2005). Finally, the Reynolds stresses were calculated from the measured velocity variances, with a relative uncertainty of 6%.

Remark 3.8.3. The experimental uncertainties presented in the paragraph above are accounted in the comparison between the numerical and experimental data.

Further information on the configuration and the experiment conditions can be found in Gresse et al. (2020) and Kuznik (2005).

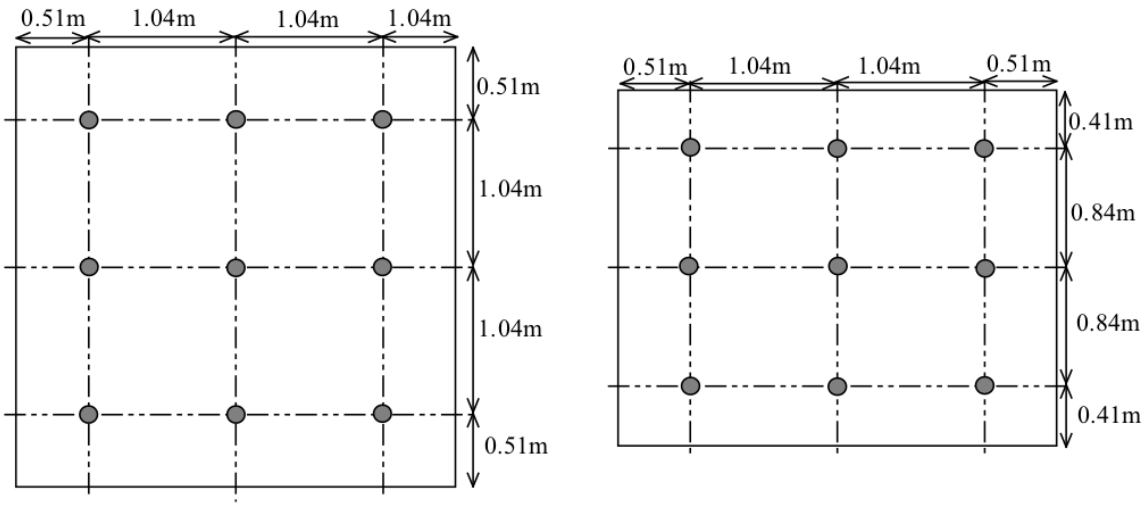

Figure 3.36: Wall thermocouples location for the temperature measurements (from Kuznik (2005)).

Simulations settings

In the experimental configuration and first simulations carried by Kuznik (2005), an inlet duct was considered, represented in Figure 3.38. A consequent work was made to reproduce correctly the inlet jet conditions according to the experimental setup and data. Two different systems were studied in the manuscript: the first takes into account the whole system geometry, including the inlet duct and the second one uses a radial interpolation on the inlet experimental measurements to define the room inlet conditions. Appendix 3.F presents the detailed content concerning the inlet interpolation. Appendix 3.G provides the main reasons concerning the choice on the system inlet treatment. Only the second system, which uses the experimental interpolation of the velocity, temperature and turbulent kinetic energy at the inlet faces is used in this section.

Remark 3.8.4. Only velocities, temperature and the components of the turbulent Reynolds stress tensor are available in the experimental database.

To illustrate this interpolation, the resulting 2-D inlet velocity field for the jet (I) is shown in Figure 3.39. One can see that as a direct consequence of the experimental inlet duct, the flow deviates along the x axis, making the jet non-symmetric.
The system walls are considered with no slip and with a Dirichlet condition on the temperature. Table 3.9 shows for each jet case these conditions. The outlet is set as a free inlet outlet.
A first hexahedral mesh (Figure 3.40) composed of around 10^6 cells was created based on the reference system using the Salome platform with a refinement in the inlet zone.

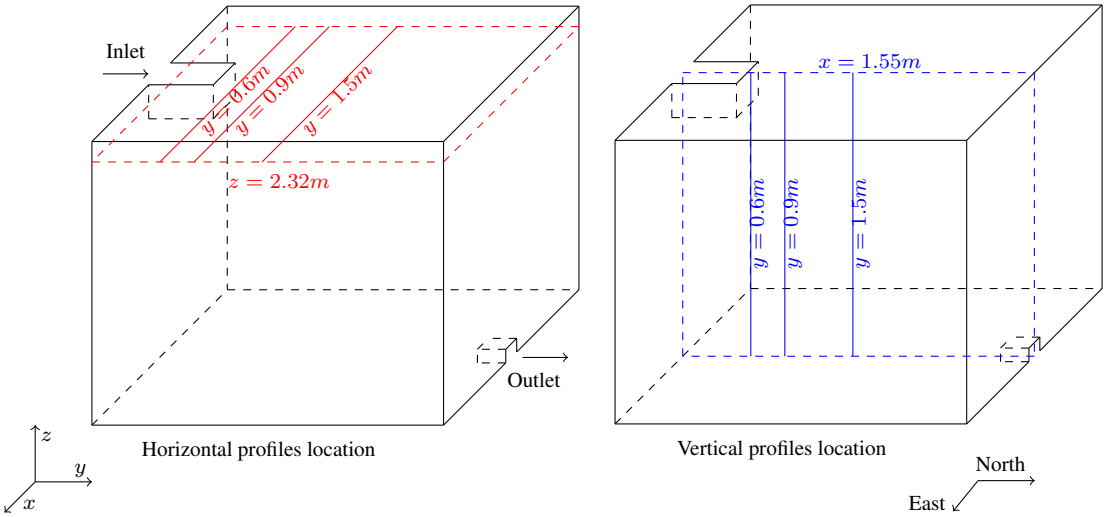

Figure 3.37: System geometry and location of the horizontal and vertical line segments where the numerical and experimental results are compared.

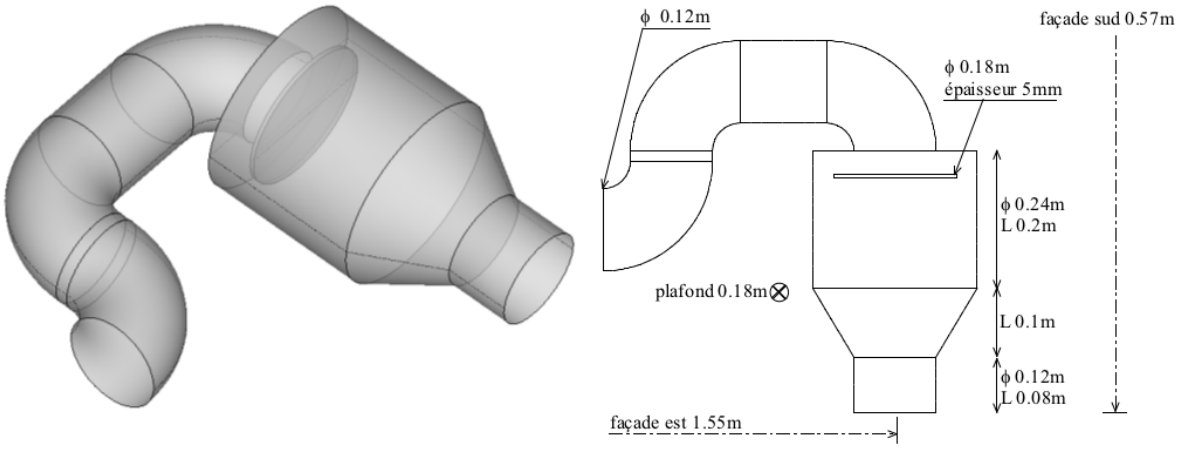

Figure 3.38: Inlet geometry used for the experimental measurements and simulations in the reference work (from Kuznik (2005)).

Jet	south	north	east	west	ceiling	floor	T_{in}	$\overline{U_{in}}[\mathrm{m\,s^{-1}}]$
Isothermal	295.6	295.6	295.5	295.5	295.6	295.7	294.98	2.96
Hot	295.2	296.3	296	296.1	297.3	296	304	1.3
Cold	295.1	294	294.2	294.2	294.1	294	285.6	1.7

Table 3.9: Boundaries conditions for three studied jets. All units are in K except the mean inlet velocity $\overline{U_{in}}$.

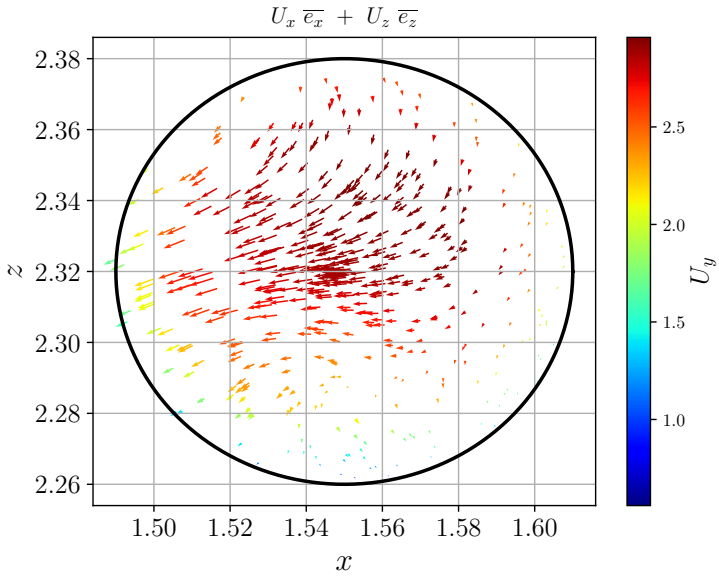

Figure 3.39: Quiver plot representing the velocity field interpolation over the inlet faces.

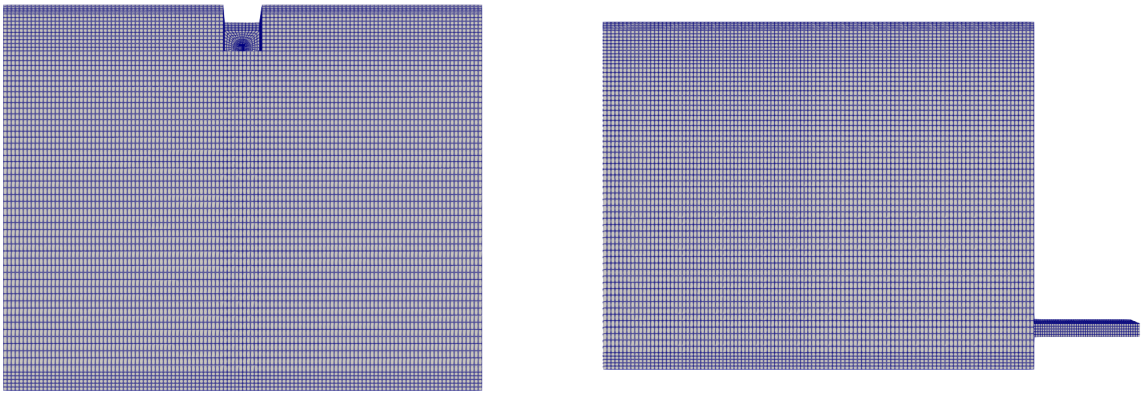

Figure 3.40: Example of hexahedral mesh used for the simulations.

The dynamic quantities such as the velocity magnitude, the Reynolds tensor components and the temperature are compared to their experimental values at the different vertical and horizontal profiles defined along the y axis, represented in Figure 3.37. However, before doing this comparison, some preliminary simulations on the jet (I) are performed to evaluate important elements related to a CFD study:

- The simulation convergence in time.
- The inlet condition on the turbulent kinetic energy dissipation rate.
- The numerical results' mesh sensitivity.
- Finally, three turbulent approaches are tested for the three different jets and the aforementioned dynamic and thermal numerical quantities are compared to the experimental data.

Preliminary simulations

For the isothermal jet (I), preliminary simulations are run using the $k-\varepsilon$ model. The inlet kinetic energy k is calculated through a polar interpolation of $\sum_{i=1}^{3} \frac{1}{2} R_{ii}$ from the experimental data.
Keeping the one million cells mesh, a first long simulation is run in order to study the steady state convergence for a RANS method.
The velocity magnitude is studied during 400 seconds of simulation. The time step is set as $\Delta t = 0.005\,\mathrm{s}$ and two inner iterations are performed ($\varepsilon_{piso_0} = 10^{-8}$). 6 different monitoring probes are defined at $x = 1.55\,\mathrm{m}$ following the jet diffusion at $y = 0.9, 1.5$ and $2.4\,\mathrm{m}$. For each y value, two probes are placed in two jet zones as represented in Figure 3.41, right. In the same figure on the left, one can see that a semi steady state is reached after approximately 300 seconds. Moreover, the more distanced probes present a larger velocity absolute variation.
It is fixed for the preliminary studies that the global variables will be analysed after an averaging time starting from $300\,\mathrm{s}$ until the end of the simulation for the jet (I) (taken at $330\,\mathrm{s}$).

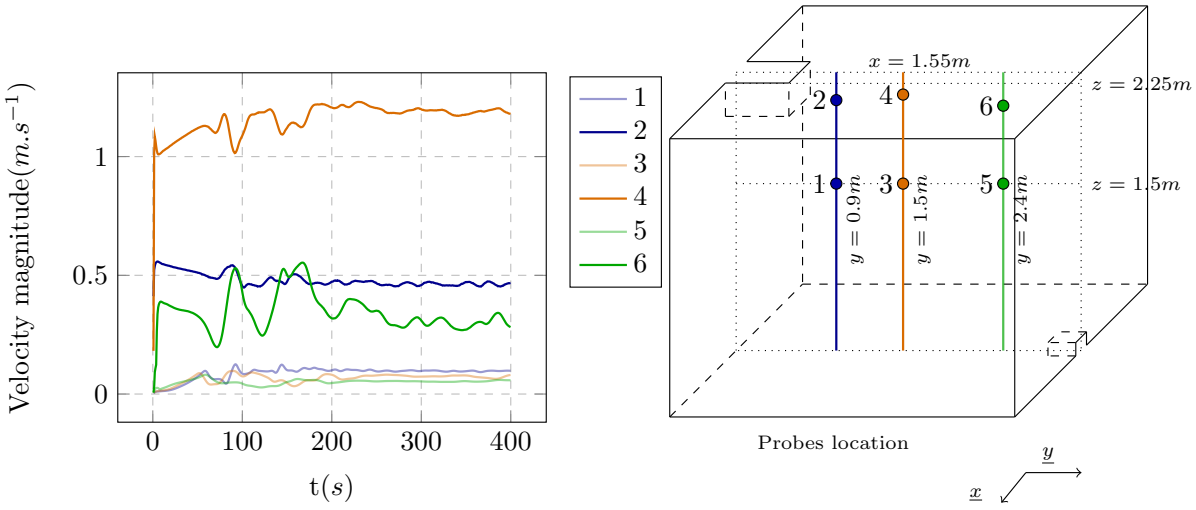

Figure 3.41: Isothermal jet. (Left) Velocity magnitude evolution over time at the six monitoring probes. (Right) Probes location.

From this first simulation, it was observed that the jet decay and diffusion were over estimated; one possible reason is that the inlet conditions were not properly reproduced.
The only field with no experimental data avalaible for a $k-\varepsilon$ simulation is the turbulent kinetic energy dissipation rate ε_{in}. The expression for this quantity, also used in the reference Kuznik (2005) is first set as:

$$\varepsilon_{in}(r) = \frac{1}{\kappa}\mu^{2/3}\frac{k^{3/2}}{R - r + 0.2R} = \varepsilon_0(r), \tag{3.57}$$

with $\kappa = 0.41$. Before doing any further study, it is decided to run a parametric study on the inlet ε_{in} value. Since it was observed that the jet dissipation was too important using Equation (3.57), an hypothesis is made that the jet is more turbulent than it should be. Thus, several $k-\varepsilon$ simulations are performed, where the inlet ε expression (3.57) is multiplied by 2, 5, 7.5 and 10.
Figure 3.42 shows the velocity magnitude for three vertical line segments for this study. It is clearly visible that the inlet epsilon boundary condition impacts the jet diffusion as presumed. While imposing $\varepsilon_{in} = 2\varepsilon_0$ as inlet condition led to an important jet diffusion (one can see that at $y = 1.5\,\mathrm{m}$, the numerical profile is less important than the experimental one), the simulations above $5\varepsilon_0$ underestimate the jet diffusion.

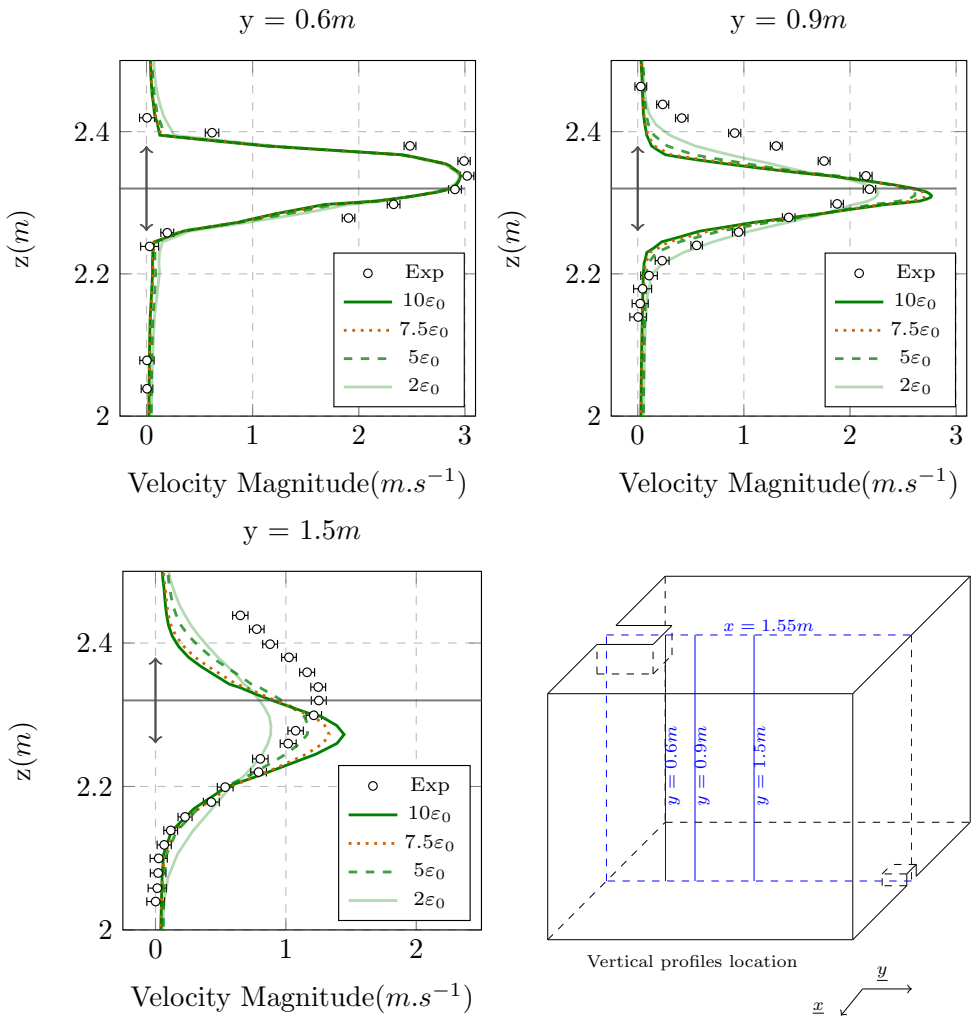

Figure 3.42: Isothermal jet. Profiles of the velocity magnitude at the vertical line segments for different inlet epsilon values.

Figure 3.43 presents the velocity magnitude horizontal profiles for the parametric study. Globally, the simulation with $5\varepsilon_0$ led to the closer results regarding the expected experimental ones. Nevertheless, all simulations above $2\varepsilon_0$ overestimated the velocity amplitude on $y = 0.9\,\mathrm{m}$. Moreover, in the horizontal profiles, the velocity for the simulation with $\varepsilon_{in} = 2\varepsilon_0$ presents smoother velocity profiles.
It is complicated to conclude on which value of ε_{in} to take. On the one hand, a higher dissipation led to overall better vertical profiles for high y values. On the other hand, it overestimated the velocity for small y values. The choice of keeping $\varepsilon_{in} = 2\varepsilon_0$ for the next simulations is made; maybe the jet diffusion comes rather from the $k - \varepsilon$ model (which is known to be more diffusive than other turbulence approaches) than the inlet kinetic energy dissipation itself.

Remark 3.8.5. Since the experimental data provides values for the R_{ij} components, no model for the inlet ε is needed for the RSM and LES simulations.

Now that the simulation convergence and inlet ε profile are studied, a sensitivity mesh analysis can be realised.
The initial 10^6 cells mesh is refined to respectively a 8.10^6 and 60.10^6 cell meshes. The main objective is to find a correct mesh refinement, coherent with the previous validation case and computationally affordable. Only the velocity magnitude profiles are studied for the moment.

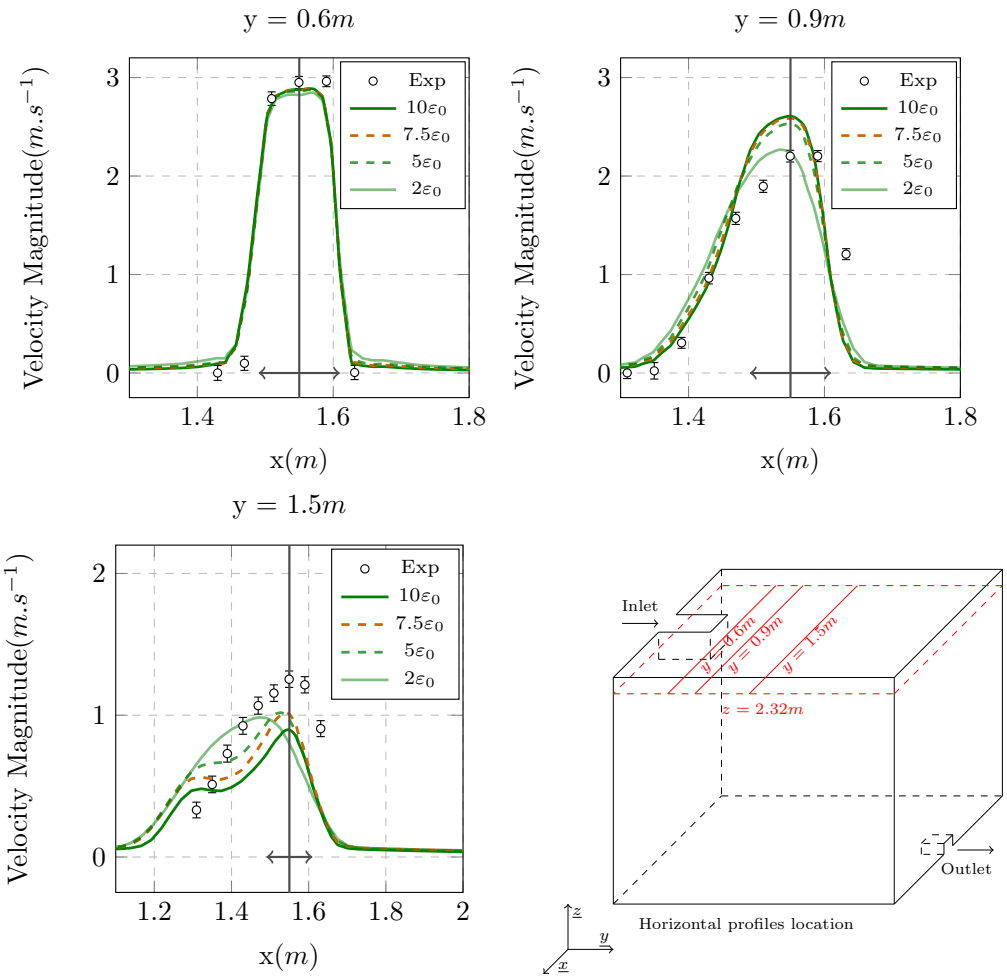

Figure 3.43: Isothermal jet. Profiles of the velocity magnitude at the horizontal line segments for different inlet epsilon values.

Figure 3.44 shows the velocity magnitude on the horizontal and vertical profiles for the isothermal jet as the distance to the inlet increases.
Globally, the numerical results are close to the experimental ones and very little difference exist between the different mesh refinements. Moreover, simulations did not catch correctly the light jet deviation, noticeable on the horizontal velocity profiles.
The more refined mesh simulation is also used to compute the turbulent length scales related to the Minibat configuration. The integral and Taylor scales are represented respectively in Figures 3.45 and 3.46. The purpose is to set a minimal mesh refinement for the LES simulation. Indeed, in order to have consistent results, the mesh should be able to solve at least the half of the Taylor scale, as shown in the last validation case.
In both figures, isolines of the integral and Taylor scales are presented as well. If one wants to solve half of the Taylor scale, then the axial spatial step in the jet axis direction y should be around $2\,\mathrm{cm}$. The first mesh composed of 10^6 cells has a spatial step of $0.027\,\mathrm{m}$ in the y axis, which is not enough refined to perform LES simulations. The second mesh has a spatial step of $0.0135\,\mathrm{m}$, which should be able to solve this length scale.
Moreover, given the little variation of the numerical results and the rise of computational time between the second and third mesh simulations, the choice of keeping the second mesh, composed of $8\ 10^6$ cells, is made for the next simulations.

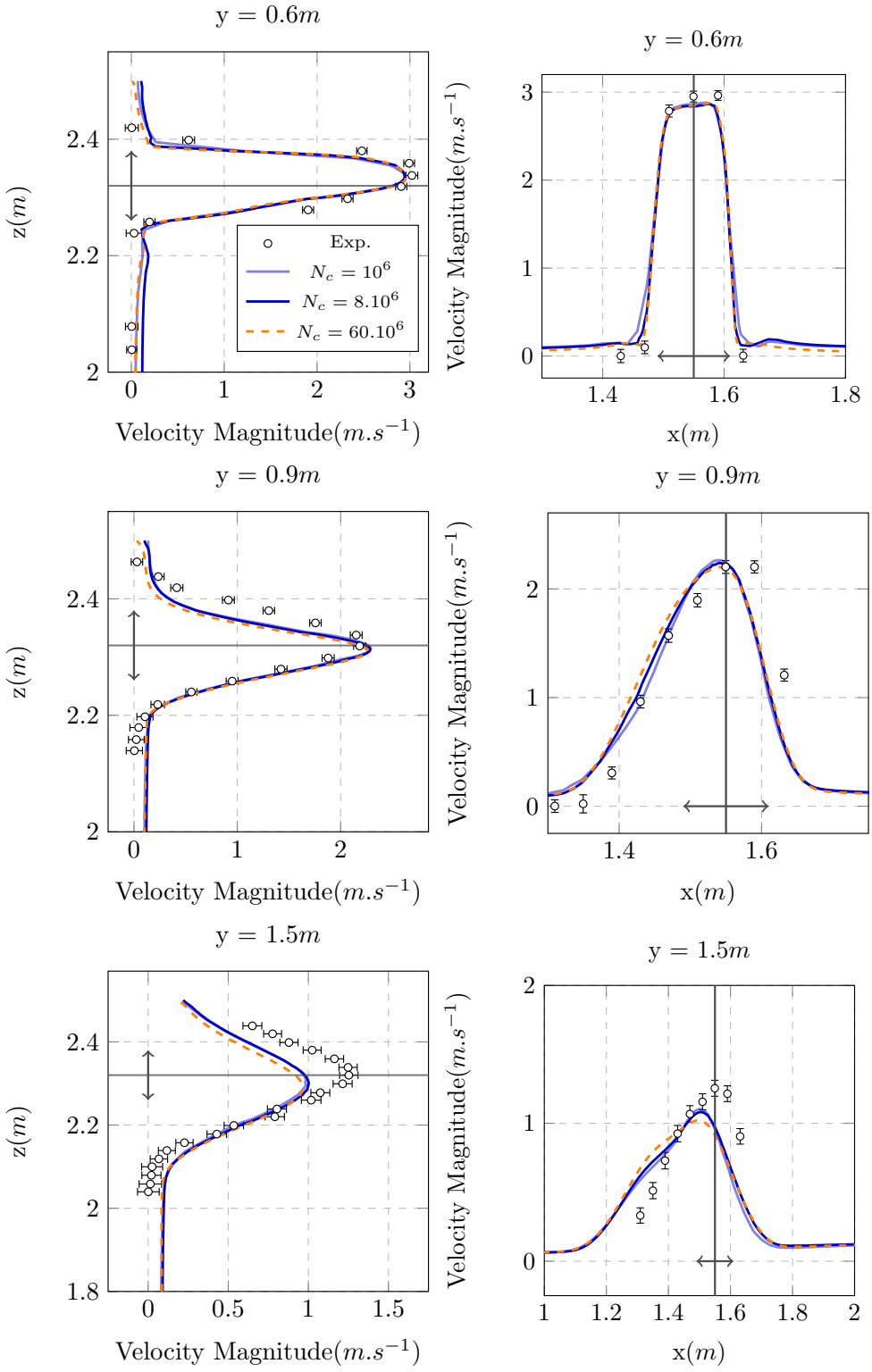

Figure 3.44: Profiles of the velocity magnitude at the vertical and horizontal line segments for different mesh refinements.

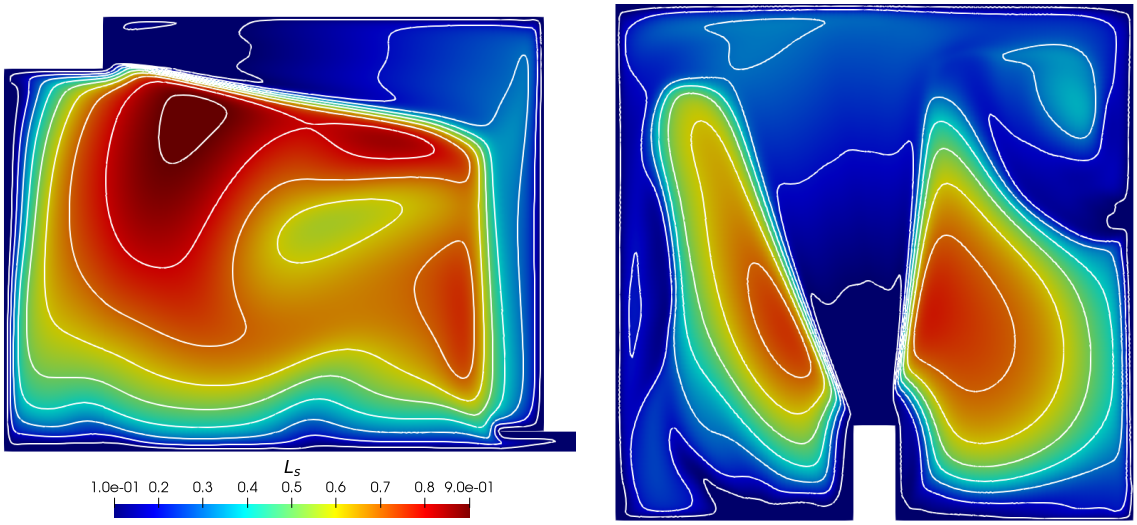

Figure 3.45: Isothermal jet. Turbulent integral length scale represented at 330 s of the $k-\varepsilon$ simulation using the 60.10^6 cells mesh. Isolines are spaced by 0.1 m.

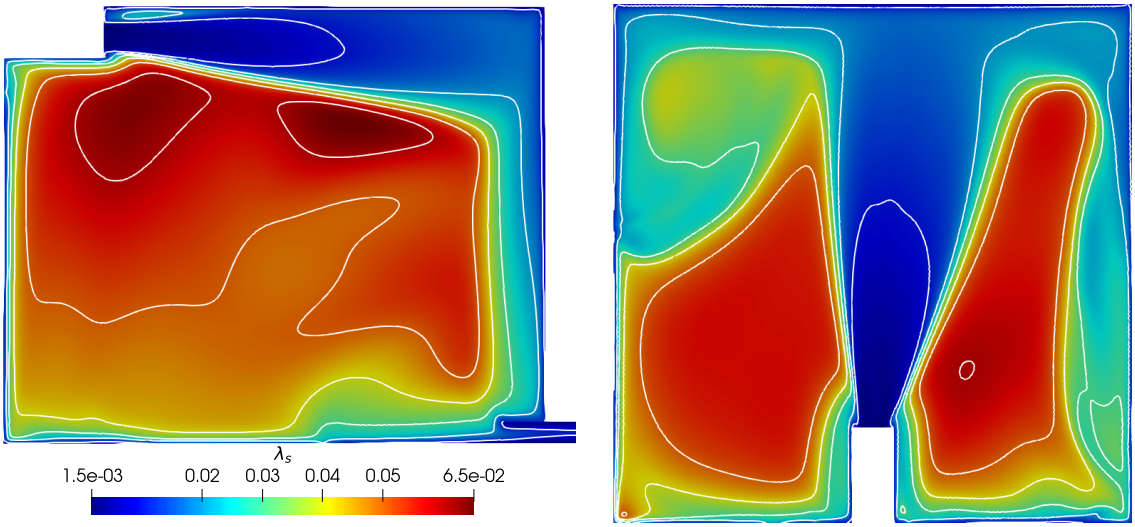

Figure 3.46: Isothermal jet. Turbulent Taylor length scale represented after at 330 s of the $k-\varepsilon$ simulation using the 60.10^6 cells mesh. Isolines are spaced by 0.01 m.

Turbulent approaches comparison

The preliminary simulations provided us essential information concerning the problem steady state, inlet boundary condition and mesh refinement regarding the isothermal jet Minibat configuration. Now, different turbulent approaches comparison is made. Keeping the same profiles over both x and z axis, a $k-\varepsilon$, $R_{ij}-\varepsilon$ and LES simulations are performed for the three different jets.
The R_{ij} simulation uses the SSG and Shir model and the LES the dynamic Smagorinsky model. Simulations of a constant CFL $= 0.8$ are performed during $330\,\mathrm{s}$. Two inner iterations ($\varepsilon_{piso_0} = 10^{-8}$) are ran. The quantities of interest (velocity magnitude, Reynolds stress tensor components and temperature) are averaged during the 30 last seconds of simulation to be consistent with the experimental data sampling.
For the LES simulation, $\theta = 1/2$ and for the RANS simulations, $\theta = 1$. A system initial velocity equal to zero is considered.
Lastly, the Lumley triangle is plotted for each simulation (see Appendix 3.H for further details on the invariants calculation) and compared to the experimental ones from Kuznik (2005) [↗]. To do so, the invariants are calculated using 1000 samples from the vertical profiles at $y = 0.6, 0.9, 1.2$ and $1.5\,\mathrm{m}$, from $z = 2$ to $2.5\,\mathrm{m}$.

Jet (I)

For a qualitative comparison, the averaged velocity profile is compared for all simulations at their final time step. Figure 3.47 shows that there is no important differences in the average velocity field between all simulations for the represented view. However, small differences can be observed quantitatively. Figure 3.48 shows the different velocity magnitude profiles over the presented vertical and horizontal segment lines for the three simulations. The $k-\varepsilon$ and R_{ij} simulations underestimate the velocity magnitude as the distance to the jet inlet increases. The LES simulation leads to a less important jet diffusion, resulting on larger profiles in both directions, notably by overestimating the velocity magnitude at $y = 0.9\,\mathrm{m}$. However, the vertical and horizontal profiles at $y = 1.5\,\mathrm{m}$ are better reproduced. Globally, any simulation was able to reproduce the jet shift correctly.
Figures 3.49, 3.50 and 3.51 present the horizontal and vertical R_{ii} profiles for respectively $y = 0.6\,\mathrm{m}$, $y = 0.9\,\mathrm{m}$ and $y = 1.5\,\mathrm{m}$.
At $y = 0.6\,\mathrm{m}$, while the R_{ij} and $k-\varepsilon$ simulations correctly reproduce the experimental data (which is expected, since their values are set in the inlet condition), the LES simulation does not. This can be explained by the non-use of any turbulence generation technique, such as the synthetic eddy method (SEM, Jarrin et al. (2006) [↗]). As shown in Appendix 3.I, the use of the SEM led to R_{ii} profiles in agreement with the expected data for small y values, but also to an important diffusion of the jet. Note that globally the R_{ij} simulation is slightly more precise than the $k-\varepsilon$.
As the distance to the jet inlet increases, at $y = 0.9\,\mathrm{m}$, turbulence is created in the LES simulation, but the R_{ii} profiles still underestimate the experimental ones. In the other hand, the $k-\varepsilon$ simulation reproduces well the R_{11} and R_{33} profiles, but underestimates the R_{22} ones.
Finally, for the last figure, the $k-\varepsilon$ simulation led to an overestimation of the R_{11} and R_{33} values and an underestimation of the axial component. The LES profiles are no longer below the experimental data, slightly overestimating it for all three components. Lastly, the R_{ij} simulation provided the most accurate profiles. Indeed, the global shape and profiles amplitude are close to the measurements. Transporting the Reynolds stress tensor components led thus to the better reproduction of the R_{ii} profiles, with a good accuracy from small to high y values.

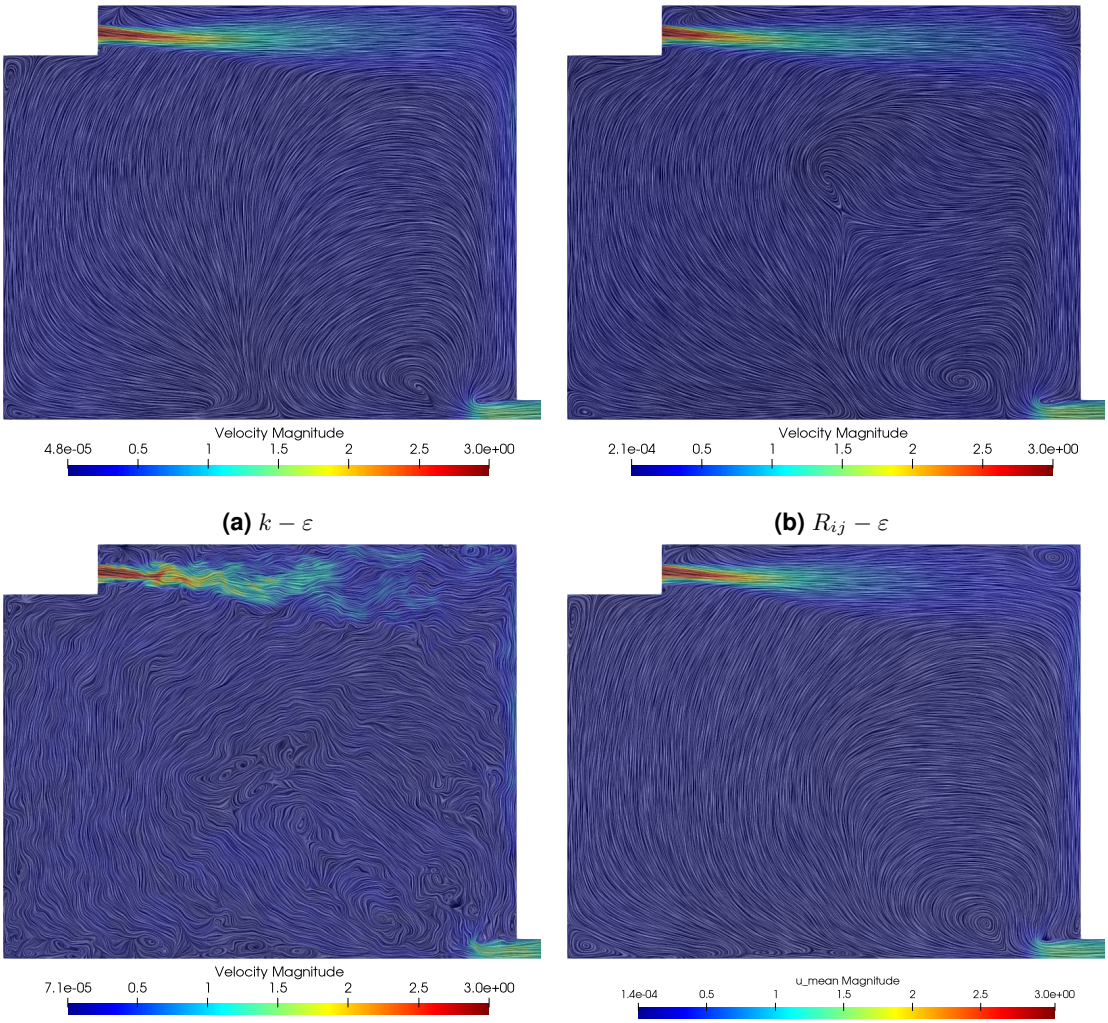

(a) $k - \varepsilon$

(b) $R_{ij} - \varepsilon$

(c) LES instantaneous ($t = t_{max}$)

(d) LES averaged

Figure 3.47: Isothermal jet. Velocity magnitude field over the axis $x = 1.55\,\mathrm{m}$ for the three simulations.

Figure 3.52 shows the Lumley triangles for the jet (I) for each simulation. The experimental triangle provides some information concerning the jet turbulent structure; an axysimmetrical expansion in the cigar form tending to an one dimensional turbulence. The Lumley triangles from the three simulation are very distinct. The $k-\varepsilon$ and R_{ij} simulations show two categories of turbulence (axysimmetrical expansion and contraction), the LES one tend to a more one dimensional turbulence, closer to the experimental triangle.

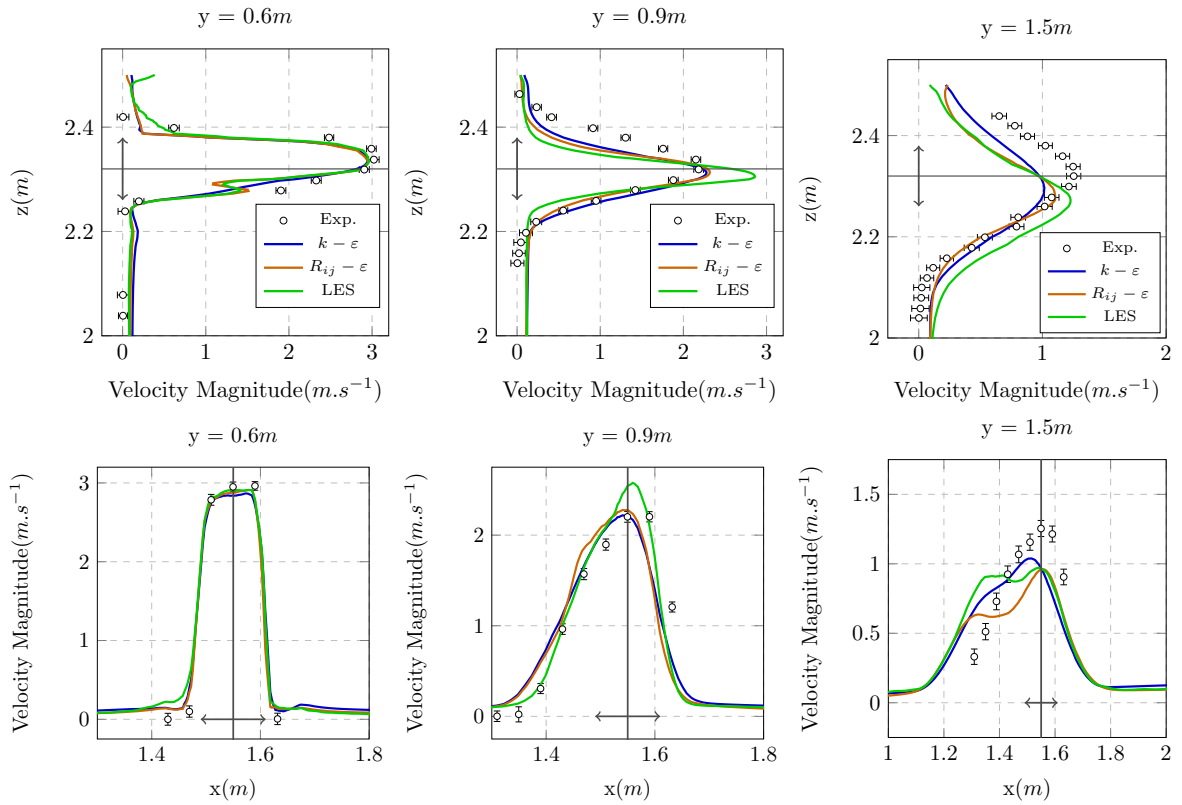

Figure 3.48: Isothermal jet. Velocity magnitude profiles over the vertical and horizontal segments lines.

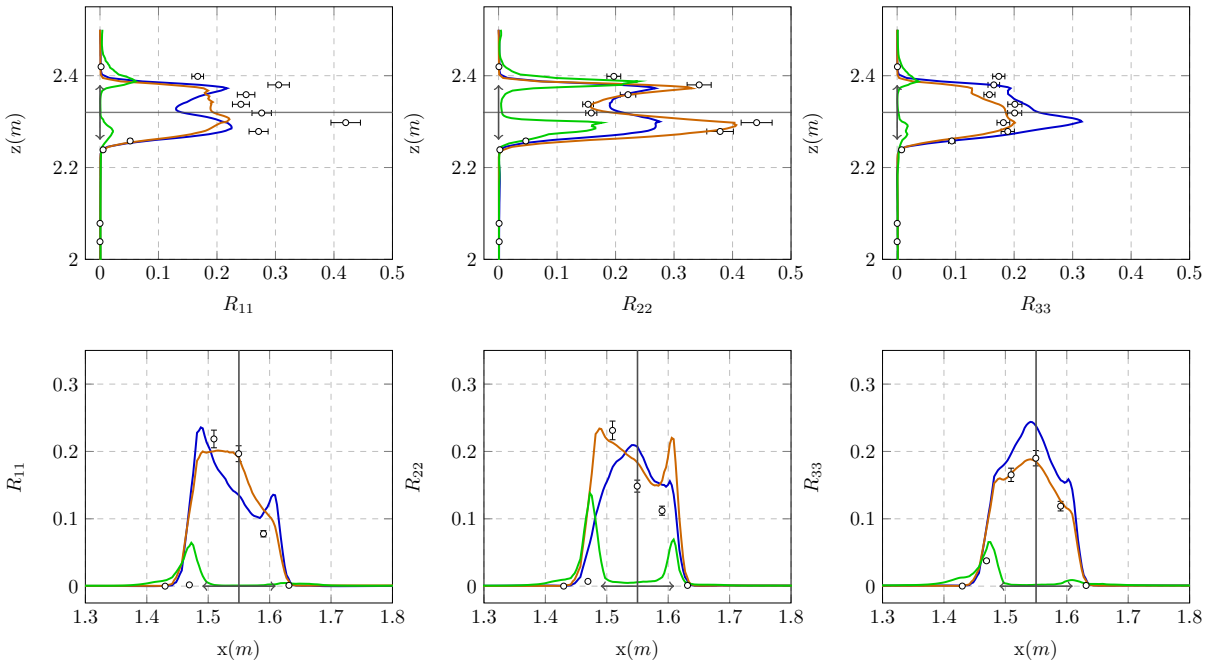

Figure 3.49: Isothermal jet. R_{ii} value at $y = 0.6\,\mathrm{m}$ at the vertical and horizontal Minibat profiles.

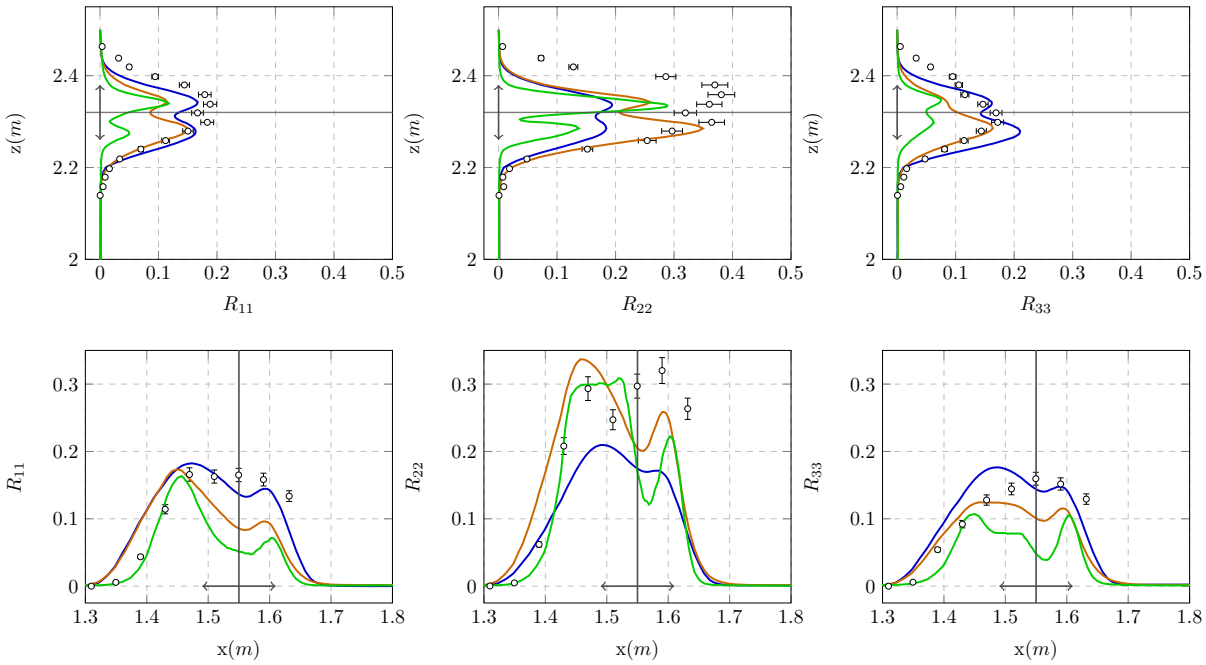

Figure 3.50: Isothermal jet. R_{ii} value at $y = 0.9\,\mathrm{m}$ at the vertical and horizontal Minibat profiles.

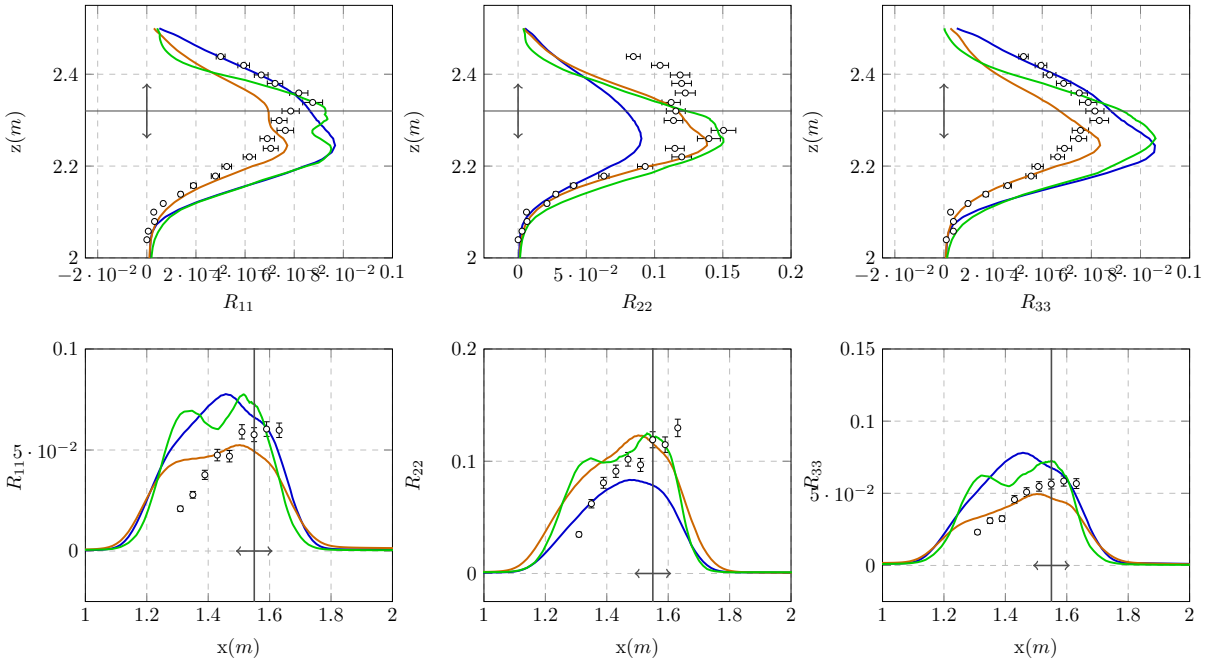

Figure 3.51: Isothermal jet. R_{ii} value at $y = 1.5m$ at the vertical and horizontal Minibat profiles.

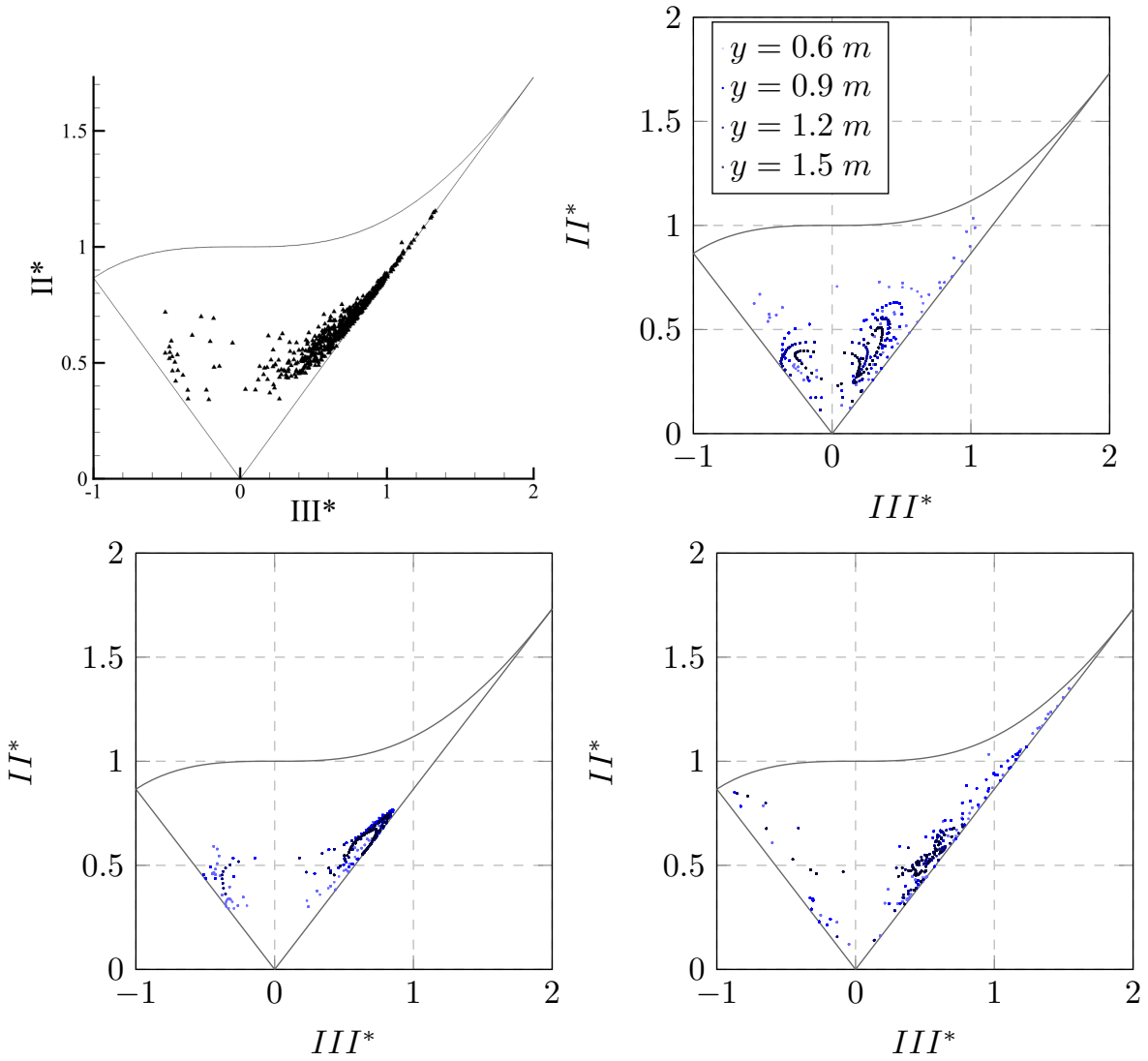

Figure 3.52: Lumley triangles for the isothermal jet case. Top left: experimental. Top right: $k - \varepsilon$. Bottom left: $R_{ij} - \varepsilon$. Bottom right: LES simulation.

Hot jet (H)

The same type of study is performed with the hot jet. Simulations are carried out with the $8\ 10^6$ cells mesh. However, this time the quasi-steady state is reached after about $600\,\mathrm{s}$ for the velocity and after $900\,\mathrm{s}$ for the temperature (see Figure 3.53 for the monitoring probes fields evolution). Thus, simulations are performed until $930\,\mathrm{s}$, with an averaging process between 900 and $930\,\mathrm{s}$. The average velocity

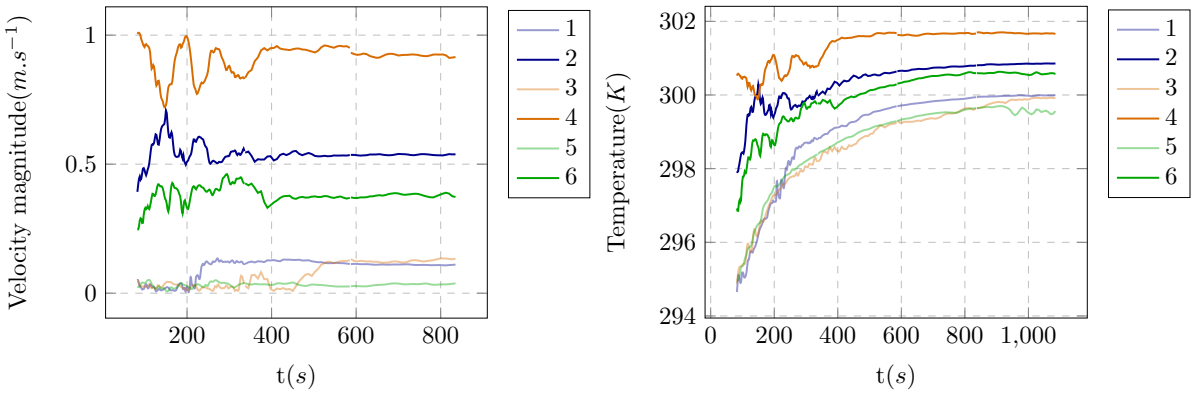

Figure 3.53: Velocity and temperature over time on the different monitoring probes for the hot jet case.

magnitude (Figure 3.54) and temperature (Figure 3.55) are studied over the vertical and horizontal profiles.

Globally, concerning the velocity magnitude profiles, the numerical results are in agreement with the expected ones. Yet, at $y = 0.9\,\mathrm{s}$, the $k-\varepsilon$ and LES simulation underestimates the jet diffusion. At $y = 1.5\,\mathrm{m}$, both perform better; the LES simulation profiles are the closest to the experimental data. The R_{ij} simulation seems to underestimate the jet velocity.

Concerning the temperature profiles, some similarities are observed related to the dynamic profiles. While all simulations overestimate the temperature at $y = 0.9\,\mathrm{m}$, the LES simulation performed better at $y = 1.5\,\mathrm{m}$.

Figures 3.58, 3.59 and 3.60 present the numerical R_{ii} profiles as the distance to the jet inlet increases for the three simulations. At $y = 0.6\,\mathrm{m}$, only the R_{ij} simulation provided results close to the experimental one. For the LES, this is understandable given the inlet turbulent conditions. For the $k-\varepsilon$ simulation, this means that the model has decreased the jet turbulence imposed at the inlet faces.

At $y = 0.9\,\mathrm{m}$ the turbulence starts to be developed for the LES, but the profiles still underestimates the R_{ii} components. The R_{ij} profiles are globally better than the $k-\varepsilon$ ones, except for the axial component R_{22} which is importantly overestimated. This may be the numerical reason of the R_{ij} simulation overestimation of the jet diffusion at $y = 1.5\,\mathrm{m}$. At this distance, the numerical simulations can hardly reproduce the experimental profiles. For the R_{11} component, the vertical profile is underestimated and the horizontal one slightly overestimated. The R_{ij} simulation led to an underestimation of all quantities.

The Lumley triangles are represented in Figure 3.61. The expected triangle presents a turbulent axysimmetrical expansion (cigar shape) and contraction (pancake shape), with a clear separation between the two types of turbulent structures. This is correctly reproduced by the $k-\varepsilon$ and the R_{ij} simulations.

In this test case, even if the LES simulation led to a bad reproduction of the R_{ii} components and Lumley triangle, the global averaged dynamic and thermal profiles were better reproduced, compared to the two other turbulence approaches. Quantifying the impact of the instantaneous velocities on the averaged quantities may be an interesting subject for further investigations.

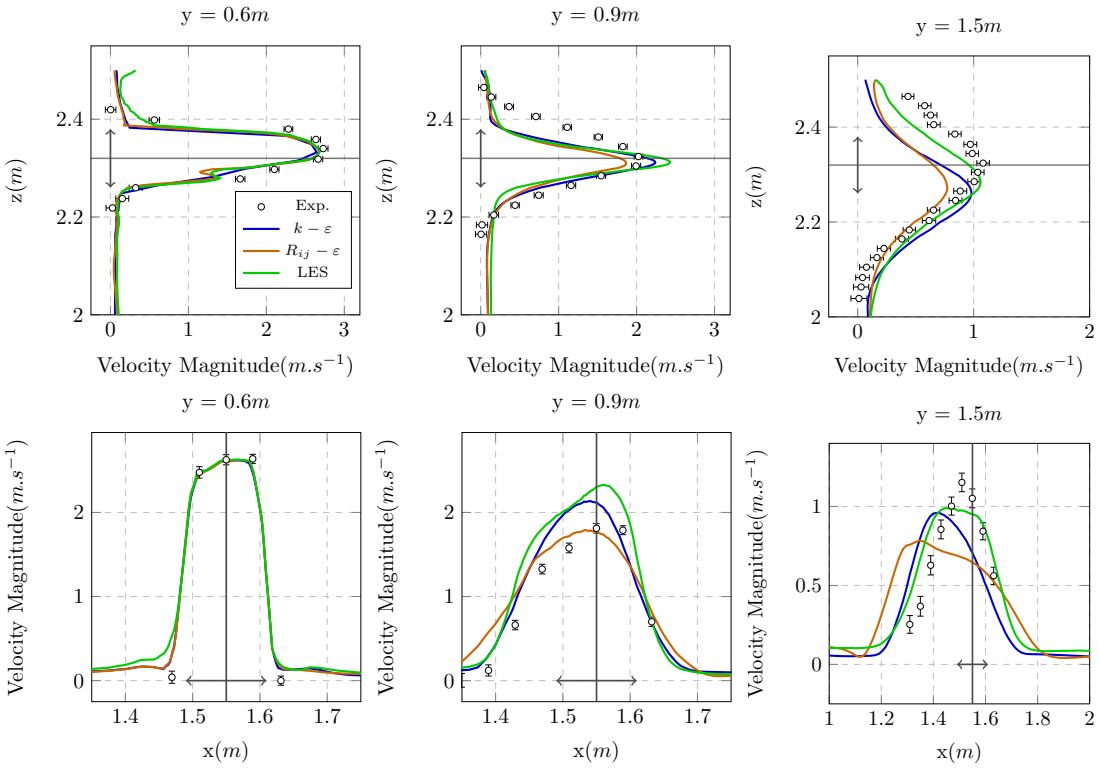

Figure 3.54: Hot jet. Velocity magnitude profiles over the vertical and horizontal segments lines.

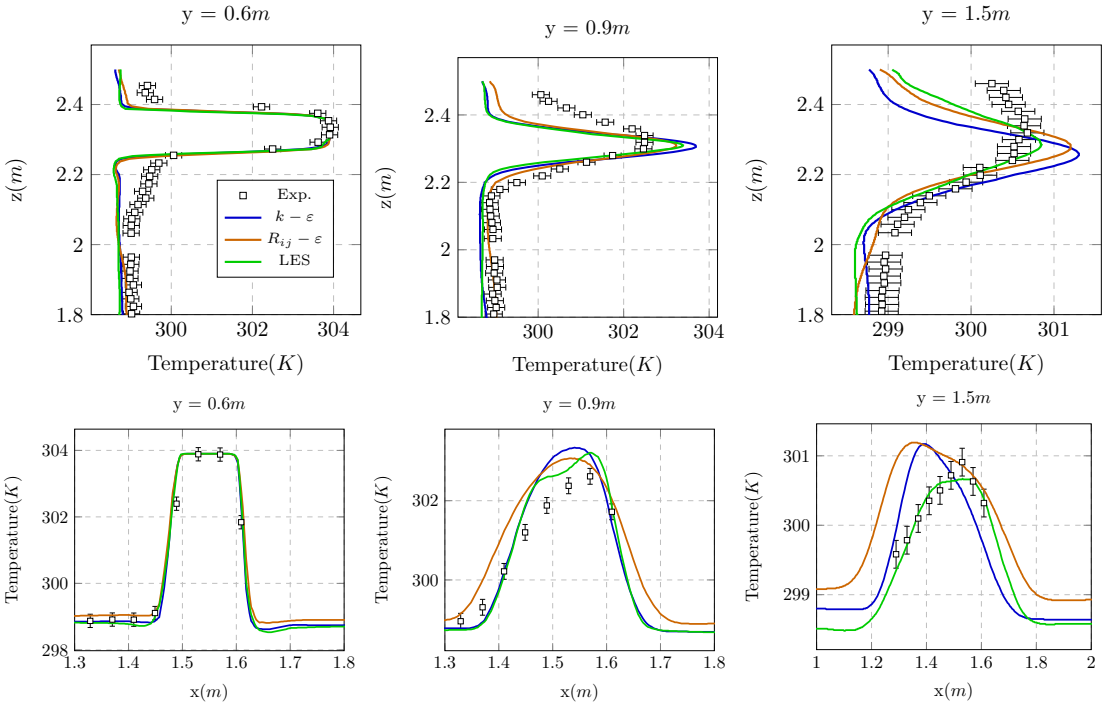

Figure 3.55: Hot jet. Temperature magnitude profiles over the vertical and horizontal segments lines.

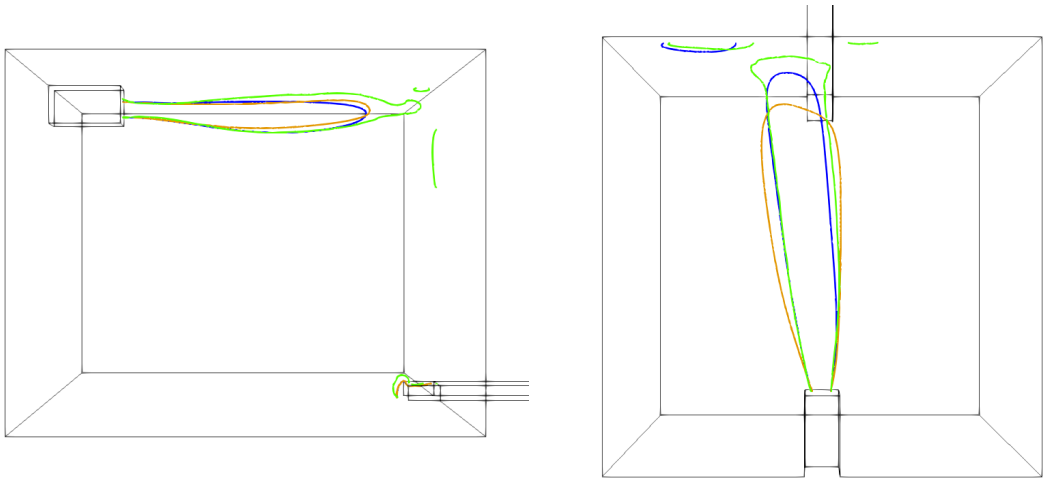

Figure 3.56: Hot jet. Velocity magnitude $u_{mag} = 0.4\,\mathrm{m\,s^{-1}}$ isoline for all three hot jet simulations. In blue, the $k-\varepsilon$ simulation, in orange, the R_{ij} and in green the LES.

Figure 3.56 presents the velocity magnitude $u_{mag} = 0.4\,\mathrm{m}$ isoline for the three hot jet simulations. While the LES simulation presents the less important jet diffusion, the R_{ij} is the turbulent approach that diffused it the most. All simulations seem to reproduce the buoyant effects on the flow. Lastly, these results are in agreement with the presented velocity profiles.
Finally, a comparison is made on the simulation computational time between the IPC and CPC schemes. Figure 3.57, left, shows that the CPC scheme leads to a total time per iteration smaller than the IPC (an average of 75% of the IPC time for each iteration). Figure 3.57, right, shows the absolute time per iteration for the CPC simulation. This difference of simulation time can be explained by a faster solving of the numerical system, notably with the solve of the Helmholtz equation for the pressure, where the diagonal terms were reinforced.

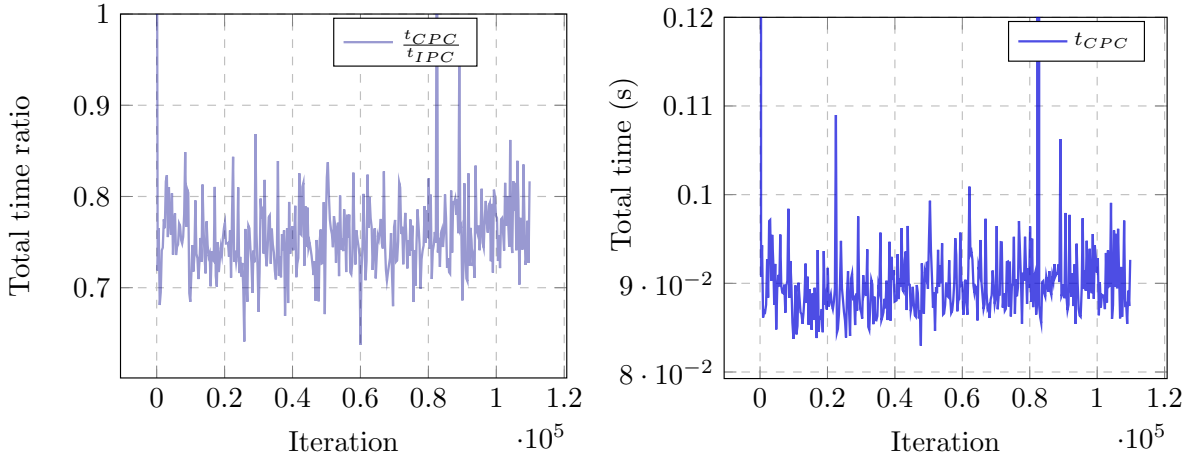

Figure 3.57: (Left) Ratio (CPC/IPC schemes) of the total time per iteration for the hot jet $k-\varepsilon$ simulation. (Right) Absolute total time per iteration for the CPC scheme.

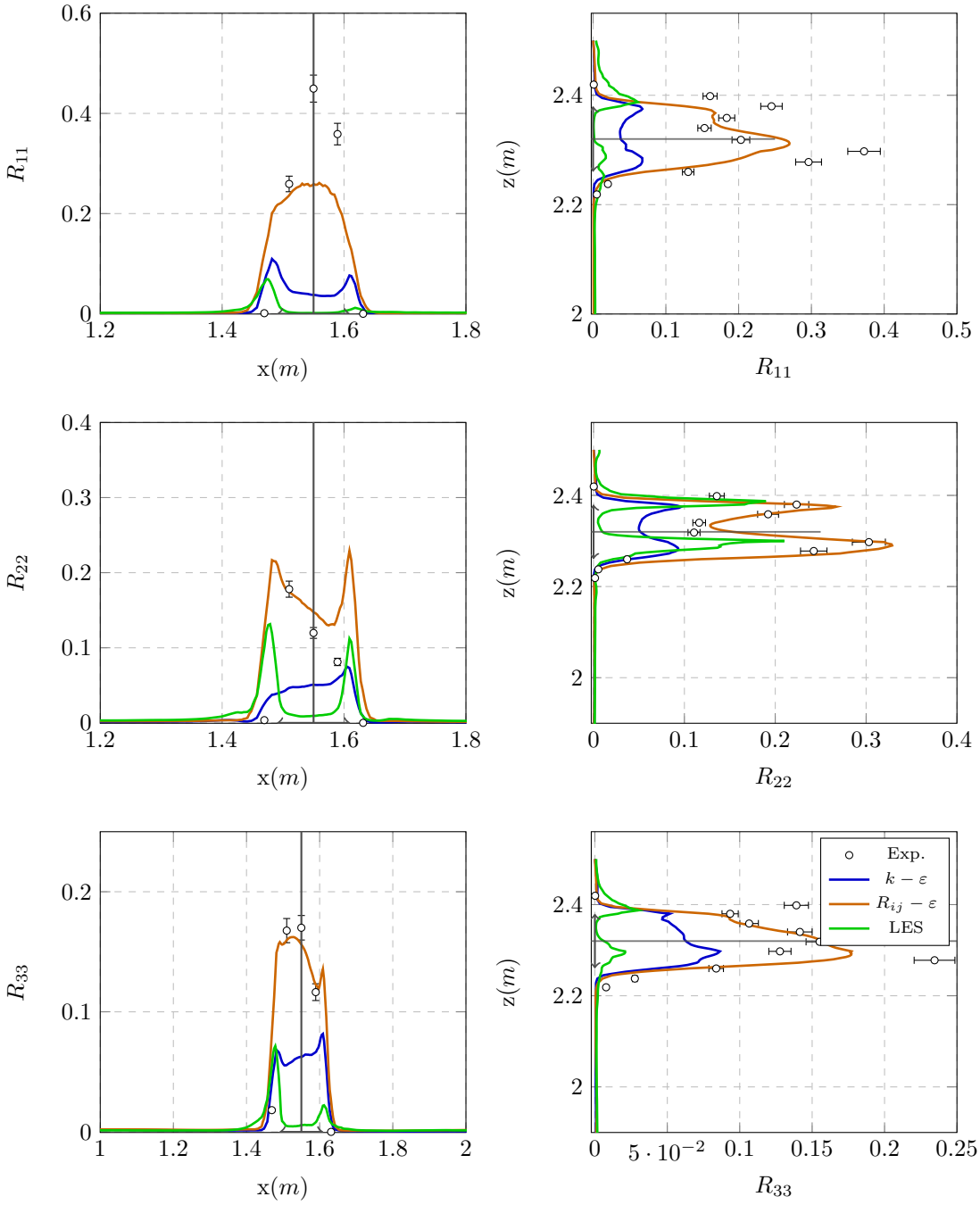

Figure 3.58: Hot jet. R_{ii} components at $y = 0.6\,\mathrm{m}$ for the vertical and horizontal profiles.

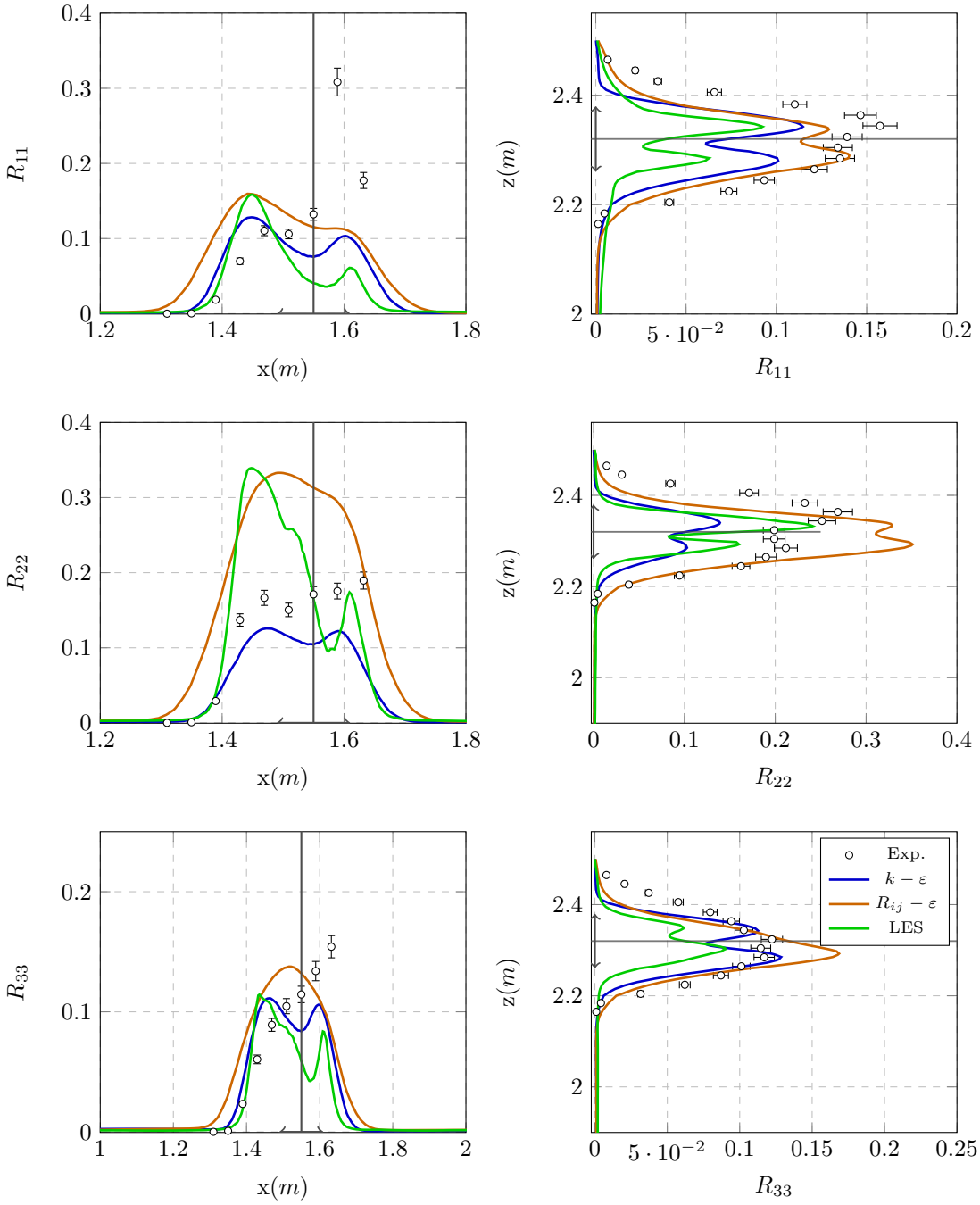

Figure 3.59: Hot jet. R_{ii} components at $y = 0.9\,\mathrm{m}$ for the vertical and horizontal profiles.

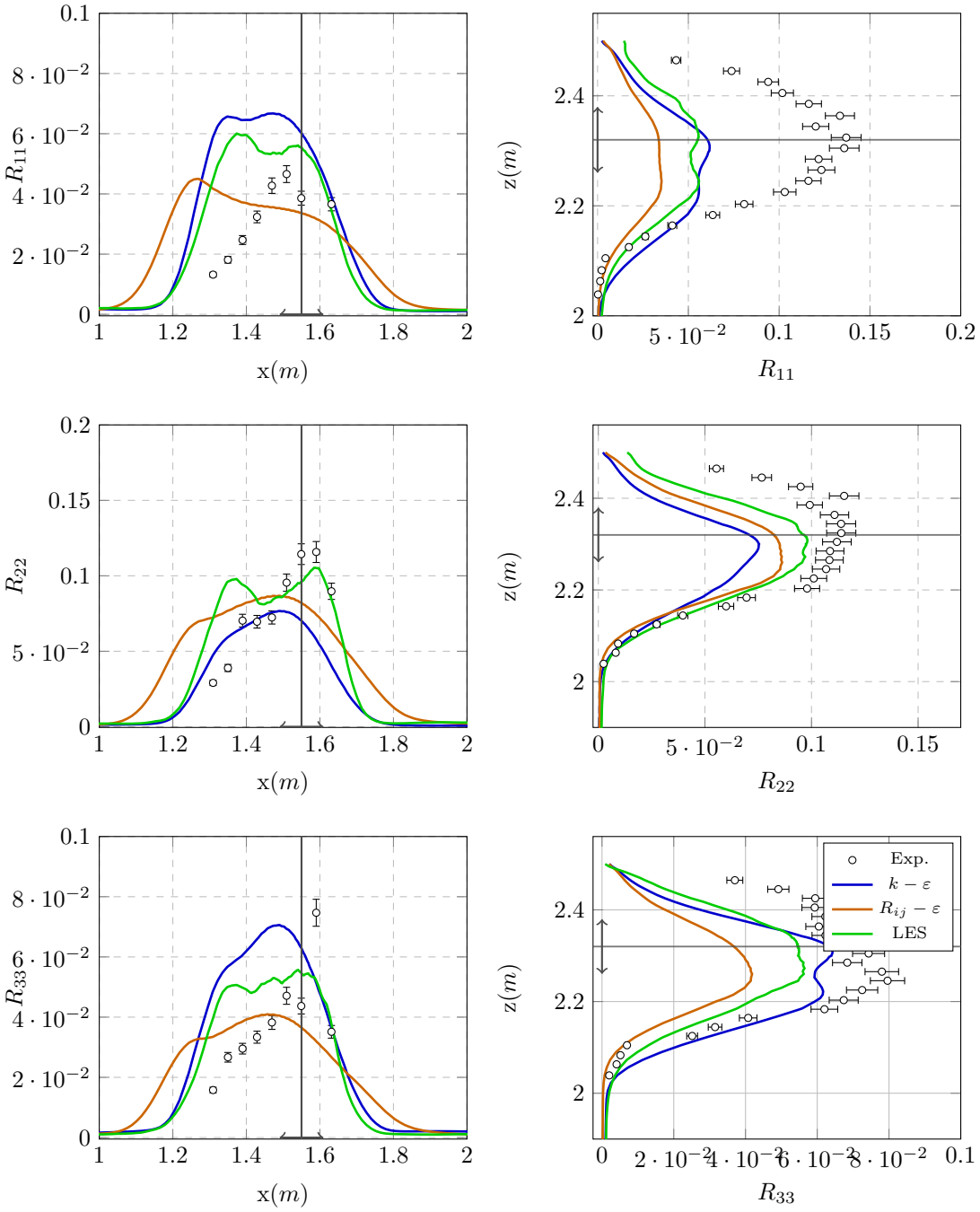

Figure 3.60: Hot jet. R_{ii} components at $y = 1.5\,\mathrm{m}$ for the vertical and horizontal profiles.

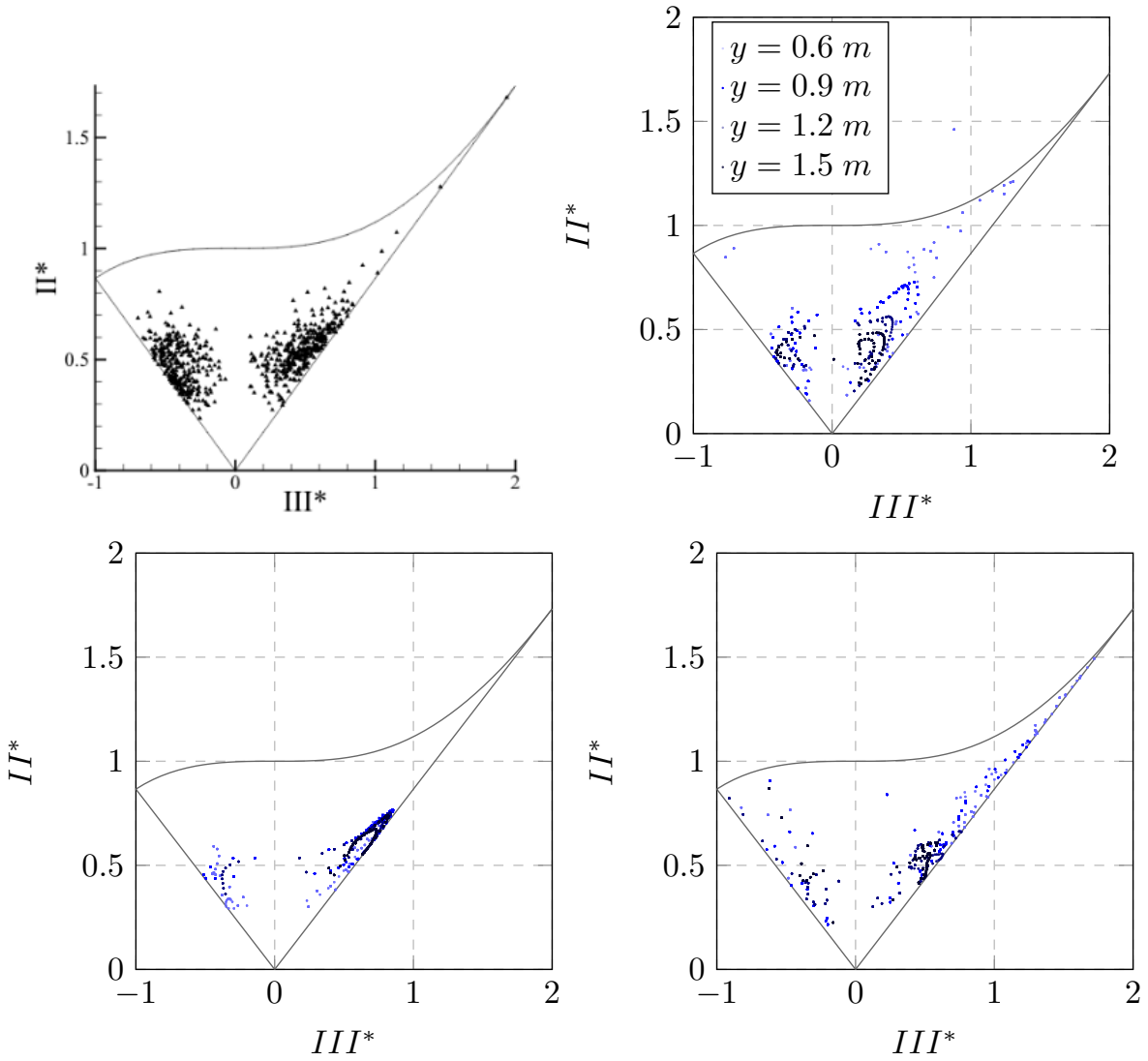

Figure 3.61: Lumley triangles for the hot jet case. Top left: experimental. Top right: $k - \varepsilon$. Bottom left: $R_{ij} - \varepsilon$. Bottom right: LES simulation.

Cold jet (C)

Finally, a cold jet is studied to conclude the turbulent approaches comparison. The CPC scheme numerical results are compared to the experimental data and to the $k - \varepsilon$ and $R_{ij} - \varepsilon$ simulations performed in Kuznik (2005). In Figure 3.62 are represented the evolution of the velocity magnitude and temperature among time for the 6 probes previously defined. The amplitude of variation of both quantities are more important than for the jets studied before. However, after $400\,\mathrm{s}$ of simulation a pseudo-steady state seems to be reached, which is set for this jet study as the starting averaging time, which lasts $30\,\mathrm{s}$.

A qualitative representation of the velocity magnitude isoline $u_{mag} = 0.15\,\mathrm{m\,s^{-1}}$ is represented in Figure 3.63. One can see that the jet cold temperature impacts importantly its diffusion. Simarly to the hot jet, the LES simulation led to the less diffused jet while the $k - \varepsilon$ diffused it the most. Moreover, Figure 3.63, right, shows that the $k - \varepsilon$ approach was not able to reproduce correctly the jet shift, which should be confirmed in the quantitative comparisons presented hereafter.

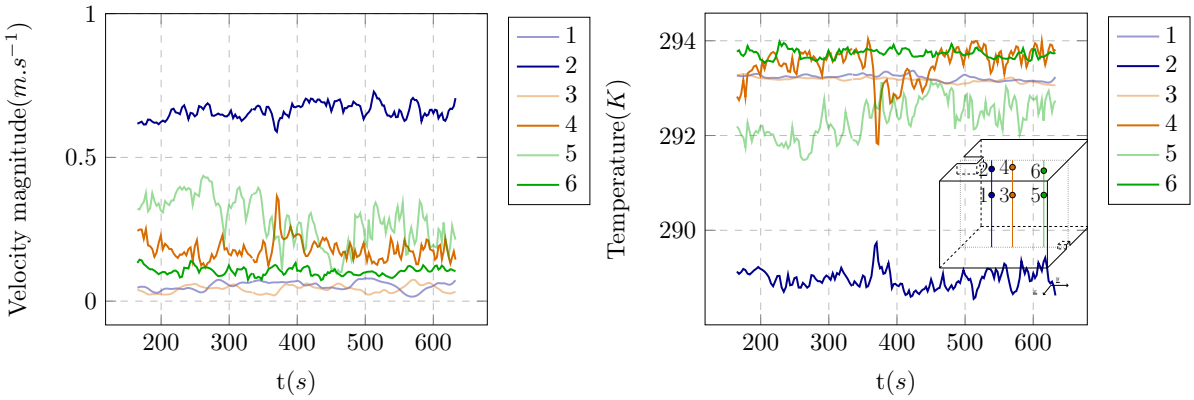

Figure 3.62: Velocity and temperature at the monitoring probes for the cold jet. The $k-\varepsilon$ model was used.

The velocity magnitude profiles are represented in Figure 3.64. Compared to the other jets, all vertical and horizontal CPC numerical profiles are close to the experimental ones, except for the horizontal profile at $y = 1.5\,\mathrm{m}$. One can highlight that the LES simulation even reproduced the jet shift at $y = 0.9\,\mathrm{m}$.
However, the vertical thermal profiles (Figure 3.65) underestimate the minimum temperature, which is also the case of the two reference simulations. Globally both references and CPC simulations led to similar temperature profiles, except for the horizontal one at $y = 1.5\,\mathrm{m}$.
Similarly to the previous jets, the $R_{ij}-\varepsilon$ simulation reproduced better the R_{ii} profiles for small y values and the LES performed better at $y = 1.5\,\mathrm{m}$. Still, any simulation was able to accurately reproduce the horizontal R_{ii} profiles at this distance of the inlet (Figures 3.66, 3.67, 3.68).
The experimental Lumley triangle (Figure 3.69) describes a two dimensional turbulence, hardly reproduced by the three different simulations, with the LES triangle being the closest one to the experimental. Globally, it can be observed that each turbulent approach leads to a type of Lumley triangle, for all jets. While for a $k-\varepsilon$ model, the turbulence presents both an asymmetrical expansion and contraction, the $R_{ij}-\varepsilon$ model usually has a majority of points close to the expansion. The LES at its turn tends to the one dimensional turbulence, with still some points in the contraction zone. From the three approaches, the $k-\varepsilon$ is the closest to the isotropic turbulence, which is in agreement with the theory. Moreover, the reference $k-\varepsilon$ and R_{ij} simulations triangles (Figure 3.70) may confirm the aforementioned conclusion.

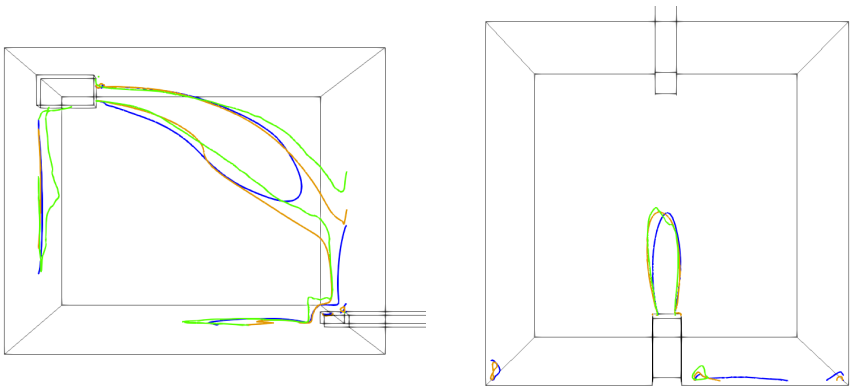

one

Figure 3.63: Velocity magnitude isoline $u_{mag} = 0.15\,\mathrm{m\,s^{-1}}$ for all three cold jet simulations. In blue, the $k-\varepsilon$ simulation, in orange, the R_{ij} and in green the LES.

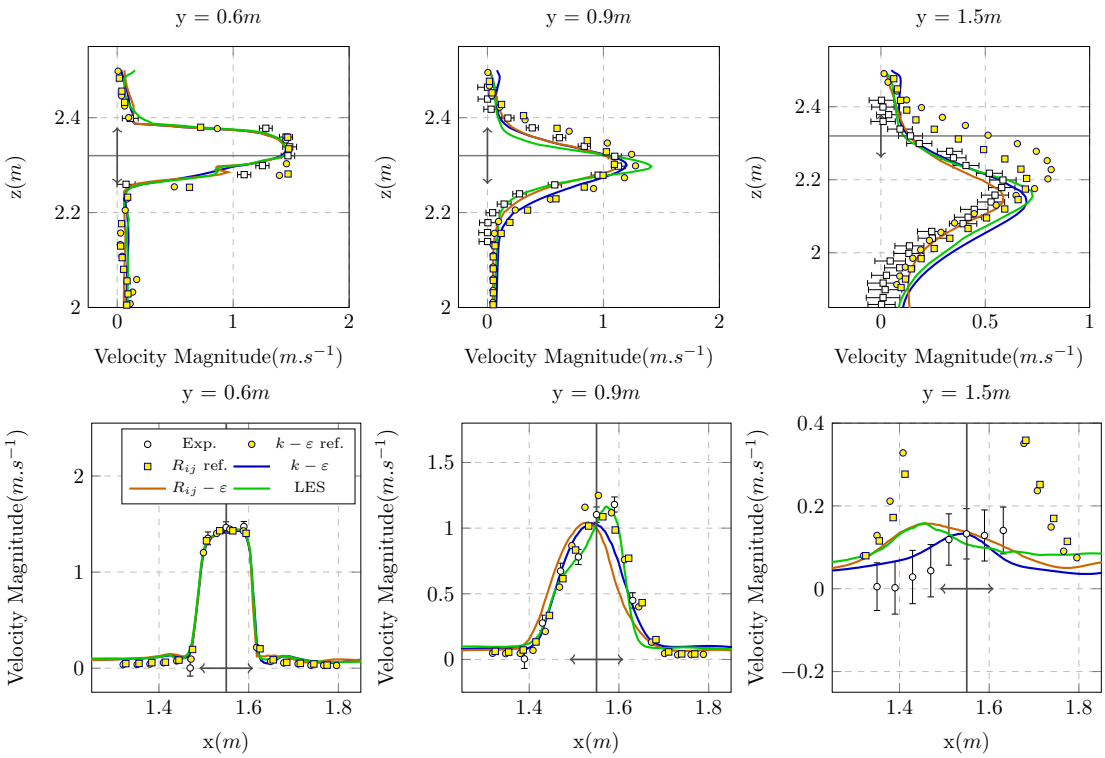

Figure 3.64: Cold jet. Velocity magnitude profiles over the vertical and horizontal segments lines.

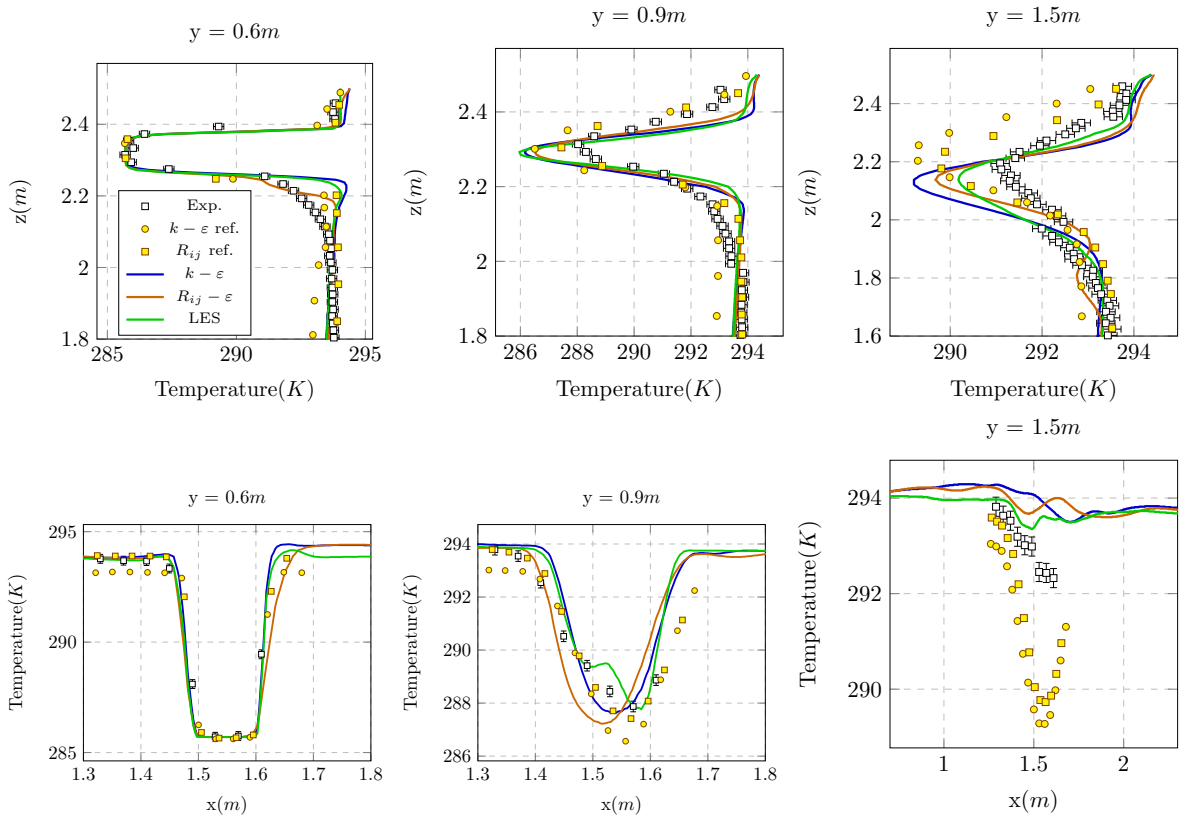

Figure 3.65: Cold jet. Temperature profiles over the vertical and horizontal segments lines.

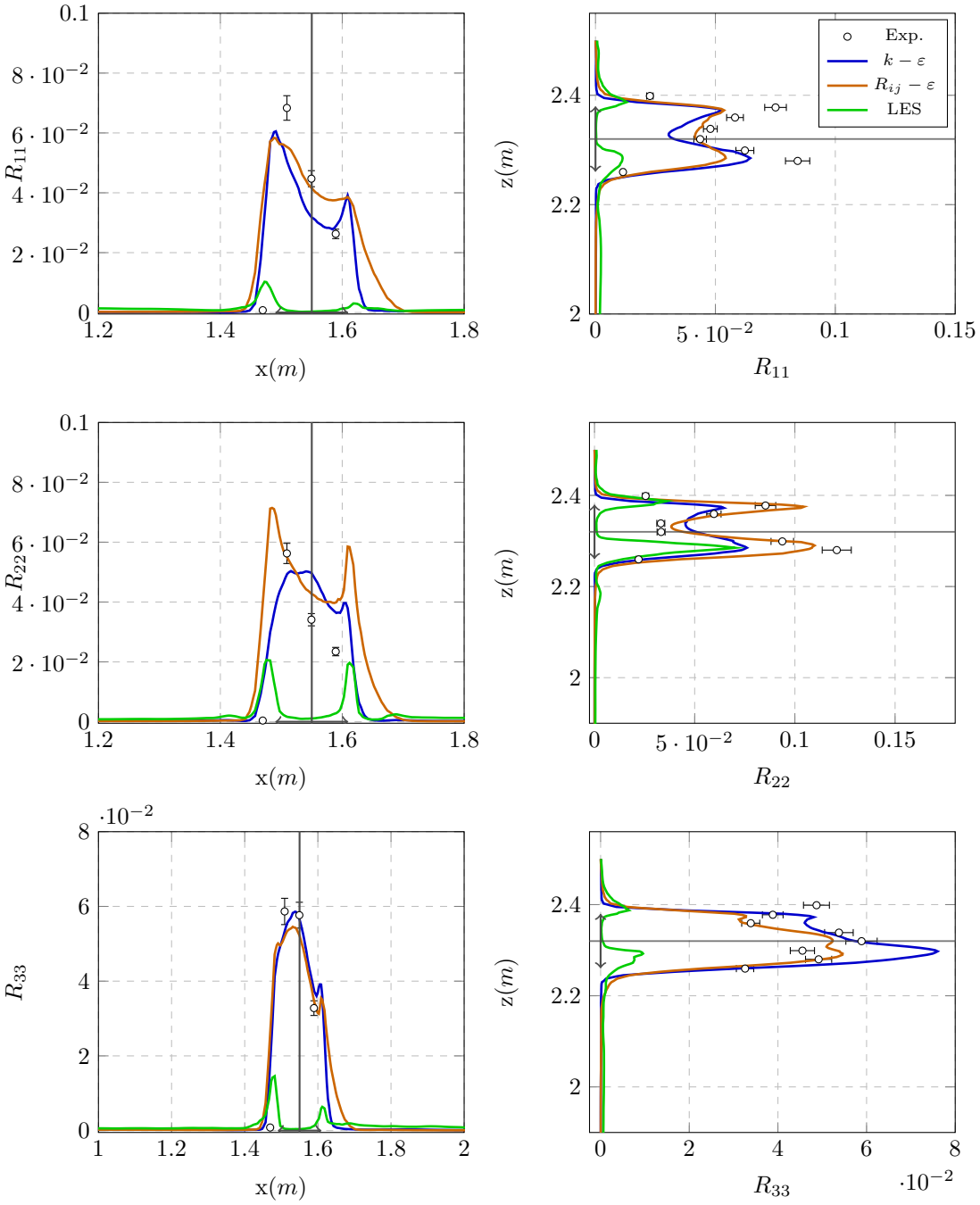

Figure 3.66: Cold jet. R_{ii} components at $y = 0.6\,\mathrm{m}$ for the vertical and horizontal profiles.

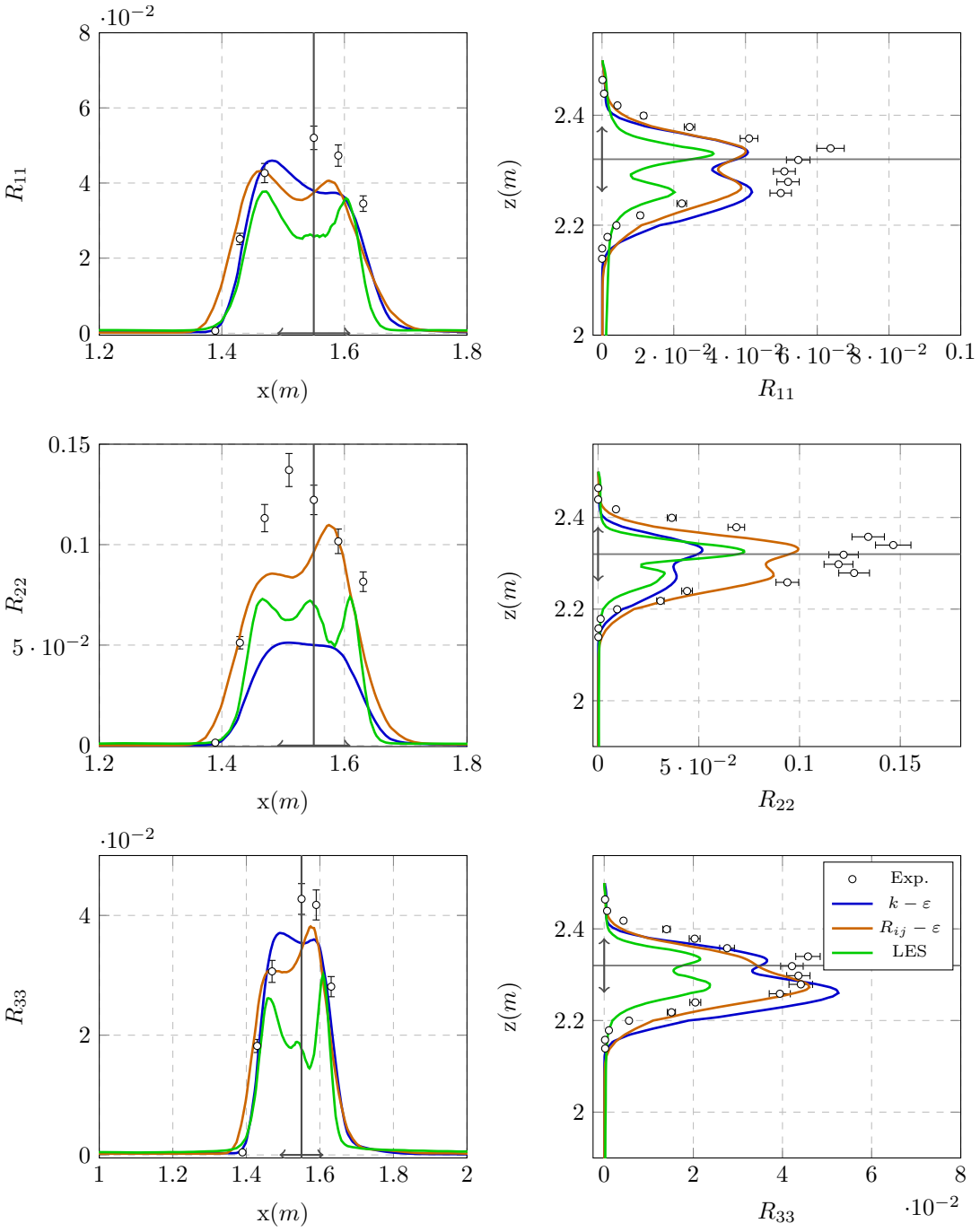

Figure 3.67: Cold jet. R_{ii} components at $y = 0.9\,\mathrm{m}$ for the vertical and horizontal profiles.

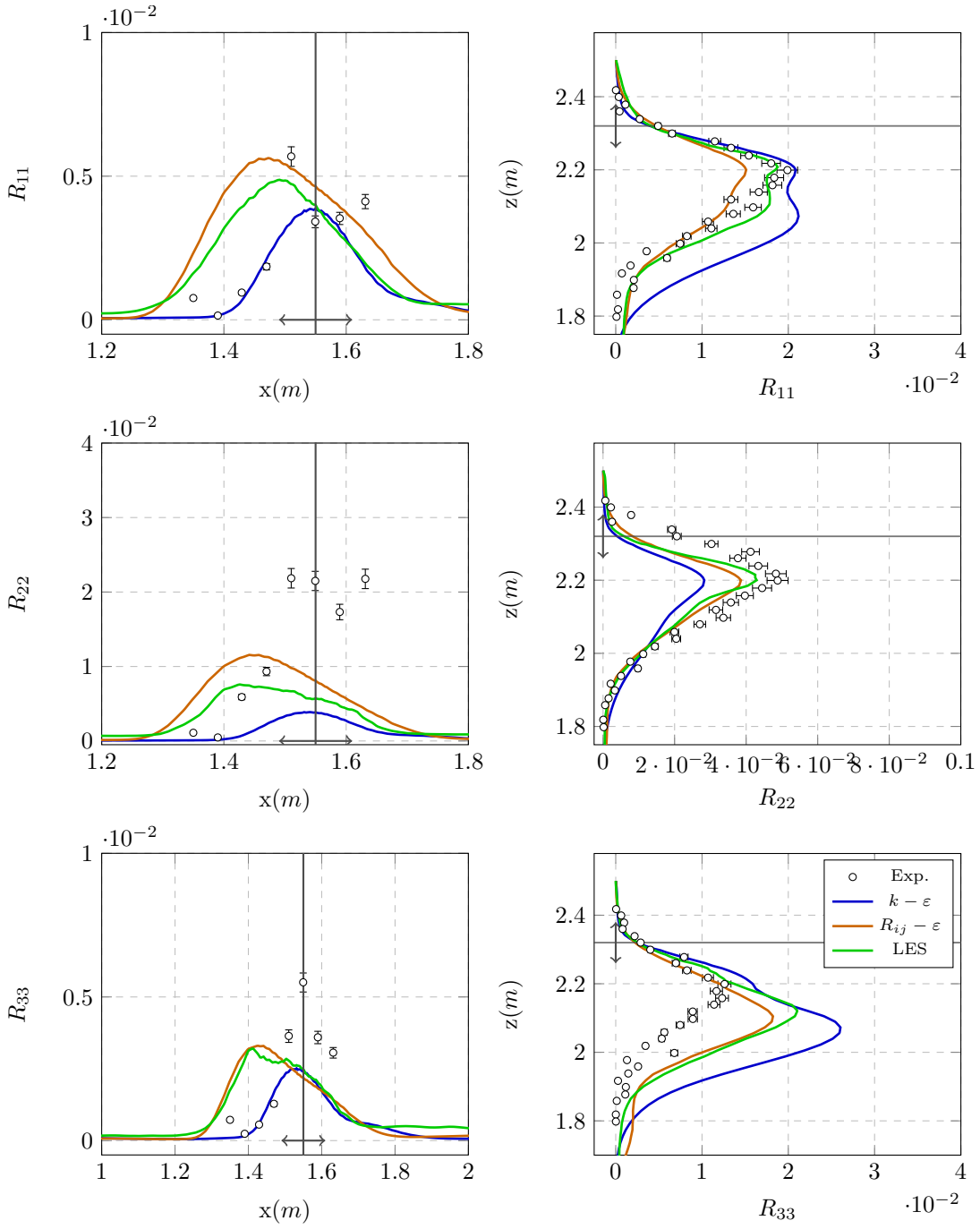

Figure 3.68: Cold jet. R_{ii} components at $y = 1.5\,\mathrm{m}$ for the vertical and horizontal profiles.

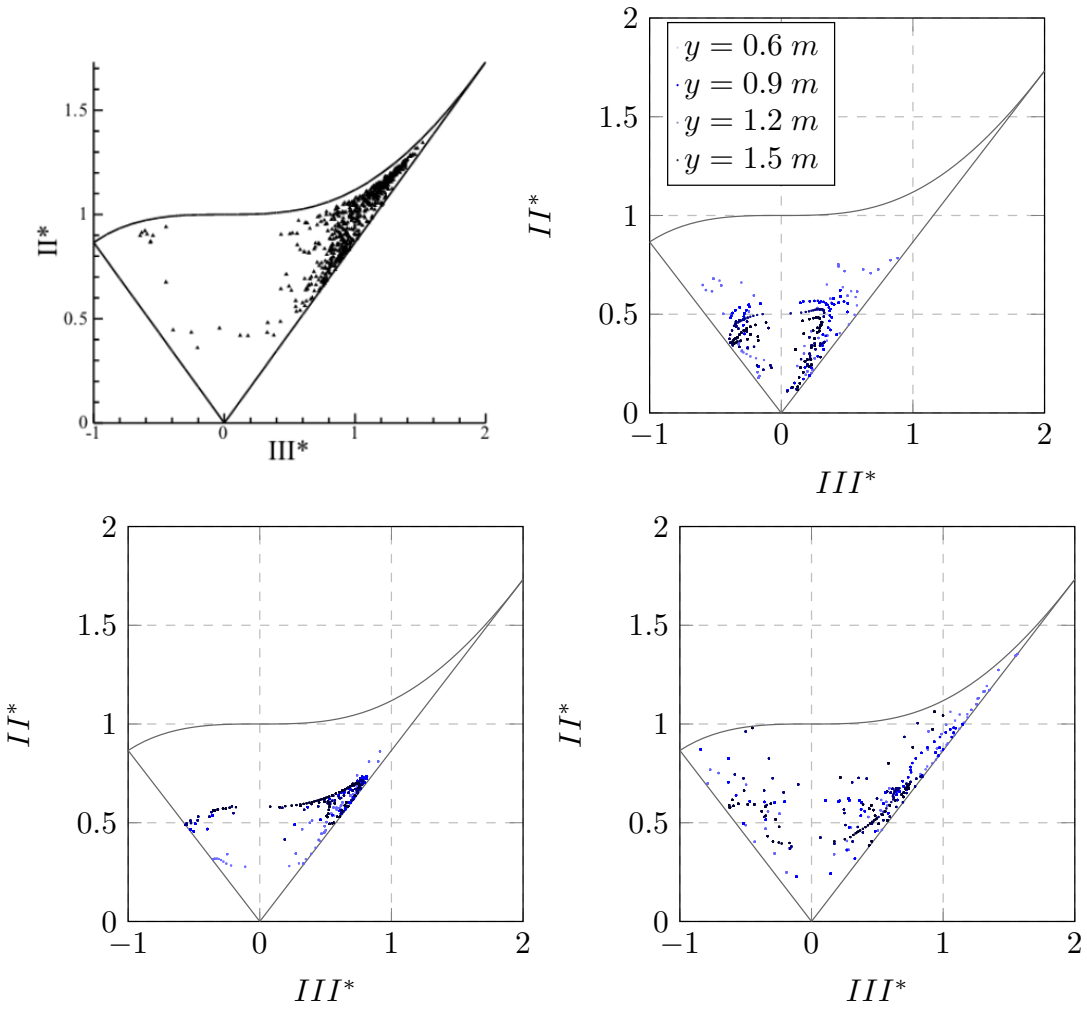

Figure 3.69: Lumley triangles for the cold jet case. (Top left) Experimental. (Top right) $k - \varepsilon$. (Bottom left) $R_{ij} - \varepsilon$. (Bottom right) LES simulation.

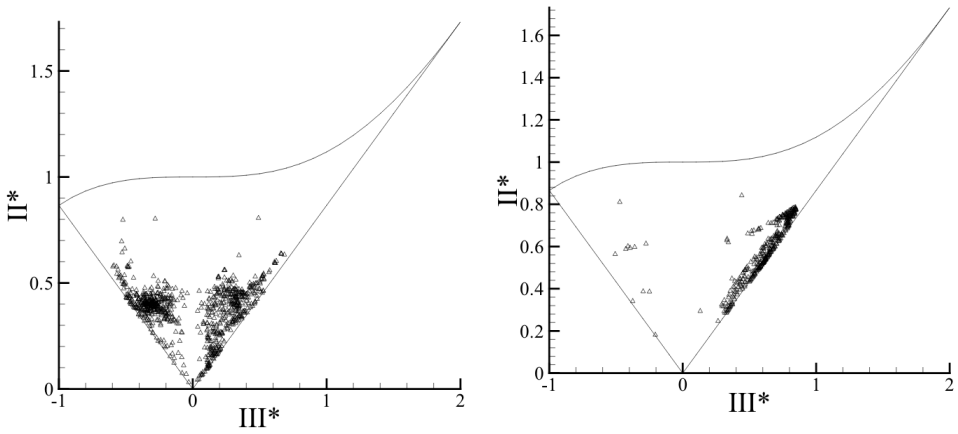

Figure 3.70: Lumley triangles from Kuznik (2005) for the cold jet case. (Left) $k - \varepsilon$ simulation. (Right) $R_{ij} - \varepsilon$ simulation.

3.9 Summary

This chapter presented a numerical time scheme designed to answer the physical and numerical stakes aforementioned related to indoor simulations.
More precisely, a second-order accurate conservative scheme for variable-density flow was developed as an extension of the work of Pierce *et al.* (Wall et al., 2003) The staggered time variable arrangement is used but for the finite volume discretisation. an Helmholtz equation is solved in the correction step. This allows the thermodynamic pressure variation to be considered while avoiding a time-step restriction linked to the acoustic waves. Further, the use of the internal energy equation supplemented with a kinetic energy-based source term, presented by Herbin et al. (2020) , was extended for the proposed sub-iterative algorithm architecture. Hence, shock solutions were well reproduced by simulations. After implementation in the CFD solver code_saturne, the time scheme accuracy and properties were verified and validated against the analytical solutions and experimental values of various compressible and incompressible flows related to the indoor environment.
First, we showed that the scheme can accurately consider pressure variations while conserving the mass. The second order accuracy was then achieved, and the conservation of mass and momentum were ensured in an one-dimensional convection test case. Moreover, the proposed method provided consistent solutions for regular and irregular shock problems, even for a material velocity-based Courant number equal to one. Two new CFL-like conditions to ensure the positivity of the pressure, temperature and density were provided and shown to be less constraining than the classical CFL condition during the verification process. For the validation process, a natural convection benchmark case was used, where the scheme provided results in agreement with the reference. A comparison between the presented time algorithm and one using a Poisson equation in the correction step emphasised the importance of considering the thermodynamical pressure during this crucial scheme step in order to reproduce such phenomena correctly. Finally, RANS and LES turbulent simulations were performed on a 3D ventilation geometry, emphasising the potential of the scheme for tertiary studies. In this test case, three different turbulent approaches were tested. Globally, the numerical results tend to underestimate the jet dynamics as the distance of its inlet increases. Nevertheless, the LES provided slightly more accurate profiles related to the experimental ones, notably by better catching the jet deviation, even without turbulence generation in the inlet faces. It is interesting to highlight as well that the CPC scheme led to faster simulations related to an incompressible scheme (about a quarter of reduction of the computational time). Note that all developments were made considering the flow composed only of dry air. Thus, the next chapter will focus on the extension of the presented algorithm to moist air, notably with phase change.
Also, it may be interesting to push the verification and validation processes of this numerical scheme to high Mach number flows to test it accuracy related to more complex compressible problems. Testing it as well on a atmospheric application and compare it to the existing code_saturne atmospheric module would be useful to evaluate its ability to perform in and outdoor flow simulations. Moreover, natural and forced convection were studied separately in this chapter; further studies could focus on validating the scheme for mixed convection.
Lastly, understanding why the correct reproduction of the velocities fluctuations in the ventilation inlet did not lead to correct averaged profiles (Minibat configuration, LES simulation for the isothermal jet, Appendix 3.I) should be useful to optimise the synthetic turbulence generation method and improve the accuracy of LES simulations in this type of configuration.

Appendix

3.A Derivation of the kinetic energy source term for the time staggered scheme

In this section, the source term $\Gamma_c^{u^2/2}\Big|_n^{n+1,k}$ expression is detailed. To do so, the discrete kinetic energy equation is derived. The following methodology, based on Herbin et al. (2020), extends the utilisation of a source term in the internal energy equation to time-staggered schemes using sub-iterations. The time scheme architecture implies that the source term used in the buoyant step in the temperature equation at time step $n+1,k$ is calculated after the corrective step at time step $n+1,k-1$. Thus, for the sake of simplicity, we consider $k>1$ and the Euler equations for this section. The mass flux at a given face is denoted by $\dot{M}_f = \underline{q}_f \cdot \underline{S}_f$ and its positive and negative face contributions $\dot{M}_f^+ = \max(\dot{M}_f, 0)$ and $\dot{M}_f^- = \min(\dot{M}_f, 0)$. It is recalled that the momentum equation is solved between the time steps $[n-1+\theta; n+\theta, k]$:

$$\Omega_c \frac{\Theta\left(\rho_c^n,\, \rho_c^{n+1,k-1}\right)\widetilde{\underline{u}}_c^k - \Theta\left(\rho_c^{n-1},\, \rho_c^{n,k-1}\right)\underline{u}_c^{n-1+\theta}}{\Delta t} + \sum_{f\in\mathcal{F}_c}\left\langle \Theta\left(\underline{u}^{n-1+\theta},\, \widetilde{\underline{u}}^k\right)\right\rangle_f \dot{M}_f\Big|_{n-1+\theta}^{n+\theta,k-1} + \Omega_c \underline{\mathrm{Grad}}_c\left(\left\langle p|_{n-1+\theta}^{n+\theta,k-1}\right\rangle_f\right) = \underline{0}. \tag{3.58}$$

The mass equation between the time steps $[n-1+\theta; n+\theta, k-1]$ is multiplied by $\widetilde{\underline{u}}_c^k$:

$$\Omega_c \widetilde{\underline{u}}_c^k \frac{\Theta\left(\rho_c^n,\, \rho_c^{n+1,k-1}\right) - \Theta\left(\rho_c^{n-1},\, \rho_c^{n,k-1}\right)}{\Delta t} + \sum_{f\in\mathcal{F}_c} \widetilde{\underline{u}}_c^k \dot{M}_f\Big|_{n-1+\theta}^{n+\theta,k-1} = 0. \tag{3.59}$$

(3.58) - (3.59) reads:

$$\Theta\left(M_c^{n-1},\, M_c^{n,k-1}\right)\frac{\widetilde{\underline{u}}_c^k - \underline{u}_c^{n-1+\theta}}{\Delta t} + \sum_{f\in\mathcal{F}_c}\left(\left\langle \Theta\left(\underline{u}^{n-1+\theta},\, \widetilde{\underline{u}}^k\right)\right\rangle_f - \widetilde{\underline{u}}_c^k\right)\dot{M}_f\Big|_{n-1+\theta}^{n+\theta,k-1} + \Omega_c \underline{\mathrm{Grad}}_c\left(\left\langle p|_{n-1+\theta}^{n+\theta,k-1}\right\rangle_f\right) = 0. \tag{3.60}$$

Multiplying equation (3.60) by $\widetilde{\underline{u}}_c^k$ and using $(a-b)a = \dfrac{a^2-b^2}{2} + \dfrac{|a-b|^2}{2}$ yields:

$$\begin{aligned}
&\Theta\left(M_c^{n-1},\, M_c^{n,k-1}\right)\frac{|\widetilde{\underline{u}}_c^k|^2 - |\underline{u}_c^{n-1+\theta}|^2}{2\Delta t} + \Theta\left(M_c^{n-1},\, M_c^{n,k-1}\right)\frac{\left|\widetilde{\underline{u}}_c^k - \underline{u}_c^{n-1+\theta}\right|^2}{2\Delta t} \\
&+ \sum_{f\in\mathcal{F}_c}\left(\frac{\left|\left\langle\Theta\left(\underline{u}^{n-1+\theta},\, \widetilde{\underline{u}}^k\right)\right\rangle_f\right|^2}{2} - \frac{|\widetilde{\underline{u}}_c^k|^2}{2}\right)\dot{M}_f\Big|_{n-1+\theta}^{n+\theta,k-1} \\
&- \sum_{f\in\mathcal{F}_c}\frac{\left|\left\langle\Theta\left(\underline{u}^{n-1+\theta},\, \widetilde{\underline{u}}^k\right)\right\rangle_f - \widetilde{\underline{u}}_c^k\right|^2}{2}\dot{M}_f\Big|_{n-1+\theta}^{n+\theta,k-1} + \Omega_c\underline{\mathrm{Grad}}_c\left(\left\langle p|_{n-1+\theta}^{n+\theta,k-1}\right\rangle_f\right)\cdot\widetilde{\underline{u}}_c^k = \underline{0}.
\end{aligned} \tag{3.61}$$

Then, the mass equation between the time steps $[n-1+\theta; n+\theta, k-1]$, multiplied by $\dfrac{1}{2}|\widetilde{\underline{u}}_c^k|^2$ is added to (3.61), leading to

$$\begin{aligned}
&\frac{\Theta\left(M_c^n,\, M_c^{n+1,k-1}\right)|\widetilde{\underline{u}}_c^k|^2 - \Theta\left(M_c^{n-1},\, M_c^{n,k-1}\right)|\underline{u}_c^{n-1+\theta}|^2}{2\Delta t} + \sum_{f\in\mathcal{F}_c}\frac{\left|\left\langle\Theta\left(\underline{u}^{n-1+\theta},\, \widetilde{\underline{u}}^k\right)\right\rangle_f\right|^2}{2}\dot{M}_f\Big|_{n-1+\theta}^{n+\theta,k-1} \\
&+ \Omega_c\underline{\mathrm{Grad}}_c\left(\left\langle p|_{n-1+\theta}^{n+\theta,k-1}\right\rangle_f\right)\cdot\widetilde{\underline{u}}_c^k = \\
&- \Theta\left(M_c^{n-1},\, M_c^{n,k-1}\right)\frac{\left|\widetilde{\underline{u}}_c^k - \underline{u}_c^{n-1+\theta}\right|^2}{2\Delta t} + \sum_{f\in\mathcal{F}_c}\frac{\left|\left\langle\Theta\left(\underline{u}^{n-1+\theta},\, \widetilde{\underline{u}}^k\right)\right\rangle_f - \widetilde{\underline{u}}_c^k\right|^2}{2}\dot{M}_f\Big|_{n-1+\theta}^{n+\theta,k-1}.
\end{aligned} \tag{3.62}$$

The simplified momentum equation is used to replace $\underline{\mathrm{Grad}}_c\left(\left\langle p|_{n-1+\theta}^{n+\theta,k-1}\right\rangle_f\right)\cdot\widetilde{\underline{u}}_c^k$:

$$\frac{\Theta\left(M_c^n,\, M_c^{n+1,k}\right)\underline{u}_c^{n+\theta,k}}{\Delta t} + \Omega_c\underline{\mathrm{Grad}}_c\left(\left\langle p|_{n-1+\theta}^{n+\theta,k}\right\rangle_f\right) = \frac{\Theta\left(M_c^n,\, M_c^{n+1,k-1}\right)\widetilde{\underline{u}}_c^k}{\Delta t} + \Omega_c\underline{\mathrm{Grad}}_c\left(\left\langle p|_{n-1+\theta}^{n+\theta,k-1}\right\rangle_f\right). \tag{3.63}$$

Taking the square of this and multiplying by $\dfrac{\Delta t}{2\Theta\left(M_c^n,\, M_c^{n+1,k-1}\right)}$:

$$\begin{aligned}
&\Omega_c\widetilde{\underline{u}}_c^k\cdot\underline{\mathrm{Grad}}_c\left(\left\langle p|_{n-1+\theta}^{n+\theta,k-1}\right\rangle_f\right) = \\
&\frac{\Omega_c^2\Delta t}{2\Theta\left(M_c^n,\, M_c^{n+1,k-1}\right)}\left[\left|\underline{\mathrm{Grad}}_c\left(\left\langle p|_{n-1+\theta}^{n+\theta,k}\right\rangle_f\right)\right|^2 - \left|\underline{\mathrm{Grad}}_c\left(\left\langle p|_{n-1+\theta}^{n+\theta,k-1}\right\rangle_f\right)\right|^2\right] \\
&+ \frac{\left[\Theta\left(M_c^n,\, M_c^{n+1,k}\right)\right]^2}{\Theta\left(M_c^n,\, M_c^{n+1,k-1}\right)}\frac{|\underline{u}_c^{n+\theta,k}|^2}{2\Delta t} \\
&- \Theta\left(M_c^n,\, M_c^{n+1,k-1}\right)\frac{|\widetilde{\underline{u}}_c^k|^2}{2\Delta t}\Omega_c\frac{\left[\Theta\left(M_c^n,\, M_c^{n+1,k}\right)\right]}{\Theta\left(M_c^n,\, M_c^{n+1,k-1}\right)} + \underline{\mathrm{Grad}}_c\left(\left\langle p|_{n-1+\theta}^{n+\theta,k}\right\rangle_f\right)\cdot\underline{u}_c^{n+\theta,k}.
\end{aligned} \tag{3.64}$$

By replacing $\Omega_c \underline{\text{Grad}}_c \left(\left\langle p|_{n-1+\theta}^{n+\theta,k-1} \right\rangle_f \right) \cdot \widetilde{\underline{u}}_c^k$ in (3.62) and multiplying it by $\dfrac{\Theta\left(M_c^n,\, M_c^{n+1,k-1}\right)}{\Theta\left(M_c^n,\, M_c^{n+1,k}\right)}$, we obtain

$$
\begin{aligned}
&\frac{\Theta\left(M_c^n,\, M_c^{n+1,k}\right) |\underline{u}_c^{n+\theta,k}|^2}{2\Delta t} - \left[\frac{\Theta\left(M_c^n,\, M_c^{n+1,k-1}\right)}{\Theta\left(M_c^n,\, M_c^{n+1,k}\right)} + 1 - 1 \right] \frac{\Theta\left(M_c^{n-1},\, M_c^{n,k-1}\right) |\underline{u}_c^{n-1+\theta}|^2}{2\Delta t} \\
&+ \left[\frac{\Theta\left(M_c^n,\, M_c^{n+1,k-1}\right)}{\Theta\left(M_c^n,\, M_c^{n+1,k}\right)} + 1 - 1 \right] \sum_{f \in \mathcal{F}_c} \frac{\left| \left\langle \Theta\left(\underline{u}^{n-1+\theta},\, \widetilde{\underline{u}}^k\right) \right\rangle_f \right|^2}{2} \dot{M}_f \Big|_{n-1+\theta}^{n+\theta,k-1} \\
&+ \Omega_c \underline{\text{Grad}}_c \left(\left\langle p|_{n-1+\theta}^{n+\theta,k} \right\rangle_f \right) \cdot \underline{u}_c^{n+\theta,k} \\
&= -\Theta\left(M_c^{n-1},\, M_c^{n,k-1}\right) \frac{\Theta\left(M_c^n,\, M_c^{n+1,k-1}\right)}{\Theta\left(M_c^n,\, M_c^{n+1,k}\right)} \frac{\left|\widetilde{\underline{u}}_c^k - \underline{u}_c^{n-1+\theta}\right|^2}{2\Delta t} \\
&+ \frac{\Theta\left(M_c^n,\, M_c^{n+1,k-1}\right)}{\Theta\left(M_c^n,\, M_c^{n+1,k}\right)} \sum_{f \in \mathcal{F}_c} \frac{\left| \left\langle \Theta\left(\underline{u}^{n-1+\theta},\, \widetilde{\underline{u}}^k\right) \right\rangle_f - \widetilde{\underline{u}}_c^k \right|^2}{2} \dot{M}_f \Big|_{n-1+\theta}^{n+\theta,k-1} - \Gamma_c^p|_{n-1+\theta}^{n+\theta,k},
\end{aligned}
\tag{3.65}
$$

where:

$$
\Gamma_c^p|_{n-1+\theta}^{n+\theta,k} = \frac{\Omega_c^2 \Delta t}{2\Theta\left(M_c^n,\, M_c^{n+1,k}\right)} \left[\left| \underline{\text{Grad}}_c \left(\left\langle p|_{n-1+\theta}^{n+\theta,k} \right\rangle_f \right) \right|^2 - \left| \underline{\text{Grad}}_c \left(\left\langle p|_{n-1+\theta}^{n+\theta,k-1} \right\rangle_f \right) \right|^2 \right]. \tag{3.66}
$$

The discrete kinetic energy equation is then written as:

$$
\begin{aligned}
&\frac{\Theta\left(M_c^n,\, M_c^{n+1,k}\right) |\underline{u}_c^{n+\theta,k}|^2 - \Theta\left(M_c^{n-1},\, M_c^{n,k-1}\right) |\underline{u}_c^{n-1+\theta}|^2}{2\Delta t} + \sum_{f \in \mathcal{F}_c} \frac{|\Theta\left(\underline{u}_f^{n-1+\theta},\, \widetilde{\underline{u}}_f^k\right)|^2}{2} \dot{M}_f \Big|_{n-1+\theta}^{n+\theta,k-1} \\
&+ \Omega_c \underline{\text{Grad}}_c \left(\left\langle p|_{n-1+\theta}^{n+\theta,k} \right\rangle_f \right) \cdot \underline{u}_c^{n+\theta,k} \\
&= -\Gamma_c^p|_{n-1+\theta}^{n+\theta,k} + \Theta\left(M_c^{n-1},\, M_c^{n,k-1}\right) \frac{\Theta\left(M_c^n,\, M_c^{n+1,k-1}\right)}{\Theta\left(M_c^n,\, M_c^{n+1,k}\right)} \frac{\left[|\underline{u}_c^{n-1+\theta}|^2 - |\widetilde{\underline{u}}_c^k - \underline{u}_c^{n-1+\theta}|^2 \right]}{2\Delta t} \\
&- \Theta\left(M_c^{n-1},\, M_c^{n,k-1}\right) \frac{|\underline{u}_c^{n-1+\theta}|^2}{2\Delta t} + \sum_{f \in \mathcal{F}_c} \frac{\left| \left\langle \Theta\left(\underline{u}^{n-1+\theta},\, \widetilde{\underline{u}}^k\right) \right\rangle_f \right|^2}{2} \dot{M}_f \Big|_{n-1+\theta}^{n+\theta,k-1} \\
&+ \frac{\Theta\left(M_c^n,\, M_c^{n+1,k-1}\right)}{\Theta\left(M_c^n,\, M_c^{n+1,k}\right)} \sum_{f \in \mathcal{F}_c} \left[\frac{\left| \left\langle \Theta\left(\underline{u}^{n-1+\theta},\, \widetilde{\underline{u}}^k\right) \right\rangle_f - \widetilde{\underline{u}}_c^k \right|^2}{2} - \frac{\left| \left\langle \Theta\left(\underline{u}^{n-1+\theta},\, \widetilde{\underline{u}}^k\right) \right\rangle_f \right|^2}{2} \right] \dot{M}_f \Big|_{n-1+\theta}^{n+\theta,k-1}.
\end{aligned}
\tag{3.67}
$$

Two terms compose this discrete equations right hand side: the kinetic energy dissipation into heat, $\Gamma_c^{u^2/2}\Big|_{n-1+\theta}^{n+\theta,k}$ and the second-order term $\Gamma_c^p|_{n-1+\theta}^{n+\theta,k}$, defined by Equation (3.66) and not taken into account in the source term for the sake of implementation and because its value tends to zero as the spatial discretisation is refined, as explained in Herbin et al. (2020).

3.B Variable time step

In case of variable time step, equations presented in Section 3.5 change.
In the initialisation step, $\underline{q}_f\Big|_n^{n+1,0} \cdot \underline{S}_f = \frac{\Delta t|_{n-1}^n}{\Delta t|_n^{n+1}} \underline{q}_f\Big|_{n-1}^n \cdot \underline{S}_f$.
In the buoyant scalars step, the discretised equations read:

$$
\begin{aligned}
&\text{(a)}: \ \frac{\rho_c^{n+1,k-1} Y_c^{n+1,k} - \rho_c^{n,k-1} Y_c^n}{\Delta t|_n^{n+1}} + \mathrm{Div}_c \left(\left\langle \Theta \left(Y^n,\, Y^{n+1,k} \right) \right\rangle_f \underline{q}_f\Big|_n^{n+1,k-1} \right) = \\
&\mathrm{Lap}_c \left(K, \Theta \left(Y^n,\, Y^{n+1,k} \right) \right), \text{for scalars,} \\
&\text{(b)}: \ c_v \left[\frac{\rho_c^{n+1,k-1} T_c^{n+1,k} - \rho_c^{n,k-1} T_c^n}{\Delta t|_n^{n+1}} + \mathrm{Div}_c \left(\left\langle \Theta \left(T^n,\, T^{n+1,k} \right) \right\rangle_f \underline{q}_f\Big|_n^{n+1,k-1} \right) \right] = \\
&\Omega_c \mu (S_c^2)^{n+\theta} + \Gamma_c^{u^2/2}\Big|_n^{n+1,k-1} + \mathrm{Lap}_c \left(\lambda, \Theta \left(T^n,\, T^{n+1,k} \right) \right) - \mathrm{Div}_c \left(\left\langle \Theta \left(p^n,\, p^{n+1,k-1} \right) \underline{u}^{n+\theta,k-1} \right\rangle_f \right) \\
&+ \Omega_c \underline{u}_c^{n+\theta,k-1} \cdot \underline{\nabla}_c p|_{n-1+\theta}^{n+\theta,k-1}, \text{for temperature.}
\end{aligned}
\tag{3.68}
$$

The corresponding kinetic energy source terms expression is modified as well:

$$
\begin{aligned}
&\frac{\Delta t|_n^{n+1}}{\Delta t|_{n-1+\theta}^{n+\theta}} \Gamma_c^{u^2/2}\Big|_n^{n+1,k-1} = \\
&\left[1 - \frac{\Theta \left(\rho_c^n,\, \rho_c^{n+1,k-2} \right)}{\Theta \left(\rho_c^n,\, \rho_c^{n+1,k-1} \right)} \right] \left[\Theta \left(\rho_c^{n-1},\, \rho_c^n \right) \frac{|\underline{u}_c^{n-1+\theta}|^2}{2\,\Delta t|_{n-1+\theta}^{n+\theta}} - \mathrm{Div}_c \left(\frac{\left| \left\langle \Theta \left(\underline{u}^{n-1+\theta},\, \widetilde{\underline{u}}^{k-1} \right) \right\rangle_f \right|^2}{2} \underline{q}_f\Big|_{n-1+\theta}^{n+\theta,k-2} \right) \right] \\
&- \frac{\Theta \left(\rho_c^n,\, \rho_c^{n+1,k-2} \right)}{\Theta \left(\rho_c^n,\, \rho_c^{n+1,k-1} \right)} \mathrm{Div}_c \left(\frac{\left| \left\langle \Theta \left(\underline{u}^{n-1+\theta},\, \widetilde{\underline{u}}^{k-1} \right) \right\rangle_f - \widetilde{\underline{u}}_c^{k-1} \right|^2}{2} \underline{q}_f\Big|_{n-1+\theta}^{n+\theta,k-2} \right) \\
&+ \frac{\Theta \left(\rho_c^n,\, \rho_c^{n+1,k-2} \right)}{\Theta \left(\rho_c^n,\, \rho_c^{n+1,k-1} \right)} \Theta \left(\rho_c^{n-1},\, \rho_c^n \right) \frac{\left[|\widetilde{\underline{u}}_c^{k-1} - \underline{u}_c^{n-1+\theta}|^2 \right]}{2\,\Delta t|_{n-1+\theta}^{n+\theta}}.
\end{aligned}
\tag{3.69}
$$

The mass flux $\underline{q}_f\Big|_{n-1+\theta}^{n+\theta,k-1}{}_f$ is defined by

$$
\underline{q}_f\Big|_{n-1+\theta}^{n+\theta,k-1} = \Theta \left(\frac{\Delta t|_{n-1}^n}{\Delta t|_{n-1+\theta}^{n+\theta}} \underline{q}_f\Big|_{n-1}^n,\, \frac{\Delta t|_n^{n+1}}{\Delta t|_{n-1+\theta}^{n+\theta}} \underline{q}_f\Big|_n^{n+1,k-1} \right).
$$

The prediction step reads:

$$
\begin{aligned}
&\frac{\Theta \left(\rho_c^n,\, \rho_c^{n+1,k-1} \right) \widetilde{\underline{u}}_c^k - \Theta \left(\rho_c^{n-1},\, \rho_c^{n,k-1} \right) \underline{u}_c^{n-1+\theta}}{\Delta t|_{n-1+\theta}^{n+\theta}} + \mathrm{Div}_c \left(\left\langle \Theta \left(\underline{u}^{n-1+\theta},\, \widetilde{\underline{u}}^k \right) \right\rangle_f \otimes \underline{q}_f\Big|_{n-1+\theta}^{n+\theta,k-1} \right) = \\
&- \underline{\mathrm{Grad}}_c \left(\left\langle p|_{n-1+\theta}^{n+\theta,k-1} \right\rangle_f \right) + \mathrm{Div}_c \left(\underline{\tau}_f^k \right) + \underline{f}_c\Big|_{n-1+\theta}^{n+\theta,k-1}.
\end{aligned}
\tag{3.70}
$$

Finally, the Helmholtz equation turns into:

$$\begin{aligned}&\frac{\rho_c^{n+1,k}-\rho_c^n}{\Delta t|_n^{n+1}}-\theta\text{Lap}_c\left(\tau|_{n-1+\theta}^{n+\theta},p^{n+1,k}\right)=(1-\theta)\text{Lap}_c\left(\frac{\Delta t|_n^{n+1}}{\Delta t|_{n-1}^n}\tau|_{n-1+\theta}^{n+\theta},p|_{n-2+\theta}^{n-1+\theta}\right)\\&-\text{Div}_c\left(\left\langle\Theta\left(\rho^n,\rho^{n+1,k-1}\right)\widetilde{\underline{u}}^k+\Delta t|_{n-1+\theta}^{n+\theta}\left(\underline{\nabla}p|_{n-1+\theta}^{n+\theta,k-1}+\delta\underline{f}^k\right)\right\rangle_f\right).\end{aligned}\tag{3.71}$$

where $\left(1-(1-\theta)\left(1-\dfrac{\Delta t|_n^{n+1}}{\Delta t|_{n-1}^n}\right)\right)\tau|_{n-1+\theta}^{n+\theta}=\Delta t|_{n-1+\theta}^{n+\theta}$. With the pressure increment:

$$\phi_c^k=\frac{\Theta\left(\dfrac{\Delta t|_n^{n+1}}{\Delta t|_{n-1}^n}p_c|_{n-2+\theta}^{n-1+\theta},p_c^{n+1,k}\right)}{\left(1-(1-\theta)\left(1-\dfrac{\Delta t|_n^{n+1}}{\Delta t|_{n-1}^n}\right)\right)}-p_c|_{n-1+\theta}^{n+\theta,k-1}.\tag{3.72}$$

3.C code_saturne incompressible pressure correction time scheme (IPC)

The main steps of the incompressible pressure correction time scheme is presented in this section. Proposed by Ma et al. (2019) [↗], the following belongs to the pressure correction class of schemes and has a sub-iterative process. The second order Crank Nicolson scheme is employed for the time advancement.

Remark 3.C.1. The IPC scheme was first designed for low-Mach number variable density applications and possibly reactive flows.

The set of equations used is the following:

$$\begin{aligned}&\frac{\partial\rho}{\partial t}=\text{div}\left(\rho\underline{u}\right)=\Gamma,\\&\frac{\partial(\rho\underline{u})}{\partial t}+\underline{\text{div}}\left(\underline{u}\otimes\rho\underline{u}\right)=-\underline{\nabla}p+\underline{\text{div}}\left(\underline{\tau}\right)+\underline{f},\\&\frac{\partial(\rho Y)}{\partial t}+\text{div}\left(\rho Y\underline{u}\right)=\text{div}\left(K\underline{\nabla}Y\right)+\Gamma_Y,\\&\rho=f(Y).\end{aligned}\tag{3.73}$$

The first step is the initialisation of the variables for $k=0$:

$$\begin{aligned}&\underline{q}^{n+\frac{1}{2},0}=2\underline{q}^{n+\frac{1}{2}-1}-\underline{q}^{n+\frac{1}{2}-2},\\&p^{n+\frac{1}{2},0}=p^{n+\frac{1}{2}-1},\\&\underline{f}^{n+\frac{1}{2}}=\frac{3}{2}\underline{f}^n-\frac{1}{2}\underline{f}^{n-1},\\&\Gamma_Y^{n+\frac{1}{2}}=\frac{3}{2}\Gamma_Y^n-\frac{1}{2}\Gamma_Y^{n-1},\text{ and}\\&\rho^{n+1,0}=3\rho^n-3\rho^{n-1}+\rho^{n-2}.\end{aligned}$$

Remark 3.C.2. The density is initialised in that way to insure the mass conservation.

This step is followed by the solving of the scalar equation (enthalpy equation, for instance), to get $\tilde{Y}^{n+1,k+1}$, an intermediate scalar.
The equation of state is used to compute the density $\rho^{n+1,k+1}$ from the scalar previously computed.
Then, an update of the scalar field is made to insure the conservativity:

$$Y^{n+1,k+1} = \frac{\rho^{n+1,k}\tilde{Y}^{n+1,k+1}}{\rho^{n+1,k+1}}. \tag{3.74}$$

The momentum equation is solved during the prediction step to get the predicted velocity $\underline{\tilde{u}}^{n+1,k+1}$.
This step is followed by the correction of the pressure, where, similarly to this scheme correction step, an equation is solved for the pressure increment $\Phi^{n+1,k+1}$. Nevertheless, the combination of the momentum and mass equations yields to a Poisson equation:

$$\text{div}\left(\Delta t\underline{\nabla}\Phi^{n+1,k+1}\right) = \text{div}\left(\rho^{n+1,k+1}\underline{\tilde{u}}^{n+1,k+1}\right) + \frac{3}{2}\frac{\rho^{n+1,k+1}-\rho^{n}}{\Delta t} + \frac{1}{2}\text{div}\left(\underline{q}\right)^{n-\frac{1}{2}}. \tag{3.75}$$

The pressure increment is used to correct the new pressure:

$$p^{n+\frac{1}{2},k+1} = p^{n+\frac{1}{2},k} + \Phi^{n+1,k+1},$$

and so is the mass flux

$$\underline{q}^{n+1,k+1} = (\rho^{n+1,k+1}\underline{u}^{n+1,k+1}) = -\Delta t\underline{\nabla}\Phi^{n+1,k+1} + (\rho^{n+1,k}\underline{\tilde{u}}^{n+1,k+1}),$$

and the velocity

$$u^{n+1,k+1} = \frac{\underline{q}^{n+1,k+1}}{\rho^{n+1,k}}.$$

Lastly, the mass flux $\underline{q}^{n+\frac{1}{2},k+1}$ is reconstructed:

$$\underline{q}^{n+\frac{1}{2},k+1} = \frac{2}{3}\underline{q}^{n+1,k+1} + \frac{1}{3}\underline{q}^{n+\frac{1}{2}-1}. \tag{3.76}$$

3.D code_saturne isentropic compressible time scheme (IC)

The main steps of the isentropic compressible time scheme available in code_saturne are presented in this section. Note that only the time discretisation is detailed. Further details on the spatial discretisation can be found in Colas et al. (2019) and Archambeau et al. (2009). Globally, the main differences between this time scheme and the CPC one are the use of the Euler equations, a first order in time, the absence of inner iterations, the solve of the total energy equation and finally, an isentropic pressure correction step.
First, an intermediate pressure p^* is computed solving the mass equation and using an acoustic approximation of the variation of ρ i.e.

$$\frac{p^* - p^n}{(c^2)^n} + \Delta t\text{div}\ \left(\rho^n\underline{u}^n - \Delta t\underline{\nabla}p^*\right) = 0. \tag{3.77}$$

The density ρ^{n+1} and an intermediate mass flux $\underline{q}^*$ are then updated

$$\rho^{n+1} = \rho^n + \frac{p^* - p^n}{(c^2)^n}, \quad \text{and } \underline{q}^* = \rho^n\underline{u}^n - \Delta t\underline{\nabla}p^*.$$

The second step is to solve the momentum equation to get $\underline{u}^{n+1}$:

$$\frac{\rho^{n+1}\underline{u}^{n+1} - \rho^n \underline{u}^n}{\Delta t} + \underline{\text{div}}\left(\underline{u}^{n+1} \otimes \underline{q}^*\right) = -\underline{\nabla} p^* + \rho^{n+1}\underline{f}^n. \tag{3.78}$$

Finally, the last step is to compute the total energy E^{n+1} by solving its conservation equation (here written with no source terms):

$$\frac{E^{n+1} - E^n}{\Delta t} + \text{div}\left(\frac{E^{n+1}}{\rho^{n+1}}\underline{q}^*\right) = -\text{div}\left(\frac{p^*}{\rho^{n+1}}\underline{q}^*\right) + \rho^{n+1}\left(\underline{f}^n \cdot \underline{u}^{n+1}\right). \tag{3.79}$$

The new pressure is finally updated using an EOS:

$$p^{n+1} = P(\rho^{n+1}, e^{n+1}), \quad \text{with } e^{n+1} = \frac{E^{n+1}}{\rho^{n+1}} - \frac{1}{2}\left(\underline{u}^{n+1} \cdot \underline{u}^{n+1}\right)$$

Remark 3.D.1. This scheme was shown to be conservative, with positive density (given some spatial discretisation choices) and with a total enthalpy preserved (Archambeau et al., 2009).

3.E Wall functions

3.E.1 Velocity wall function

The purpose of the velocity wall function is to provide to the finite volume solver a dimensionless analytical velocity value, denoted u^+, representing the non linear real velocity profile close to the wall. This value is proportional to the cell centre to the wall dimensionless distance, denoted y^+. For the velocity, u^+ and y^+ are made dimensionless by the wall shear stress τ_w and the turbulent kinetic energy. Note that only smooth walls are considered here.

Remark 3.E.1. In case of using only the wall shear stress, one may talk about "one scale friction velocity". If the turbulent kinetic energy is used, the wall function is named "two friction velocity scales".

Remark 3.E.2. Walls functions are usually derived from EVM.

One friction velocity scale

The first boundary cell simplified momentum equations reads:

$$(\mu + \mu_T)\frac{\partial u}{\partial y} = \tau_w. \tag{3.80}$$

The friction velocity $u^\star$ is defined as

$$u^\star = \sqrt{\frac{\tau_w}{\rho}}.$$

Equation (3.80) is then rewritten as

$$\left(1 + \frac{\mu_T}{\mu}\right)\frac{\partial u^+}{\partial y^+} = 1, \tag{3.81}$$

with

$$u^+ = \frac{|\underline{u}_{I'}|}{u^\star}, \text{ and}$$

$$y^+ = \frac{y u^\star}{\nu}.$$

Two layers are defined. The first one, where $\mu_T/\mu < 1$ is called the viscous sub-layer; the velocity profile in this zone is linear i.e.

$$u^+ = y^+. \tag{3.82}$$

If $\mu_T/\mu < 1$, then the velocity profile becomes logarithmic:

$$u^+ = \frac{1}{\kappa}\ln(y^+) + C_{log}, \tag{3.83}$$

where $C_{log} = 5.2$ and $\kappa = 0.42$ are constants. In code_saturne, the viscous sub-layer is valid for $y^+ < 5$ and the logarithm layer for $y^+ > 30$. Between them there is a gap, called the buffer layer. Some models can cover it but are beyond the scope of this manuscript. Instead, a dimensionless limit, denoted y^+_{lim} is set, usually equal to $1/\kappa$ for RANS simulations for instance.
Finally, the friction velocity $u^\star$ is computed as following:

$$\begin{cases} u^\star = \sqrt{\dfrac{|\underline{u}_{I'}|\nu}{y}}, & \text{if } \dfrac{|y\underline{u}_{I'}|}{\nu} < (y^+_{lim})^2, \\ (u^\star)^0 = \exp(-\kappa C_{log})\dfrac{\nu}{y}, \quad (u^\star)^{q+1} = \dfrac{\kappa|\underline{u}_{I'} + (u^\star)^q}{\ln\left(\dfrac{y(u^\star)^q}{\nu}\right) + \kappa C_{log} + 1}, & \text{otherwise (iterative solving in q).} \end{cases} \tag{3.84}$$

Two friction velocity scales

The turbulent kinetic energy is used as well in the non 6dimensional process.
A new friction velocity based in the boundary first cell turbulent energy is defined:

$$u_k = \sqrt{\sqrt{C_\mu}k}.$$

Remark 3.E.3. In code_saturne, the latter definition of the friction velocity is only valid for important y^+ values. For smaller ones, a blending is performed if the turbulent intensity is low:

$$u_k = \sqrt{g\frac{\nu|\underline{u}_{I'}|}{y} + (1-g)\sqrt{C_\mu}k}. \tag{3.85}$$

g is a blending factor defined as

$$g = \exp\left(-\frac{\sqrt{k}y}{11\nu}\right).$$

The final form of the friction velocity is thus expressed following the wall shear stress and the turbulent kinetic energy friction velocity:

$$u^\star = \frac{\tau_w}{\rho u_k}.$$

The momentum equation is now rewritten using the new notations (see Saturne (2019) for further details):

$$(1+\kappa y_k^+)\frac{\partial u^+}{\partial y_k^+}=1, \tag{3.86}$$

with

$$u^+=\frac{|\underline{u}_{I'}|}{u^\star}, \text{ and} \tag{3.87}$$

$$y_k^+=\frac{yu_k}{\nu}. \tag{3.88}$$

The two zones presented for the one friction velocity scale still hold, but with y_k^+ instead of y^+.

3.E.2 Scalars wall function

For scalars, such as the temperature, the approach is similar for the fluid velocity.
The simplified scalar T balance (considering the fluid properties constant) on the considered wall neighbour cell reads:

$$q_{ib}=-\left(\lambda+c_p\frac{\mu_T}{Pr_T}\right)\frac{\partial T}{\partial y}. \tag{3.89}$$

q_{ib} is the heat flux at the boundary. This equation is made dimensionless by the introduction of

$$T^\star=-\frac{q_{ib}}{\rho c_p u_k}$$

Equation (3.89) is finally written as

$$\left(\frac{1}{Pr}+\frac{1}{Pr_T}\frac{\mu_T}{\mu}\right)\frac{\partial T^\star}{\partial y^+}=1, \tag{3.90}$$

where

$$y^+=\frac{yu_k}{\nu},$$

$$T^+=\frac{T-T_w}{T^\star},$$

with T_w the wall temperature. Similarly to the velocity, three different layers (the buffer layer is disconsidered) are defined and T^+ is computed as following:

$$\begin{cases}\dfrac{y^+}{T^+}=\dfrac{1}{Pr}, & \text{if } y^+<y_0^+,\\ \dfrac{y^+}{T^+}=\dfrac{y^+}{\dfrac{Pr_T}{\kappa}\ln\left(\dfrac{y^+}{y_0^+}\right)+Pry_0^+}, & \end{cases} \tag{3.91}$$

with

$$y_0^+=\frac{Pr_T}{\kappa Pr}. \tag{3.92}$$

3.F Minibat polar interpolation on the inlet quantities

In this section the polar interpolation on the Minibat configuration inlet variables is detailed. Considering the variables in the polar coordinates, we no longer work with u_1, u_2, u_3 but rather with u_r, u_θ and u_2, reminding that the axial velocity follows $\underline{e}_y$. The Reynolds stress tensor in the polar coordinates is composed of $R_{rr}, R_{\theta\theta}, R_{yy}, R_{r\theta}, R_{ry}$ and $R_{\theta y}$. The interpolation of a given variable $\phi(r, \theta)$ chosen is :

$$\phi_{interp} = \frac{\beta - \alpha}{\beta}\phi^0(r, \theta_\alpha) + \frac{\alpha}{\beta}\phi^0(r, \theta_\beta). \tag{3.93}$$

Three types of interpolation are tested:

- I0 : interpolation using r on the experimental data + a linear θ interpolation considering every quantity as a scalar (i.e. ϕ^0 is the variable itself projected on the given axis experimental data. $\alpha = \theta, \beta = \pi/2, \gamma = \phi$.
- I1 : interpolation using r on the experimental data + a linear θ interpolation. $\alpha = \theta, \beta = \pi/2$.
- I2 : interpolation using r on the experimental data + a sin θ interpolation. $\alpha = sin(\theta), \beta = sin(\pi/2)$.

	$\theta \in [0, \frac{\pi}{2}]$	$\theta \in [\frac{\pi}{2}, \pi]$	$\theta \in [\pi, \frac{3\pi}{2}]$	$\theta \in [\frac{3\pi}{2}, 2\pi]$
θ_α	0	$\frac{\pi}{2}$	π	$\frac{3\pi}{2}$
θ_β	$\frac{\pi}{2}$	π	$\frac{3\pi}{2}$	2π

Table 3.F.1: Summary of the different values of θ_α and θ_β according to the angle value.

θ	u_r	u_θ	u_2	R_{rr}	$R_{\theta\theta}$	R_{22}	$R_{r\theta}$	R_{r2}	$R_{\theta 2}$
0	u_1	u_3	u_2	R_{11}	R_{33}	R_{22}	R_{13}	R_{12}	R_{23}
$\frac{\pi}{2}$	u_3	$-u_1$	u_2	R_{33}	R_{11}	R_{22}	$-R_{13}$	R_{23}	$-R_{12}$
π	$-u_1$	u_3	u_2	R_{11}	R_{33}	R_{22}	R_{13}	$-R_{12}$	$-R_{23}$
$\frac{3\pi}{2}$	$-u_3$	u_1	u_2	R_{33}	R_{11}	R_{22}	$-R_{13}$	$-R_{23}$	R_{12}

Table 3.F.2: Polar equivalent interpolation variable ϕ^0 according to the different angle value.

$\phi^0(r, \theta_\alpha)$ and $\phi^0(r, \theta_\beta)$ are calculated from a linear interpolation of the experimental available data on the $\underline{e}_x$ and $\underline{e}_z$ axis based on Table 3.F.2 and Figure 3.F.1 for interpolations I1 and I2. The polar quantities are estimated following (3.93) and converted into the reference axis readable by the solver. Since $\underline{e}_r =$

$cos(\theta)\underline{e}_y + sin(\theta)\underline{e}_z$ and $\underline{e}_\theta = -sin(\theta)\underline{e}_y + cos(\theta)\underline{e}_z$, the velocity vector in $(\underline{e}_x, \underline{e}_y, \underline{e}_z)$ reads:

$$\underline{u} = \begin{pmatrix} 0 \\ u_r cos(\theta) - u_\theta sin(\theta) \\ u_r sin(\theta) + u_\theta cos(\theta) \end{pmatrix}, \tag{3.94}$$

and

$$\begin{aligned} R_{11} &= R_{rr}cos^2(\theta) + R_{\theta\theta}sin^2(\theta) - 2cos(\theta)sin(\theta)R_{r\theta}, \\ R_{22} &= R_{xx}, \\ R_{33} &= R_{rr}sin^2(\theta) + R_{\theta\theta}cos^2(\theta) + 2cos(\theta)sin(\theta)R_{r\theta}, \\ R_{12} &= R_{ry}cos(\theta) - R_{\theta y}sin(\theta), \\ R_{13} &= cos(\theta)sin(\theta)(R_{rr} - R_{\theta\theta}) + R_{r\theta}(cos^2(\theta) - sin^2(\theta)), \\ R_{23} &= R_{ry}sin(\theta) + R_{\theta y}cos(\theta). \end{aligned} \tag{3.95}$$

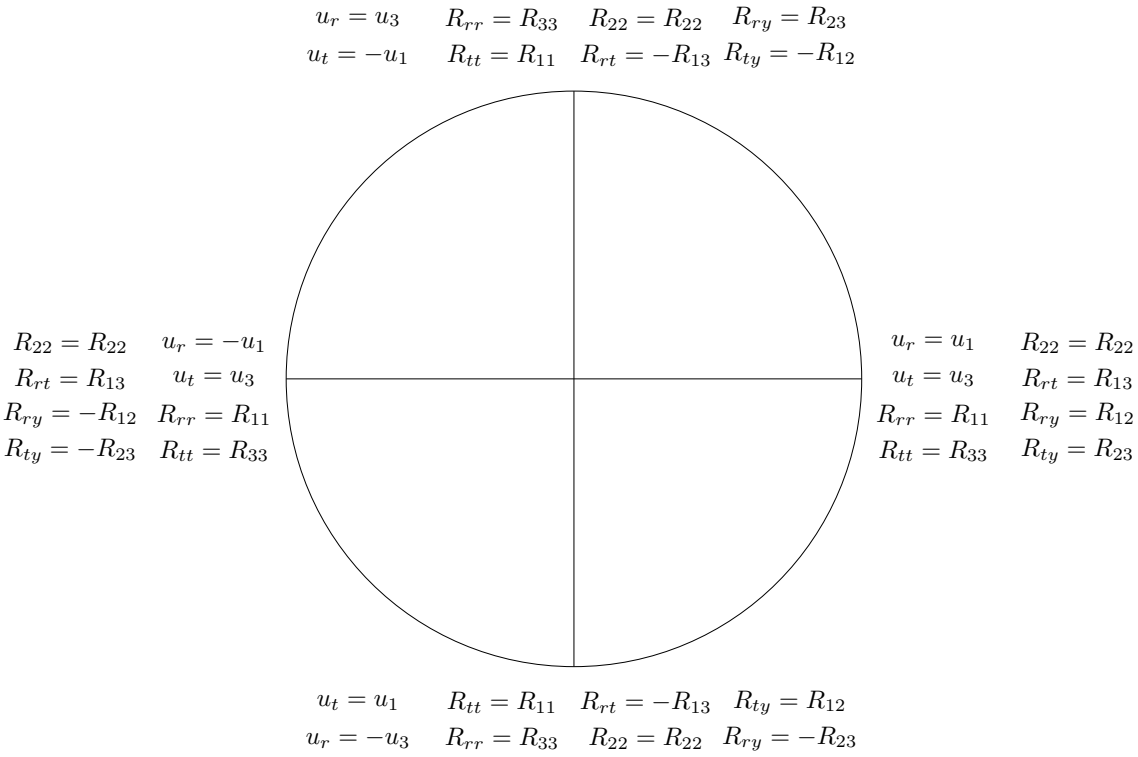

Figure 3.F.1: Conversion of the reference coordinates values into the polar ones depending on θ.

3.F.1 Verification

Two analytical velocity solutions are used to verify the inlet polar interpolation. The center of the inlet is located at $[x_0, y_0, z_0] = [1.55, 0.57, 2.32]$ m.

Rotating cylinder

First we consider a rotating inlet i.e. with only a tangential and axial velocity. The radial velocity u_r is fixed to zero. The axial velocity reads:

$$u_2^x = u_2^z = u_{max}\left(1 - \frac{r^2}{R^2}\right). \tag{3.96}$$

u_{max} is fixed and R is the inlet radius. The tangential velocity $u_\theta = \dot{\theta} r$ can be translated to $u_1^{z>z_0} = -ru_0$, $u_1^{z<z_0} = ru_0$ and $u_1^x = 0\,\mathrm{m\,s^{-1}}$. $u_0 = 1\,\mathrm{m\,s^{-1}}$ is a reference velocity.
Similarly, $u_3^{x>x_0} = ru_0$, $u_3^{x<x_0} = -ru_0$ and $u_3^z = 0\,\mathrm{m\,s^{-1}}$. The three different polar interpolation led to the velocity components represented on Figure 3.F.2. The L_2 error norm of the tangential velocity is also represented. On a first look, the different velocity fields seems similar, but the error related to the angular velocity shows that the interpolations I1 and I2 performed better for this test case. This is an expected result since the interpolation I0 interpolates the wrong quantities over the experimental axis.

Constant axial velocity

As the title says, here the axial velocity is fixed as $u_2^x = u_2^z = 1.5\,\mathrm{m\,s^{-1}}$ and other are considered equal to zero. In this test case it is expected that the interpolations I1 and I2 perform poorly. Figure 3.F.3 shows the horizontal and vertical components of the velocity as well as the L_2 error norm related to u_1. One can observe that besides the experimental imposed data equal to zero for the vertical and axial velocity components, the interpolation I1 and I2 led to a non null vertical velocity field. On the opposite, the first interpolation I0 led to a correct velocity field.
From these two test cases, it seems that there is no proper interpolation strategy: the interpolations I1 and I2 performed better for a rotating cylinder and the interpolation I0 for the constant axial velocity.
In this case, a choice is made according to the type of flow to be reproduce. In the one hand, if there is heterogeneous velocity fields, the I1 I2 strategies should be more appropriated. In the other, using the I0 interpolation would be a better choice in case of quasi homogeneous horizontal and vertical velocity field.

Minibat configuration (isothermal jet)

Considering the isothermal jet of the Minibat configuration, the three interpolation are ran over the available experimental data. Figures 3.F.4 to 3.F.10 show the different velocity and Reynolds stress tensor components fields over the system inlet. While the two radial interpolation I1 and I2 present similar results, the first interpolation method present clear differences, for both velocity and stress tensors.
It can be noticed that for the interpolation I0 the profiles are smoother. Even if some rotation may be present (given the jet deviation), the chosen of keeping this interpolation is made for the third chapter simulations.

Conclusion

Since the interpolation I0 led to the smoothest velocity fields and that only the information of the velocity horizontal and vertical profiles are provided by the experimental database, it is used for the final Minibat configuration simulations.

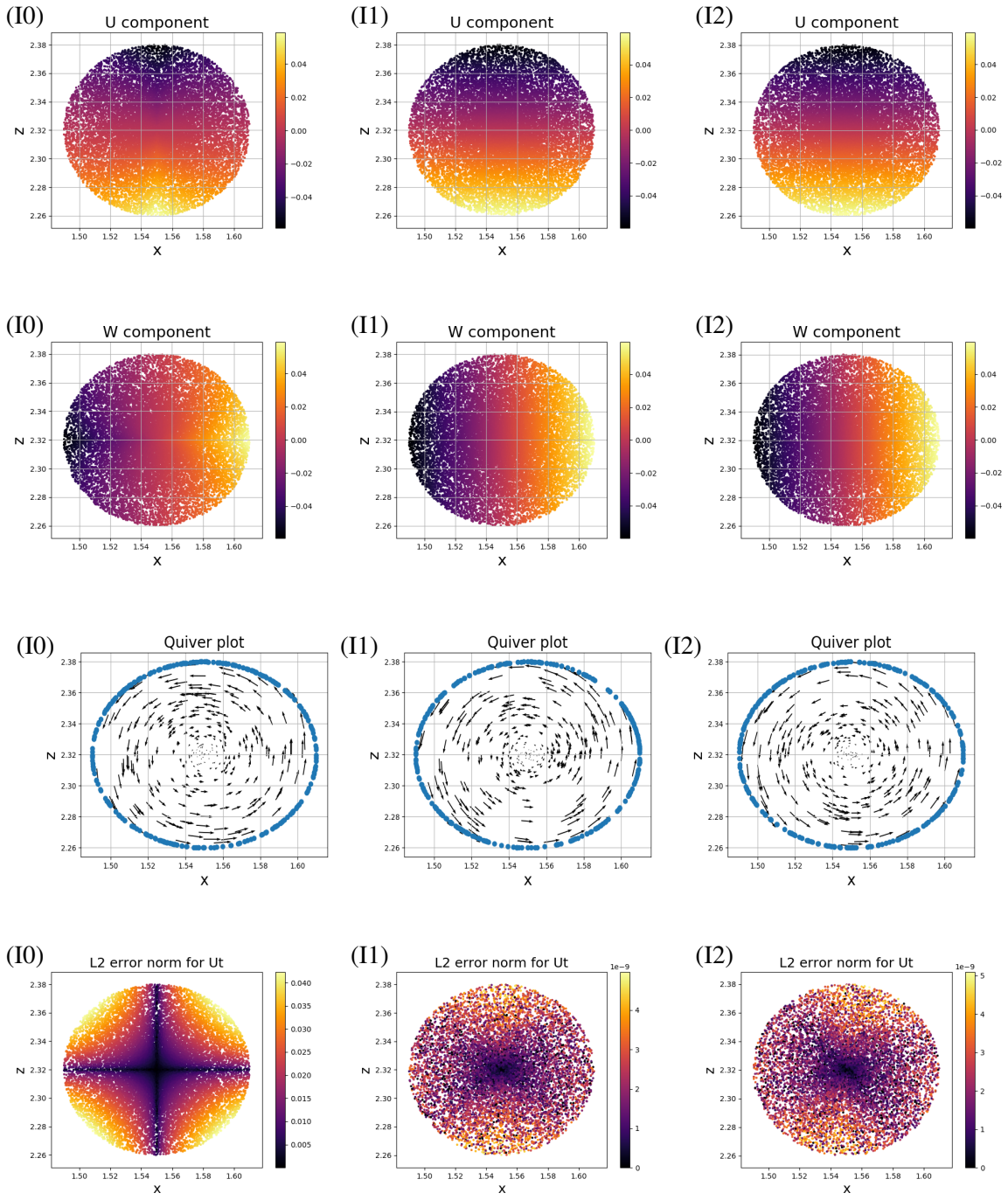

Figure 3.F.2: First test case. Velocity components fields, quiver plot and L_2 error norm related to the tangential velocity for the three different interpolations.

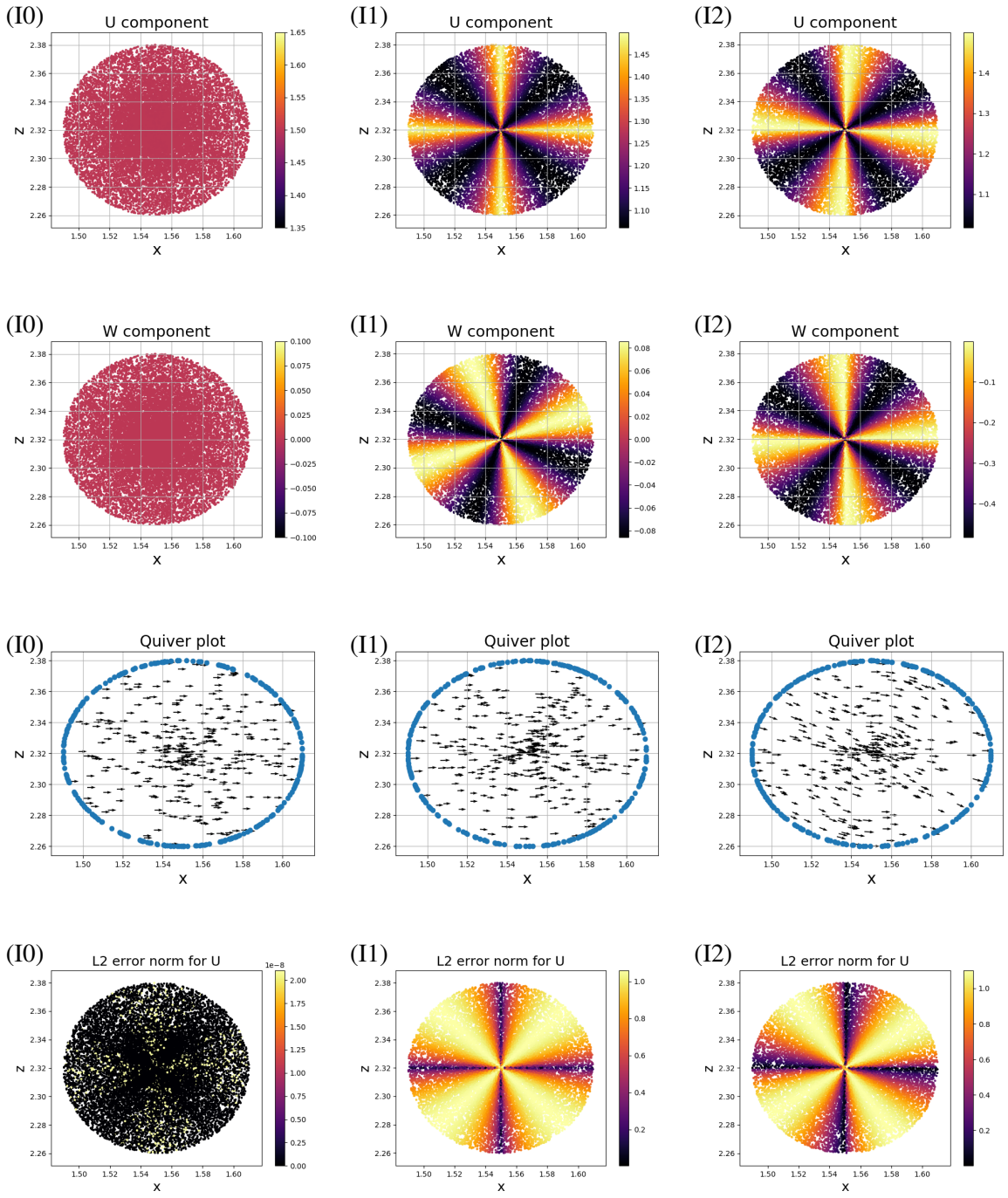

Figure 3.F.3: Second test case. Velocity components fields, quiver plot and L_2 error norm related to the horizontal velocity for the three different interpolations.

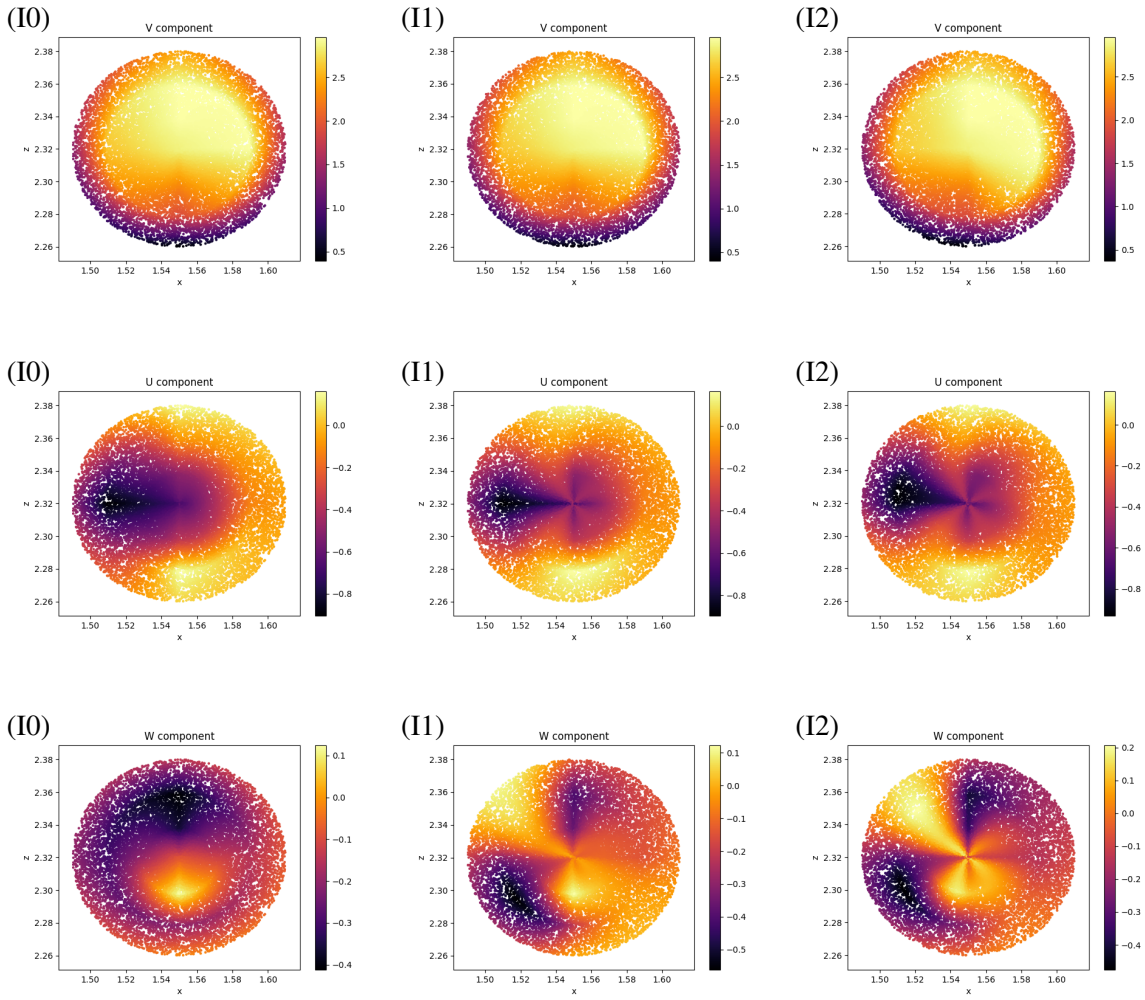

Figure 3.F.4: Velocity field for the three types of interpolation.

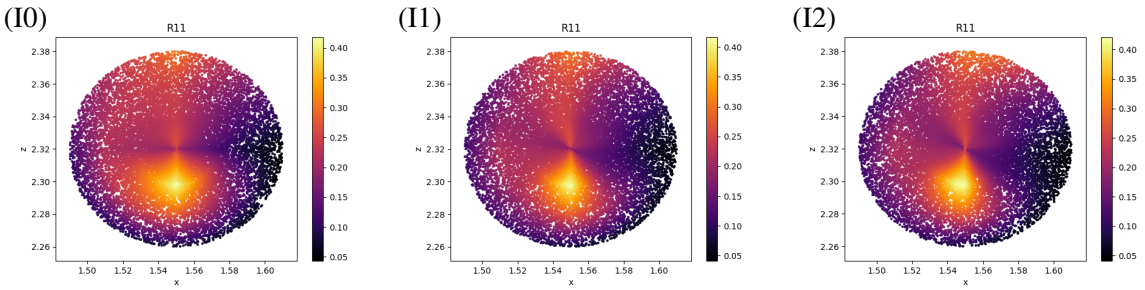

Figure 3.F.5: R_{11} components for the Minibat inlet.

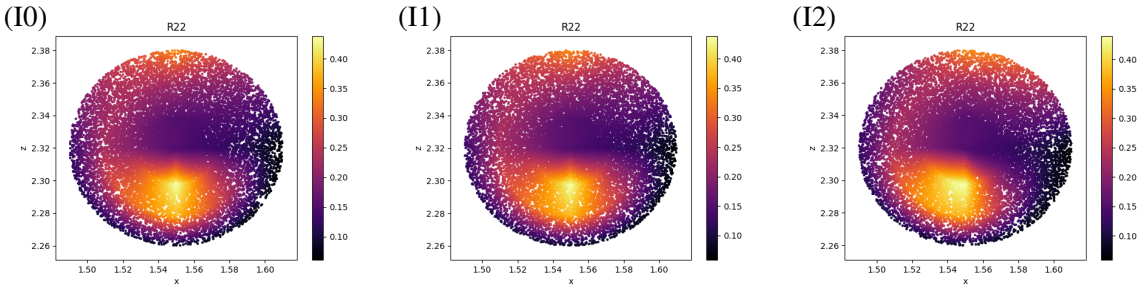

Figure 3.F.6: R_{22} components for the Minibat inlet.

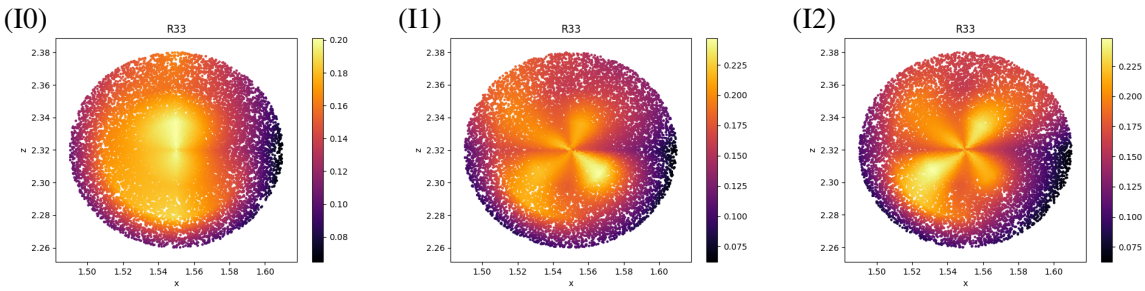

Figure 3.F.7: R_{33} components for the Minibat inlet.

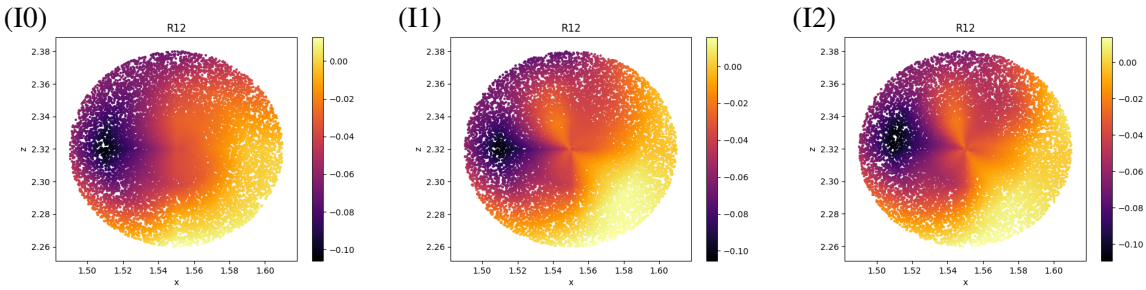

Figure 3.F.8: R_{12} components for the Minibat inlet.

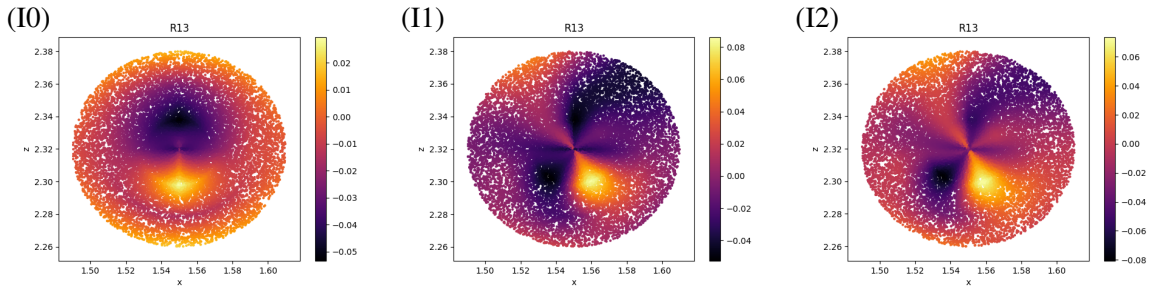

Figure 3.F.9: R_{13} components for the Minibat inlet.

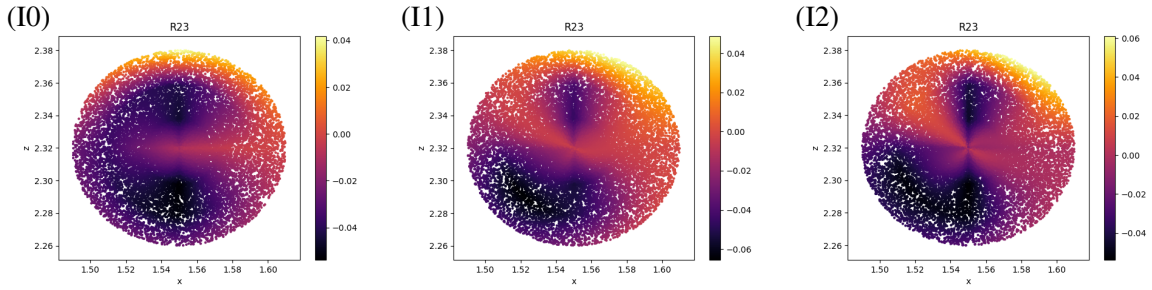

Figure 3.F.10: R_{23} components for the Minibat inlet.

3.G Minibat results: comparison between the full mesh and the inlet interpolation simulations

The complete mesh for the Minibat configuration, including the inlet duct is represented in Figure 3.G.1. The discretised system is composed here of 11.10^6 hexahedral cells.
Both geometry and mesh discretisation were made on the Salome platform, reconstructed from a .stl file.

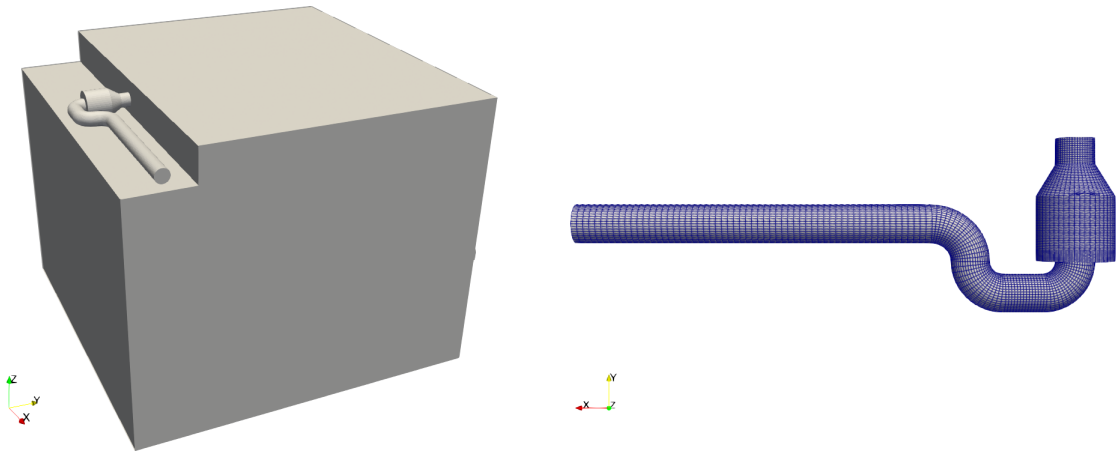

Figure 3.G.1: (Left) System geometry including the inlet ventilation duct. (Right) Focus on the ventilation duct discretisation.

To see if this configuration is more interesting than performing an interpolation on the experimental inlet data a first study on the kinetic energy dissipation is made. Considering the isothermal jet (I), an uniform

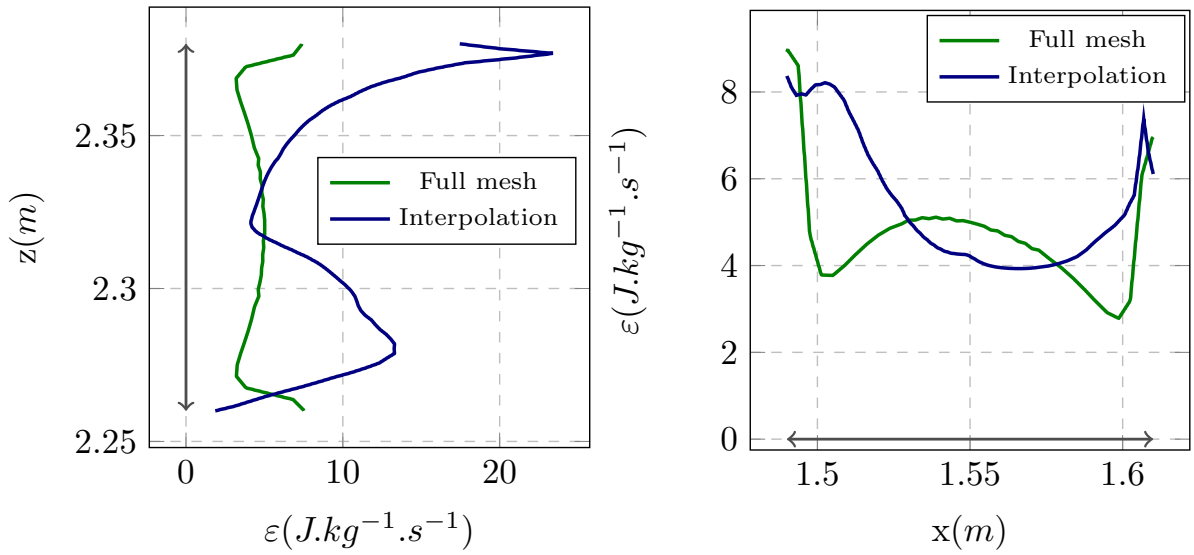

Figure 3.G.2: Vertical and horizontal ε profiles at $y = 0.58\,\mathrm{m}$ for the full mesh simulation and the inlet interpolation simulation.

velocity profile, with a magnitude of $2.8\,\mathrm{m\,s^{-1}}$ is imposed in the beginning of the ventilation duct. This choice was made in order to have a correct velocity magnitude on the room flow inlet. The turbulent variable ε profiles from two $k-\varepsilon$ simulations (full mesh and inlet interpolation 3.F, with $\varepsilon_{in} = 2\varepsilon_0$) are compared at $y = 0.58\,\mathrm{m}$ (entering flow in the room). The time of comparison is equal to $3\,\mathrm{s}$, when the flow is established in the ventilated room. For both simulation, two inner iterations are performed ($\varepsilon_{piso_0} = 10^{-6}$) and the CFL number remains under the unity.

Figure 3.G.2 shows that the ε field at the room inlet is clearly different in both z and x axis. This is probably due to a bad reproduction of the inlet duct flow in the full mesh simulation. A particular treatment of the boundary conditions on the duct walls and inlet velocity profile may lead to different results.

Moreover, Figure 3.G.3 shows for the simulation using the full mesh geometry an overestimation of the velocity in both vertical and horizontal profiles.

Note that at $y = 0.6\,\mathrm{m}$, one may observe that the full mesh simulation mass flow entering the room is superior to the other. We are aware that this should explain the overestimation of the velocity profile in higher y values. Nevertheless, when reducing the mass flow in the entering ventilation duct for the complete mesh configuration, the velocity profile at $y = 0.6\,\mathrm{m}$ was too insufficient (way below the expected magnitude of around $3\,\mathrm{m\,s^{-1}}$). Additionally, few information concerning the flow in the ventilation duct is available in the literature. Thus, for reasons of time, the choice of using interpolated inlet quantities for the final Minibat studies was made. Of course, this topic deserves further investigation for a better understanding of the ventilation duct impact on the system air flow.

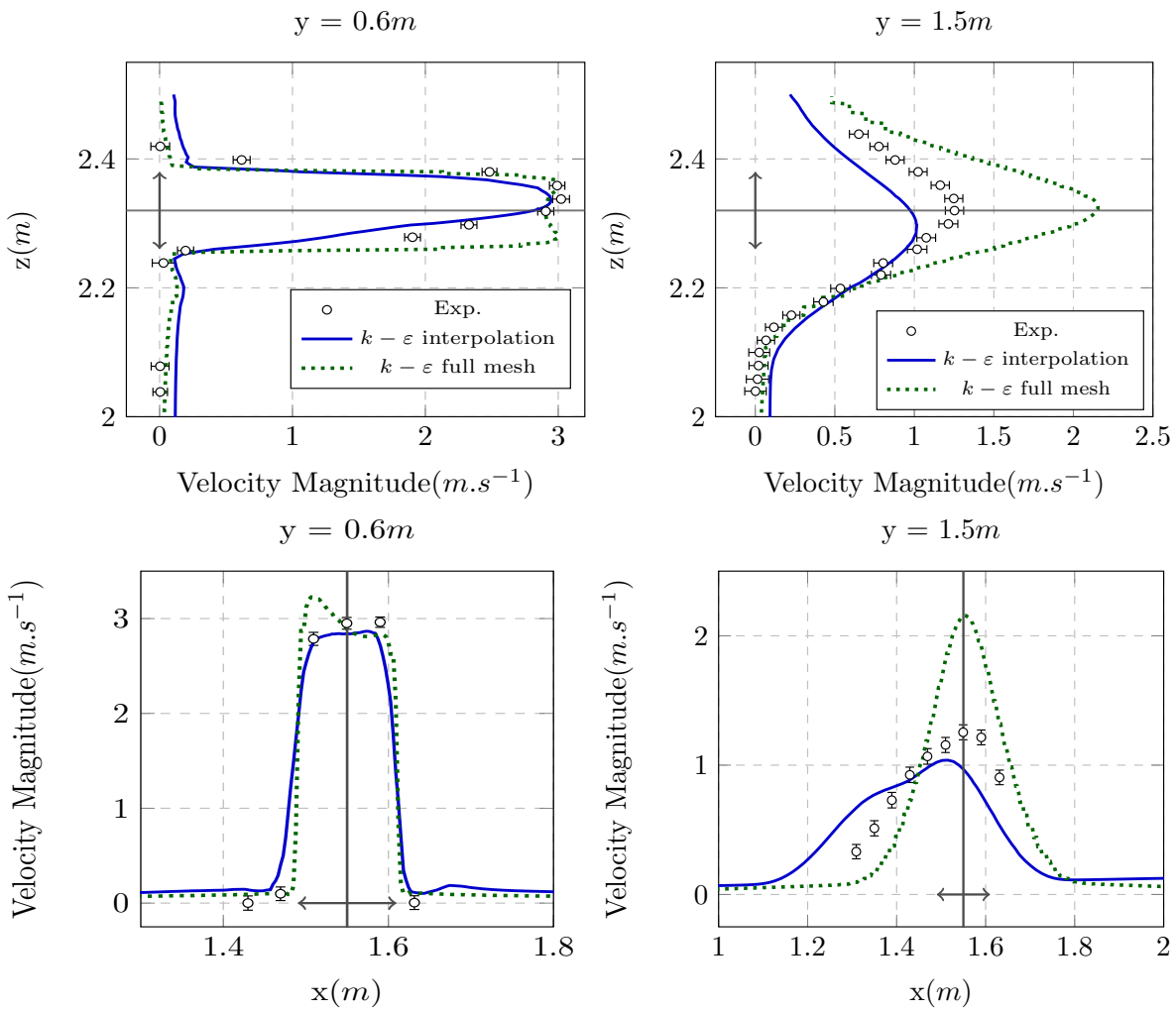

Figure 3.G.3: Vertical (top) and horizontal (bottom) velocity magnitude profiles profiles at $y = 0.6\,\mathrm{m}$ and $y = 1.5\,\mathrm{m}$ for the full mesh simulation and the inlet interpolation simulation.

3.H Reynolds stress tensor realisability and Lumley triangle

Realisability can be defined as a robustness of a numerical method related to its physical reliability.
For instance, in the Navier–Stokes equations, this can be seen as the preservation of the positivity of the thermodynamical variables and scalars concentration.
This is applied as well to the turbulent quantities and the Reynolds stress tensor. Its transport equation is derived from the conservative relations (mass, momentum, energy); properties related to these quantities are preserved if exact derived equations are used.
Nevertheless, this is not the case in turbulent approaches, where enclosures and models are used. This can break the realisability conditions, which reads, for the Reynolds Stress Tensor (Du Vachat, 1977; Schumann, 1977; Lumley, 1979; Norddine, 2020) [1][2][3][4]:

$$\begin{aligned} &(a) \qquad R_{ii} \geq 0 \qquad i \in \{1,2,3\} \\ &(b) \qquad R_{ii}R_{jj} - R_{ij}^2 \geq 0 \qquad (i,j) \in \{1,2,3\}^2 \\ &(c) \qquad \det(\underline{\underline{R}}) > 0. \end{aligned} \tag{3.97}$$

Condition (a) means that that the velocity field is real and the kinetic energy is positive. Condition (b) correspond to the Cauchy-Schawarz inequality (Steele, 2004) [↗]. The last condition is consequence of the definition of the Reynolds stress tensor as a statistical average.
These conditions can be studied using the anisotropy tensor $\underline{\underline{a}}$ defined as:

$$\underline{\underline{a}} = \frac{1}{2k}\underline{\underline{R}} - \frac{1}{3}\underline{\underline{I}}.$$

Lumley (1979) [↗] proposed that two linearly independent scalar invariants of the anisotropy tensor exist. Denoted II and III, they are defined as:

$$II = \frac{1}{2}\text{tr}(\underline{\underline{a}} \cdot \underline{\underline{a}}),$$

$$III = \frac{1}{3}\text{tr}(\underline{\underline{a}} \cdot \underline{\underline{a}} \cdot \underline{\underline{a}}).$$

Provided a positive turbulent kinetic energy, a sufficient condition for ensuring the realisability of the Reynolds Stress Tensor is that both invariants of the anisotropy tensor are in the closed and bounded space Ω_I defined as:

$$\Omega_I = \left\{ (II, III) \in \mathbb{R}^2, \quad 3\left(\frac{|III|}{2}\right)^{2/3} \leq -II \leq \frac{1}{9}(1 + 27III), III \in \left[-\frac{1}{108}, \quad \frac{2}{27}\right] \right\}$$

For a better analysis, Pope (2000) [↗] proposed a new graphical representation, based on two functions, $\eta(II, III)$ and $\xi(II, III)$ defined as:

$$\eta(II, III) = \sqrt{-\frac{1}{3}II}, \text{ and}$$

$$\xi(II, III) = \left(\frac{1}{3}III\right)^{1/3}.$$

A new space is defined for $\underline{\underline{R}}$ to be realisable. The new two variables need to belong to the following closed set $\Omega_{I'}$:

$$\Omega_{I'} = \left\{ (\eta, \xi) \in \mathbb{R}^2, \quad |\xi| \leq \eta \leq \sqrt{\frac{1}{27} + 2\xi^3}, \quad \xi \in \left[-\frac{1}{6}, \frac{1}{3}\right] \right\}$$

This set is commonly called Lumley's triangle.
In this manuscript, this triangle is studied for the Minibat validation case. For an ease of comparison with the experimental data from the reference (Kuznik, 2005) [↗], a different graphical representation, based on the invariants functions II^* and III^* is used:

$$II^* = 3\sqrt{-II}, \text{ and}$$

$$III^* = 6\left(\frac{1}{2}III\right)^{1/3}.$$

In the reference work, these invariants are used to measure linearly the turbulence anisotropy, which is very useful for studying jets for instance. The Lumley's triangle is modified as well, with new boundaries (see Figure 3.H.1):

$$II^* = \sqrt{1 + \frac{1}{4}III^*}, \quad \text{and}$$

$$II^* = \frac{1}{2}\sqrt{3}|III^*|.$$

At any point and time in a turbulent flow, III^* and II^* can be computed from the Reynolds Stress Tensor and plotted in the $II^* - III^*$ plane. If the point is in the Lumley's triangle, then the Reynolds stress is realisable. Otherwise, every point outside the triangle corresponds to a non realisable Reynolds stress, with negative or complex eigenvalues.

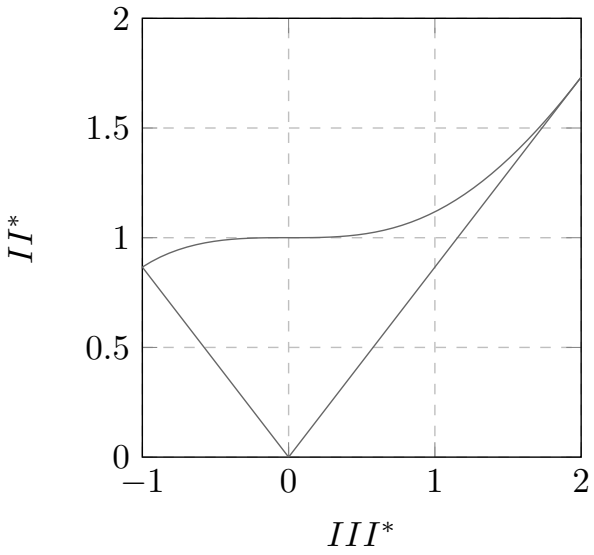

Figure 3.H.1: Lumley's triangle using III^* and II^*.

3.I Synthetic Eddy Method

In this section the Synthetic Eddy Method (SEM), used to generate an unsteady inlet boundary condition in the Minibat LES simulations, is presented.
This method, proposed by Jarrin et al. (2006), consists on generating synthetic eddies in a given zone which fluctuations satisfy statistical moments, provided for instance with a RANS calculation. The synthetic generated eddies in a virtual Cartesian box contribute to a preliminary velocity field (Skillen et al., 2016):

$$u_j^*(\underline{x},t) = \sum_{i=1}^{N} \sqrt{\frac{\Omega_b}{\Omega_i}} \epsilon_j f(x - x_i, \sigma_i). \tag{3.98}$$

where Ω_b and Ω_i are respectively the box and eddy volumes. ϵ is an integer representing the sign of the eddy i.e. $\epsilon = \pm 1$. N is the total number of eddies and f is a shape function, based on the eddy distance to the box centre. σ is the eddy length scale (Integral, Taylor for instance).
The inner product of the fluctuating field $u_j^*(x,t)$ with the Cholesky decomposition of the Reynolds stress tensor forms a velocity field with the prescribed second order statistics and a mean equal to zero. From the mean velocity, denoted here U_i, the new velocity field $u_i(\underline{x},t)$ reads:

$$u_i(x,t) = L_{ij} u_j^*(x,t) + U_i, \tag{3.99}$$

with:

$$\underline{\underline{L}} = \begin{bmatrix} \sqrt{R_{11}} & 0 & 0 \\ R_{21}/L_{11} & \sqrt{R_{22} - L_{21}^2} & 0 \\ \frac{R_{31}}{L_{11}} & \frac{R_{32} - L_{21}L_{31}}{L_{22}} & \sqrt{R_{33} - L_{31}^2 - L_{32}^2} \end{bmatrix}. \tag{3.100}$$

At each time iteration, the eddy positions are updated using the bulk inflow velocity. If an eddy leaves the box, it is automatically regenerated at a random location on the opposite face where it left.
For further information and latest developments on the SEM, the reader may refer to De Laage de Meux et al. (2015) and Duffal (2020).

3.I.1 Example on the Minibat configuration

The SEM impact on the numerical results is illustrated for the Minibat validation test case.
Considering the jet (I), different eddy threshold length scales are tested. Indeed, when creating a SEM structure, the algorithm set a length σ_i to each structure i as:

$$\sigma_i = \min\left\{\max\left\{\frac{(\frac{3}{2}\overline{u_i'^2})^{3/2}}{\varepsilon}, \Delta i\right\}, \delta\right\}. \tag{3.101}$$

Two different SEM simulations are compared to a LES simulation with no SEM. The parameter δ is set first as $\frac{2}{3}r_{in}$ and then as $\frac{1}{2}r_{in}$, with r_{in} the inlet radius. The mean and instantaneous velocities are studied.

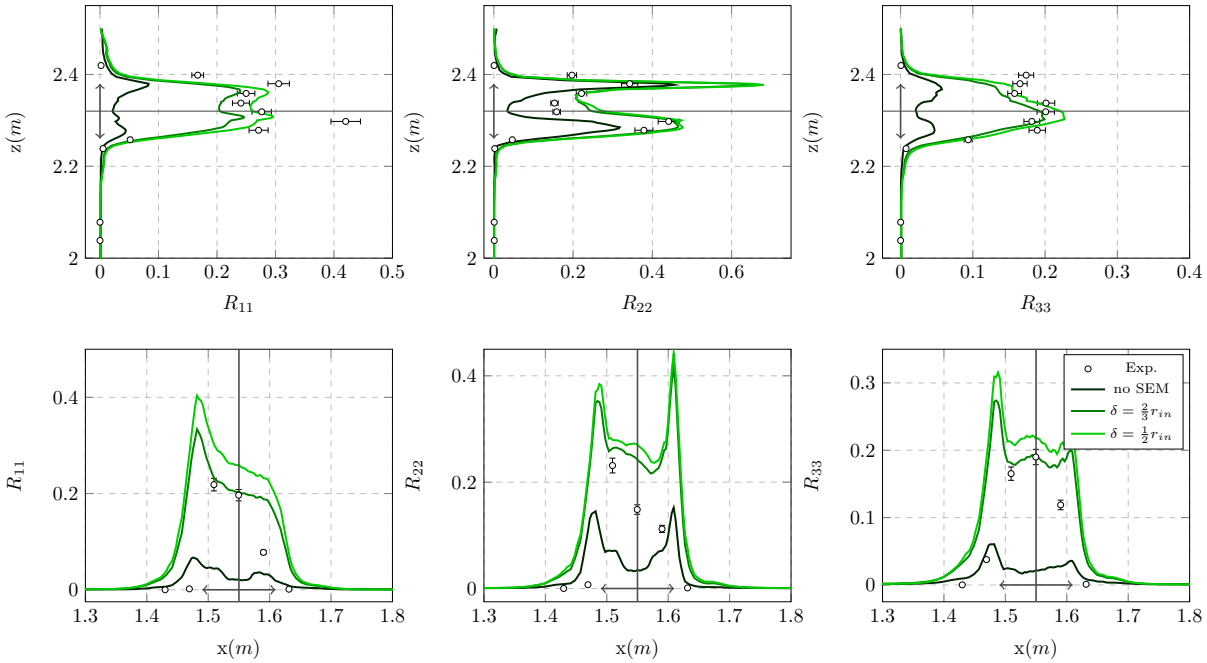

Figure 3.I.1: R_{ii} at $y = 0.6\,\mathrm{m}$ for a simulation without SEM and two simulations with different eddy spatial length threshold values.

Close to the inlet zone (Figure 3.I.1), the SEM leads to instantaneous velocities that are closer to the expected ones than the simulation with no particular treatment regarding the inlet condition. Note that the R_{ii} values are close to zero without SEM. For a more important y value (Figure 3.I.2), the opposite is observed. Both SEM simulations underestimate the R_{ii} amplitudes in both vertical and horizontal profiles, while the simulation with no SEM leads to closer numerical results (even if it slightly overestimates it sometimes).
A better performance can be observed as well concerning the mean velocity for the simulation with no SEM (Figure 3.I.3). Similarly to the instantaneous profiles, the SEM simulations underestimated the velocity when increasing the axial distance from the jet inlet.
Moreover, when keeping the parameter $\delta = 1/3r_{in}$ and refining the mesh to 60.10^6 cells (Figure 3.I.4), one can see that the velocity profiles do not improve, where at $y = 1.5\,\mathrm{m}$ the velocity profile is underestimated.
To conclude on this subsection, even if the SEM allowed a better reproduction of the inlet instantaneous quantities, it led to less accurate global results. Thus, for the simulations presented in Chapter 3, no SEM was used for the inlet flow.

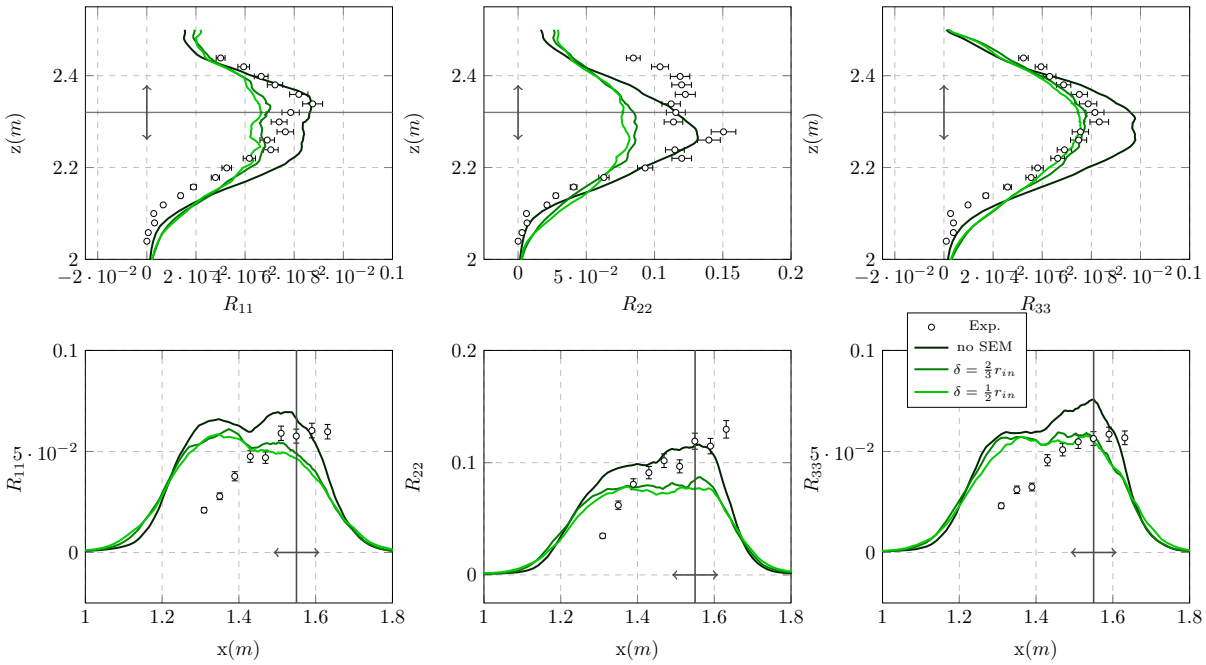

Figure 3.I.2: R_{ii} at $y = 1.5\,\mathrm{m}$ for a simulation without SEM and two simulations with different eddy spatial length threshold values.

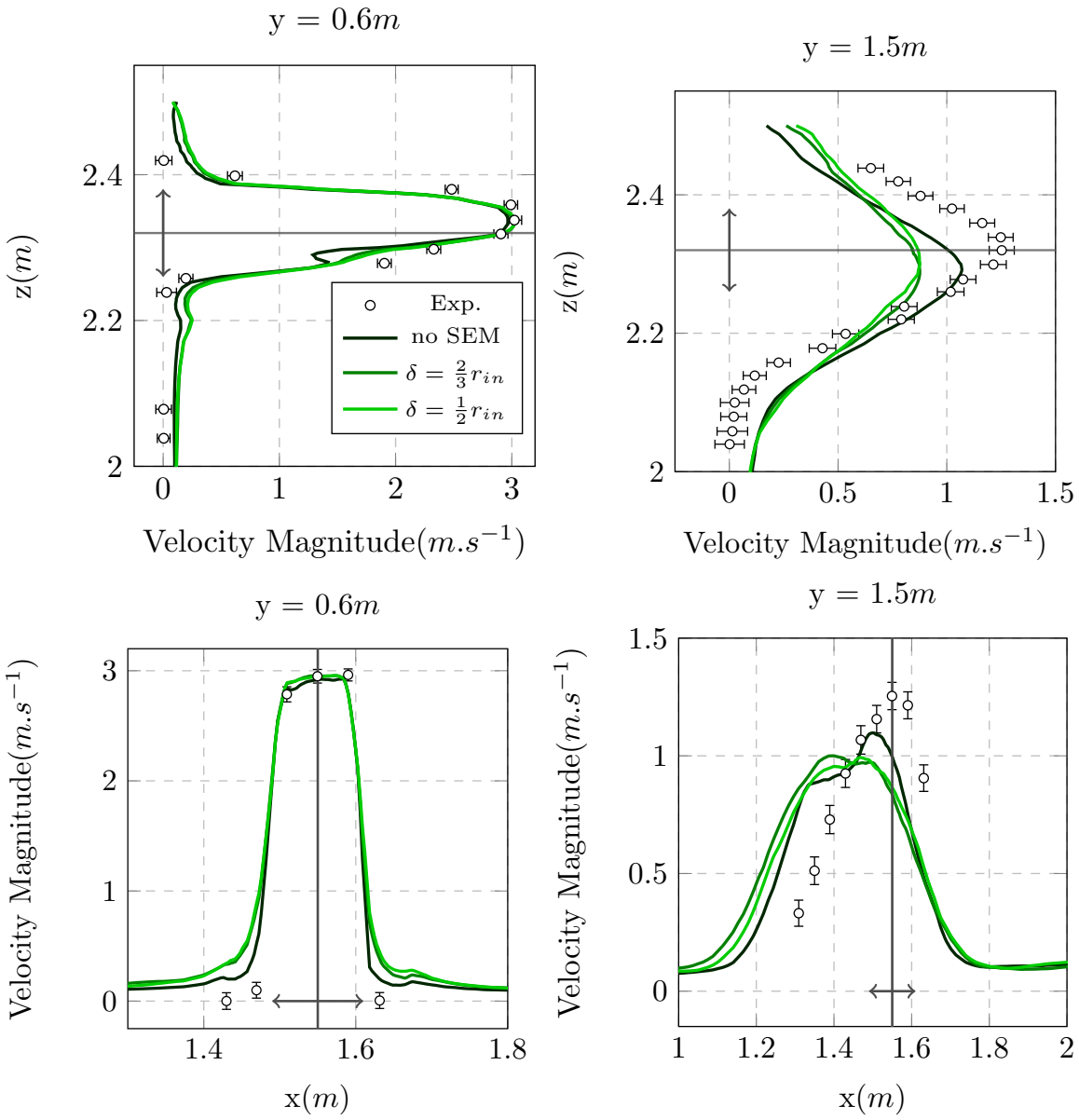

Figure 3.I.3: Vertical and horizontal velocity magnitude profiles for the different simulations.

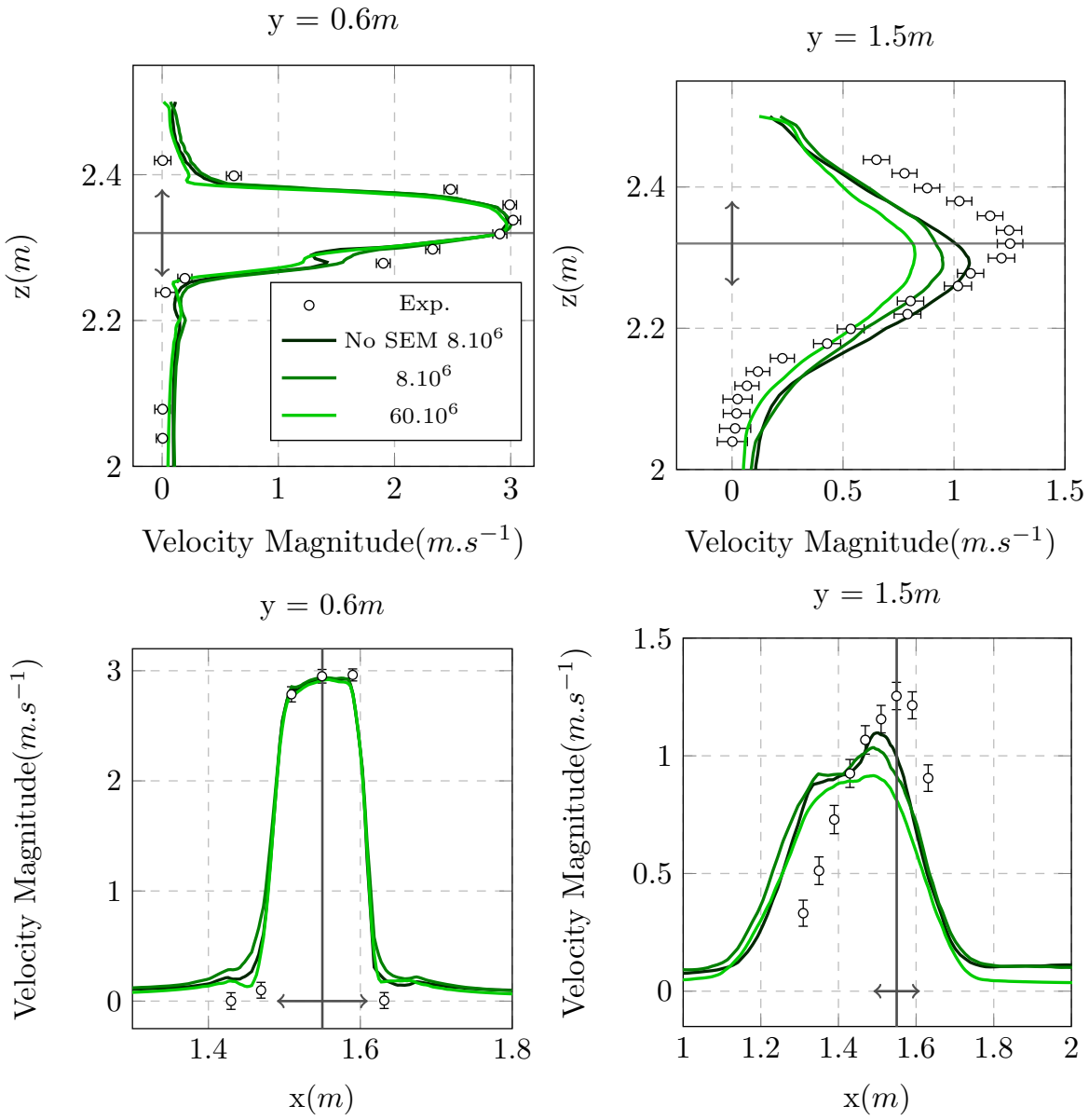

Figure 3.I.4: Vertical and horizontal velocity magnitude profiles for two different mesh refinements with $\delta = 1/3r_{in}$.

3.J Focus on the simulation time

In this section we study the simulation time using both CPC and IPC schemes for different problems. For all simulations, the preconditioned conjugate gradient method is used to solve the different equations (Hager and Zhang, 2006) and a number of inner-iterations of 2 is set.

3.J.1 Minibat configuration

We begin by analysing the time of simulation using the $k - \varepsilon$ model for both numerical schemes.

Solver	**IPC time** (s)	**CPC time** (s)
Temperature	3.3	14.2
Velocity	17.675	16.843
k	2.8	6.93
ε	2.3	2.2
Pressure	124.4	128.0
Total time	238.4	253.9

Table 3.J.1: Minibat isothermal jet. Solvers total simulation time for the CPC and IPC schemes.

Table 3.J.1 shows the total solver time for each variable and for both simulations related to the isothermal jet. 330 s were simulated using a mesh composed of 6 millions hexahedral cells and 99 processors. It can be noticed that the IPC scheme total time of simulation for this isothermal case is slightly (reduction of 7% of the simulation time) faster than the CPC. This difference is due mostly to the temperature and the turbulent kinetic energy solvers, which is at least expected for the first variable, where new terms where implemented. When the jet becomes anisotropic, the thermal effects affect the time of simulation, shown in Table 3.J.2.

Keeping the same physical simulated time and processors, the mesh is now composed of 8 millions cells. Results show that the CPC scheme led to a faster simulation time (40% of simulation time reduction) explained by a gain of 55% in the pressure equation solver time. This can be explained by the reinforcement of the diagonal of the Helmholtz equation system, which accelerates the system resolution. Again, the time of the thermal equation solver is highly increased, but remains relatively small related to the pressure equation gain of time.

A focus on the diagonal reinforcement would lead to a better understanding of this simulation time reduction.

Lastly, Figure 3.J.1 presents for the isothermal jet and the CPC scheme the total time per iteration of three turbulence approaches simulations. Results show a faster simulation performed by the $k-\varepsilon$ model, which is expected. The $R_{ij} - \varepsilon$ and LES simulations present relatively close time per iterations.

Solver	**IPC time** (s)	**CPC time** (s)
Temperature	19.3	30.6
Velocity	94.251	87.0
k	53.8	50.9
ε	29.3	23.9
Pressure	4341.7	2451.6
Total time	5066.5	3131.7

Table 3.J.2: Minibat hot jet. Solvers total simulation time for the CPC and IPC schemes.

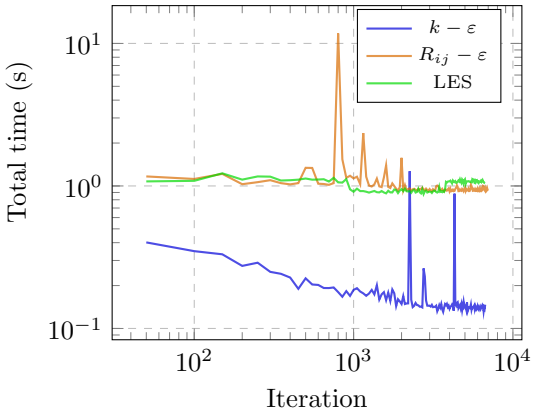

Figure 3.J.1: Total time of simulation per iteration using the CPC scheme for three turbulence approaches.

3.J.2 Natural convection cavity

The same comparison is performed for the natural convection validation case, where 2.5 seconds are simulated using a mesh composed of 10^4 hexahedral cells and 10 processors. This goal here is to observe the simulation time for an enclosed system with buoyant effects. Table 3.J.3 shows that the CPC scheme led to a longer simulation, similarly to the isothermal jet study on the Minibat configuration. A small gain of time is observed for the pressure equation which is far exceeded by the temperature time of simulation (increased by a factor 10). This can be explained by the importance of the thermal effects in this test case. Even if a pressure variation was observed in this case reference numerical results, the reduction of the pressure equation solving time seems to be partially related to the presence of in and outlets.

3.J.3 Coubertin stadium

Lastly two simulations are performed for the Pierre de Coubertin stadium. This time the jets are isothermal and we focus on a case with numerous inlets and outlets. The mesh presented in Chapter 5, composed of 2 millions of cells, is used, using 150 processors to simulate 100 physical seconds. Again, the CPC and IPC scheme are compared using the $k-\varepsilon$ model. The hypothesis of the link between the reduction of the simulation time and the presence of inlet and outlets can be confirmed by

Solver	**IPC time** (s)	**CPC time** (s)
Temperature	1.7	17.8
Velocity	36.5	52.9
Pressure	31.1	28.9
Total time	70.6	101.0

Table 3.J.3: Natural convection cavity. Solvers total simulation time for the CPC and IPC schemes.

the results represented in Table 3.J.4. The gain of simulation is about a factor 10, which is mostly due to the pressure equation solve. This shows the importance of further studies related to the impact of boundaries conditions, specially those with mass fluxes, on the pressure field.

Solver	**IPC time** (s)	**CPC time** (s)
Temperature	1.17	3.3483
Velocity	10.4	11.8
k	2.38	2.84
ε	2.6	3.0
Pressure	2143.5 (2096.2)	195.1
Total time	2206.4	260.4

Table 3.J.4: Coubertin stadium, isothermal ventilation. Solvers total simulation time for the CPC and IPC schemes.

3.J.4 Conclusion

This conclusion is representative of the few test cases studied. For the author, many points remain to be investigated related to the impact of the numerical scheme on the simulation time. Since this stake is very important in an industrial context, some exploratory results showed that the time of simulation is affected by the numerical scheme mainly in two equations.
First, the thermal equation resolution time is increased due to the new terms implemented. Then, the pressure equation is globally solved faster in the correction step. Yet, the degree of gain of time seems to be related to two main factors. A possible dependence of the presence of thermal effects was shown in the hot jet for the Minibat configuration. On the other hand, for an enclosed cavity with buoyant effects, no time was gained in the pressure equation step. A possible impact of the boundary conditions, specially inlets and/or outlets is to be investigated: indeed, an important reduction of the time of resolution of the pressure equation was observed for the Coubertin Stadium simulations.

CHAPTER 4

Scheme extension to moist air

Résumé

Ce chapitre présente l'extension du schéma développé pour l'air sec à l'air humide. Comme mentionné à la section 2.3, l'humidité est omniprésente en environnements intérieurs. En termes physiques, les propriétés du fluide sont affectées et un éventuel changement de phase peut avoir lieu. En termes numériques, l'objectif est de préserver les propriétés numériques du schéma proposé au chapitre précédent. Ce chapitre est structuré de la manière suivante. Après une introduction concernant les différents modèles existants pour la modélisation d'écoulements d'air humide avec changement de phase, les équations continues du mélange considéré sont écrites. Ensuite, leur discrétisation en espace et en temps est présentée, suivie par une analyse numérique et la vérification du nouveau schéma en temps.

4.1 Introduction

Flows with different phases are widely found in many industrial applications such as transport systems (pipeline transport, air-lift pumps...), geo-meteorological phenomena (sedimentation, rain droplets), power systems (pressurised water in nuclear reactors, boilers and evaporators), among others, including the indoor environment (moisture studies, electronic cooling systems, air conditioners, refrigerators).
According to the combination of the two phases the flow can be characterised either as a gas-solid, gas-liquid, liquid-solid or liquid-liquid mixtures. In this chapter, the focus is only made on the water effect on the airflow i.e. a gas-gas-liquid mixture. In that scope, three classes of flow are defined, according to the problem geometry and configuration: separated (atomisation, jet condenser, film condensation), transitional (steam generator, boiling reactor channel) and dispersed (chemical reactors, spray cooling) flows (see Ishii and Hibiki (2010) for a more detailed description of each class).
In this manuscript, we are interested in dispersed flows and more particularly in the droplet flow typical regime, corresponding to liquid droplets in gas.
When it comes to simulate moist airflow with phase change, one may differentiate the homogeneous and the two fluid models. The first considers the fluid as an unique pseudo compound, a mixture, composed of both air and water components (Downar-Zapolski et al., 1996; Clerc, 2000; Hurisse, 2017) ; therefore, the flow can be treated as if it had one phase, leading to a simplified set of equations. The second solves equations for both gas and liquid phases separately, which can be computationally more expensive but is more accurate when the phasic disequilibrium is important (Hérard and Hurisse, 2012) . In the homogeneous models framework, if the fluid components are ideal gases, the mixture thermodynamic expressions, such as the density, can be written as combinations of analytic formulas.
Section 2.2 presented the importance of accounting humidity for indoor flow simulations. For instance, this is useful when studying ventilation scenarios (Liu et al., 2004) , historical buildings and art conservation (D'Agostino et al., 2014; D'Agostino and Congedo, 2014) or indoor air quality (Heseltine and Rosen, 2009; Wolkoff, 2018) . Concerning the numerical methods used for moisture in CFD simulations, Gan and Awbi (1994) studied the air quality of a ventilated room by considering a same water vapor pressure for all cells. Teodosiu et al. (2003) proposed a moisture transport model included in the CFD simulation which used a first order SIMPLE scheme. The transport of the vapour of water mass fraction was performed and the Dalton (1802) law was used to determine the mixture density, composed of dry air and vapour. Kilic and Sevilgen (2008) used a thermo-physiological model (Gagge et al., 1986) to study the moisture transport around a standing human body and validate it against experimental data.
Finally, Lu and Viljanen (2009) used neural networks to predict both temperature and relative humidity quantities in an indoor environment.
Note that another important numerical stake when simulating moist air is the heat and moisture transfer in building envelopes, considered as porous media. Given the complexity of this process and the focus of this thesis related to the flow transport, this issue is out of the scope of this chapter (for further, a heat and moisture transfer model is presented and applied in Lü (2002a,b) .
Yet, any of the previous cited work do take account of a possible water phase change in the flow (condensation in walls, modelled by laws exist (Ambrosini et al., 2005; Zschaeck et al., 2014)) except Teodosiu et al. (2003) model, extended to surface and volume condensation (Teodosiu, 2013) . Even if in most of the indoor studies no phase change occurs, a part of the system can sometimes reach saturation. This happens by two major factors. The first one is by adding moisture sources in the system, that can be for instance a high concentration of occupants (classroom, theatre) or by the presence of a sink or shower. Also, in some cases (mostly industrial) the environment conditions may lead to a high variability of the temperature and pressure, leading to a phase change. Condensation can thus be

deposited in the structures or walls, which may, according to its presence time, lead to material damage and to the emissions of other pollutant species, such as VOC.
The present chapter introduces an homogeneous model for moist air implemented in the previously introduced dry air scheme for indoor airflow applications. The fluid is composed of dry air, water vapor and depending on the context, liquid water and uses a strategy similar to Teodosiu et al. (2003), where the mixture pressure is computed using the Dalton law. A particular attention is given to the saturation state; in order to stay in the range of homogeneous models and given the indoor scope of studies related to the scheme, in case of presence of liquid water, it is assumed that its volume fraction is small compared to the others. The numerical choices made in this chapter have the main goal to modify the less possible the properties of the dry air scheme, such as the time staggered variables arrangement, the solve of the Helmholtz equation for the pressure and the conservation of the total energy while adding a new transport equation and accounting for a possible phase change.
The outline of the chapter is the following. The governing equations, based on Satoh (2013) are first introduced, followed by the scheme space and time discretisation and the numerical strategy to take into account saturation. Then, a numerical analysis is performed on the scheme properties. Next, the solution of the Riemann problem is derived for the moist air set of equations, used by the verification process carried out right after.

4.2 Governing equations

An homogeneous mixture of air (a) and water in liquid (l) and vapor (v) phases is considered at the same velocity $\underline{u}$ and temperature T. An additional transport equation for the total water mass fraction is solved. In the indoor airflow framework, the hypothesis is made of a negligible water liquid volume fraction α_l compared to the others.
The compressible Navier–Stokes equations are written for each mixture component. Then, the three equations are summed leading to the mixture governing equations used to design the moist air time scheme (see Appendix 4.A for the derivation):

$$
\begin{aligned}
&(a)\ \frac{\partial \rho}{\partial t} + \text{div}\left(\underline{q}\right) = 0,\\
&(b)\ \frac{\partial \underline{q}}{\partial t} + \underline{\text{div}}\left(\underline{u}\otimes\underline{q}\right) = -\underline{\nabla} p + \underline{\text{div}}\left(\underline{\underline{\tau}}\right) + \underline{f},\\
&(c)\ \frac{\partial\left(\rho\, e\right)}{\partial t} + \text{div}\left(e\underline{q}\right) = -p\text{div}\left(\underline{u}\right) + \underline{\underline{\tau}} : \underline{\underline{\nabla u}} + \text{div}\left(\lambda\underline{\nabla} T\right),\\
&(d)\ \frac{\partial\left(\rho\, y_w\right)}{\partial t} + \text{div}\left(y_w\underline{q}\right) = \text{div}\left(K\underline{\nabla} y_w\right),\\
&(e)\ p = p_a + p_v = \rho R_a T\left[1 - y_w + y_v(p,T)\epsilon_m^{-1}\right],\\
&(f)\ e(y_w,p,T) = c_{v_m}(y_w,p,T)T + y_v(p,T)L_{00}.
\end{aligned}
\tag{4.1}
$$

ρ is the mixture density, $\underline{q} = \rho\underline{u}$ its momentum and e its internal energy. The mixture total water mass fraction is denoted y_w, with $y_w = y_v + y_l$ and $y_a + y_w = 1$. The mixture pressure p (Equation (4.1), (e)) is the sum of the partial pressures of dry air and water vapor following the Dalton (1802) law.

$$
\epsilon_m = \frac{R_a}{R_w} = 0.62197 \tag{4.2}
$$

is the ratio between the molar masses of water ($R_w = 461.500\,\text{J}\,\text{kg}^{-1}\text{K}^{-1}$) and dry air ($R_a = 287.058\,\text{J}\,\text{kg}^{-1}\text{K}^{-1}$). $\underline{f}$ and $\underline{\underline{\tau}}$ are respectively the external forces field and the shear stress tensor whose expressions are the same as Equation (2.2). $R_a = R/M_a$ is the specific dry air constant. The mixture temperature is directly linked to the internal energy through Equation (4.1), (f), where c_{v_m} is the mixture

heat capacity defined as:

$$c_{v_m}(y_w, p, T) = (1 - y_w)c_{va} + y_v(p, T)c_{vv} + y_l c_{vl}. \tag{4.3}$$

c_{va}, c_{vv} and c_{vl} are respectively the specific heat capacities of the dry air, vapor and liquid water, assumed constant in this chapter and whose expression (Satoh, 2013) reads:

$$c_{va} = c_{pa} - R_a, \qquad c_{vv} = c_{pv} - R_w, \qquad c_{vl} = c_{pl}. \tag{4.4}$$

Where:

$$\begin{aligned} c_{pa} &= \frac{7R_a}{2} = 1004.6\,\mathrm{J\,kg^{-1}\,K^{-1}}, \\ c_{pv} &= 4R_w = 1846\,\mathrm{J\,kg^{-1}\,K^{-1}}, \\ c_{pl} &= 4218\,\mathrm{J\,kg^{-1}\,K^{-1}}. \end{aligned} \tag{4.5}$$

L_{00} is the water latent heat related to the reference temperature $T_0 = 273.15\,\mathrm{K}$ and reads $L_{00} = L_0 - (c_{pv} - c_{pl})T_0$, with $L_0 = 2.5.10^6\mathrm{J\,kg^{-1}}$.

Remark 4.2.1. The fluid properties such as the molecular viscosity μ, thermal conductivity λ, heat capacities c_{vi} and scalar diffusivity K are considered constant in this chapter. These parameters variation, according to the situation, need to be accounted for. Appendix 4.B presents some models related to these properties proposed in the literature. The variability of these properties is let to further implementations complementary to those made in this chapter.

4.2.1 Saturation treatment

A numerical strategy is set up to take into account the saturation. Note that only the phase change between the water liquid and vapor phases is considered. Outside the saturation regime, the vapor of water mass fraction is equal to the total water mass fraction value i.e. $y_v(p, T) = y_w$.
Otherwise, its value $y_v(p, T)$ depends on both pressure and temperature and is calculated using the humidity ratio at saturation, denoted $x_s(p, T)$:

$$y_v(p, T) = \frac{x_s(p, T)}{1 + x_s(p, T)}, \tag{4.6}$$

where:

$$x_s(p, T) = \frac{\epsilon_m p_s(T)}{p - p_s(T)}, \tag{4.7}$$

with:

$$p_s(T) = \exp\left(A + \frac{B(T - T_0)}{C + (T - T_0)}\right) \tag{4.8}$$

the pressure at saturation calculated using the Antoine (1888) law, with $T_0 = 273.15\,\mathrm{K}$. The constants are set as $A = 6.4147\ln(\mathrm{Pa})$, $B = 17.438\ln(\mathrm{Pa})$ and $C = 239.78\,\mathrm{K}$. The final saturation vapor mass fraction reads:

$$y_v(p, T) = \frac{\epsilon_m p_s(T)}{p - (1 - \epsilon_m)p_s(T)}. \tag{4.9}$$

Remark 4.2.2. The expression for the vapor pressure at saturation (Equation (4.8)) is equivalent to the Antoine law:

$$\ln(p_s(T)) = A - \frac{B}{C + T - T_0}. \tag{4.10}$$

Note that $p_s(T)$ can be calculated in mmHg, Pa or bar, depending on the coefficient units. Its formula uses either the temperature in Kelvin or in Celsius and be written using log_e or log_{10}. Figure 4.2.1 compares Equation (4.8) with two other versions of Antoine equation with different coefficients based respectively on Banat (1994) and Bridgeman and Aldrich (1964). In the indoor temperature range (273 to 330 K), the three equations lead to very close results.

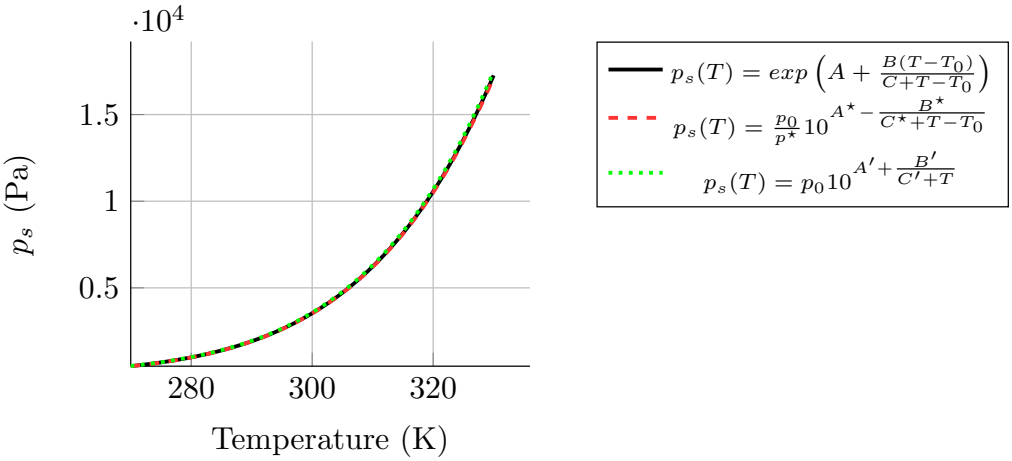

Figure 4.2.1: Comparison between the Antoine law expression for the saturation pressure used in this manuscript and the original law expression. $p_0 = 101325$ Pa is the reference pressure and $p^\star = 760$ mmHg. Coefficients with * are $A^\star = 8.07131$ ln(mmHg), $B^\star = 1730.63$ ln(mmHg) K and $C^\star = 233.426$ K, from Banat (1994). Coefficients with $'$ are $A' = 5.40221$ ln(Pa), $B' = 1838.675$ ln(Pa) and $C' = -31.737$ K, from Bridgeman and Aldrich (1964).

Remark 4.2.3. Equation (4.9) results from

- The definition of the absolute humidity ratio $x_s(p,T) = \dfrac{y_s(p,T)}{y_a}$ i.e. $y_s(p,T) = \dfrac{x_s(p,T)}{1 + x_s(p,T)}$, where $y_s(p,T)$ is the vapor of water mass fraction at saturation.
- The relation between the absolute and relative humidity:

  $$x_s(p,T) = \frac{M_w}{M_a} \frac{p_s(T)}{p - p_s(T)}.$$

  This comes from the definition of the absolute humidity:

  $$x(p,T) = \frac{m_w}{m_a} = \frac{y_v(p,T)}{y_a}.$$

Applying the equation of state considered yields

$$x(p,T) = \frac{R_a}{R_w}\frac{p_v(T)}{p_a(p,T)} = \epsilon_m \frac{p_v(T)}{p - p_v(T)}.$$

At saturation, $x = x_s$ and $p_v = p_s$.

4.3 Space and time discretisation

The time staggered scheme presented in the last chapter (Amino et al., 2022) is extended to an ideal gas mixture with a small volume fraction of liquid. The iterative process with inner-iterations and the global main steps before introduced are retained. However, some modifications are made and are highlighted here. The time step Δt is supposed constant in this section.

Initialisation: for $k = 1$, no changes are applied regarding the dry air scheme, excepted the addition of the initial total water mass fraction $y_{w,c}^{n+1,0} = y_{w,c}^{n}$.

Sub-iterations for $k \in [1, M-1]$:

Buoyant scalars step: The water mass fraction $y_w^{n+1,k}$ is computed by solving its transport equation in the interval $[n, n+1]$:

$$\frac{\rho_c^{n+1,k-1} y_{w,c}^{n+1,k} - \rho_c^{n,k-1} y_{w,c}^{n}}{\Delta t} + \mathrm{Div}_c\left(\left\langle \Theta\left(y_w^n,\, y_w^{n+1,k}\right)\right\rangle_f \underline{q}_f\Big|_n^{n+1,k-1}\right) = \mathrm{Lap}_c\left(K, \underline{\nabla}\Theta\left(y_w^n,\, y_w^{n+1,k}\right)\right). \tag{4.11}$$

Remark 4.3.1. The face terms ψ_f and $\langle . \rangle_f$ remain to be spatially discretised.

The equation for the internal energy, also solved in $[n, n+1]$ remains unchanged (including the kinetic energy source term $\Gamma_c^{u^2/2}\Big|_n^{n+1,k-1}$):

$$\frac{\rho_c^{n+1,k-1} e_c^{n+1,k} - \rho_c^{n,k-1} e_c^{n}}{\Delta t} + \mathrm{Div}_c\left(\left\langle \Theta\left(e^n,\, e^{n+1,k}\right)\right\rangle_f \underline{q}_f\Big|_n^{n+1,k-1}\right) = \mu(S_c^2)^{n+\theta,k-1} + \Gamma_c^{u^2/2}\Big|_n^{n+1,k-1}$$
$$+ \mathrm{Lap}_c\left(\lambda, \Theta\left(T^n,\, T^{n+1,k-1}\right)\right) - \mathrm{Div}_c\left(\left\langle \Theta\left(p^n,\, p^{n+1,k-1}\right)\underline{u}^{n+\theta,k-1}\right\rangle_f\right) + \underline{u}_c^{n+\theta,k-1}\cdot\underline{\nabla}_c p\Big|_{n-1+\theta}^{n+\theta,k-1}. \tag{4.12}$$

Note that the temperature on the diffusive right-hand-side of the equation is explicited for implementation reasons.
The mixture temperature $T^{n+1,k}$ is then computed from the mixture internal energy $e^{n+1,k}$ using Equation (4.1), (f). In case of non-saturation, its expression is straightforward, with $y_v = y_w$:

$$T_c^{n+1,k} = \frac{e_c^{n+1,k} - y_{w,c}^{n+1,k} L_{00}}{(1 - y_{w,c}^{n+1,k})c_{va} + y_{w,c}^{n+1,k} c_{vv}}. \tag{4.13}$$

In case of saturation, a constant pressure $p^{n+1,k-1}$ and total water mass fraction $y_{w,c}^{n+1,k}$ are considered. Then, the internal energy expression is written as a function of $T_c^{n+1,k}$:

$$e_c^{n+1,k} = \left[(1 - y_{w,c}^{n+1,k})c_{va} + y_v(p_c^{n+1,k-1}, T_c^{n+1,k})c_{vv} + (y_{w,c}^{n+1,k} - y_v(p_c^{n+1,k-1}, T_c^{n+1,k}))c_{vl}\right] T_c^{n+1,k}$$
$$+ y_v(p_c^{n+1,k-1}, T_c^{n+1,k}) L_{00},$$

(4.14)

with:

$$
\begin{aligned}
y_v(p_c^{n+1,k-1}, T_c^{n+1,k}) &= \frac{\epsilon_m p_s(T_c^{n+1,k})}{p_c^{n+1,k-1} - (1-\epsilon_m)\, p_s(T_c^{n+1,k})}, \\
p_s(T_c^{n+1,k}) &= \exp\left(A + \frac{B(T_c^{n+1,k} - T_0)}{C + T_c^{n+1,k} - T_0}\right).
\end{aligned}
\tag{4.15}
$$

T_0 is the reference temperature fixed here as $273.15\,\mathrm{K}$. Equation (4.14) is then solved for T using the Newton method (Equation (4.16)). Thus, an iterative process inside the inner iteration, denoted by the superscript l, is performed to compute the temperature at a given precision (absolute error, fixed by the user and denoted $\varepsilon_{e_0} = 10^{-4}$, by default):

$$
T_c^{n+1,k,l} = \frac{e_c^{n+1,k} - e(y_{w,c}^{n+1,k}, T_c^{n+1,k,l-1}, p_c^{n+1,k-1})}{\left.\dfrac{\partial e}{\partial T}\right|_{y_w}\left(y_{w,c}^{n+1,k}, T_c^{n+1,k,l-1}, p_c^{n+1,k-1}\right)} + T_c^{n+1,k,l-1}. \tag{4.16}
$$

The initial temperature $T^{n+1,k,0}$ and internal energy $e^{n+1,k,0}$ depend on the previous cell state (i.e. saturated or not). Algorithm 3 and Figure 4.3.1 details this methodology. Note that a study concerning the Newton method convergence is made in the first verification case.

Remark 4.3.2. The internal energy derivative related to the temperature reads:

$$
\begin{aligned}
\left.\frac{\partial e}{\partial T}\right|_{y_w}(y_w, p, T) =& (1-y_w)c_{va} + y_w c_{vl} + \frac{\epsilon_m(c_{vv} - c_{vl})}{p(p_s(T))^{-1} - (1-\epsilon_m)} \\
&- \frac{\epsilon_m[L_{00} + T(c_{vv} - c_{vl})]}{[p(p_s(T))^{-1} - (1-\epsilon_m)]^2}\left(\left.\frac{\partial p}{\partial T}\right|_{y_w,e}(p_s(T))^{-1} - \frac{BC(p_s(T))^{-1}}{(C+T-T_0)^2}\right)
\end{aligned}
\tag{4.17}
$$

where:

$$
\left.\frac{\partial p}{\partial T}\right|_{y_w,e} = -\left.\frac{\partial e}{\partial T}\right|_{y_w,p}\left(\left.\frac{\partial e}{\partial p}\right|_{y_w,T}\right)^{-1}. \tag{4.18}
$$

Proof: the internal energy is supposed constant during the Newton method i.e.:

$$
\left.\mathrm{d}e(p,T)\right|_{y_w,e} = 0 = \left.\frac{\partial e}{\partial T}\right|_{y_w,p}\mathrm{d}T + \left.\frac{\partial e}{\partial p}\right|_{y_w,T}\mathrm{d}p \Leftrightarrow \mathrm{d}p = -\left(\left.\frac{\partial e}{\partial p}\right|_{y_w,T}\right)^{-1}\left.\frac{\partial e}{\partial T}\right|_{y_w,p}\mathrm{d}T. \tag{4.19}
$$

Note that:

$$
\begin{aligned}
\left.\frac{\partial e}{\partial T}\right|_{y_w,p}(y_w, T, p) =& c_{va}(1-y_w) + c_{vl}y_w + \frac{\epsilon_m\, B\, C\, p\,(L_{00} - c_{vl}T + c_{vv}T)\, p_s(T)^{-1}}{(C+T-T_0)^2\,(p\, p_s(T)^{-1} - (1-\epsilon_m))^2} \\
&+ \frac{\epsilon_m(c_{vv} - c_{vl})}{p\, p_s(T)^{-1} - (1-\epsilon_m)}.
\end{aligned}
\tag{4.20}
$$

and:

$$
\left.\frac{\partial e}{\partial p}\right|_{y_w,T}(y_w, p, T) = \frac{-(p_s(T))^{-1}\epsilon_m[L_{00} + T(c_{vv} - c_{vl})]}{[p(p_s(T))^{-1} - (1-\epsilon_m)]^2}. \tag{4.21}
$$

The mass fractions $y_{v,c}^{n+1,k} = y_v(p_c^{n+1,k-1}, T_c^{n+1,k})$ and $y_l^{n+1,k} = y_{w,c}^{n+1,k} - y_{v,c}^{n+1,k}$ are then updated using the new temperature value.
The intermediate density is then calculated using the equation of state:

$$\widetilde{\rho}_c^k = \frac{p_c^{n+1,k-1}}{R_a T_c^{n+1,k-1}\left[1 - y_{w,c}^{n+1,k} + y_v(p_c^{n+1,k-1}, T_c^{n+1,k})\epsilon_m^{-1}\right]}. \tag{4.22}$$

Again, the new density is not balanced by the mass flux yet. The mass conservation is insured in the correction step.

Prediction step: No changes are made in the prediction step, where the intermediate velocity $\widetilde{\underline{u}}$ is obtained by solving the momentum equation in the interval $[n-1+\theta, n+\theta]$:

$$\begin{aligned}&\frac{\Theta\left(\rho_c^n,\, \rho_c^{n+1,k-1}\right)\widetilde{\underline{u}}_c^k - \Theta\left(\rho_c^{n-1},\, \rho_c^{n,k-1}\right)\underline{u}_c^{n-1+\theta}}{\Delta t} + \mathrm{Div}_c\left(\left\langle \Theta\left(\underline{u}^{n-1+\theta},\, \widetilde{\underline{u}}^k\right)\right\rangle_f \otimes \underline{q}_f\Big|_{n-1+\theta}^{n+\theta,k-1}\right)\\ &= -\underline{\mathrm{Grad}}_c\left(\left\langle p|_{n-1+\theta}^{n+\theta,k-1}\right\rangle_f\right) + \underline{\mathrm{Div}}_c\left(\underline{\underline{\tau}}_f^k\right) + \underline{f}_c\Big|_{n-1+\theta}^{n+\theta,k-1}.\end{aligned} \tag{4.23}$$

Correction step: The Helmholtz equation for the pressure is solved for the pressure increment $\phi^k = p|_{n-1+\theta}^{n+\theta,k} - p|_{n-1+\theta}^{n+\theta,k-1}$ and is the same compared to the dry air scheme. The following equations are combined in the interval $[n, n+1]$:

$$\begin{cases} \dfrac{\Theta\left(\rho_c^n,\, \rho_c^{n+1,k}\right)\underline{u}_c^{n+\theta,k} - \Theta\left(\rho_c^n,\, \rho_c^{n+1,k-1}\right)\widetilde{\underline{u}}_c^k}{\Delta t} + \underline{\nabla}_f\phi^k = \delta\underline{f}_c^k, \\ \mathrm{Div}_c\left(\underline{q}_f\Big|_n^{n+1,k}\right) + \dfrac{\rho_c^{n+1,k} - \rho_c^n}{\Delta t} = 0, \end{cases} \tag{4.24}$$

with

$$\delta\underline{f}_c^k = \underline{f}_c\Big|_{n-1+\theta}^{n+\theta,k} - \underline{f}_c\Big|_{n-1+\theta}^{n+\theta,k-1}$$

and:

$$\underline{q}_f\Big|_n^{n+1,k} = \left\langle \Theta\left(\rho^n,\, \rho^{n+1,k}\right)\underline{u}^{n+\theta,k}\right\rangle_f = \left\langle \Theta\left(\rho^n,\, \rho^{n+1,k-1}\right)\widetilde{\underline{u}}^k\right\rangle_f - \Delta t\left(\underline{\nabla}_f\phi^k - \delta\underline{f}_c^k\right), \tag{4.25}$$

leading to:

$$\begin{aligned}\frac{\rho_c^{n+1,k} - \rho_c^n}{\Delta t} - \theta\mathrm{Lap}_c\left(\Delta t, p^{n+1,k}\right) = &-\mathrm{Div}_c\left(\left\langle \Theta\left(\rho^n,\, \rho^{n+1,k-1}\right)\widetilde{\underline{u}}^k + \Delta t\left(\underline{\nabla} p|_{n-1+\theta}^{n+\theta,k-1} + \delta\underline{f}^k\right)\right\rangle_f\right)\\ &+ (1-\theta)\mathrm{Lap}_c\left(\Delta t, p|_{n-2+\theta}^{n-1+\theta}\right).\end{aligned} \tag{4.26}$$

The pressure $p_c^{n+1,k}$ is linked to ϕ_c^k through:

$$\phi_c^k = \Theta\left(p_c|_{n-2+\theta}^{n-1+\theta},\, p_c^{n+1,k}\right) - p_c|_{n-1+\theta}^{n+\theta,k-1}. \tag{4.27}$$

It is reminded that the thermodynamical pressure $p_c^{n+1,k}$ is distinguished from the mechanical pressure $p_c|_{n-1+\theta}^{n+\theta,k}$ which contributes to the momentum equation. The non change of the Helmholtz is a direct consequence of the form of the mixture equation of state, which can be linearised (considering a total

water mass fraction and internal energy constant in the correction step) and used to correct the density $\rho^{n+1,k}$:

$$\rho_c^{n+1,k} = \widetilde{\rho_c}^{\,k} + \left(p_c^{n+1,k} - p_c^{n+1,k-1}\right)\left(\left.\frac{\partial\rho}{\partial p}\right|_{y_w,e}\left(y_{w,c}^{n+1,k}, T_c^{n+1,k}, p_c^{n+1,k-1}\right)\right). \tag{4.28}$$

where:

$$\left.\frac{\partial\rho}{\partial p}\right|_{y_w,e}(y_w,T,p) = \begin{cases} \dfrac{1}{R_a T\left[1 - y_w + y_w\epsilon_m^{-1}\right]}, & \text{without saturation. Else:} \\ -\left.\dfrac{\partial\rho}{\partial T}\right|_{y_w,p}\left(\left.\dfrac{\partial e}{\partial T}\right|_{y_w,p}\right)^{-1}\left.\dfrac{\partial e}{\partial p}\right|_{y_w,T} + \left.\dfrac{\partial\rho}{\partial p}\right|_{y_w,T}. \end{cases} \tag{4.29}$$

The expressions of the saturation pressure $p_s(T)$ and vapor fraction at saturation $y_v(p,T)$ are given respectively by Equations (4.10) and (4.9). In case of saturation, the vapour mass fraction depends on the temperature and the pressure. Thus, the correction of the pressure is followed by the update of $\rho_c^{n+1,k}$, $\underline{u}_c^{n+\theta,k}$ and of the couple $T_c^{n+1,k}$ and $y_{v,c}^{n+1,k}$. The two last variables are corrected by performing the Newton method presented in the buoyant scalars step by the Equations (4.13), (4.14), (4.15) and (4.16). However Equation (4.14) is solved using $e^{n+1,k}$ and the new pressure $p^{n+1,k}$.

Remark 4.3.3.

$$\left.\mathrm{d}\rho\right|_{y_w,e}(p,T) = \left.\frac{\partial\rho}{\partial T}\right|_{y_w,p} dT + \left.\frac{\partial\rho}{\partial p}\right|_{y_w,T} dp. \tag{4.30}$$

one wants $\left.\dfrac{\partial\rho}{\partial p}\right|_{y_w,e}$. The internal energy is supposed constant in the correction step. Thus, $\mathrm{d}e(p,T) = 0$, i.e.:

$$\left.\frac{\partial e}{\partial T}\right|_{y_w,p}\mathrm{d}T = \left.\frac{\partial e}{\partial p}\right|_{y_w,T}\mathrm{d}p,$$

which yields:

$$\mathrm{d}T = -\left(\left.\frac{\partial e}{\partial T}\right|_{y_w,p}\right)^{-1}\left.\frac{\partial e}{\partial p}\right|_{y_w,T}\mathrm{d}p.$$

From Equation (4.30),

$$\left.\frac{\mathrm{d}\rho}{\mathrm{d}p}\right|_{y_w,e} = -\left.\frac{\partial\rho}{\partial T}\right|_{y_w,p}\left(\left.\frac{\partial e}{\partial T}\right|_{y_w,p}\right)^{-1}\left.\frac{\partial e}{\partial p}\right|_{y_w,T} + \left.\frac{\partial\rho}{\partial p}\right|_{y_w,T}. \tag{4.31}$$

The next step is to express the derivatives. Equation (4.20) and (4.21) defines $\left.\dfrac{\partial e}{\partial T}\right|_{y_w,p}$ and $\left.\dfrac{\partial e}{\partial p}\right|_{y_w,T}$ respectively. The others are defined as:

$$\begin{aligned}\left.\frac{\partial\rho}{\partial T}\right|_{y_w,p} =& \frac{-p}{R_a T^2(1 - y_w + y_v(p,T)\epsilon_m^{-1})} \\ &+ \frac{pBC(p_s(T))^{-1}}{R_a T(1 - y_w + y_v(p,T)\epsilon_m^{-1})^2(p(p_s(T))^{-1} - (1-\epsilon_m))^2(C + T - T_0)^2}.\end{aligned} \tag{4.32}$$

$$\left.\frac{\partial \rho}{\partial p}\right|_{y_w,T} = \frac{1}{R_a T\left[1 - y_w + y_v(p,T)\epsilon_m^{-1}\right]} + \frac{(R_a T)^{-1}(p_s(T))^{-1} p}{\left[p(p_s(T))^{-1} - (1-\epsilon_m)\right]^2\left[1 - y_w + y_v(p,T)\epsilon_m^{-1}\right]^2}. \tag{4.33}$$

Similarly to the dry air scheme, the sub-iterative process for the time step ends when the error

$$\varepsilon_{piso}^k = \sqrt{\sum_{c=1}^{N_{cell}} \Omega_c \left|\underline{u}_c^{n+\theta,k} - \underline{u}_c^{n+\theta,k-1}\right|^2}$$

is below a fixed value ε_{piso_0}. Algorithm (2) summarises the moist air scheme main steps.

Remark 4.3.4. The inner iterative process error threshold ε_{piso_0} is speed dependent. Such condition was sufficient for the dry air scheme. However, the moist air scheme presents more couplings between its variables. Thus, defining a new error dependent of both speed and pressure could be of interest.

Algorithm 2 Moist air time scheme main steps

First time step initialisation,
Time loop
for `n = 0, N-1` **do**
  Initialisation of variables at the first sub-iteration $k = 1$,
  for `k = 1, M` **do**
    Compute the water mass fraction $y_{w,c}^{n+1,k}$, ▷ Equation (4.11)
    Compute the internal energy $e_c^{n+1,k}$, ▷ Equation (4.12)
    Compute the temperature $T_c^{n+1,k}$ and vapor of water mass fraction $y_{v,c}^{n+1,k}$ from $e_c^{n+1,k}$ and $p_c^{n+1,k-1}$, ▷ Algorithm (3)
    Update of the density $\widetilde{\rho}_c$ with $T_c^{n+1,k}$, ▷ Equation (4.22)
    Compute the predicted velocity $\underline{\widetilde{u}}_c^k$, ▷ Equation (4.23)
    Correction step: compute $\phi^k \rightarrow p_c|_{n-1+\theta}^{n+\theta}$, ▷ Equation (4.26)
    Correct the thermodynamic pressure $p_c^{n+1,k}$, ▷ Equation (4.27)
    Correct the density $\rho_c^{n+1,k}$, ▷ Equation (4.28)
    Compute the temperature $T_c^{n+1,k}$ and vapor of water mass fraction $y_{v,c}^{n+1,k}$ from $e_c^{n+1,k}$ and $p_c^{n+1,k}$, ▷ Algorithm (3)
    Correct the velocity $\underline{u}_c^{n+1,k}$, ▷ Equation (4.25)
    if $\epsilon_{piso}^k \leq \epsilon_{piso_0}$ **then**
      Break the for loop
    else
      Compute the kinetic energy source term $\Gamma_c^{u^2/2}\Big|_n^{n+1}$, ▷ Equation (3.11)
    end if
  end for
end for

Algorithm (3) summarises the numerical strategy related to the saturation. Its main idea is to consider a non saturated volume first. Then, using Equation (4.15), the vapor mass fraction at the pressure and the new temperature $\hat{T}$ is computed. If this quantity is inferior to the total water mass fraction, the Newton method is ran. Figure 4.3.1 illustrates this strategy related to saturation.

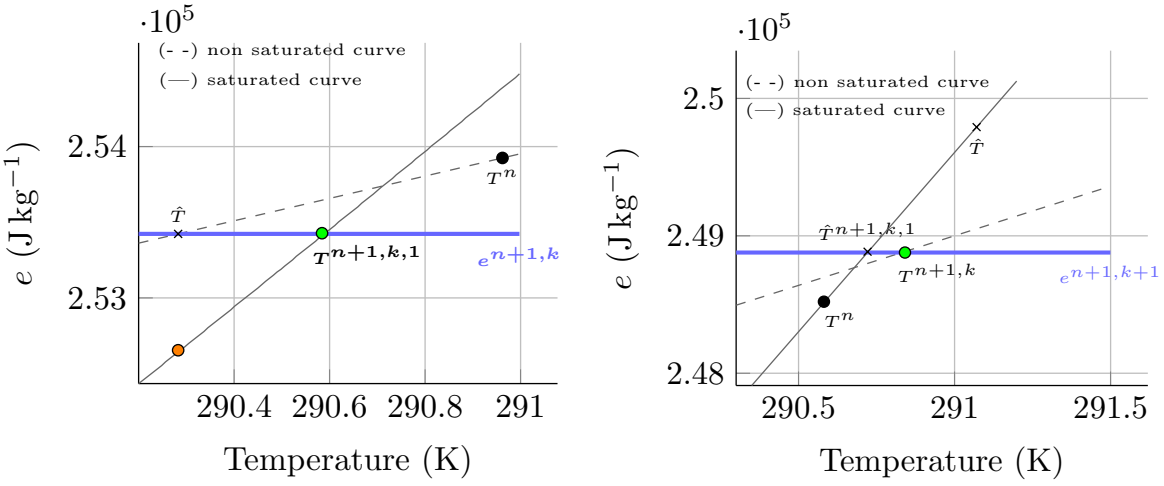

Figure 4.3.1: Strategy when treating saturation, with one Newton's method iteration. (Left) Example while getting in saturation. The orange filled dot corresponds to the point $\{\hat{T}, e(\hat{T}, y_s)\}$ (see Algorithm (3)). (Right) Example when leaving saturation. The final temperature $T^{n+1,k}$ is a result of the correction of the vapor of water mass fraction related to $T^{n+1,k,1}$, which was superior in that case to $y_w^{n+1,k}$. These Figures do not represent a test case in particular and were drawn only for illustrating the Newton's method.

4.4 Properties of the moist air scheme

A similar analysis made for the dry air scheme is made on the internal energy, pressure and density positivity, leading to new CFL and Fourier like conditions. The upwind spatial scheme is used for the convective terms in this analysis.

4.4.1 Positivity of the internal energy

Let's first analyse the internal energy discretised equation between $[n, n+1]$ and determine if stability conditions exist so the equation variable is strictly positive. For $k > 1$, Equation (4.12) is written:

$$\begin{aligned}
&\left[M_c^n \frac{e_c^{n+1,k} - e_c^n}{\Delta t|_n^{n+1}} + \sum_{f \in \mathcal{F}_c} \left(\left\langle \Theta\left(e^n,\, e_c^{n+1,k}\right) \right\rangle_f - e_c^{n+1,k} \right) \dot{M}_f \Big|_n^{n+1,k-1} \right] \\
&+ \sum_{f \in \mathcal{F}_c} \lambda |\underline{S}_f| \frac{\Theta\left(T_c^n,\, T_c^{n+1,k-1}\right) - \Theta\left(T_{\widetilde{c}}^n,\, T_{\widetilde{c}}^{n+1,k-1}\right)}{d_{c\widetilde{c}}} = \Omega_c \mu (S_c^2)^{n+\theta} + \Gamma_c^{u^2/2} \Big|_n^{n+1,k-1} \\
&- \sum_{f \in \mathcal{F}_\rfloor} \left\langle \Theta\left(p^n,\, p^{n+1,k-1}\right) \underline{u}^{n+\theta,k-1} \right\rangle_f \cdot \underline{S}_f + \Omega_c \underline{u}_c^{n+\theta,k-1} \cdot \underline{\nabla}_c p \Big|_{n-1+\theta}^{n+\theta,k-1}.
\end{aligned} \tag{4.34}$$

The equation (4.34) yields a linear system $\underline{\underline{A}}\,\underline{X} = \underline{B}$, where $\underline{X} = (e_c^{n+1,k})_{c \in \{1,..,N_{cell}\}}$. Considering the cell initial internal energy, λ, R_a, and Δt positive, $\underline{\underline{A}}$ is diagonal dominant and a M-matrix if:

$$\mathrm{Max}_c \left(\mathrm{CFL}_{T_1}^+ \right)_c < 1, \tag{4.35}$$

where:

$$(\mathrm{CFL}_{T_1}^+)_c := (1-\theta) \frac{\Delta t}{M_c^n} \sum_{f \in \mathcal{F}_c} \dot{M}_f^+ \Big|_n^{n+1,k-1}. \tag{4.36}$$

Algorithm 3 Saturation numerical treatment. $\hat{p}_c$ can be either $p_c^{n+1,k-1}$ or $p_c^{n+1,k}$

Compute internal energy $e_c^{n+1,k}$ for all N_{cell} cells, ▷ Equation (4.12)
for $c = 0, N_{cell}$ **do**
  Compute the mixture temperature without saturation $\hat{T}_c$, ▷ Equation (4.13)
  Compute the saturated vapor of water mass fraction $y_{s,c}(\hat{p}_c, \hat{T}_c)$, ▷ Equation (4.15)
  if $y_{s,c} < y_{w,c}^{n+1,k}$ **then**
    Initialise $T_c^{n+1,k,0} = \hat{T}_c$,
    Initialise the error $E_{e,c}^0 = |e_c^{n+1,k} - e_c(\hat{p}_c, \hat{T}_c)|$,
    while $E_{e,c}^l < \varepsilon_{e_0}$ **do**
      Compute $\left.\frac{\partial e}{\partial T}\right|_{y_w} (\hat{p}_c, y_{w,c}^{n+1,k}, \mathrm{T}_c^{n+1,k,l})$, ▷ Equation (4.17)
      Update $T_c^{n+1,k,l}$, ▷ Equation (4.16)
      Update the error $E_{e,c}^l = |e_c^{n+1,k} - e_c(\hat{p}_c, T_c^{n+1,k,l})|$
    end while
    `Verify the boudedness of the mass fractions`
    if $y_{v,c}^{n+1,k} > y_{w,c}^{n+1,k}$ **then**
      $y_{v,c}^{n+1,k} = y_{w,c}^{n+1,k}$,
      Correct $T_c^{n+1,k}$, ▷ Equation (4.13)
    else
      $T_c^{n+1,k} = T_c^{n+1,k,l}$,
      Correct $y_{v,c}^{n+1,k}$, ▷ Equation (4.15)
    end if
  else
    $y_{v,c}^{n+1,k} = y_{w,c}^{n+1,k}$,
    $T_c^{n+1,k} = \hat{T}_c$.
  end if
end for

$$\mathrm{Max}_c(\mathrm{CFL}_{T_2}^+)_c < 1, \tag{4.37}$$

where:

$$(\mathrm{CFL}_{T_2}^+)_c \coloneqq \frac{\Delta t}{M_c^n} \sum_{f \in \mathcal{F}_c} \left[(1-\theta) + \frac{R_a \Theta\left(T_c^n,\, T_c^{n+1,k-1}\right)}{e_c^n} \right] \dot{M}_f^+ \Big|_n^{n+1,k-1} - \frac{\Delta t \underline{u}_c^{n+\theta,k-1} \cdot \underline{\nabla}_c p|_{n-1+\theta}^{n+\theta,k-1}}{\rho_c^n e_c^n}. \tag{4.38}$$

$$\mathrm{Max}_c(Fo_T^+)_c < 1, \tag{4.39}$$

where:

$$(Fo_T^+)_c \coloneqq \frac{\lambda_c \Delta t}{M_c^n} \sum_{f \in \mathcal{F}_c} |\underline{S}_f| \frac{\Theta\left(T_c^n - T_{\widetilde{c}}^n,\, T_c^{n+1,k-1} - T_{\widetilde{c}}^{n+1,k-1}\right)}{e_c^n d_{c\widetilde{c}}}. \tag{4.40}$$

Remark 4.4.1. The internal energy is positive if the conditions (4.36), (4.38) and (4.40) are verified. However this does not enforce the positive of the mixture temperature $T^{n+1,k}$.

In case of non-saturation, the temperature is computed using Equation (4.13). Considering that y_w is bounded in $[0, 1]$, the positivity of a given cell c temperature in that case is insured if:

$$e_c^{n+1,k} > y_{w,c}^{n+1,k} L_{00}. \tag{4.41}$$

Remark 4.4.2. In the indoor context, the humidity absolute ratio highest values are around $30\,\mathrm{g\,kg^{-1}}$ of dry air, leading to a total water (with no saturation) mass fraction of $y_w = 0.029$. Thus, condition (4.41) is respected and the temperature would stay positive in this context of application.

In case of saturation, two conditions must be respected to preserve the temperature positivity. The first is the function $e(T)$ monotony (at fixed pressure and water mass fraction). Figure 4.4.1 shows this derivative in the indoor airflow conditions. Note that the total water mass fraction is constant; its variation, which is relatively small, has a little impact in the derivative value. For three different pressures, it can be seen that the internal energy partial derivative related to the temperature is positive. Thus, the Newton's method has an unique solution. However, this still does not insure the temperature positivity; a last condition, written as:

$$\frac{e_c^{n+1,k} - e\left(y_{w,c}^{n+1,k}, p_c^{n+1,k-1}, T_c^{n+1,k,l-1}\right)}{\left.\dfrac{\partial e}{\partial T}\right|_{y_w}\left(y_{w,c}^{n+1,k}, p_c^{n+1,k-1}, T_c^{n+1,k,l-1}\right)} + T_c^{n+1,k,l-1} > 0, \tag{4.42}$$

should be satisfied, which is the case for non important internal energy variations.

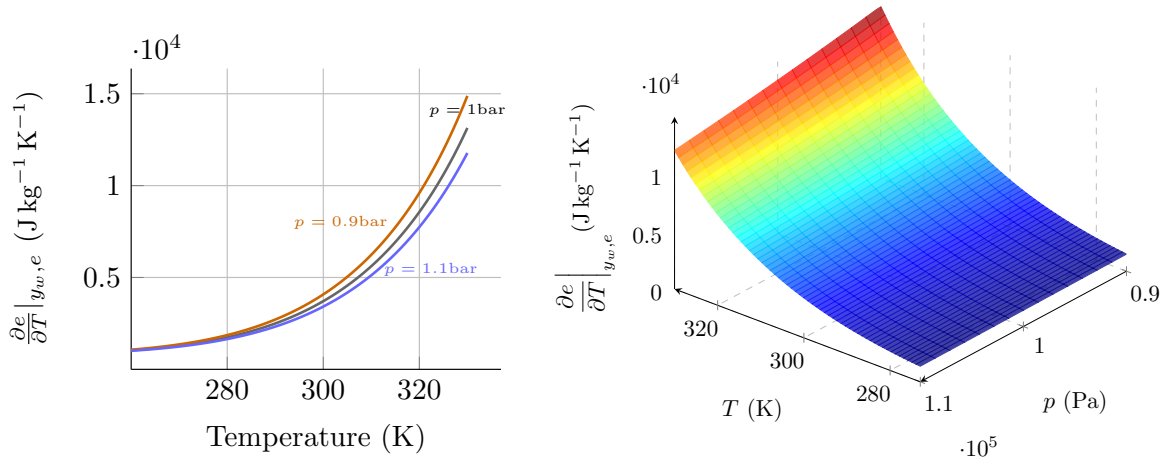

Figure 4.4.1: (Left) 2-D representation of the internal energy partial derivative related to the temperature between 260 K and 330 K for three different pressures in the indoor airflow range and with $y_w = 0.0125$. (Right) 3-D representation of the internal energy partial derivative related to the temperature with $y_w = 0.0125$.

4.4.2 Positivity of the pressure

Similarly to the internal energy equation, the Helmholtz equation solved for the pressure increment for $k > 1$ is written with the spatial discretisation (note that the Rhie and Chow filter is included in the following):

$$\begin{aligned}&\frac{\Omega_c p_c^{n+1,k}}{\Delta t}\left.\frac{\partial \rho}{\partial p}\right|_{y_w,e}(y_{w,c}^{n+1,k}, p_c^{n+1,k-1}, T_c^{n+1,k}) - \theta\Delta t \sum_{f\in\mathcal{F}_c} \underline{\nabla}_f p^{n+1,k}\cdot\underline{S}_f = \frac{\rho_c^n \Omega_c}{\Delta t}\\ &(1-\theta)\Delta t \sum_{f\in\mathcal{F}_c} \underline{\nabla}_f p|_{n-2+\theta}^{n-1+\theta}\cdot\underline{S}_f - \sum_{f\in\mathcal{F}_c}\left\langle \Theta\left(\rho^n,\, \rho^{n+1,k-1}\right)\widetilde{\underline{u}}^k + \Delta t \underline{\nabla}_c p|_{n-1+\theta}^{n+\theta,k-1}\right\rangle_f \cdot \underline{S}_f,\end{aligned} \tag{4.43}$$

If the volume is not saturated,

$$\left.\frac{\partial \rho}{\partial p}\right|_{y_w,e}(y_{w,c}^{n+1,k}, p_c^{n+1,k-1}, T_c^{n+1,k}) = \frac{1}{R_a T_c^{n+1,k}\left[1 - y_{w,c}^{n+1,k} + y_{v,c}^{n+1,k}\epsilon_m^{-1}\right]},$$

with:

$$y_{v,c}^{n+1,k} = y_{w,c}^{n+1,k}.$$

From the thermal equation, if the internal energy is positive so is the temperature and the vapor pressure at saturation $p_s(T)$.

Moreover, $\left.\frac{\partial \rho}{\partial p}\right|_{y_w,e}(y_{w,c}^{n+1,k}, p_c^{n+1,k-1}, T_c^{n+1,k})$ is strictly positive if $y_{v,c}^{n+1,k}$ is, i.e. if:

$$p_c^{n+1,k-1} > (1-\epsilon_m)\, p_s(T_c^{n+1,k}). \tag{4.44}$$

This is verified in the indoor context. Indeed, the water saturation pressure at the indoor temperature range (around 10^4Pa, see Figure 4.2.1) is less important than the indoor pressure values (around 10^5Pa). In case of saturation,

$$\begin{aligned}&\left.\frac{\partial \rho}{\partial p}\right|_{y_w,e}(y_{w,c}^{n+1,k}, p_c^{n+1,k-1}, T_c^{n+1,k}) =\\ &\left[-\left.\frac{\partial \rho}{\partial T}\right|_{y_w,p}\left(\left.\frac{\partial e}{\partial T}\right|_{y_w,p}\right)^{-1}\left.\frac{\partial e}{\partial p}\right|_{y_w,T} + \left.\frac{\partial \rho}{\partial p}\right|_{y_w,T}\right](y_{w,c}^{n+1,k}, p_c^{n+1,k-1}, T_c^{n+1,k}).\end{aligned}$$

Given the complexity to write an analytical positivity condition for this derivative, in this section a qualitative analysis is made. To do so, $\left.\frac{\partial \rho}{\partial p}\right|_{y_w,e}(y_w, p, T)$ is represented in Figure 4.4.2, for a very low total water mass fraction ($y_w = 0.002$) and its maximum value considered in the indoor environment framework ($y_w = 0.029$). Two main points can be highlighted. First, the variation of water mass fraction has a little impact (not negligible) in the partial derivative value. Second, in the indoor environment context, this derivative is positive. This will be also the case when $y_w = 0$, since the derivative will tend to the dry air equation of state derivative presented in Chapter 3.3. One interesting point to investigate in further studies could be an analysis on how this derivative expression, which is not simple in case of saturation, is impacted by the different terms. According to the result, its expression could be simplified.

Equation (4.43) is a linear system $\underline{\underline{A}}\,\underline{X} = \underline{B}$, where $\underline{X} = (p_c^{n+1,k})_{c\in\{1,..,N_{cell}\}}$. Considering the cell internal energy, λ, R_a, and Δt positive, $\underline{\underline{A}}$ is diagonal dominant and a M-matrix if the condition (4.44) and the following CFL condition are respected:

$$\text{Max}_c(\text{CFL}_p^+)_c < 1, \tag{4.45}$$

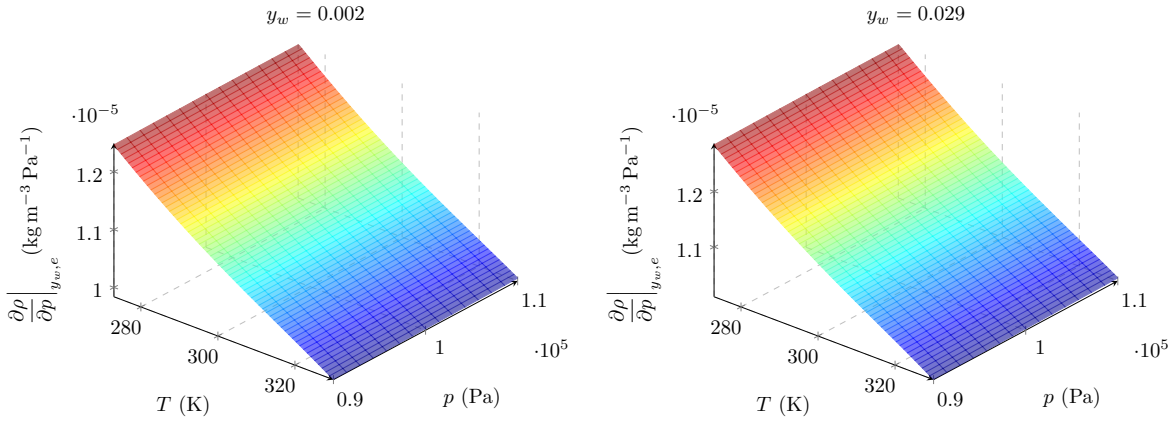

Figure 4.4.2: $\left.\frac{\partial \rho}{\partial p}\right|_{y_w,e}(y_w, p, T)$ according to the temperature and total pressure for two total water mass fraction values.

where:

$$(\mathrm{CFL}_p^+)_c := \frac{\Delta t}{\rho_c^n \Omega_c^n} \sum_{f \in \mathcal{F}_c} a_f^\phi, \tag{4.46}$$

and

$$a_f^\phi = \left\langle \Theta\left(\rho^n,\, \rho^{n+1,k-1}\right) \widetilde{\underline{u}}^k + \Delta t \underline{\nabla} p\big|_{n-1+\theta}^{n+\theta,k-1} \right\rangle_f \cdot \underline{S}_f - (1-\theta)\Delta t \underline{\nabla}_f p\big|_{n-2+\theta}^{n-1+\theta} \cdot \underline{S}_f.$$

4.5 Solution of the Riemann problem related to the moist air system of equations with no phase change

This section presents the derivation of the solution of the Riemann problem related to the mixture set of equations. The solution is then used for the moist air scheme verification.

4.5.1 Introduction

Riemann problems are well known and documented in the literature. Often used to verify numerical schemes (Archambeau et al., 2009; Colas et al., 2019; Herbin et al., 2020; Amino et al., 2022) [][][][], they represent the propagation of waves in a given system. However, finding the exact solution of this problem related to a set of equations is not always possible.
This section work is strongly inspired by Smoller (2012) []book. The reader may refer to the latter for the derivation of the Riemann problem exact solution for the Euler equations for instance.
In this type of problem, two fluid initial states are separated by an interface. The different left and right initial states are called respectively $\underline{W}_L$ and $\underline{W}_R$ (which are known and steady). According to the initialisation, shock, expansion and contact waves propagate over the system.
In order to derive an exact solution related to the Riemann problem, some hypothesis have been made. First, diffusive terms are disabled. Then, phase change is not considered. This yields $y_v = y_w$ and $y_l = 0$. Finally, an one-dimensional problem in space is considered.

Proposition

- The one-dimensional Riemann problem associated with the System (4.1) with initial data:

$$\underline{W}(x < 0, t = 0) = \underline{W}_L, \quad \underline{W}(x > 0, t = 0) = \underline{W}_R,$$

neglecting the diffusive terms, admits an unique self-similar solution $\underline{W}(\xi)$, with $\xi = x/t$, with no vacuum occurrence, if and only if the following condition (4.47) is respected:

$$u_R - u_L < \frac{2}{\Gamma(y_{w,R}) - 1} c_R + \frac{2}{\Gamma(y_{w,L}) - 1} c_L, \tag{4.47}$$

with c and Γ defined as following:

$$c(y_w, \rho, p) = \left(\frac{p}{\rho} \Gamma(y_w) \right)^{\frac{1}{2}}, \qquad \Gamma(y_w) = \frac{R_a(1 - y_w(1 - \epsilon_m^{-1}))}{c_{vm}} + 1. \tag{4.48}$$

- The solution is composed by constant intermediate states, $\underline{W}_L$, $\underline{W}_1$, $\underline{W}_2$ and $\underline{W}_R$, separated respectively by a genuinely nonlinear wave (1-wave), a double contact discontinuity wave and a last genuinely nonlinear wave (4-wave). With those are associated the eigenvalues $\lambda_{1/4} = u \pm c$ and $\lambda_{2/3} = u$ (see Figure 4.5.1).

The proof, which is detailed in the next subsections, is classically obtained (Smoller, 2012) by construction using the Rankine–Hugoniot conditions and considering the entropy inequality:

$$\frac{\partial(\rho s)}{\partial t} + \text{div}\,(\rho s \underline{u}) < 0, \tag{4.49}$$

where $s(y_w, \rho, p) = p\rho^{-\Gamma(y_w)}$. The methodology to derive the exact solution of the Riemann problem can be summarised in three main steps. First, the verification of the hyperbolicity of the system is made by studying its eigenvalues. The eigenvectors and Riemann invariants are then calculated. The next step is to respectively connect the left (L) and right (R) states to the intermediate ones (1 and 2). This is done by writing expressions linking those states at the 1- and 4- waves, that can be either an expansion or a shock wave. This induces four different possible cases, summarised in Figure 4.5.2. The final step is to connect an intermediate state (in this study, the state (1)) to to the states (L) and (R).

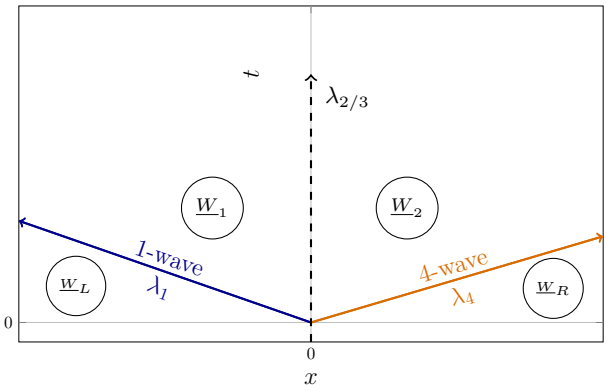

Figure 4.5.1: Presentation of the different Riemann problem waves and states.

After introducing the studied set of equations in Subsection 4.5.2, the hyperbolocity of the system is studied in Subsection 4.5.3. Then the Rankine–Hugoniot relations are presented and the connection between the states $L - 1$ and $2 - R$ for the four different cases is made in Subsection 4.5.5. Finally, the intermediate state calculation strategy is explained in Subsection 4.5.7.

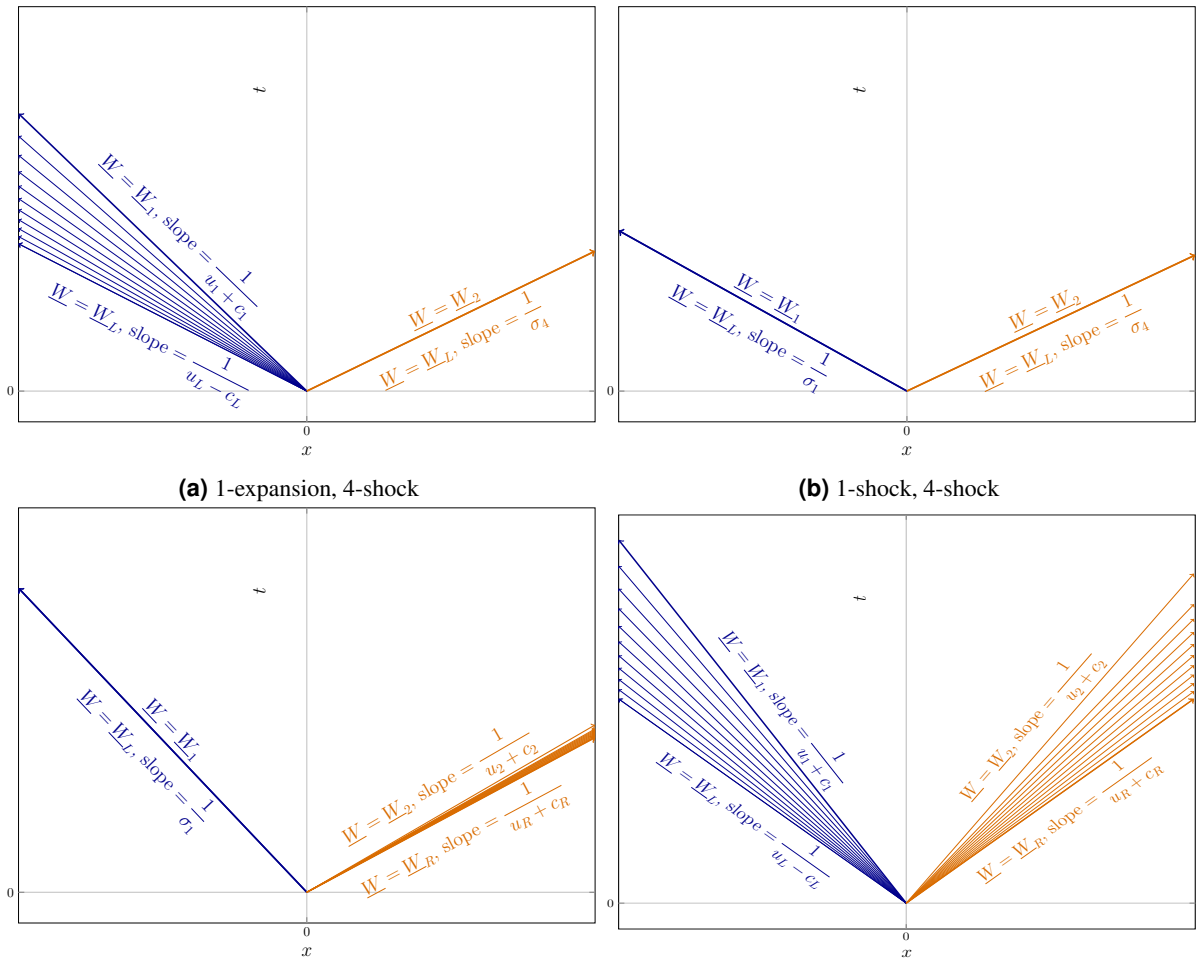

(a) 1-expansion, 4-shock

(b) 1-shock, 4-shock

(c) 1-shock, 4-expansion

(d) 1-expansion, 4-expansion

Figure 4.5.2: Sketch of the four possible cases for the one-dimensional Riemann problem.

4.5.2 Set of equations

The mixture Euler equations (4.116) are written using the total energy equation and in their conservative form:

$$\begin{aligned} \frac{\partial(\rho y_w)}{\partial t} + \operatorname{div}(\rho y_w \underline{u}) &= 0, \\ \frac{\partial \rho}{\partial t} + \operatorname{div}(\rho \underline{u}) &= 0, \\ \frac{\partial(\rho \underline{u})}{\partial t} + \underline{\operatorname{div}}(\rho \underline{u} \otimes \underline{u}) + \underline{\nabla} p &= \underline{0}, \\ \frac{\partial(\rho E)}{\partial t} + \operatorname{div}(\rho E \underline{u} + p \underline{u}) &= 0. \end{aligned} \tag{4.50}$$

The total energy is defined by:

$$E = u^2/2 + e. \tag{4.51}$$

The equation of state is written as:

$$e = \frac{p c_{vm}}{\rho R_a (1 - y_w (1 - \epsilon_m^{-1}))} + y_w L_{00} \tag{4.52}$$

For regular solutions, system (4.50) is equivalent to the following non conservative one:

$$\begin{aligned}
\frac{\partial y_w}{\partial t} + \underline{\nabla} y_w \cdot \underline{u} &= 0, \\
\frac{\partial s}{\partial t} + \underline{\nabla} s \cdot \underline{u} &= 0, \\
\frac{\partial \underline{u}}{\partial t} + \underline{u} \cdot \underline{\underline{\nabla}} \underline{u} + \tau \underline{\nabla} p &= 0, \\
\frac{\partial p}{\partial t} + \underline{\nabla} p \cdot \underline{u} + \rho c^2 \text{div}\,(\underline{u}) &= 0.
\end{aligned} \tag{4.53}$$

The new set of variable is, considering an one dimensional problem, $\underline{Y} = (y_w, s, \underline{u}, p)^t$, where s is the system entropy defined as:

$$s(y_w, \rho, p) = p\rho^{-\Gamma(y_w)}, \qquad \Gamma(y_w) = \frac{R_a(1 - y_w(1 - \epsilon_m^{-1}))}{c_{vm}} + 1. \tag{4.54}$$

And c is the system celerity:

$$c = \left(\frac{p}{\rho}\Gamma(y_w)\right)^{\frac{1}{2}}. \tag{4.55}$$

Remark 4.5.1 – Equivalence between systems (4.50) and (4.53). Combining the momentum and total energy equations leads to the internal energy equation. The system associated, in its non conservative form reads:

$$\begin{aligned}
\frac{\partial y_w}{\partial t} + \underline{\nabla} y_w \cdot \underline{u} &= 0, \\
\frac{\partial \rho}{\partial t} + \underline{\nabla} \rho \cdot \underline{u} + \rho \text{div}\,(\underline{u}) &= 0, \\
\frac{\partial \underline{u}}{\partial t} + \underline{u} \cdot \underline{\underline{\nabla}} \underline{u} + \frac{1}{\rho}\underline{\nabla} p &= 0, \\
\frac{\partial e}{\partial t} + \underline{\nabla} e \cdot \underline{u} + p\frac{1}{\rho}\text{div}\,(u) &= 0.
\end{aligned} \tag{4.56}$$

The internal energy e differential (function of y, ρ and p) is written:

$$\left.\frac{\partial e}{\partial p}\right|_{y_w,\rho}\left(\frac{\partial p}{\partial t} + \underline{\nabla} p \cdot \underline{u}\right) - \left.\frac{\partial e}{\partial \rho}\right|_{y_w,p}\rho\text{div}\,(\underline{u}) + \left.\frac{\partial e}{\partial y_w}\right|_{\rho,p}\left(\frac{\partial y_w}{\partial t} + \underline{\nabla} y_w \cdot \underline{u}\right) + p\frac{1}{\rho}\text{div}\,(\underline{u}) = 0. \tag{4.57}$$

With some manipulations, the latter leads to an equation for the pressure:

$$\frac{\partial p}{\partial t} + \underline{\nabla} p \cdot \underline{u} + \rho c^2 \text{div}\,(\underline{u}) = 0, \tag{4.58}$$

where c^2 is defined as:

$$c^2 := \frac{\dfrac{p}{\rho^2} - \left.\dfrac{\partial e}{\partial \rho}\right|_{y_w,p}}{\left.\dfrac{\partial e}{\partial p}\right|_{\rho,y_w}} = \frac{\dfrac{p}{\rho^2} + \dfrac{pc_{vm}}{\rho^2 R_a(1 - y_w(1 - \epsilon_m^{-1}))}}{\dfrac{c_{vm}}{R_a\rho(1 - y_w(1 - \epsilon_m^{-1}))}} = \frac{p}{\rho}\left(\frac{R_a(1 - y_w(1 - \epsilon_m^{-1}))}{c_{vm}} + 1\right). \tag{4.59}$$

The celerity is positive if p and ρ are, which is the case if the CFL conditions presented in Section 4.4 are respected. Introducing:

$$\Gamma(y_w) \coloneqq \frac{R_a(1 - y_w(1 - \epsilon_m^{-1}))}{c_{vm}} + 1, \tag{4.60}$$

yields:

$$c^2 = \frac{p}{\rho}\Gamma. \tag{4.61}$$

Moreover, we define the system entropy $s(y_w, \rho, p)$ whose derivative verifies:

$$\frac{\partial s}{\partial t} + \underline{\nabla} s \cdot \underline{u} + \rho \left(\left.\frac{\partial s}{\partial \rho}\right|_{y_w,p} + c^2 \left.\frac{\partial s}{\partial p}\right|_{y_w,\rho} \right) \text{div}\,(\underline{u}) = 0. \tag{4.62}$$

Indeed,

$$\mathrm{d}s = \frac{\partial s}{\partial t} + \underline{\nabla} s \cdot \underline{u} = \left.\frac{\partial s}{\partial y_w}\right|_{\rho,p} \frac{\mathrm{d}y_w}{\mathrm{d}t} + \left.\frac{\partial s}{\partial \rho}\right|_{y_w,p} \frac{\mathrm{d}\rho}{\mathrm{d}t} + \left.\frac{\partial s}{\partial p}\right|_{y_w,\rho} \frac{\mathrm{d}p}{\mathrm{d}t},$$

where:

$$\frac{\mathrm{d}y_w}{\mathrm{d}t} = 0, \qquad \frac{\mathrm{d}\rho}{\mathrm{d}t} = -\rho \text{div}\,(\underline{u}), \qquad \frac{\mathrm{d}p}{\mathrm{d}t} = -\rho c^2 \text{div}\,(\underline{u}).$$

Defining $s(y_w, \rho, p) = p\rho^{-\Gamma}$,

$$\left.\frac{\partial s}{\partial \rho}\right|_{y_w,p} + c^2 \left.\frac{\partial s}{\partial p}\right|_{y_w,\rho} = 0 \tag{4.63}$$

is respected and Equation (4.62) reads:

$$\frac{\partial s}{\partial t} + \underline{\nabla} s \cdot \underline{u} = 0. \tag{4.64}$$

Note that $\rho = (p/s)^{1/\Gamma}$. The final system uses the entropy and pressure equations rather than the momentum and internal energy ones, which facilitates the calculation of its eigenvalues, eigenvectors and Riemann invariants, presented in the next Subsection.

4.5.3 System hyperbolicity

The set of equations presented on Equation (4.53) is kept. The latter reads

$$\frac{\partial \underline{Y}}{\partial t} + \underline{\underline{A}}(\underline{Y}) \underline{\underline{\nabla Y}} = 0, \tag{4.65}$$

with $\underline{Y} = (y_w, s, u, p)^T$. $\underline{\underline{A}}$ is the associated Jacobian matrix:

$$\underline{\underline{A}}(\underline{Y}) = \begin{pmatrix} u & 0 & 0 & 0 \\ 0 & u & 0 & 0 \\ 0 & 0 & u & \frac{1}{\rho} \\ 0 & 0 & \rho c^2 & u \end{pmatrix}.$$

Let's verify that this system is hyperbolic, i.e. that $\underline{\underline{A}}$ is diagonalisable and has eigenvalues in $\mathbb{R}$. Its eigenvalues are the following:

$$\lambda_1 = u - c, \quad \lambda_2 = \lambda_3 = u, \quad \lambda_4 = u + c,$$

with $\lambda_1 < \lambda_{2/3} < \lambda_4$. The eigenvectors r_i associated to the λ_i are:

$$\underline{r}_1 = (0, 0, 1, -\rho c),$$
$$\underline{r}_2 = (1, 0, 0, 0),$$
$$\underline{r}_3 = (0, 1, 0, 0),$$
$$\underline{r}_4 = (0, 0, 1, \rho c).$$

Moreover, Riemann invariants ϕ_i for each eigenvector can be calculated. They verify:

$$\underline{r}_i \cdot \underline{\nabla}\phi_i = 0.$$

For the double eigenvalue $\lambda_2 = \lambda_3$, the couple of invariants $\phi_{2/3}$ is straightforward and reads

$$\phi_{2/3} = \{u, p\}.$$

Then, y_w and ρ are two invariants of the first and fourth waves. The other invariants of these waves verify:

$$\left.\frac{\partial \phi}{\partial u}\right|_{y_w,\rho,p} - \rho c \left.\frac{\partial \phi}{\partial p}\right|_{y_w,u,p} = 0 \tag{4.66}$$

Searching ϕ of the form $\phi = u + \psi(y_w, s, p)$ leads to:

$$\phi_1^3 = u + \int_{p_0}^{p} \frac{\mathrm{d}p'}{\rho c(p', s, y)}, \quad \phi_4^3 = u - \int_{p_0}^{p} \frac{\mathrm{d}p'}{\rho c(p', s, y)}. \tag{4.67}$$

Table (4.5.1) summarises the last results, which are useful to derive the exact solution.
Moreover, we recall that $c^2(y_w, \rho, p) = p\rho^{-1}\Gamma$, so

$$\rho c(y_w, \rho, p) = (\rho p \Gamma)^{\frac{1}{2}}. \tag{4.68}$$

Since $\rho = p^{1/\Gamma} s^{-1/\Gamma}$, the latter becomes:

$$\rho c(y_w, s, p) = \Gamma^{\frac{1}{2}} s^{-\frac{1}{2}\Gamma} p^{\frac{1}{2}-\frac{1}{2}\Gamma}. \tag{4.69}$$

We define

$$I(y_w, s, p) = \int_{p_0}^{p} \frac{\mathrm{d}p'}{\rho c(p', y_w, s)} = \int_{p_0}^{p} \frac{\mathrm{d}p'}{\Gamma^{\frac{1}{2}} s^{-\frac{1}{2}\Gamma} p'^{\frac{1}{2}+\frac{1}{2}\Gamma}} \tag{4.70}$$

Integrating this expression yields:

$$I(y_w, s, p) = \frac{2c(y_w, s, p)}{\Gamma - 1}. \tag{4.71}$$

Note that $\Gamma = \Gamma(y_w)$, defined in Equation (4.60).

i =	1	2	3	4
λ_i	$u-c$	u	u	$u+c$
$\underline{r}_i$	$(0,0,1,-\rho c)^t$	$(1,0,0,0)^t$	$(0,1,0,0)^t$	$(0,0,1,\rho c)^t$
ϕ_i	$\{y_w, s, u+\int_{p_0}^{p}\frac{dp'}{\rho c(p',s,y)}\}$	$\{u,p\}$	$\{u,p\}$	$\{y_w, s, u-\int_{p_0}^{p}\frac{dp'}{\rho c(p',s,y)}\}$

Table 4.5.1: Eigenvalues, eigenvectors and Riemann invariants for the system (4.53)

Remark 4.5.2. The results presented in Table 4.5.1 can be compared to the classical Euler system of equations Riemann problem solution. First, an additional eigenvalue exists $\lambda_3 = u$ related to the solve of the total water transport equation. This leads as well to three (instead of two) invariants for the first and fourth waves. Moreover, the second invariants for those waves present similarities to the Euler system ones, where only the definition of the celerity and Γ are different.

4.5.4 Jump conditions

For system (4.53), the jump conditions, also called the Rankine–Hugoniot conditions (Smoller, 2012) [↗], are:

$$\begin{aligned} -\sigma[\rho y_w] + [\rho u y_w] &= 0, \\ -\sigma[\rho] + [\rho u] &= 0, \\ -\sigma[\rho u] + [\rho u^2 + p] &= 0, \\ -\sigma[\rho E] + [u(\rho E + p)] &= 0, \end{aligned} \tag{4.72}$$

where $[\psi] \coloneqq \psi_r - \psi_l$ (the subscripts l and r are the shock left and right states respectively) and σ is the shock speed in the frame of reference moving with the shock. A more convenient way to write these conditions is to introduce the variable $v = u - \sigma$. Equation (4.72) becomes then:

$$\begin{aligned} [\rho v y_w] &= 0, \\ [\rho v] &= 0, \\ [u]^2 &= \frac{[p][\rho]}{\rho_l \rho_r}, \\ [e] + \overline{p}[\frac{1}{\rho}] &= 0, \end{aligned} \tag{4.73}$$

where $\overline{p} \coloneqq \frac{1}{2}(p_r + p_l)$. Some useful information for solving the Riemann problem can be deduced from these relations. For instance, using the entropy inequality (Smoller, 2012; Gavrilyuk et al., 2022) [↗↗]yields

$$[u] = -\left(\frac{[p][\rho]}{\rho_l \rho_r}\right)^{\frac{1}{2}}. \tag{4.74}$$

Thus,

$$u_r = u_l - \left(\frac{(p_r - p_l)(\rho_r - \rho_l)}{\rho_r \rho_l}\right)^{\frac{1}{2}}. \tag{4.75}$$

Combining the first two Rankine–Hugoniot conditions leads to:

$$\rho v[y] = 0. \tag{4.76}$$

For genuinely non-linear (GNL) fields, $v \neq 0$ and ρ is assumed strictly positive. Thus,

$$[y] = 0, \tag{4.77}$$

i.e. there is no jump for the total water mass fraction in case of shock. Also,

$$[e] + \overline{p}\left[\frac{1}{\rho}\right] = 0. \tag{4.78}$$

Using the definition of the internal energy (Equation (4.52)) and multiplying Equation (4.78) by $(\Gamma - 1)$ leads to:

$$\left[p\frac{1}{\rho}\right] + (\Gamma - 1)\overline{p}\left[\frac{1}{\rho}\right] = \overline{\frac{1}{\rho}}[p] + \Gamma\overline{p}\left[\frac{1}{\rho}\right] = 0,$$

i.e.

$$\frac{1}{2}\left(\frac{1}{\rho_r} + \frac{1}{\rho_l}\right)(p_r - p_l) + \Gamma/2\,(p_r + p_l)\left(\frac{1}{\rho_r} - \frac{1}{\rho_l}\right) = 0. \tag{4.79}$$

The normalised pressure

$$\Phi = \frac{p_r}{p_l}, \tag{4.80}$$

and density variables

$$z = \frac{\rho_r}{\rho_l}, \tag{4.81}$$

related to a wave are defined. Equation (4.79) reads then:

$$\begin{aligned} &\Phi\left[(1+z) + \Gamma(1-z)\right] = 1 + z_1 + \Gamma_L(z_1 - 1), \\ &\Leftrightarrow \Phi(\Gamma - 1)\left(\frac{\Gamma+1}{\Gamma-1} - z\right) = (\Gamma - 1)\left(\frac{\Gamma+1}{\Gamma-1}z - 1\right), \\ &\Leftrightarrow \Phi = \frac{\beta z - 1}{\beta - z}, \qquad \text{and} \qquad z = \frac{\beta\Phi + 1}{\beta + \Phi}. \end{aligned} \tag{4.82}$$

Where:

$$\beta = \frac{\Gamma+1}{\Gamma-1}.$$

The use of the R.H conditions for a shock wave provided the essential expression (4.82) linking the pressure and density variables that is used in the problem exact solution derivation.

4.5.5 States connection

In this subsection we want to find the connections between the different system states i.e. the connections in the 1- and 4- waves for the unknowns $\underline{Y} = (y_w, s, u, p)^t$.
As a reminder, each 1- 4- waves can either be an expansion or shock wave. We introduce the left ($\underline{W}_L$) and right ($\underline{W}_R$) system states related to the problem initialisation which are known and steady. The

found connections lead to the Riemann problem solution presented in the next section, where the contact wave invariants

$$u_1 = u_2, \quad p_1 = p_2, \tag{4.83}$$

are used to connect all states together.
The normalised pressure and density variables associated to states 1 and 2 are defined:

$$\Phi_1 = \frac{p_1}{p_L}, \quad \Phi_2 = \frac{p_2}{p_R}, \tag{4.84}$$

and

$$z_1 = \frac{\rho_1}{\rho_L}, \quad z_2 = \frac{\rho_2}{\rho_R}. \tag{4.85}$$

The choice to solve the pressure variable Φ_1 is made in the following.

The main goal here is to write expressions for the 1-wave and 4-wave expressions linking the unknowns variables and the known states $\underline{W}_L$ and $\underline{W}_R$ i.e.:

$$\begin{aligned} \frac{u_1 - u_L}{c_L} &= f_1(\underline{W}_L, \Phi_1), \\ z_1 &= h_1(\underline{W}_L, \Phi_1), \\ \frac{u_2 - u_R}{c_R} &= f_4(\underline{W}_R, \Phi_2), \\ z_2 &= h_2(\underline{W}_R, \Phi_2). \end{aligned} \tag{4.86}$$

Connection of the L-state to the 1-state through an expansion

In case of expansion ($0 < \Phi_1 \leq 1$), the Riemann invariants are conserved between the state L and the state 1. For the 1-wave, they read:

$$\phi_1 = \left\{ y_w, s, u + \frac{2c(y_w, s, p)}{\Gamma(y_w) - 1} \right\}.$$

Thus,

$$y_{w,L} = y_{w,1}, \qquad s_L = s_1, \quad \text{and} \quad \Gamma(y_{w,1}) = \Gamma(y_{w,L}) = \Gamma_L.$$

Let's write the condition related to the third Riemann invariant, using the notation for the constant $c(y_{w,L}, s_L, p_L) = c_L$:

$$u_L + \frac{2c_L}{\Gamma_L - 1} = u_1 + \frac{2c(y_{w,L}, s_L, p_1)}{\Gamma_L - 1}. \tag{4.87}$$

This leads to:

$$u_1 = u_L + \frac{2c_L}{\Gamma_L - 1} - \frac{2c(y_{w,L}, s_L, p_1)}{\Gamma_L - 1} = u_L + \frac{2}{\Gamma_L - 1}(c_L - c(y_{w,L}, s_L, p_1)), \tag{4.88}$$

which is rewritten using c_L and Φ_1:

$$\frac{u_1 - u_L}{c_L} = f_1(\underline{W}_L, \Phi_1), \tag{4.89}$$

where:

$$f_1(\underline{W}_L, \Phi_1) \coloneqq \frac{2}{\Gamma_L - 1}\left(1 - \Phi_1^{\frac{1}{2}\left(1-\Gamma_L^{-1}\right)}\right).$$

The next step is to find a link between pressure and density for the 1-wave using the definition of the invariant s:

$$s = p\rho^{-\Gamma_L}.$$

This yields:

$$z_1 = \Phi_1^{\frac{1}{\Gamma_L}}. \tag{4.90}$$

Connection of the L-state to the 1-state through a shock

Equation (4.79) is written for the 1-wave with z_1 and Φ_1 (in case of shock, i.e. if $\Phi_1 > 1$):

$$\begin{aligned} &\Leftrightarrow \Phi_1(\Gamma_L - 1)\left(\frac{\Gamma_L + 1}{\Gamma_L - 1} - z_1\right) = (\Gamma_L - 1)\left(\frac{\Gamma_L + 1}{\Gamma_L - 1}z_1 - 1\right), \\ &\Leftrightarrow \Phi_1 = \frac{\beta_L z_1 - 1}{\beta_L - z_1}, \qquad \text{and} \qquad z_1 = \frac{\beta_L \Phi_1 + 1}{\beta_L + \Phi_1} = h_1(\underline{W}_L, \Phi_1). \end{aligned} \tag{4.91}$$

With

$$\beta_L = \frac{\Gamma_L + 1}{\Gamma_L - 1}.$$

This expression is essential to link the pressure and density in the linearly degenerated wave. Now we look for an expression linking the velocity and Φ_1. The Rankine–Hugoniot condition (Equation (4.75)) is used:

$$u_1 = u_L - \sqrt{\frac{(p_1 - p_L)(\rho_1 - \rho_L)}{\rho_1 \rho_L}} = u_L - c_L\sqrt{\frac{(\Phi_1 - 1)(z_1 - 1)}{\Gamma_L z_1}} \tag{4.92}$$

i.e.

$$\frac{u_1 - u_L}{c_L} = f_1(\underline{W}_L, \Phi_1), \tag{4.93}$$

where,

$$f_1(\underline{W}_L, \Phi_1) \coloneqq -\sqrt{\frac{(\Phi_1 - 1)(z_1 - 1)}{\Gamma_L z_1}}.$$

Summary of the relations for the 1-wave

To sum up, for the 1-wave, the final connection between the states $1 - L$ is:

$$\frac{u_1 - u_L}{c_L} = f_1(\underline{W}_L, \Phi_1) = \begin{cases} \dfrac{2}{\Gamma_L - 1}\left(1 - \Phi_1^{\frac{1}{2}\left(1-\Gamma_L^{-1}\right)}\right), & \text{if } 0 < \Phi_1 \leq 1 \text{ (1-expansion)}, \\ -\left(\dfrac{(\Phi_1 - 1)(z_1 - 1)}{\Gamma_L z_1}\right)^{\frac{1}{2}}, & \text{if } \Phi_1 > 1 \text{ (1-shock)}. \end{cases} \tag{4.94}$$

with

$$z_1 = h_1(\underline{W}_L, \Phi_1) = \begin{cases} \Phi_1^{\frac{1}{\Gamma_L}}, & \text{if } 0 < \Phi_1 \leq 1 \text{ (1-expansion)}, \\ \dfrac{\beta_L \Phi_1 + 1}{\beta_L + \Phi_1}, & \text{if } \Phi_1 > 1 \text{ (1-shock)}. \end{cases} \tag{4.95}$$

Connection of the R-state to the 2-state through an expansion

Similarly, the invariants for the 4-wave are:

$$\phi_2 = \left\{ y_w, s, u - \frac{2c(y_w, s, p)}{\Gamma(y_w) - 1} \right\}.$$

Thus:

$$y_{w,R} = y_{w,2}, \qquad s_R = s_2,$$

and $\Gamma(y_w) = \Gamma(y_{w,R}) = \Gamma_R$. Let's write the expression related to the third Riemann invariant, using the notation for the constant $c(y_{w,R}, s_R, p_R) = c_R$:

$$u_R - \frac{2c_R}{\Gamma_R - 1} = u_2 - \frac{2c(y_{w,R}, s_R, p_2)}{\Gamma_R - 1}, \tag{4.96}$$

which can be written as:

$$\frac{u_2 - u_R}{c_R} = f_4(\underline{W}_R, \Phi_2), \quad \text{if } \ 0 < \Phi_2 \leq 1, \tag{4.97}$$

where:

$$f_4(\underline{W}_R, \Phi_2) \coloneqq -\frac{2}{\Gamma_R - 1} c_R \left(1 - \Phi_2^{\frac{1}{2}\left(1 - \Gamma_R^{-1}\right)} \right).$$

Similarly, the link between pressure and density for the 4-wave using the definition of the invariant s is:

$$z_2 = \Phi_2^{\frac{1}{\Gamma_R}}. \tag{4.98}$$

Connection of the R-state to the 2-state through a shock

Equation (4.79) is written for the 4-wave in case of shock ($\Phi_1 > 1$) leading to:

$$\Phi_2 = \frac{1 - z_2 \beta_R}{z_2 - \beta_R}, \qquad \text{and} \qquad z_2 = \frac{\beta_R \Phi_2 + 1}{\beta_R + \Phi_2}, \tag{4.99}$$

with

$$\beta_R = \frac{\Gamma_R + 1}{\Gamma_R - 1}.$$

Using the Rankine–Hugoniot condition (Equation (4.75)) again:

$$u_2 = u_R + \sqrt{\frac{(p_R - p_2)(\rho_R - \rho_2)}{\rho_R \rho_2}} = \sqrt{\frac{(1 - \Phi_2)(1 - z_2)}{\Gamma_R z_2}} \tag{4.100}$$

i.e.

$$\frac{u_2 - u_R}{c_R} = f_4(\underline{W}_R, \Phi_2), \tag{4.101}$$

where:

$$f_4(\underline{W}_R, \Phi_2) \coloneqq \sqrt{\frac{(1 - \Phi_2)(1 - z_2)}{\Gamma_R z_2}}.$$

Summary of the relations for the 4-wave

Finally, the 4-wave relations are:

$$\frac{u_2 - u_R}{c_R} = f_4(\underline{W}_R, \Phi_2) = \begin{cases} -\dfrac{2}{\Gamma_R - 1}\left(1 - \Phi_2^{\frac{1}{2}\left(1-\Gamma_R^{-1}\right)}\right), & \text{if } 0 < \Phi_2 \leq 1 \text{ (4-expansion)}, \\ \left(\dfrac{(1-\Phi_2)(1-z_2)}{\Gamma_R z_2}\right)^{\frac{1}{2}}, & \text{if } \Phi_2 > 1 \text{ (4-shock)}. \end{cases} \tag{4.102}$$

with

$$z_2 = h_4(\underline{W}_R, \Phi_2) = \begin{cases} \Phi_2^{\frac{1}{\Gamma_R}}, & \text{if } 0 < \Phi_2 \leq 1 \text{ (4-expansion)}, \\ \dfrac{\beta_R \Phi_2 + 1}{\beta_R + \Phi_2}, & \text{if } \Phi_2 > 1 \text{ (4-shock)}. \end{cases} \tag{4.103}$$

4.5.6 Summary

Table 4.5.2 summarises the different states relations for all waves.

Wave	Φ_i	**Relations**
1-wave	$0 < \Phi_1 \leq 1$ (expansion)	$\dfrac{u_1 - u_L}{c_L} = f_1(\underline{W}_L, \Phi_1) = \dfrac{2}{\Gamma_L - 1}\left(1 - \Phi_1^{\frac{1}{2}\left(1-\Gamma_L^{-1}\right)}\right)$
		$z_1 = \Phi_1^{\frac{1}{\Gamma_L}}$
	$\Phi_1 > 1$ (shock)	$\dfrac{u_1 - u_L}{c_L} = f_1(\underline{W}_L, \Phi_1) = -\left(\dfrac{(\Phi_1 - 1)(z_1 - 1)}{\Gamma_L z_1}\right)^{\frac{1}{2}}$
		$z_1 = \dfrac{\beta_L \Phi_1 + 1}{\beta_L + \Phi_1}$
4-wave	$0 < \Phi_2 \leq 1$ (expansion)	$\dfrac{u_2 - u_R}{c_R} = f_4(\underline{W}_R, \Phi_2) = -\dfrac{2}{\Gamma_R - 1}\left(1 - \Phi_2^{\frac{1}{2}\left(1-\Gamma_R^{-1}\right)}\right)$
		$z_2 = \Phi_2^{\frac{1}{\Gamma_R}}$
	$\Phi_2 > 1$ (shock)	$\dfrac{u_2 - u_R}{c_R} = f_4(\underline{W}_R, \Phi_2) = \left(\dfrac{(\Phi_2 - 1)(z_2 - 1)}{\Gamma_R z_2}\right)^{\frac{1}{2}}$
		$z_2 = \dfrac{\beta_R \Phi_2 + 1}{\beta_R + \Phi_2}$
2/3-wave		$u_1 = u_2$
		$\Phi_2 = p_L {p_R}^{-1} \Phi_1$

Table 4.5.2: Summary of the relations between each system state.

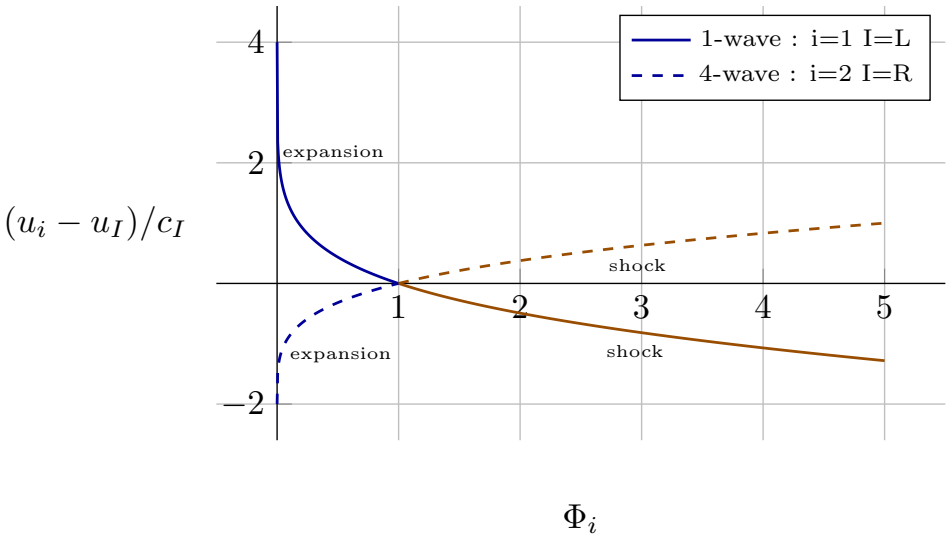

Figure 4.5.3: Connection function for both 1- and 4- waves with $\Gamma_L = 1.5$ and $\Gamma_R = 2$.

4.5.7 Intermediate state

We know that in the contact wave $u_1 = u_2$ and $p_1 = p_2$ (invariants). Thus, one may link the pressure variables Φ_1 and Φ_2:

$$\Phi_2 = \frac{p_2}{p_L} = \frac{p_1}{p_L} = \frac{p_L}{p_R}\Phi_1, \tag{4.104}$$

and:

$$u_L + c_L f_1(\underline{W}_L, \Phi_1) = u_R + c_R f_4\left(\underline{W}_R, \frac{p_L}{p_R}\Phi_1\right). \tag{4.105}$$

The latter equation can be written as:

$$F(\Phi_1) = 0, \tag{4.106}$$

where:

$$F(\Phi_1) = u_L - u_R + c_L f_1(\underline{W}_L, \Phi_1) - c_R f_4\left(\underline{W}_R, \frac{p_L}{p_R}\Phi_1\right).$$

Note that the functions f_1 and f_4 depends of the type of wave (Table 4.5.2). Equation (4.106) can be solved numerically, leading to Φ_1. The other variables calculation is then straightforward.

Monotony of $F(\Phi_1)$

In order to insure that Equation (4.106) has a solution, one must study the study of $F(\Phi_1)$. From Equation (4.105), one can see that $F(\Phi_1)$ has the form of:

$$F(\Phi_1) = u_L - u_R + f_1(\Phi_1) - f_4\left(\frac{p_L}{p_R}\Phi_1\right)$$

The monotony of f_1 is first studied for $\Phi_1 > 0$. If $\Phi_1 \in]0, 1]$:

$$\frac{\partial f_1}{\partial \Phi_1} = -\frac{2}{\Gamma_L - 1}\left(\frac{1}{2} - \frac{1}{2\Gamma_L}\right)\Phi_1^{-\frac{1}{2}[1+\Gamma_L^{-1}]} < 0, \text{since } \Gamma_L > 1. \tag{4.107}$$

If $\Phi_1 > 1$, $f_1(\Phi_1)$ reads:

$$f_1(\Phi_1) = -\left[\frac{(\Phi_1 - 1)\left(\dfrac{\beta_L\Phi_1 + 1}{\beta_L + \Phi_1} - 1\right)(\beta_L + \Phi_1)}{\Gamma_L\,(\beta_L\Phi_1 + 1)}\right]^{\frac{1}{2}} \tag{4.108}$$

$\dfrac{\partial f_1}{\partial \Phi_1} < 0$ if:

$$\frac{\partial}{\partial \Phi_1}\left(\frac{(\Phi_1 - 1)\left(\dfrac{\beta_L\Phi_1 + 1}{\beta_L + \Phi_1} - 1\right)(\beta_L + \Phi_1)}{\Gamma_L\,(\beta_L\Phi_1 + 1)}\right) = g_1'(\Phi_1) > 0. \tag{4.109}$$

g_1' is positive if its numerator

$$\frac{\beta_L^2 - 1}{(\beta_L + \Phi_1)^2}\left[\Gamma_L(\beta_L\Phi_1 + 1)(\Phi_1^2 + \Phi_1(\beta_L - 1) - \beta_L)\right] + \Gamma_L\left(\frac{\beta_L\Phi_1 + 1}{\Phi_1 + \beta_L} - 1\right)(\beta_L\Phi_1^2 + 2\Phi_1 + \beta_L^2 + \beta_L - 1) \tag{4.110}$$

is positive. To ease this function study, we plot it between 0 and 2 (Figure 4.5.4, left), for three different Γ_L values belonging to our studies range. It is observed that after $\Phi_1 > 1$, which is the case for the shock condition, $g_1'(\Phi_1) > 0$, so $f_1'(\Phi_1) < 0$. Figure 4.5.5 presents the same quantity but continuously related to Γ_L and confirms the positivity of $g_1'(\Phi_1)$ for $\Phi_1 > 1$. For both shock and expansion, that is, for $\Phi_1 \in [0, +\infty[$, the function $f_1(\Phi_1)$ decreases. This is confirmed as well by Figure 4.5.3.
The same process is made with the function $-f_4(\Phi_1)$, which has a similar form compared to $f_1(\Phi_1)$. If $\Phi_2 \in]0, 1]$, i.e. if $\Phi_1 \in]0, \frac{p_R}{p_L}]$, one has:

$$\frac{\partial(-f_4(\Phi_1))}{\partial\Phi_1} = -\frac{1}{\Gamma_R - 1}\left(1 - \frac{1}{\Gamma_R}\right)\left(\frac{p_R}{p_L}\right)^{\frac{1}{2}(1-\Gamma_R^{-1})} \Phi_1^{-\frac{1}{2}[1+\Gamma_R^{-1}]} < 0, \text{since } \Gamma_R > 1. \tag{4.111}$$

If $\Phi_1 > \dfrac{p_R}{p_L}$,

$$-f_4(\Phi_1) = -\left(\frac{\left(1 - \dfrac{p_R}{p_L}\Phi_1\right)\left(1 - \dfrac{\beta_R\dfrac{p_R}{p_L}\Phi_1 + 1}{\beta_R + \dfrac{p_R}{p_L}\Phi_1}\right)\left(\beta_R + \dfrac{p_R}{p_L}\Phi_1\right)}{\Gamma_R\left(\beta_R\dfrac{p_R}{p_L}\Phi_1 + 1\right)}\right)^{\frac{1}{2}} \tag{4.112}$$

The term inside the brackets is positive if $\Phi_1 > \dfrac{p_L}{p_R}$, which is insured if $p_R > p_L$ in the given conditions. Then, the derivative of $f_4(\Phi_1)$ is negative if

$$\frac{\partial}{\partial\Phi_1}\left(\frac{\left(1 - \dfrac{p_R}{p_L}\Phi_1\right)\left(1 - \dfrac{\beta_R\dfrac{p_R}{p_L}\Phi_1 + 1}{\beta_R + \dfrac{p_R}{p_L}\Phi_1}\right)\left(\beta_R + \dfrac{p_R}{p_L}\Phi_1\right)}{\Gamma_R\left(\beta_R\dfrac{p_R}{p_L}\Phi_1 + 1\right)}\right) = g_4'(\Phi_1) > 0. \tag{4.113}$$

that is, if $g_4'(\Phi_1)$ numerator:

$$\Gamma_R\left(1 - \frac{\beta_R\alpha_p\Phi_1 + 1}{\beta_R + \alpha_p\Phi_1}\right)\left(\beta_R\alpha_p^3\Phi_1^2 - 2\alpha^2\Phi_1 - \beta_R^2\alpha_p - \beta_R\alpha_+\alpha_p\right)$$
$$+ \Gamma_R\frac{\alpha_p - \beta_R^2\alpha_p}{(\beta_R + \alpha_p\Phi_1)^2}\left((\beta_R\alpha\Phi_1 + 1)(\beta_R + \alpha_p\Phi_1 - \beta_R\alpha_p\Phi_1 - \alpha_p^2\Phi_1^2)\right) > 0,$$

where $\alpha_p = \dfrac{p_R}{p_L}$. Figure 4.5.4, right, shows, for a fixed $\alpha_p = 10$ and three different Γ_R values, the numerator of $g_4'(\Phi_1)$. For $\Phi_1 > \dfrac{1}{\alpha_p} = \dfrac{p_L}{p_R}$, the numerator is positive for all Γ_R displayed and thus $f_4(\Phi_1)$ is a decreasing function. Again, the same function is represented in three dimensions in Figure 4.5.5, right, and confirms the term positivity for $\Phi_1 > \dfrac{1}{\alpha}$. Finally, if $f_1(\Phi_1)$ and $-f_4(\Phi_1)$ are decreasing functions, so is $F(\Phi_1)$ and the Riemann problem has an unique solution. In presence of shocks, this is the case only if $\Phi_1 > \dfrac{p_L}{p_R}$, which is always verified if $\dfrac{p_R}{p_L} > 1$.

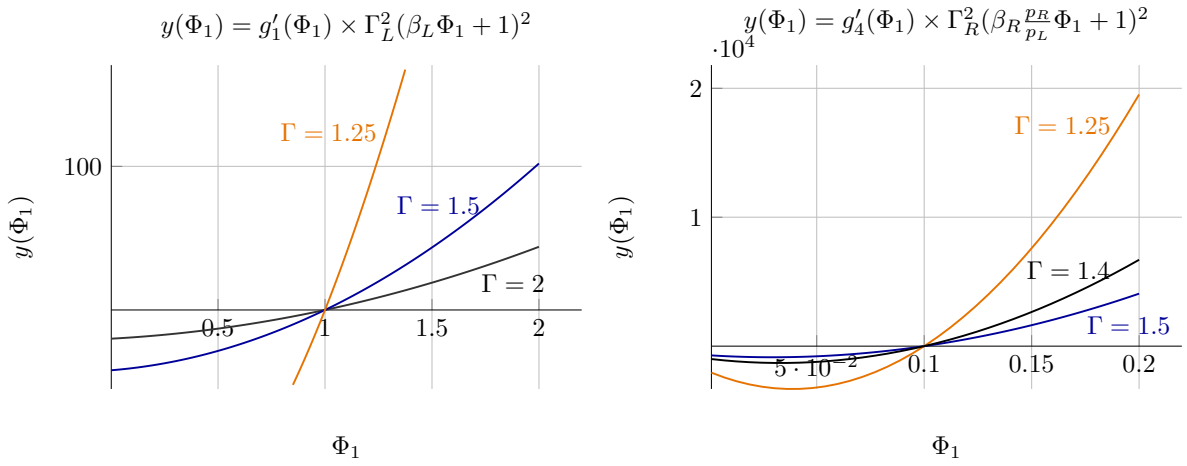

Figure 4.5.4: (Left) Numerator of $g_1'(\Phi_1)$. (Right) Numerator of $g_4'(\Phi_1)$ for $\alpha_p = 10$.

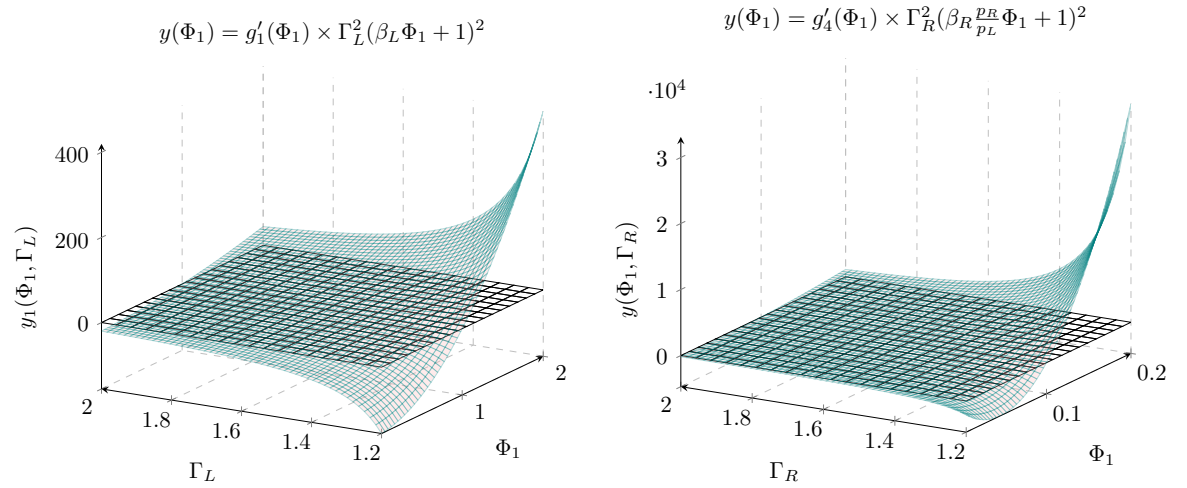

Figure 4.5.5: Surface plot for the study of the monotony of $F_1(\Phi_1)$ (Left) Numerator of $g_1'(\Phi_1)$. (Right) Numerator of $g_4'(\Phi_1)$ for $\alpha_p = 10$.

The exact solution of the Riemann problem related to the moist air time scheme set of equations was derived in this section. The latter will be used in the next section to verify the scheme accuracy on different Riemann problems.

4.6 Verification

4.6.1 0-D closed cavity with phase change

Motivations 4.6.1. This verification case test the scheme ability to correctly reproduce the water phase change while preserving the system mass with a temperature and pressure variation. The convergence of the Newton method related to the saturation treatment is studied as well.

A single [$1 \times 1 \times 1$] m cell is first considered to evaluate the treatment of the water phase change by the presented scheme. During 10 s, an outgoing heat flux ($Q_{in} = 100\,\mathrm{W\,m^{-2}}$) is imposed on the cell lateral walls, then, the same flux is injected back from 10 s to 20 s. The time step is $\Delta t = 1\,\mathrm{s}$ and 1

inner iteration is performed (the error threshold related to the inner iterations is directly reached, since the velocity is null).
The initial temperature and pressure are $T_0 = 293.15\,\mathrm{K}$ and $p_0 = 101\,325\,\mathrm{Pa}$. The cell total water mass fraction is constant and equal to $y_w = 0.0125$. With the system internal energy variation, the cell reaches saturation and the liquid and vapor water mass fractions change over time.
As shown in Figure 4.6.1, the initial state is recovered for all studied variables. It is observed as well that when the saturation is reached, the slope of the temperature variation changes, but not the internal energy one. Note that the sum of the water vapor and liquid mass fraction is always equal to the total water mass fraction, which is in agreement with the chosen moist air model. Moreover, Figure 4.6.2 shows the density and internal energy L_2 normalised error norm:

$$L_2^{\mathrm{err}}(\psi) := \sqrt{\frac{\frac{1}{\Omega_{tot}}\sum_c (\psi_c - \psi_{ex})^2 \Omega_c}{\frac{1}{\Omega_{tot}}\sum_c \psi_0^2 \Omega_c}}. \tag{4.114}$$

For the two variables, the error is below the solver precision of 10^{-8}, emphasising the simulation accuracy. Figure 4.6.3 illustrates the Newton's method used to compute the temperature from the mixture internal energy. The method error threshold is set to 10^{-4}, reached after three inner iterations. Finally, Figure 4.6.4 compares the water vapour mass fraction and pressure to their saturation values. One wants to verify that if the phase change occurs, both quantities are equal.

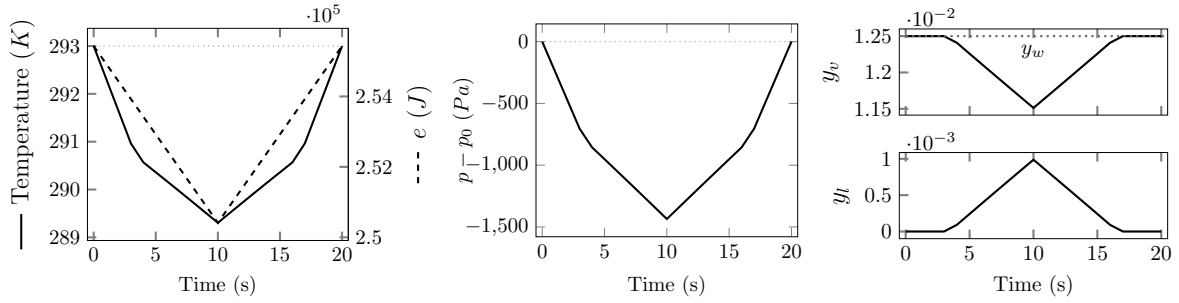

Figure 4.6.1: Variables evolution following time. (Left) Temperature and internal energy. (Middle) Pressure. (Right) water mass fractions.

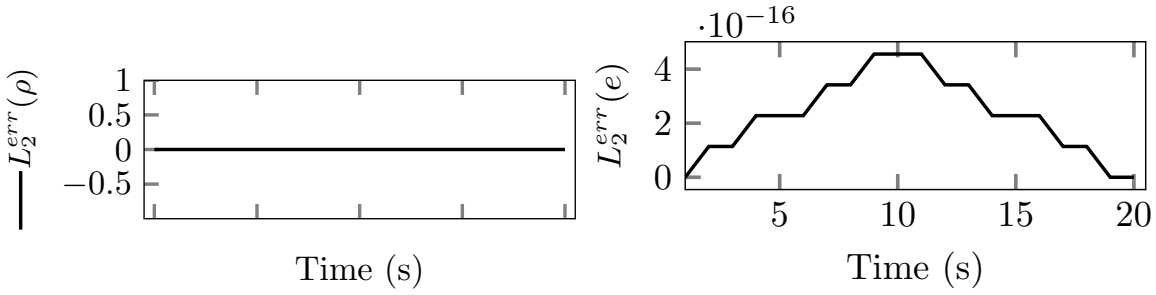

Figure 4.6.2: Variables L_2 error norm evolution following time. (Left) density. (Right) internal energy.

4.6.2 Riemann problem associated to the system

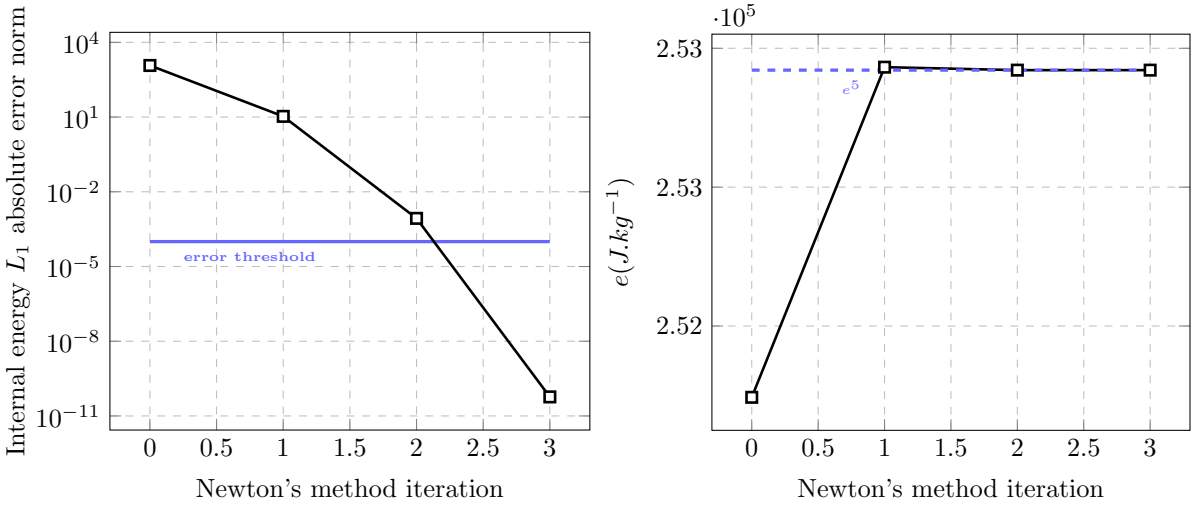

Figure 4.6.3: (Left) Internal energy L_1 error norm for each Newton's method iteration for the first time iteration in saturation. In blue, the error threshold value. (Right) Internal energy variation at the same time iteration. In blue, the value of the solved internal energy.

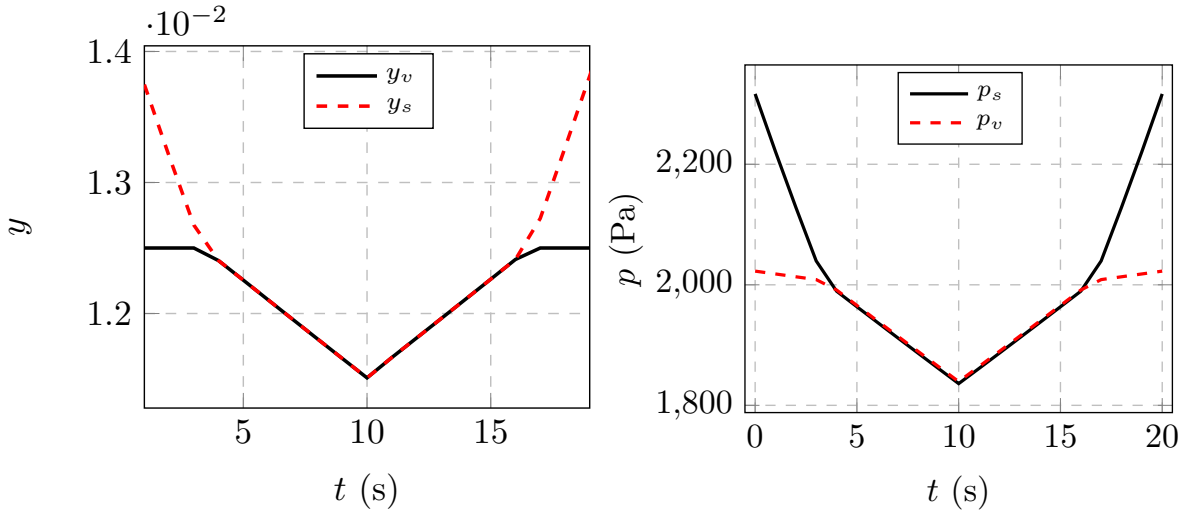

Figure 4.6.4: (Left) Vapour mass fraction compared to its value at saturation given the system pressure and temperature following time. (Right) Vapour pressure compared to its value at saturation given the system temperature following time.

Motivations 4.6.2. In this test case the time scheme is tested for the system (4.53) Riemann problem, whose exact solution was derived in Section 4.5. Its consistency, i.e. conservation of total energy through the source term in the internal energy equation, is verified through shock and contact waves.

Different test cases are studied to verify the scheme accuracy related to the Riemann problem presented in Section 4.5. First, an unsteady contact discontinuity (UCD) is considered followed by two double symmetric shock (DSS1 and DSS2) problems. No phase change is considered and the simulations are carried out on grids with $2^m \times M_0$ cells, $0 \leq m \leq 5$, with $M_0 = 800$ for the UCD and DSS2 cases and $M_0 = 80$ for the DSS1 case.
The initial conditions are given in Table 4.6.1. Note that the first DSS problem falls within the indoor environment context, while the second involves more important velocity magnitudes, which is useful to

test the kinetic energy source term in the mixture internal energy equation. The computational domain is a tube of length $L = 400\,\mathrm{m}$ for the UCD and DSS2 and $L = 40\,\mathrm{m}$ for the DSS1, extending from $x = -L/2$ to $x = L/2$, the interface being located at $x = 0\,\mathrm{m}$. Symmetry conditions are imposed on all boundary faces of the computational domain except at the two end faces of the tube, which are set to be outlets. For each case, the fields L_1 error norm (related to the Riemann problem exact solution ψ_e, Equation (4.115)) is studied for $\theta = 1$, and a constant CFL at $t = 0.3\,\mathrm{s}$ for the UCD (CFL $= 0.04$), $t = 0.03\,\mathrm{s}$ for the DSS1 (CFL $= 0.04$) and $t = 0.05\,\mathrm{s}$ for the DSS2 (CFL $= 0.8$).

Test	$y_{w,L}$	$T_L[\mathrm{K}]$	$u_L[\mathrm{m\,s^{-1}}]$	$p_L[\mathrm{Pa}]$	$y_{w,R}$	$T_R[\mathrm{K}]$	$u_R[\mathrm{m\,s^{-1}}]$	$p_R[\mathrm{Pa}]$
UCD	0.01	300	2.0	100,000	0.015	320	2.0	100,000
DSS1	0.0125	293.0	10.0	100,000	0.0125	293.0	-10.0	100,000
DSS2	0.0125	293.0	200.0	100,000	0.0125	293.0	-200.0	100,000

Table 4.6.1: Initial states for the two one-dimensional Riemann problems used.

$$L_1^{err}(\psi) = \frac{\sum_{c=1}^{N_c} |\Omega_c| \, |\psi_e(x_c) - \psi_c|}{\sum_{c=1}^{N_c} |\Omega_c| \, |\psi_e(x_c)|}. \tag{4.115}$$

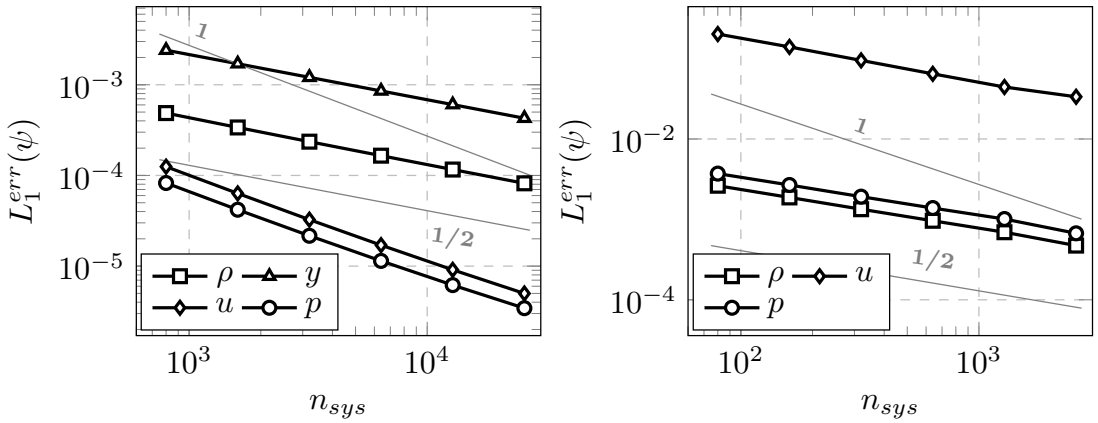

Figure 4.6.5: Variables L_1 error norm for (right) UCD at $t = 0.05\,\mathrm{s}$, (left) DSS1 at $t = 0.3\,\mathrm{s}$.

Figure 4.6.5 shows the L_1 error norm for the different system variables given the mesh refinement for the UCD and DSS1. It is observed for both cases that the numerical scheme is consistent compared to the exact solution. Moreover, for the UCD, the density and water mass fraction have a convergence rate of $\frac{1}{2}$ whereas the pressure and velocity convergence rate is close to 1, which is expected (Gallouët et al., 2002).

For the DSS1, all the variables present a convergence rate of $\frac{1}{2}$, which is expected as well (note that the error for the total water mass fraction was to the machine precision, this is the reason that it is not represented in the right figure).

Figures 4.6.6 and 4.6.7 show in a qualitative way the good agreement between the numerical results and the problems UCD and DSS1 exact solutions while the mesh is refined.

Figure 4.6.8 shows the L_1 error norm for the different DSS2 variables for different mesh refinements at $t = 0.05\,\mathrm{s}$ and $\theta = 1$). The left figure represents simulations with 4 inner iterations and the kinetic energy source term. The centre one represents simulations with 4 inner iterations but with no source term and lastly, the right figure is related to simulations with 8 inner iterations and source term. It is observed first that with no kinetic energy source term, the scheme is not consistent: an asymptotic error is reached for more refined meshes in the centre figure. This confirms the results presented in the verification section of the dry air scheme related to singular solutions (Section 3.8). For the others, the numerical error convergence rate tends to $\frac{1}{2}$, even if for coarse meshes it presents a first order rate. Although the scheme is consistent, it is observed that some numerical error is created, polluting its convergence rate. The same can be observed using $\theta = 1/2$ (Figure 4.6.8, bottom). The different fields at the final simulation time are represented in Figure 4.6.9.

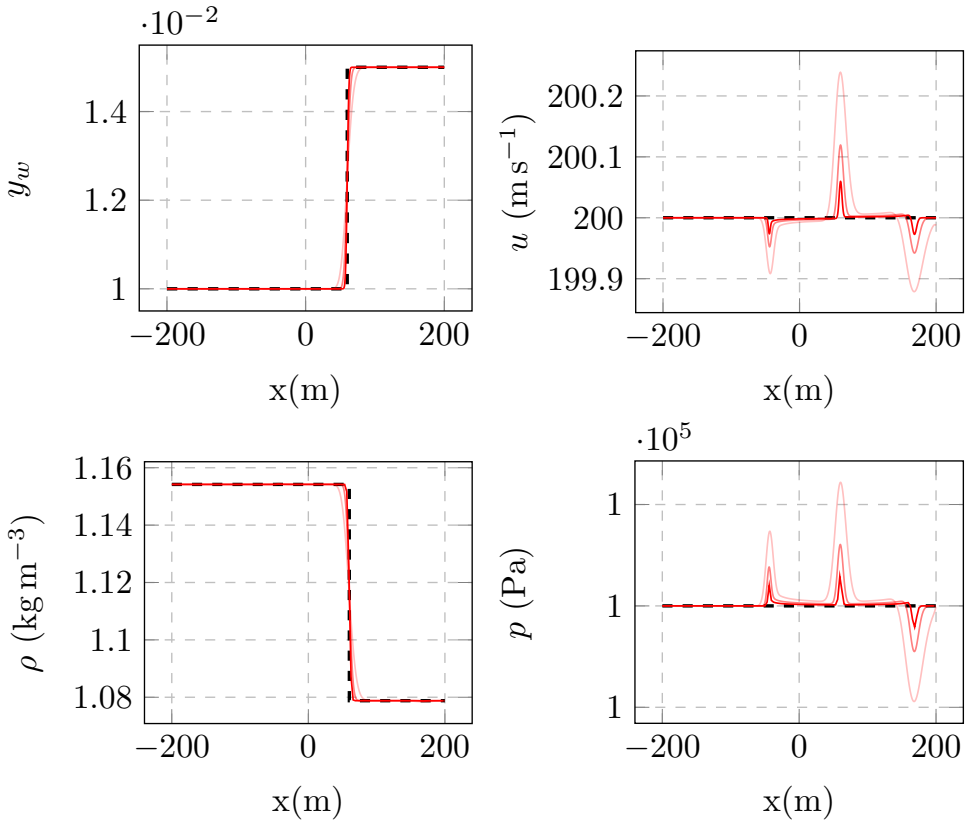

Figure 4.6.6: UCD case fields at $t = 0.3\,\mathrm{s}$ for different mesh refinements (800, 3200, 12800). (- -) Exact solution. (–) Simulation.

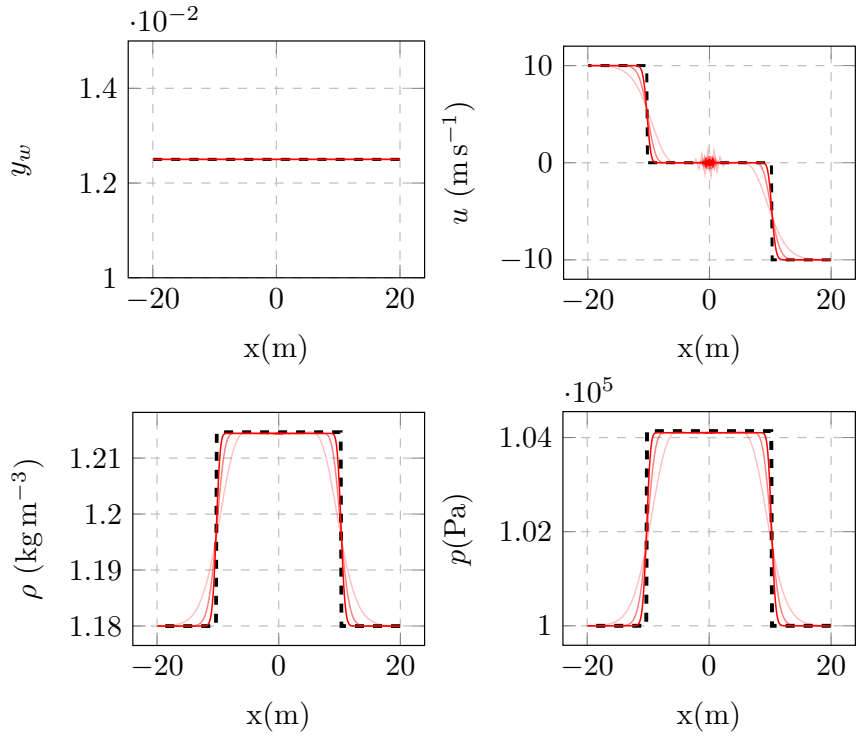

Figure 4.6.7: DSS1 case fields at $t = 0.03\,\mathrm{s}$ for different mesh refinements (80, 320, 1280). (- -) Exact solution. (–) Simulation.

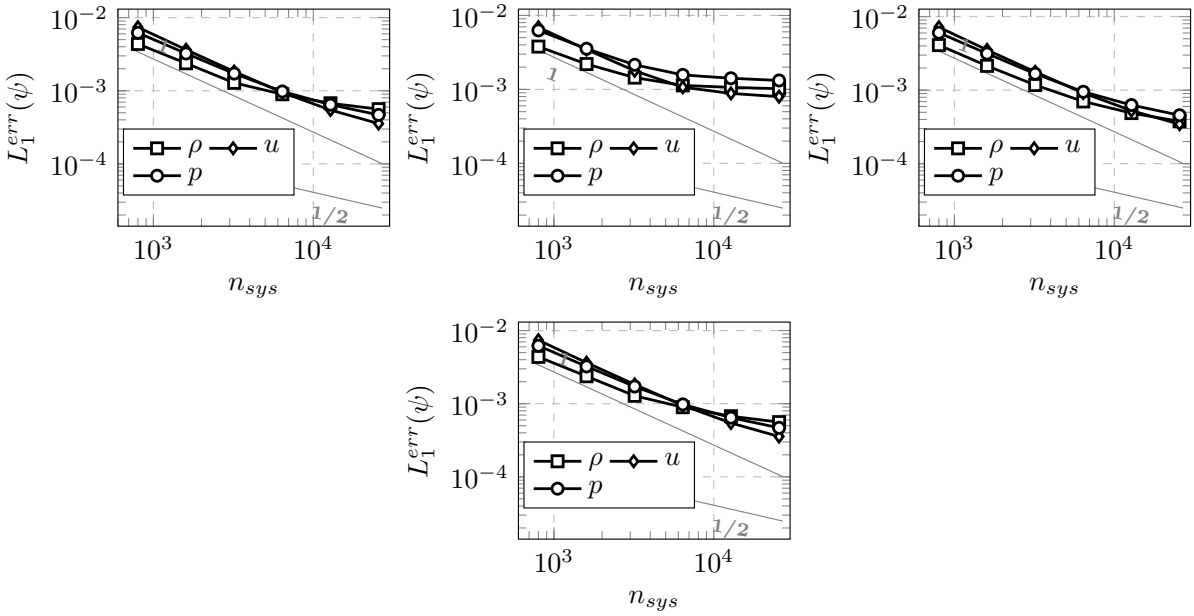

Figure 4.6.8: Variables L_1 error norm for the DSS2 test case ($\theta = 1$). (Left) With the kinetic energy source term and 4 inner iterations. (Centre) Without the kinetic energy source term and 4 inner iterations (Right) With the kinetic energy source term and 8 inner iterations. (Bottom With the kinetic energy source term, 4 inner iterations and $\theta = 1/2$.

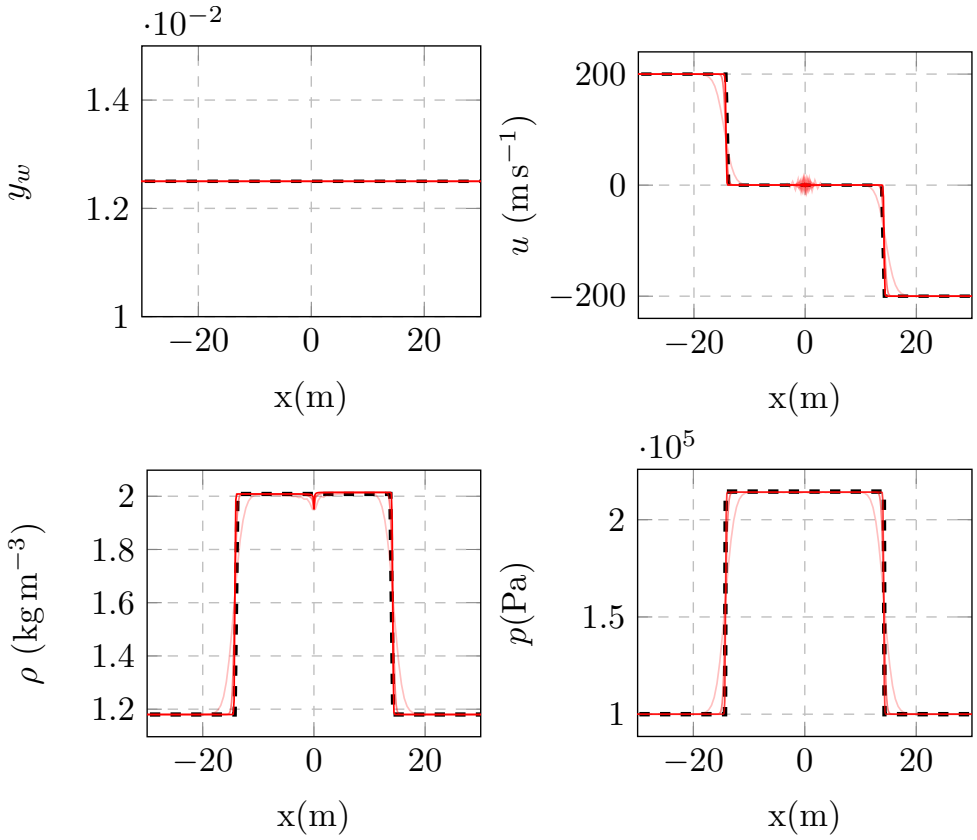

Figure 4.6.9: DSS2 case fields at $t = 0.05\,\mathrm{s}$ for different mesh refinements (80, 320, 1280). (- -) Exact solution. (–) Simulation.

4.7 Summary

In this chapter the dry air scheme, implemented in code_saturne, verified and validated in Chapter 3 is extended for moist air applications. A dispersed flow (droplet flow) is considered and an homogeneous model is used. The mixture pressure is computed through the Dalton law and the temperature is calculated from the solved internal energy using the Newton method in case of saturation. Note that all properties presented for the dry air scheme are preserved.

A numerical analysis provided similar stability conditions compared to the previous scheme; this is a direct consequence of the use of the same equations for the internal energy and pressure correction.

Then, the scheme is verified against two analytical cases. The first verifies its capability to take into account phase change. The second tests its accuracy for the Riemann problem related to the moist air scheme set of equations, which presents some differences compared to the classical Euler equations. Its exact solution derivation is detailed as well in this chapter.

We highlight in this summary that the use of this type of scheme is recommended only when the volume fraction of liquid water in the mixture is small compared to the two others, since it is an important hypothesis made while designing the scheme.

For further investigations, two main subjects can be mentioned. First, the validation of the scheme, notably in cases with diffusion and phase change. This could be done at first for nuclear safety applications (Blain et al., 2016; Tonello and Fournier, 2017) using the "cooling tower" module (already existent in code_saturne), then for an indoor environment test case, which is still to be identified.

Also, an investigation on a possible Riemann problem exact solution in case of phase change (y_v varies) shall be interesting, which was not done in this chapter for reasons of time. Other methods to compute the temperature from the internal energy could be tested as well to accelerate the calculation time.
This scheme application to the atmospheric framework can be study as well for coupling indoor and outdoor flow. The simplified model may not be able to accurately reproduce high height flow notably with the presence of nucleation. A transport equation could be added and a new verification and validation process would be necessary.

Appendix

4.A Derivation of the mixture equations

4.A.1 Mass equation

The mass equation for each element reads:

$$\begin{aligned}
&(a) \qquad \frac{\partial(y_a\rho)}{\partial t} + \text{div}\,(y_a\rho\underline{u}) = 0,\\
&(v) \qquad \frac{\partial(y_v\rho)}{\partial t} + \text{div}\,(y_v\rho\underline{u}) = \Gamma_w,\\
&(l) \qquad \frac{\partial(y_l\rho)}{\partial t} + \text{div}\,(y_l\rho\underline{u}) = -\Gamma_w,
\end{aligned} \tag{4.116}$$

where ρ is the mixture density and Γ_w is a source term related to phase change (either condensation or evaporation). The sum of the three equations leads to the mixture equation of mass:

$$\frac{\partial\rho}{\partial t} + \text{div}\ (\rho\underline{u}) = 0, \tag{4.117}$$

since $y_a + y_v + y_l = 1$.

4.A.2 Momentum equation

Similarly, one has, for the momentum equation:

$$\begin{aligned}
&(a) \qquad \frac{\partial(y_a\rho\underline{u})}{\partial t} + \text{div}\,(y_a\rho\underline{u}\otimes\underline{u}) = y_a\rho\underline{f} + \underline{\text{div}}\,(y_a\underline{\tau}) - \underline{\nabla}p_a,\\
&(v) \qquad \frac{\partial(y_v\rho\underline{u})}{\partial t} + \text{div}\,(y_v\rho\underline{u}\otimes\underline{u}) = y_v\rho\underline{f} + \underline{\text{div}}\,(y_v\underline{\tau}) - \underline{\nabla}p_v,\\
&(l) \qquad \frac{\partial(y_l\rho\underline{u})}{\partial t} + \text{div}\,(y_l\rho\underline{u}\otimes\underline{u}) = y_l\rho\underline{f} + \underline{\text{div}}\,(y_l\tau).
\end{aligned} \tag{4.118}$$

The mixture pressure p follows the Dalton (1802) law so:

$$p = p_a + p_v.$$

By adding the latter equations, the mixture momentum equation reads:

$$\frac{\partial(\rho\underline{u})}{\partial t} + \text{div}\,(\rho\underline{u}\otimes\underline{u}) = \rho\underline{f} + \underline{\text{div}}\,(\underline{\tau}) - \underline{\nabla}p. \tag{4.119}$$

4.A.3 Thermal equations

It is reminded that the goal is to use the same equations from the indoor dry air time scheme, in order to preserve as possible its numerical main features, presented in the last chapter. The internal energy equation for each mixture component is thus written.
First, the total energy equation for the dry air (with no external thermal sources) reads:

$$\frac{\partial \left(y_a \rho E_a\right)}{\partial t} + \text{div}\left(y_a \rho E_a \underline{u}\right) = \text{div}\left(\left(y_a \underline{\underline{\tau}} - p_a \underline{\underline{I}}\right) \cdot \underline{u}\right) + y_a \text{div}\left(\lambda \underline{\nabla} T\right) + y_a \rho \underline{f} \cdot \underline{u}. \tag{4.120}$$

Using the momentum equation, it has been shown in the second chapter that the kinetic energy equation e_k can be written for the dry air as:

$$\frac{\partial (y_a \rho e_k)}{\partial t} + \text{div}\ \left(y_a \rho e_k \underline{u}\right) = -\underline{u} \cdot \underline{\nabla} p_a + \underline{u} \cdot \underline{\text{div}}\left(y_a \underline{\underline{\tau}}\right) + y_a \rho \underline{f} \cdot \underline{u}. \tag{4.121}$$

Subtracting Equation (4.121) to Equation (4.120) leads to the internal energy equation for the dry air:

$$\frac{\partial \left(y_a \rho e_a\right)}{\partial t} + \text{div}\left(y_a \rho e_a \underline{u}\right) = -p_a \text{div}\left(\underline{u}\right) + y_a \text{div}\left(\lambda \underline{\nabla} T\right) + y_a \underline{\underline{\tau}} : \underline{\underline{\nabla}} \underline{u}. \tag{4.122}$$

For the vapor of water, the total energy equation is:

$$\frac{\partial \left(y_v \rho E_v\right)}{\partial t} + \text{div}\left(y_v \rho E_v \underline{u}\right) = \text{div}\left(\left(y_v \underline{\underline{\tau}} - p_v \underline{\underline{I}}\right) \cdot \underline{u}\right) + y_v \text{div}\left(\lambda \underline{\nabla} T\right) + y_v \rho \underline{f} \cdot \underline{u}. \tag{4.123}$$

Note that this equation written is the non conservative form has a new term related to the vapor of water source term in the continuity equation:

$$\begin{aligned} y_v \rho \frac{\mathrm{d}E_v}{\mathrm{d}t} + E_v \left(\frac{\partial y_v \rho}{\partial t} + \text{div}\left(y_v \rho \underline{u}\right)\right) &= y_v \rho \frac{\mathrm{d}E_v}{\mathrm{d}t} + E_v \Gamma_w, \\ &= \text{div}\left(y_v \underline{\underline{\tau}} \cdot \underline{u}\right) - \text{div}\ \left(p_v \underline{u}\right) + y_v \text{div}\ \left(\lambda \underline{\nabla} T\right) + y_v \rho \underline{f} \cdot \underline{u}. \end{aligned} \tag{4.124}$$

Similarly, the water vapor kinetic energy equation reads:

$$y_v \rho \frac{\mathrm{d}e_k}{\mathrm{d}t} + \underline{u} \Gamma_w = -\underline{u} \cdot \underline{\nabla}(p_v) + y_v \rho \underline{f} \cdot \underline{u} + \underline{u} \cdot \underline{\text{div}}\left(y_v \underline{\underline{\tau}}\right), \tag{4.125}$$

leading to the internal energy equation for the vapor of water:

$$y_v \rho \frac{\mathrm{d}e_v}{\mathrm{d}t} + \left(E_v + \underline{u}\right) \Gamma_w = -p_v \text{div}\left(\underline{u}\right) + y_v \text{div}\left(\lambda \underline{\nabla} T\right) + y_v \underline{\underline{\tau}} : \underline{\underline{\nabla}} \underline{u}. \tag{4.126}$$

Finally, using the same methodology, the internal energy for the liquid water reads:

$$y_l \rho \frac{\mathrm{d}e_l}{\mathrm{d}t} - \left(E_l + \underline{u}\right) \Gamma_w = y_l \text{div}\left(\lambda \underline{\nabla} T\right) + y_l \underline{\underline{\tau}} : \underline{\underline{\nabla}} \underline{u}. \tag{4.127}$$

Summing up the internal energy equation of each element leads to the mixture internal energy equation:

$$\begin{aligned} &\rho \left[y_a \frac{\mathrm{d}e_a}{\mathrm{d}t} + y_v \frac{\mathrm{d}e_v}{\mathrm{d}t} + y_l \frac{\mathrm{d}e_l}{\mathrm{d}t}\right] + \Gamma_w \left[e_v - e_l\right] = -(p_a + p_v) \text{div}\left(\underline{u}\right) \\ &+ \left(y_a + y_v + y_l\right) \left[\text{div}\ \left(\lambda \underline{\nabla} T\right) + \underline{\underline{\tau}} : \underline{\underline{\nabla}} \underline{u}\right]. \end{aligned} \tag{4.128}$$

Note that $E_v - E_l = e_v + e_k - e_l - e_k$. Writing the latter equation in its conservative form and denoting the mixture internal energy $e = y_a e_a + y_v e_v + y_l e_l$, one has:

$$\frac{\partial (\rho e)}{\partial t} + \text{div}\left(\rho e \underline{u}\right) = -p \text{div}\left(\underline{u}\right) + \text{div}\ \left(\lambda \underline{\nabla} T\right) + \underline{\underline{\tau}} : \underline{\underline{\nabla}} \underline{u}. \tag{4.129}$$

Each element internal energy may be written in terms of temperature (Satoh, 2013) [↗]:

$$\begin{aligned} e_a &= c_{va} T, \\ e_v &= c_{vv} T + y_v L_{00}, \\ e_l &= c_l T. \end{aligned} \tag{4.130}$$

c_{va}, c_{vv} and c_l are the different mixture components heat capacities.

4.B Moist air parameters variation

In this Section are presented some physical laws for the moist air parameters proposed in the literature (Tsilingiris, 2018) that may complement this chapter work.
Let's define some useful quantities, not yet presented, that are used in the following expressions.
The relative humidity is defined in this section as

$$RH = \frac{p_v}{p_s}.$$

The water vapor molar fraction is defined as

$$x_v = \frac{n_v}{n_a + n_v},$$

where n_a and n_v are respectively the moles of dry air and water vapor. The different formula involve the air and vapor of water components properties denoted with respectively subscripts (a) and (v). For further details on each component expression (usually empirical), the user may refer to Tsilingiris (2018) .

4.B.1 Mixture viscosity

Sutherland (1895) proposed a relation for the viscosity of a mixture based on simple kinetic theory considerations, that is the base of the extensive investigations that followed. Nevertheless, he did not take into account the effect of inter-molecular forces and collisions in his formula. These effects led to more complicated mathematical expressions. One of the most cited is the Wilke (1950) one:

$$\mu_m = \sum_{i=1}^{n} \frac{x_i \mu_i}{\sum_{j=1}^{n} x_j \phi_{ij}}, \tag{4.131}$$

where μ_i is an element i viscosity, ϕ_{ij} is an interaction parameterx:

$$\phi_{ij} = \frac{\left[1 + \left(\frac{\mu_i}{\mu_j}\right)^{\frac{1}{2}} \left(\frac{M_j}{M_i}\right)^{\frac{1}{4}}\right]^2}{\left[8\left(1 + \frac{M_i}{M_j}\right)\right]^{\frac{1}{2}}}. \tag{4.132}$$

The combination of the two previous equations yields, for the mixture components:

$$\mu_m = \frac{\left[1 - f\ RH\frac{p_s}{p_0}\right]\mu_a}{\left[1 - f\ RH\frac{p_s}{p_0}\right] + f\ RH\frac{p_s}{p_0}\Phi_{av}} + \frac{\left[1 - f\ RH\frac{p_s}{p_0}\right]\mu_v}{\left[1 - f\ RH\frac{p_s}{p_0}\right] + f\ RH\frac{p_s}{p_0}\Phi_{va}}. \tag{4.133}$$

f is a functional dependent on the temperature and pressure of the mixture which recommended expression (Greenspan, 1976) is:

$$f = \exp\left(\xi_1\left(1 - \frac{p_s}{p_0}\right) + \xi_2\left(\frac{p_s}{p_0} - 1\right)\right),$$

with $\xi_1 = \sum_{i=0}^{3} A_i T^i$ and $\xi_2 = \exp\left(\sum_{i=0}^{3} B_i T^i\right)$. The coefficients A_i and B_i can be found in Tsilingiris (2018) .

A simpler semi-empirical alternative (Touloukian et al., 1975) for Wilke's equation is:

$$\mu_m = \frac{\sum_{i=1}^{n} x_i \mu_i M_i^{0.5}}{\sum_{i=1}^{n} x_i M_i^{0.5}}. \tag{4.134}$$

For the dry air and water vapor mixture this becomes:

$$\mu_m = \frac{\mu_a (p_0 - p_v)\sqrt{M_a} + \mu_v p_v \sqrt{M_w}}{(p_0 - p_v)\sqrt{M_a} + p_v \sqrt{M_w}} \tag{4.135}$$

Studnikov (1970) proposed an empirical formula using the experimental measurements by Kestin and Whitelaw (1964) at 298, 323 and 348K. For the present mixture, it reads:

$$\mu_m = \left[\mu_a (1 - RH\frac{p_s}{p_0}) + \mu_v RH \frac{p_s}{p_0}\right]\left[1 + \frac{1}{\alpha} RH \frac{p_s}{p_0}(1 - RH\frac{p_s}{p_0})\right] \tag{4.136}$$

Finally, Nelson (RH and Chilton, 1973) proposed:

$$\mu_m = \frac{\mu_a + x_v(0.78887\mu_v - \mu_a)}{1 - 0.2113 x_v} \tag{4.137}$$

In his recent review, Tsilingiris (2018) compared Nelson's formula (4.137) and Vilke's (4.133) to experimental data. Both expressions led to similar results, with a slight underestimation of the experimental viscosity, especially at the mid temperature range of interest ($> 320\,\mathrm{K}$, about 8% of deviation).

4.B.2 Mixture thermal conductivity

Using the same analogy presented in the viscosity section, the most detailed formula for the thermal conductivity applied to the air vapor mixture is:

$$k_m = \frac{\left[1 - f\ RH\left(\frac{p_s}{p_0}\right)\right] k_a}{\left[1 - f\ RH\left(\frac{p_s}{p_0}\right)\right] - f\ RH \frac{p_s}{p_0}\Phi_{av}} + \frac{\left[1 - f\ RH\left(\frac{p_s}{p_0}\right)\right] k_v}{\left[1 - f\ RH\left(\frac{p_s}{p_0}\right)\right] - f\ RH \frac{p_s}{p_0}\Phi_{va}}, \tag{4.138}$$

where:

$$\Phi_{ij} = \varepsilon \frac{\left[1 + \left(\frac{k_i}{k_j}\right)^{\frac{1}{2}} \left(\frac{M_j}{M_i}\right)^{\frac{1}{4}}\right]^2}{\left[8\left(1 + \frac{M_i}{M_j}\right)\right]^{\frac{1}{2}}}.$$

ε is usually set as 1, but can be found also as 1.065 and 0.85. Nelson proposes the following empirical formula:

$$k_m = \frac{k_a + x_v(0.8536 k_v - k_a)}{1 - 0.1464 x_v}. \tag{4.139}$$

Similarly to the mixture viscosity, the Nelson formula (4.139) and Equation (4.138) are compared to experimental data (even if the thermal conductivity measurements in the literature are scarce). The differences between the two expressions are about 1%. Nevertheless, for the only available experimental data (above $330\,\mathrm{K}$) these formulas clearly underestimated the thermal conductivity.

4.B.3 Specific heat capacity

Tsilingiris (2018), proposes the following formula for the moist air specific air capacity:

$$c_{pm} = \frac{c_{pa}\left(1 - f\ RH\frac{p_s}{p_0}\right)M_a + c_{pv} f\ RH\ M_w\frac{p_s}{p_0}}{[1 - f\ RH\frac{p_s}{p_0}]M_a + f\ RH\ M_w\frac{p_s}{p_0}} \tag{4.140}$$

However, it is reminded that the present scheme solves the mixture internal energy equation, which uses the isobaric heat capacity c_{vm}, defined as:

$$c_{vm} = y_a c_{va} + y_v c_{vv} + y_l c_{vl}.$$

Since a specific procedure related to the variation of water vapor is done if saturation, the last expression is kept.

CHAPTER 5

Study of the Pierre de Coubertin stadium

Résumé

Ce chapitre applicatif traite de l'étude de l'aéraulique du stade Pierre de Coubertin en utilisant le schéma CFD présenté dans les deux chapitres précédents. L'étude du système se fait grâce à un maillage numérique construit à partir d'un nuage de points 3-D obtenu grâce à des mesures laser et est divisée en trois étapes principales. La première est l'identification de zones d'intérêt grâce aux premières simulations, qui servira à l'établissement d'un protocole expérimental pour une campagne qui se déroulera en 2023. La deuxième est une validation complémentaire du schéma aéraulique basée sur des données chimiques mesurées en 2021 lors d'une campagne réalisée par différents laboratoires dont le CEREA. Enfin, une comparaison entre approches turbulentes et schémas est réalisée et un exemple d'application possible est présenté pour conclure le chapitre.

5.1 Introduction

As saw in Chapter 2, the indoor airflow is highly influenced by pressure differences and buoyant effects (Linden, 1999; Hunt and Linden, 1999; Cook et al., 2003) . With the increasing number of international sports competitions and mediation, sport institutions are more likely to invest on gymnasium and stadium constructions. This comes with interesting research content to design optimal and comfortable sport structures. Indeed, as a public space, every new sport stadium shall provide requirements related to a healthy, comfortable and energy effective ventilation-system.
This chapter focuses on the study of the indoor airflow of the Pierre de Coubertin stadium, located in Paris. All numerical simulations are performed using the CPC scheme, presented in the last two chapters.

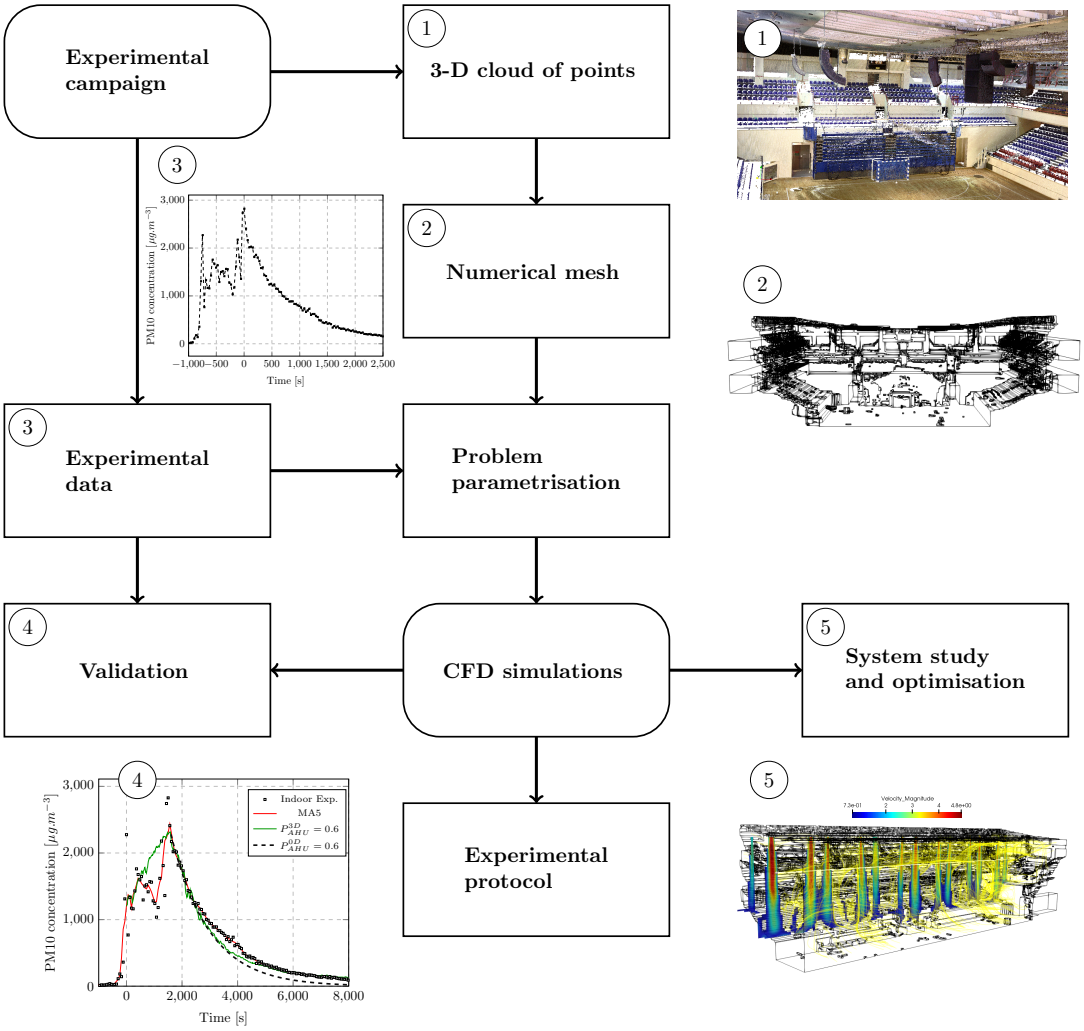

Figure 5.1.1: Main methodology steps for this chapter study.

Thermal comfort in such structures has been already widely studied in the literature. Semi (Aarts et al., 2009; van Hooff and Blocken, 2013; Shi and An, 2017; Sofotasiou et al., 2017; Guo et al., 2022) and fully enclosed (Qin et al., 2006; Sakai et al., 2007; Qian and Yang, 2016; Huang et al., 2021) structures studies have been carried out. Table 5.1.1 summarises the different applications of CFD simulations related to stadiums and gymnasiums. The various studies performed in this chapter are based on them. Note that besides the different type of studies, going from the comparison of models to the optimisation of the stadium geometry or the study of a specie propagation, no study dealt with

thermal comfort indices. Riffelli (2021) presents different global comfort indices and a review of the indoor studies related to them. Among the thermal indices, the predicted mean vote (PMV) is the most popular (Fanger, 1984). Based on the relationship between human body functions and the feeling of the thermal comfort, its values lies between -3 (too cold) and 3 (too hot), zero representing the ideal thermal condition. For an occupant, its formula (Fanger et al., 1970) is function of the air relative humidity, mean air temperature, mean radiant temperature, which takes into account the effect of incident solar radiation, the operating temperature (average of aforementioned temperatures), the mean air speed surrounding the occupant and finally its clothing insulation.
Concerning the IAQ indices, one may use one of the three following design parameters (Comité Européen de Normalisation, 2007):

- Perceived quality of air.
- Pollutant concentration criteria.
- Ventilation airflow rate.

Reference	Type of structure	Model	Studies
van Hooff and Blocken (2013)	semi-enclosed 3-D	$k-\varepsilon$	CO_2 concentration decay ventilation efficiency
Shi and An (2017)	semi-enclosed 3-D	$k-\varepsilon$	canopy optimisation
Sofotasiou et al. (2017)	semi-enclosed 2-D	$k-\varepsilon$	design optimisation of the roof geometry
Guo et al. (2022)	enclosed 3-D	$k-\varepsilon$	ventilation study on the meteorological conditions
Qin et al. (2006)	enclosed 3-D	LES	smoke filling, spread and evacuation with combustion
Sakai et al. (2007)	enclosed 3-D	$k-\varepsilon$ / LES	turbulence approaches comparison
Huang et al. (2021)	enclosed 3-D	N.A.	study on the gymnasium thermal comfort

Table 5.1.1: Summary of a number of studies related to semi and fully enclosed sport facilities using CFD.

Moreover, to perform an accurate CFD simulation, one needs a detailed geometry or 3-D model of the studied system. In a classical or simple configuration, this can be achieved using CAD softwares and a combination of basic geometries and shapes. The various studies presented in Table 5.1.1 used this technique. When it comes to study stadiums or gymnasiums, the complex system can sometimes be hard to reproduce with all its details numerically. This is the case of the Coubertin stadium. Thus, a more complex mesh generation can be used, such as the point cloud immersion.
The outline of this chapter is summarised in Figure 5.1.1: from a 3-D cloud of points, a numerical mesh is generated, whose methodology is introduced in Section 5.2. Then, based on the available experimental data and the stadium ventilation system information, the problem set up (boundary zones, boundary conditions) is detailed. Various CFD simulations are then performed with four main goals, presented respectively in the four last sections:

- Preliminary simulations are used to identify zones of interest in the stadium in order to design an experimental protocol for the next campaign, planned in 2023. More precisely, the focus is made on important flow velocity areas, "dead-zones" and a possible thermal stratification.

- Then, a study complements the CPC scheme validation, using the experimental data from a chemical campaign performed in 2021. Based on the IAQ indexes and van Hooff and Blocken (2013) study, a focus in made on the decay of the particle matter concentration during a handball game related to the stadium ventilation airflow rate.

- Then, similarly to Sakai et al. (2007) , three turbulent approaches are compared in a transient hot ventilation jet case. Additionally, simulations are performed using the CPC and IPC schemes, presented in Chapter 3.3. The jet diffusion and the simulation time are compared.

- Lastly, a study on the modification of the stadium geometry is made. The impact of installing acoustic panels in the ceiling area on the PM10 concentration decay is discussed, joining studies like Shi and An (2017) and Sofotasiou et al. (2017) .

5.2 Mesh generation

In this section the numerical mesh creation methodology is detailed. The final objective here is to generate a three dimensional hexahedral mesh from a cloud of points that reproduce correctly the stadium main details (Figure 5.2.2, left). This process can be divided in four main steps, summarised in Figure 5.2.1. First, a pre-processing treatment is made on the cloud of points. Then, an hexahedral mesh in the form of a box that covers the cloud of points is defined. The latter is used to compute a numerical field used to generate the final mesh. This field is called porosity in this section whose value lies between 0 and 1. The closer it gets to 1, the more important are the chances that the cell is a fluid volume. In the following are better detailed each step from Figure 5.2.1.

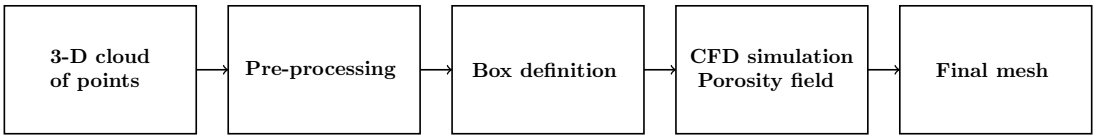

Figure 5.2.1: Main steps of the numerical mesh generation.

- 3-D laser scans were made at different locations of the stadium leading to a final cloud of points. The scanners used are the Focus M70 model . Each cloud points is represented by its position, colour value (R,G,B) and intensity (see Figure 5.2.2, right and Figure 5.2.3 for different views of the cloud).

- In order to set up the CFD simulation used to generate the final mesh, a transformation and rotation of every point is performed. This allows all points to be in a wanted zone, facilitating the immersion that leads to the final mesh. In this study, a translation of $[22.13, 40.12, 6.30]$ m and a rotation of -37.25^o were made relative to the points initial coordinates. The transformed cloud of points is represented in Figure 5.2.4, left.

- Then, a numerical box, large enough in all three dimensions to contain all points of interest is defined. In the current case, its length, width and height are respectively of $50\,\mathrm{m}$, $70\,\mathrm{m}$ and $18\,\mathrm{m}$. The initial mesh refinement uses homogeneous hexahedral cells of $[0.25, 0.25, 0.15]$ m, leading to a total cell number of about 5 millions. Note that a less refined mesh would not be able to capture the stadium details, notably in the sitting zone, and a more refined mesh would lead to more expensive simulations.

Figure 5.2.2: (Left) Overview of the stadium. Credits: Artstation. (Right) View of the 3-D cloud of points.

Figure 5.2.3: Different point of view of the cloud of points.

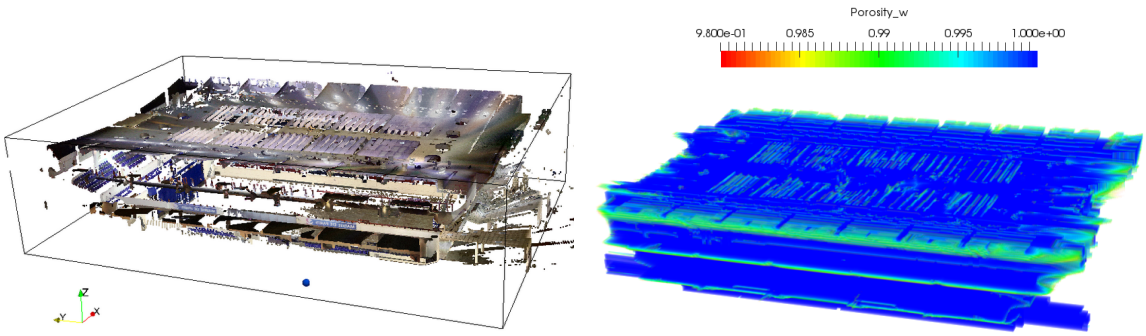

Figure 5.2.4: (Left) Cloud of points after translation and rotation. (Right) Porosity field after the first CFD simulation.

- The next step is to perform a CFD simulation transporting a passive scalar in order to compute the porosity field for the box defined previously. The latter is based on the number of cloud points on each finite volume and is used for the selection of the solid and fluid cells. For each laser scan (several scans were made to catch as much details as possible), a porosity source is defined (porosity of 1 at each source), which radiates spherically and whose value is set to zero when touching a volume with enough points of the scan (a threshold point value need to be set by the user). Naming the porosity Π Its transported equation reads:

$$\frac{\partial \Pi}{\partial t} + \text{div } (\Pi \underline{e}_r) - \text{div } (\underline{e}_r)\,\Pi = 0. \tag{5.1}$$

$\underline{e}_r = \dfrac{\underline{x} - \underline{x}_0}{|\underline{x} - \underline{x}_0|}$ is the radial direction from the considered source $\underline{x}_0$.

For illustration, the porosity field this simulation is represented in Figure 5.2.4, right. Its value is heterogeneous and the shape of stadium can be perceived. Two slices of the porosity field are presented in Figure 5.2.5. One can see that the porosity is very close (quasi equal) to 1 inside the system, representing the fluid cells. However, in its boundaries the porosity value varies importantly. According to which details one wants to reproduce in the mesh, a deeper study of this field in the stadium borders is made. The strategy is consider fluid all cells presenting a porosity above a defined threshold value.

Figure 5.2.5 presents the porosity field slices with a minimum value of $2.196\ 10^{-4}$. In that case, one can see that if the selection threshold is set to 0.25, then some fake fluid cells in the bottom left corner of the box will be retained, which does not correspond to the correct stadium shape. In the other hand, fixing an important threshold leads to a not enough detailed mesh. To illustrate that, Figure 5.2.6 shows the same porosity field, but with a minimum value of 0.98. If this value is retained for the selection threshold, the final mesh would not consider the siting zones (Figure 5.2.6).

Therefore, for this particular system, the porosity field threshold was fixed following the stadium zone, in order to find a compromise of an enough detailed mesh without fake fluid cells. Figure 5.2.7 summarises the different zones related to their porosity threshold values. Note that corridors around the sitting area were added, based on the stadium real architecture. Lastly, 4 extruded doors are added for numerical stability concerns related to outlet boundary conditions. The roof details were not considered in the first mesh since the mesh refinement was not able to catch such small details. In the public area, the porosity threshold value (0.33) is smaller in order to catch the correct border shape.

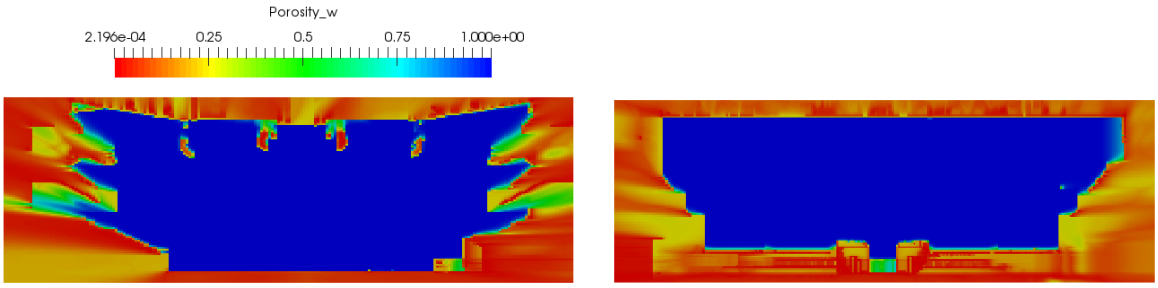

Figure 5.2.5: Example of the porosity field on two slices of the box, with a minimum legend bar value of $2.196\ 10^{-4}$.

- The final mesh retained for the first simulations, represented in Figures 5.2.8 and 5.2.9 is designed in order to study the main stadium field and its stands as it catches a minima the stadium details, notably in the siting zones. From the five millions of cells, around 2.4 millions were kept from the presented process.

5.3 Boundary conditions

To accurately simulate the stadium airflow, correct boundary conditions should be imposed. To do so, the first simulations are based on the information provided by the stadium management team. First, related to the air handling unit (AHU), which is connected to the stadium ceiling, blowing and return vents are

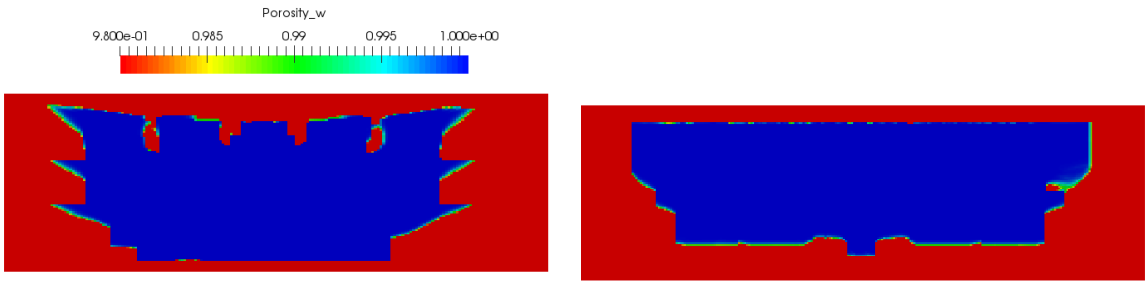

Figure 5.2.6: Example of the porosity field on two slices of the box, with a minimum legend bar value of 0.98.

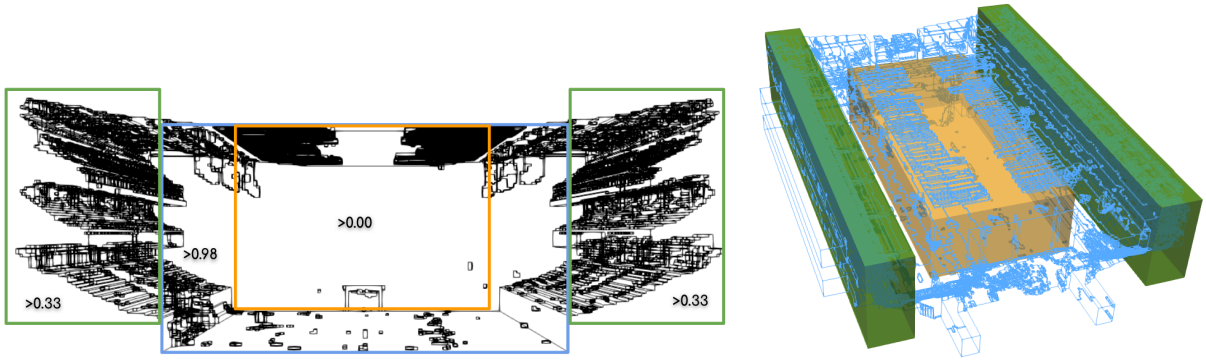

Figure 5.2.7: Mesh threshold porosity zones. (Left) 2-D slice. (Right) Volume view.

defined. Figure 5.3.1 shows two photos of these vents; on the left, the blowing vents and on the right, the extraction ones. The numerical definition of both zones is represented in Figure 5.3.2. Numerically, the blowing zone is set as an inlet boundary condition and the extraction one as an outlet. Additionally, other possible sources of in and outflow are considered at the ground level, close to the field. More precisely, outlet zones are defined (see Figure 5.3.3), corresponding to ventilation ducts directly connected with the outdoor conditions (i.e. the mass flow is induced by a pressure differential). Finally, doors are defined on the corridors and on the 4 corners of the main stadium zone, represented in Figure 5.3.4.

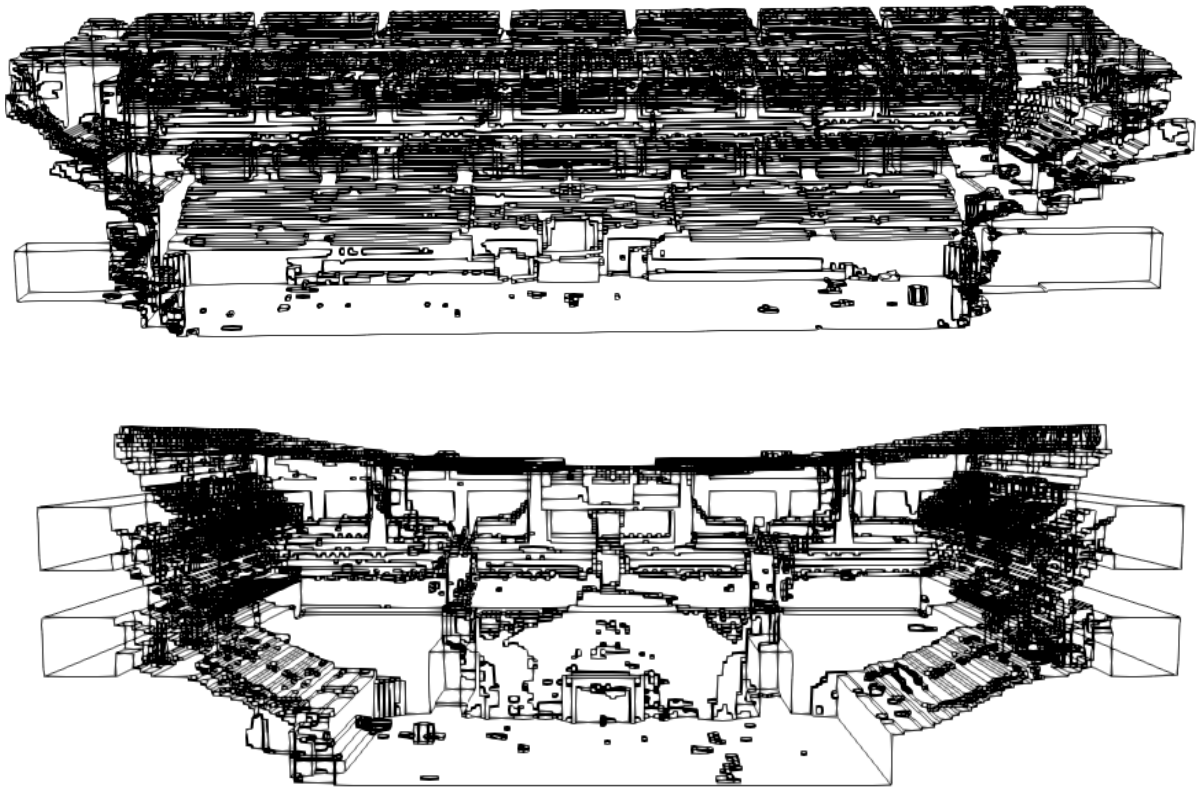

Figure 5.2.8: Slices of the mesh retained for the first simulations.

5.4 Identifying the first flow features

First simulations on the presented mesh are carried out in order to locate and identify zones of interest to be studied during an experimental campaign taking place in 2023. More precisely, a focus is made on zones with not negligible speed and on a possible thermal stratification in the given system in case of heating.

To do so, two ventilation scenarios are tested. First, an isothermal simulation (related to the initial temperature) is performed to evaluate the flow dynamic characteristics and then, the stadium is heated through a higher injected flow temperature of $T_{in} = 298\,\mathrm{K}$. In both situations, the stadium initial temperature is $T_0 = 293.15\,\mathrm{K}$. The time step is set to $\Delta t = 0.055\,\mathrm{s}$ to verify a Courant number inferior to the unity and the inner iterations error threshold (defined in Chapter 3) is set to $\varepsilon_{piso_0} = 10^{-8}$.

For these simulations, the $k-\varepsilon$ model is used. Walls are considered adiabatic. The entering mass flux is set to $60\,000\,\mathrm{m^3\,h^{-1}}$ (corresponding to approximately three time the stadium volume per hour) and the ceiling return blowers mass flux is taken as 80% of the entering flow (information given by the stadium monitoring team).

To study the simulation convergence, four monitoring probes are defined, at the mid stadium height ($z = 7.5\,\mathrm{m}$), represented in Figure 5.4.1. The velocity magnitude evolution over time is then represented in Figure 5.4.2, left. It is observed that the velocity does not reach properly a steady state, even for a large simulation time and for all probes. Thus, for exploitable results, a time average is performed, leading to the mean velocity field represented in Figure 5.4.2, right.

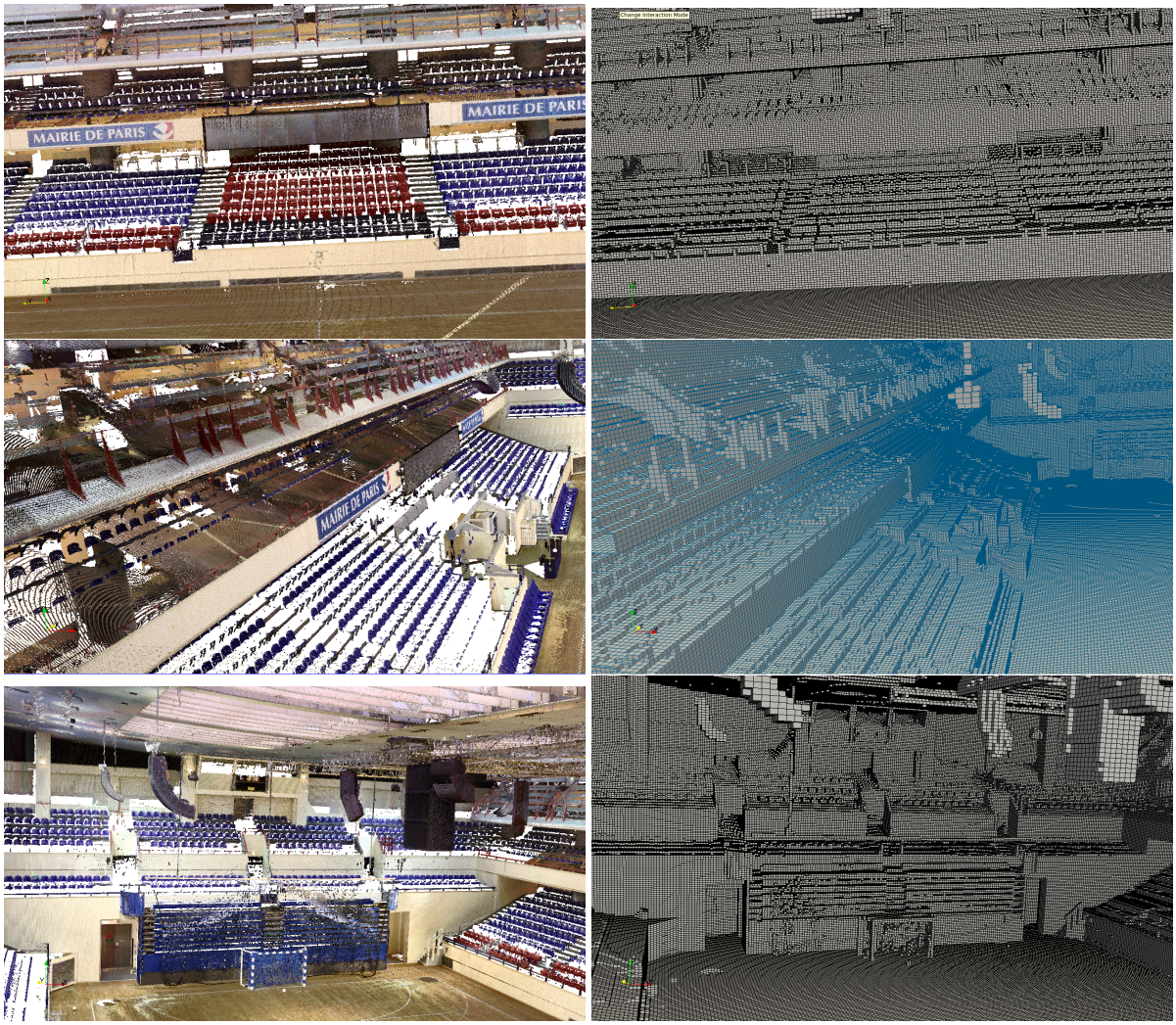

Figure 5.2.9: Different view comparing the (Left) cloud of points and (Right) final numerical mesh.

From these two simulations the velocity field, temperature and air age are studied. Figure 5.4.3 shows the velocity averaged field for the isothermal simulation at $3000\,\mathrm{s}$. The inlet jets can be clearly discerned, driving the flow and creating different recirculation zones in the stadium. Moreover, one can distinguish the impact of the extraction vents in the ceiling, which drags a part of the entering mass flux.
To better quantify the dynamic zones of interest, the volumes with a larger mean velocity magnitude value than $0.5\,\mathrm{ms}^{-1}$ are presented in Figure 5.4.4. As showed in mean velocity magnitude slices, the important velocity zones are below the blowing vents. These zones are thus interesting to measure the velocity during the experimental campaign. Now, let's focus on the anisothermal ventilation study. Figure 5.4.5 presents the temperature instantaneous field after around $14\,\mathrm{minutes}$ of simulation. Two things are clearly observed. First, the injected hot flow did not reach completely the field ground at the final simulation time, which remained at the initial temperature. Then, a vertical thermal stratification is visible and identifying it by experimental measurements would be of great interest (this data could be used to validate thermal transient simulations for instance).

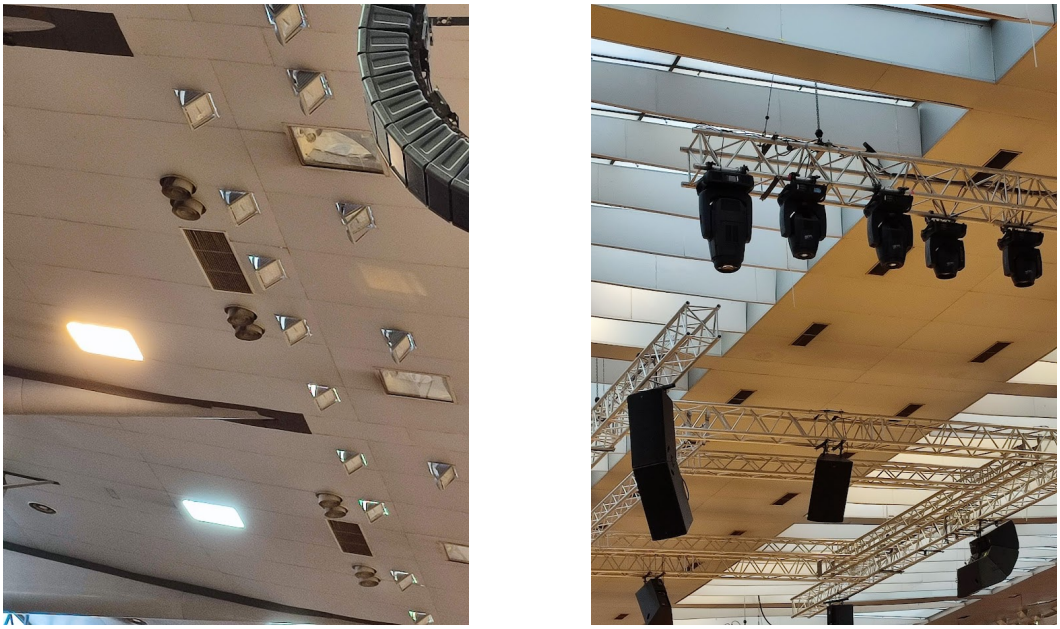

Figure 5.3.1: Photo. Vents located on the stadium ceiling related to the AHU. (Left) Blowing vents. (Right) Extraction vents.

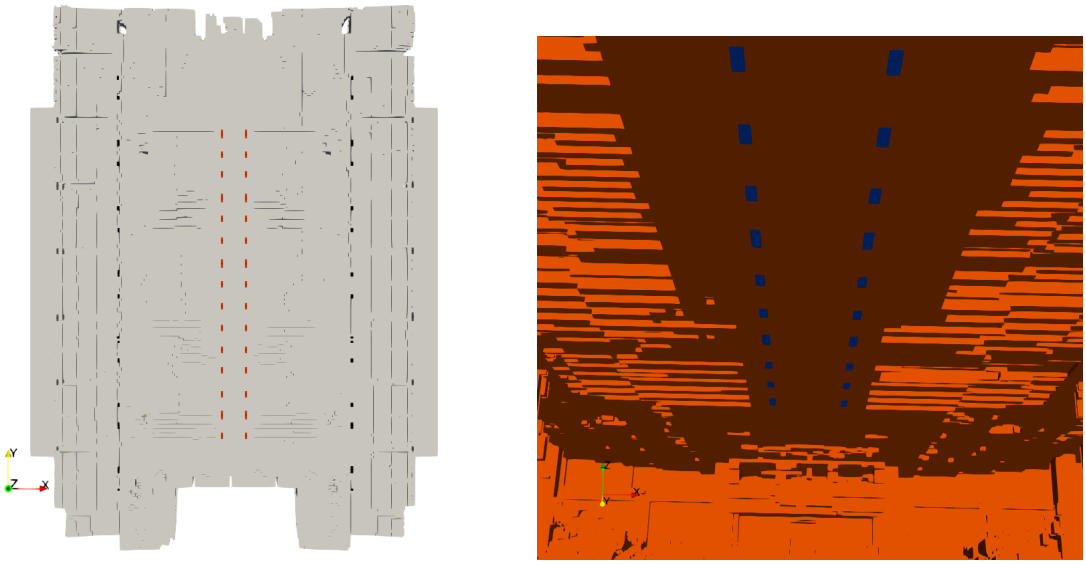

Figure 5.3.2: Numerical boundary conditions. Vents located on the stadium ceiling related to the AHU. (Left) Outside view. In blue, the blowing vents, in red, the extraction ones. (Right) Inside view. In blue, the extraction vents.

Finally, the air age is studied by transporting a passive scalar whose value is incremented at each time step. Figure 5.4.6 shows, for the anisothermal simulation, the air age field at $t = 14\,\mathrm{min}$. The results are directly linked with the thermal ones. One can confirm that the ventilation did not reach the low heights of the stadium, where the air age is higher. The external corridors also presented more important air ages. This is confirmed by Figure 5.4.7 which represents the volumes having air ages above $600\,\mathrm{s}$. This type of field is useful to identify the presence of eventual dead zones. Even if these first numerical results need to be analysed carefully, since the boundary conditions are simplified, they can already provide

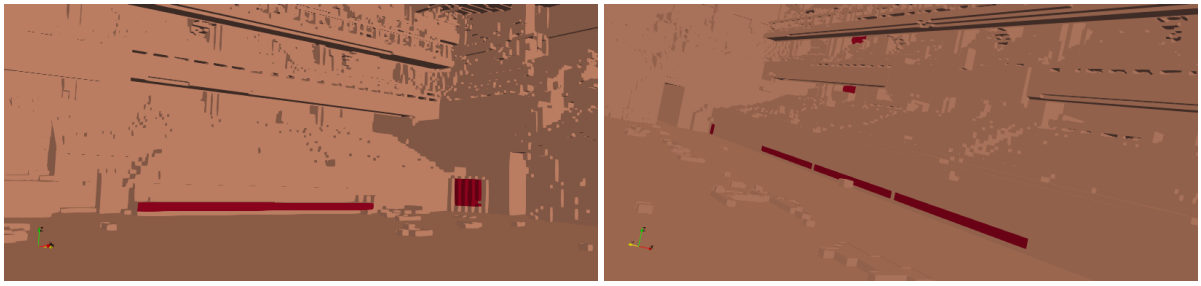

Figure 5.3.3: Numerical boundary conditions. Vents located on the ground level of the stadium in red.

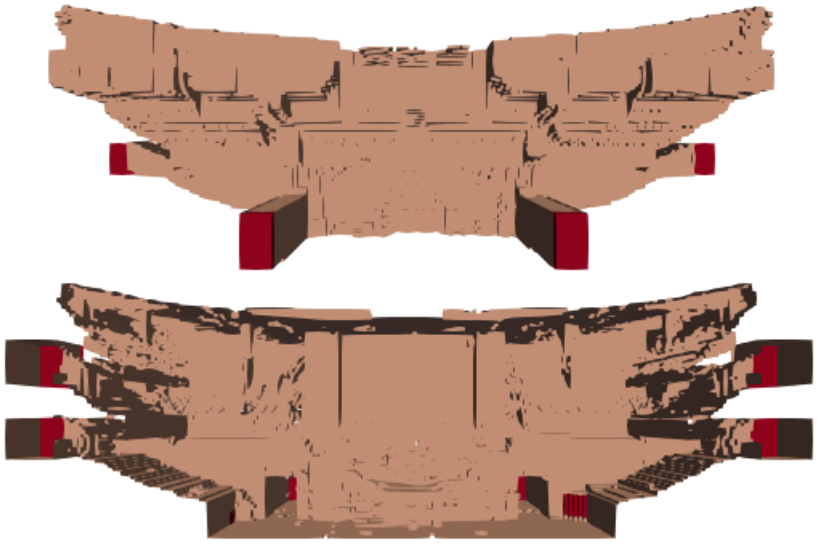

Figure 5.3.4: Numerical boundary conditions. Complementary outlet boundary conditions in red.

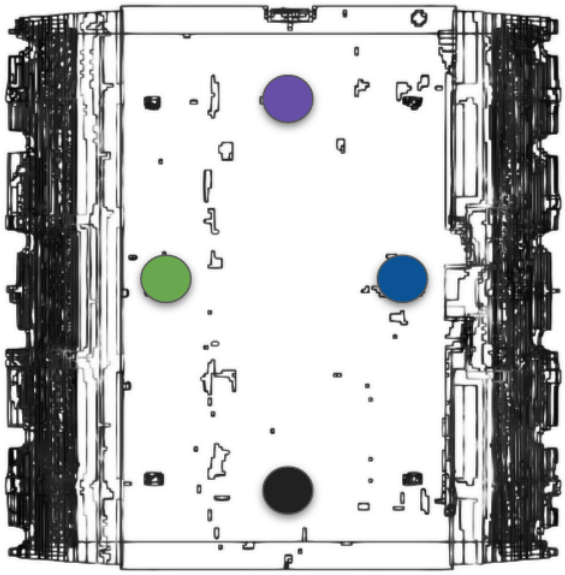

Figure 5.4.1: Monitoring probes location at $z = 7.5\,\mathrm{m}$.

some insights of the indoor air flow. Also examples of useful numerical tools, such as the air age, are presented.

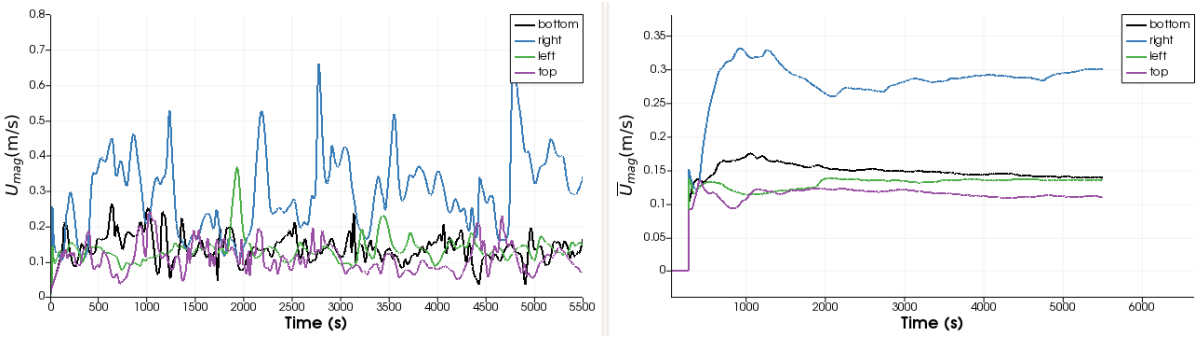

Figure 5.4.2: $k-\varepsilon$ simulation. Velocity magnitude instantaneous and averaged quantities for the different monitoring probes located at the top, bottom, right and left sides of the stadium at $z = 7.5\,\mathrm{m}$.

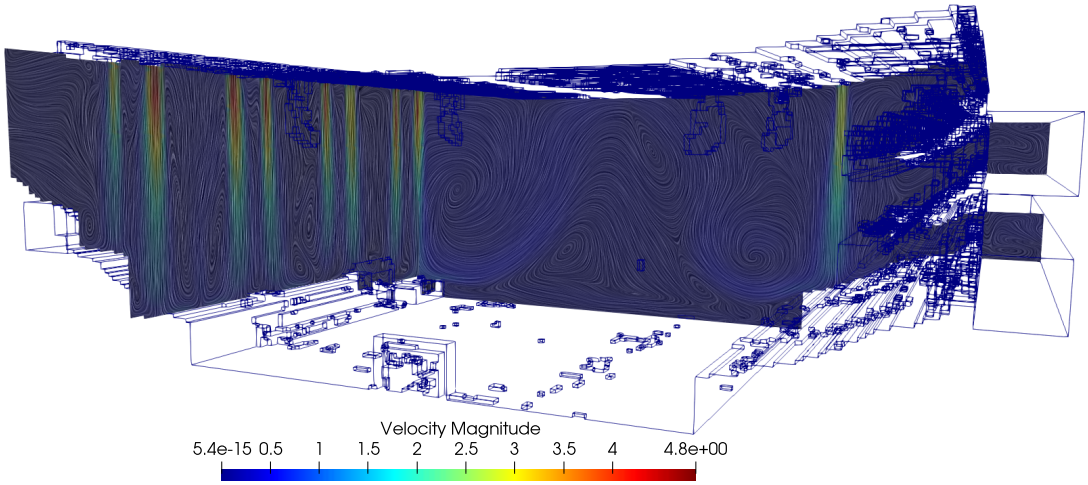

Figure 5.4.3: Averaged velocity magnitude field (in colour) over the flow streamlines for the isothermal ventilation case at $t = 3000\,\mathrm{s}$.

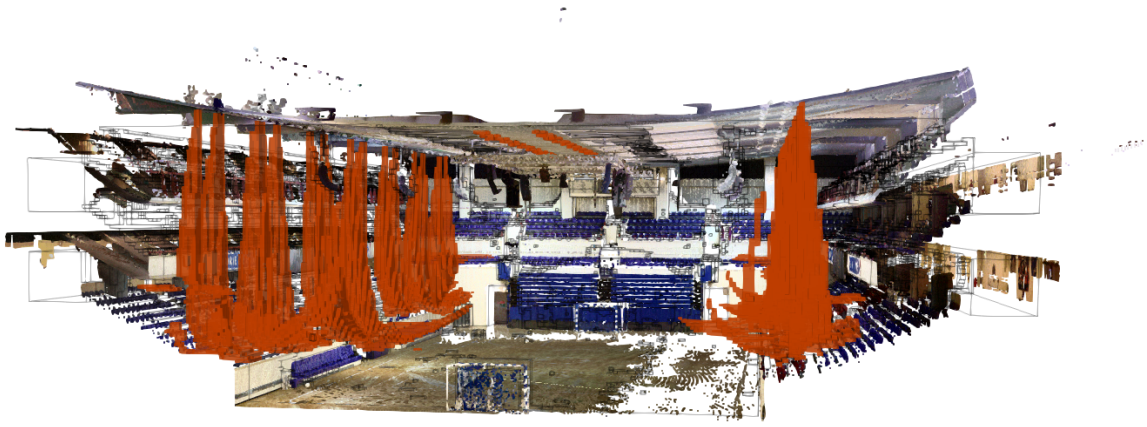

Figure 5.4.4: Volumes with a velocity magnitude higher than $0.5\,\mathrm{m\,s^{-1}}$ (red) for the isothermal ventilation case at $t = 3000\,\mathrm{s}$.

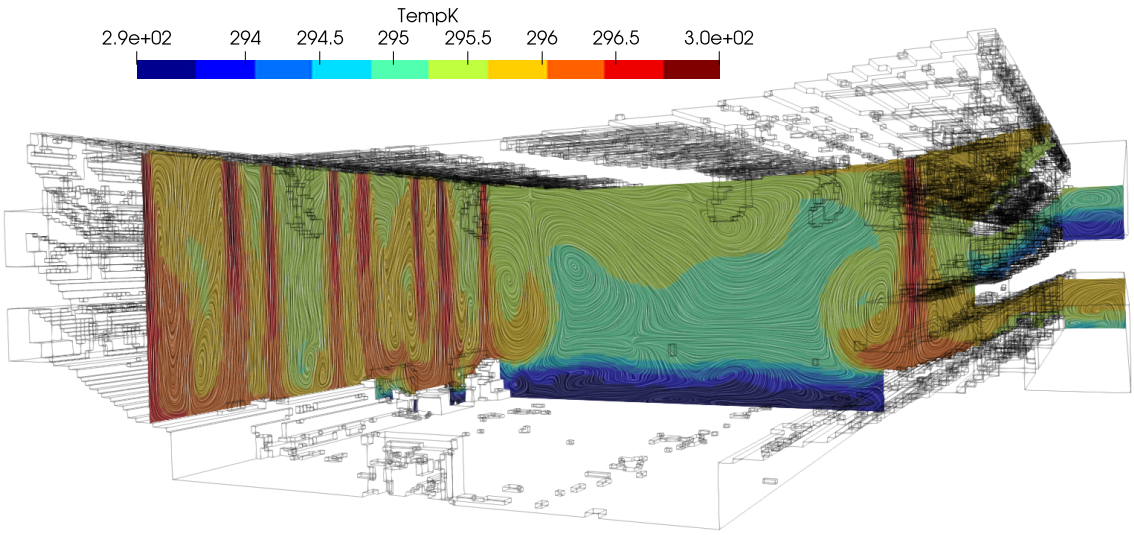

Figure 5.4.5: Instantaneous temperature field (in colour) over the flow streamlines for the anisothermal ventilation case at 14 min (825 s).

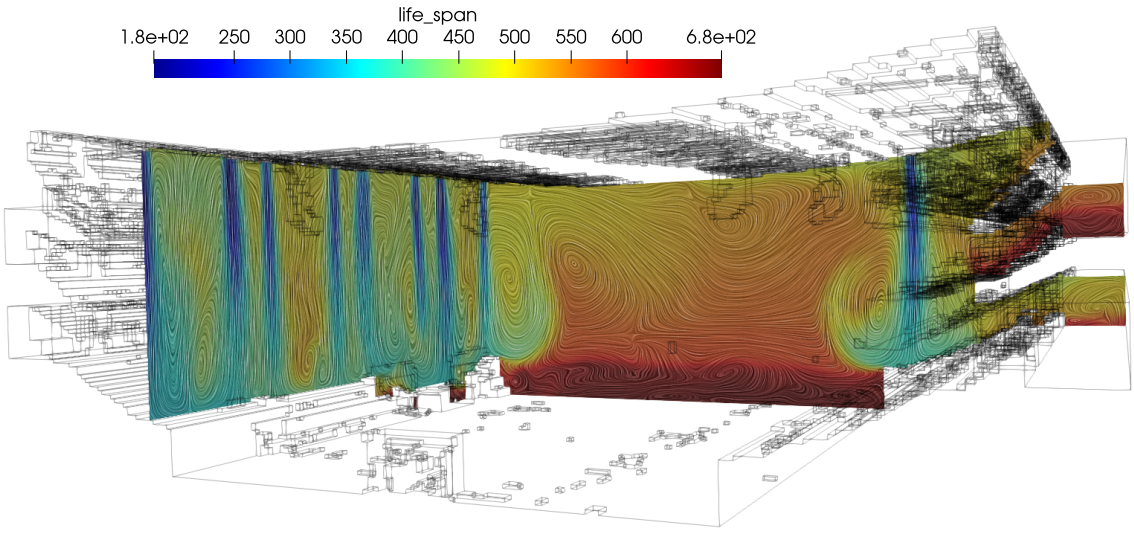

Figure 5.4.6: Air age field (in colour) over the flow streamlines for the anisothermal ventilation case at 14 min (825 s).

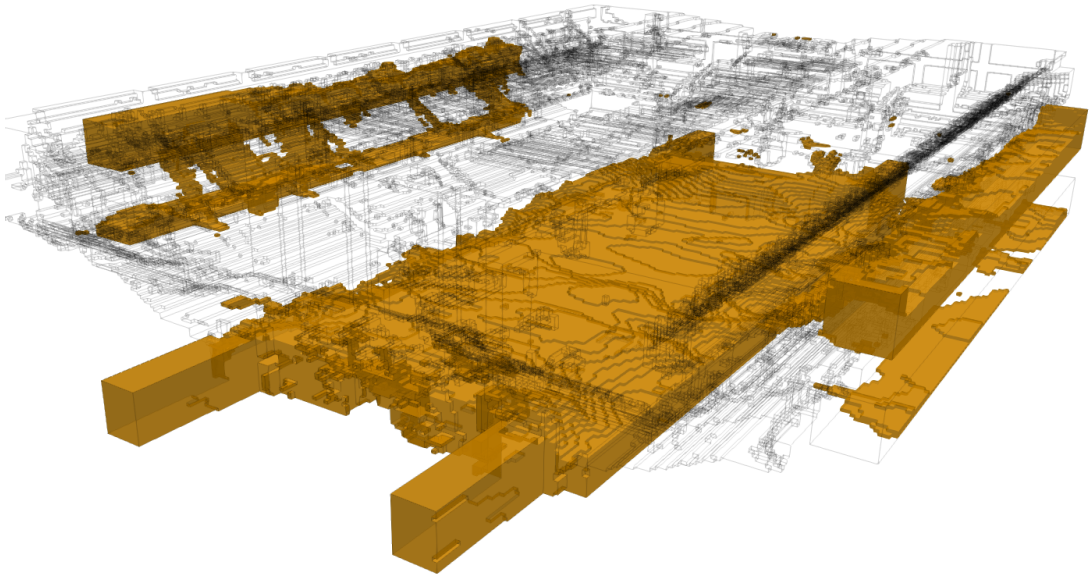

Figure 5.4.7: Volumes presenting an air age field above 600 s (yellow) for the anisothermal ventilation case at 14 min (825 s).

5.5 Validation: on the reproduction of the french handball league final

A continuous experimental campaign was made by different laboratories (CSTB, LISA, LCPP, CEREA), leading to many chemical measurements. On the 4th of June 2021 took place the french handball league final, opposing the Paris Saint Germain to the Nimes team, where the first team won both the match and the championship. This led to a festive celebration, and the ignition of some fireboxes outside the stadium by the champion club supporters. The installed sensors captured this episode, where the particle matter 10 (PM10) concentration measured at a given point in the stadium (Figure 5.5.2, left) increased consequently as shown in Figure 5.5.1.
This section main goal is to try to reproduce numerically this evolution over time using the CPC scheme. To do so, the previously presented mesh is used and the experimental sensor (Figure 5.5.2, left) is defined as a monitoring probe in the numerical mesh (Figure 5.5.2, right) . Its PM10 concentration is studied over time and compared to the experimental results.

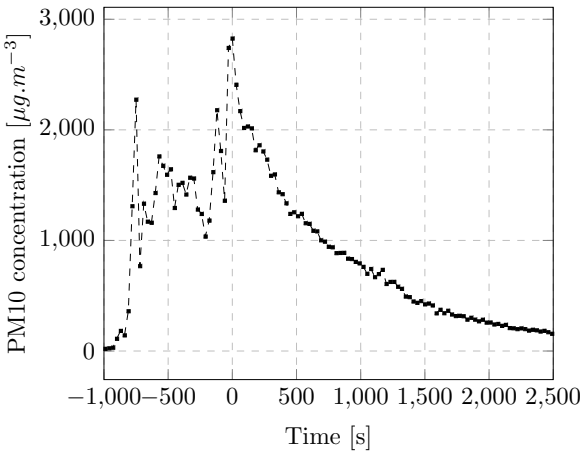

Figure 5.5.1: PM10 concentration experimental profile. Time 0 is defined according to the maximum peak of concentration.

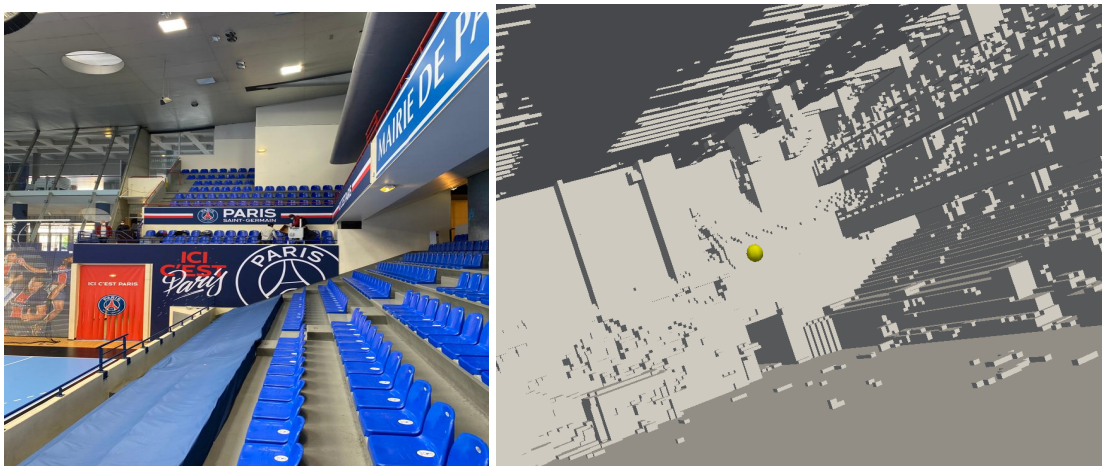

Figure 5.5.2: (Left) Experimental sensor location. (Right) Probe location to study the PM10 concentration over time.

However, during the experimental campaign, no measurements concerning the thermal and dynamics quantities of the flow were made. Again, the lack of boundary conditions information for the numerical simulation makes harder the challenge of reproducing precisely what happened that day.
Thus, two parameters are first studied. The first is the AHU power relative to its maximum mass flow $Q_{in}^{max} = 100\,000\,\mathrm{m^3\,s^{-1}}$. At first, three different AHU power P_{AHU} (60%, 80% and 100%) related to its maximum value are tested. The second parameter is the way the PM10 concentration field is numerically initialised. Given the lack of information regarding this field heterogeneity at the measurements time, three initialisations are tested, represented in Figure 5.5.3. The first considers an homogeneous PM10 initial concentration equal to the experimental maximum value (at $t = 0\,\mathrm{s}$) $C_0 = C_{max} = 2870\,\mu\mathrm{g\,m^{-3}}$ (Figure 5.5.3, left). Keeping the same initial value, the second initialisation considers only an initial non-null concentration in the sitting zones (Figure 5.5.3, center). Finally, the last one only considers the cells below $9\,\mathrm{m}$ to have an initial PM10 concentration equal to C_{max}. For all simulations performed, $\varepsilon_{piso_0} = 10^{-8}$ and the time step is set so the CFL number is equal to 0.8. All the simulations are considered isothermal.

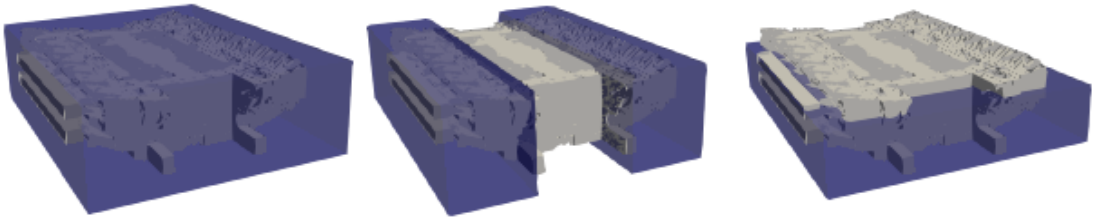

Figure 5.5.3: Different initialisations of the PM10 concentration field tested for the first simulations. (Left) Fully homogeneous initialisation. (Centre) Initialisation only in the sitting zones. (Right) Initialisation for the cells below $9\,\mathrm{m}$.

Figures 5.5.4 and 5.5.5 show that the first initialisation globally overestimate the PM10 concentration over time. Indeed, measurements are made on a single experimental location; it is very likely that at the starting time, the particle matter concentration in the system was not homogeneous. Moreover, the other two non homogeneous initialisation led to worse results: an important variation is observed as the simulation begins, deforming the decreasing exponential shape of the concentration field (even

if the second initialisation leads to correct results excepting the important gap at the beginning of the simulation). This is understandable given the discontinuous initialisation of both simulations. Thus, no interesting conclusion can be made from these first simulations, except that one should consider an initial heterogeneous PM10 initialisation. The biggest question from now on is how to correctly reproduce this initial field state with no further dynamic and thermal conditions on this day.

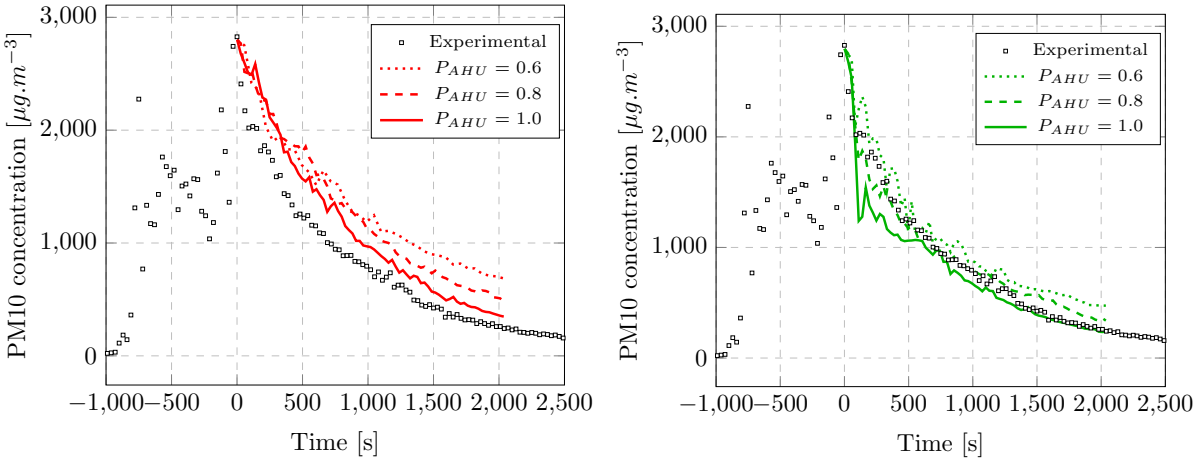

Figure 5.5.4: Comparison of the numerical PM10 concentration over time with the experimental measurements. (Left) Initialisation 1. (Right) Initialisation 2.

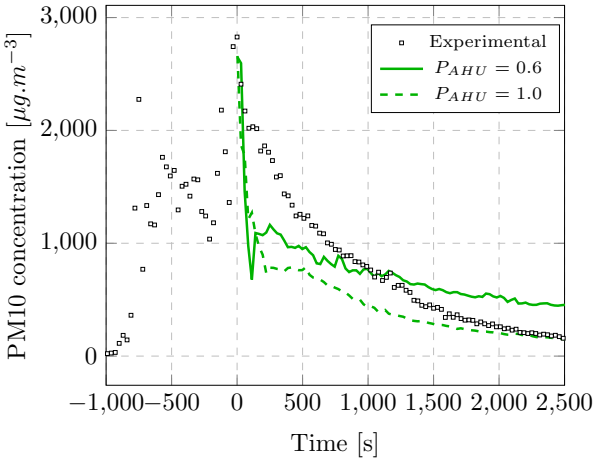

Figure 5.5.5: Comparison of the numerical PM10 concentration over time with the experimental measurements for initialisation 3.

The idea of reproducing a more accurate initial PM10 field comes in mind. To do so, the initial simulation time is set 1500 s before the previous one and the initial PM10 concentration is set homogeneous and equal to $PM10_0 = 1200\,\mu g\,m^{-3}$ (see Figure 5.5.6, left, for an illustration). Then, particle matter is injected in the blowing vents linearly (representing hypothetically the PM10 coming from outside), which leads to an increase of its concentration (illustration in Figure 5.5.6, right). The latter is set (through a calibration) so the numerical $PM10$ concentration is equal to its experimental moving average (MA5, red lines in Figure 5.5.6, left) of the last 5 points at 1500 s. Note that the hypothesis of outside PM10 sources is considered. This strategy is performed for two AHU power of 60% and 100% related to its maximum value. For each inlet mass flux, a parametric study on the PM10 inlet source term was made.

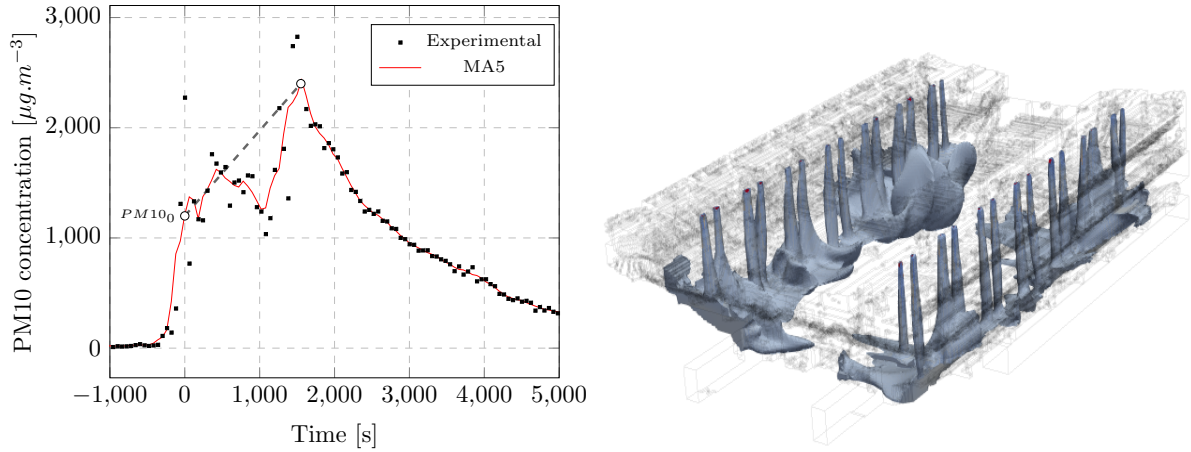

Figure 5.5.6: (Left) Strategy for the heterogeneous initialisation. Red lines are the moving average based on the last 5 values. (Right) Volumes with a PM10 concentration field > 2000 $\mu g\,m^{-}3$ using $P_{CTA} = 1.0$ at $t = 225$ s.

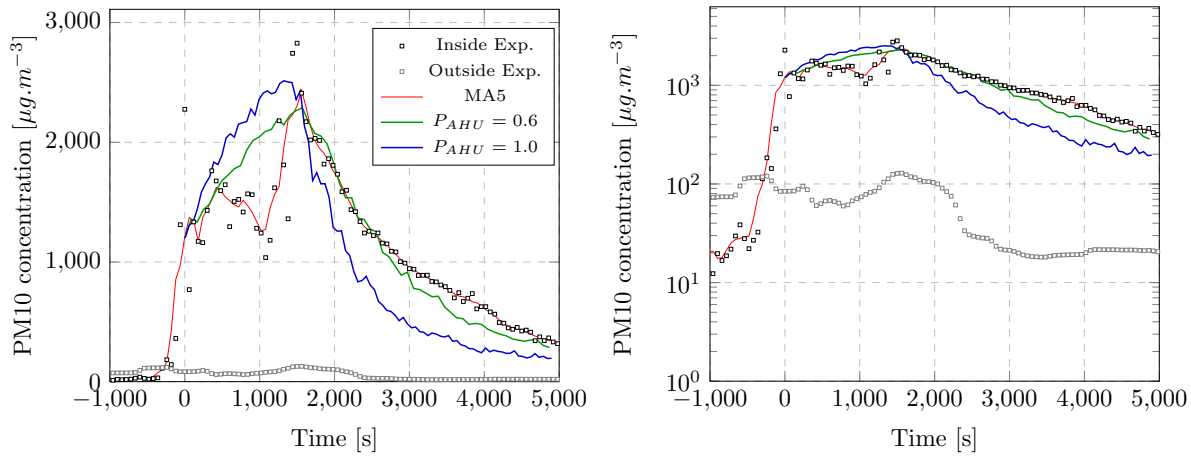

Figure 5.5.7: Numerical PM10 concentration over time for two AHU power compared to the experimental measurements. (Left) Non log plot. (Right) Semi-log plot.

Results show that despite showing correct shapes, both simulations underestimate the decreasing of the PM10 concentration. Nevertheless, the $P_{AHU} = 0.6$ simulation (Figure 5.5.7, green lines) performed better than the other simulation (in blue lines).
To eventually get better results, two additional simulations are added. The first tries to better fit the PM10 concentration between 0 and 1500 s by a transient PM10 source term in the inlet ventilation faces (Figure

5.5.9, left). The other keeps an AHU power of $P_{AHU}^{3D} = 0.6 P_{AHU_{max}}$ and the previous initialisation, but is ran longer (8000 s compared to 5000 s previously).
Additionally, the stadium can also be modeled as a 0-D cell. Its concentration C_{PM} equation reads then:

$$\frac{\partial C_{PM}}{\partial t} = -\frac{Q_{in}}{\Omega_{tot}} C_{PM} + \frac{Q_{ext}}{\Omega_{tot}} S_{PM}^{ext}, \tag{5.2}$$

where Q_{in} is the blowing mass flux and Ω_{tot} the system total volume, Q_{ext} the mass flux blown by the natural ventilation vents. S_{PM}^{ext} is a possible source term coming from the same vents, set as zero for this simulation, given the lack of experimental data. Note that S_{PM}^{ext} is positive (even if its value may be very small related to the inside mean PM10 concentration). Considering an initial concentration C_0 at $t_0 = 1500\,\mathrm{s}$, the 0-D concentration evolution is:

$$C_{PM} = C_0 e^{-\frac{Q_{in}}{\Omega_{tot}}(t - t_0)}. \tag{5.3}$$

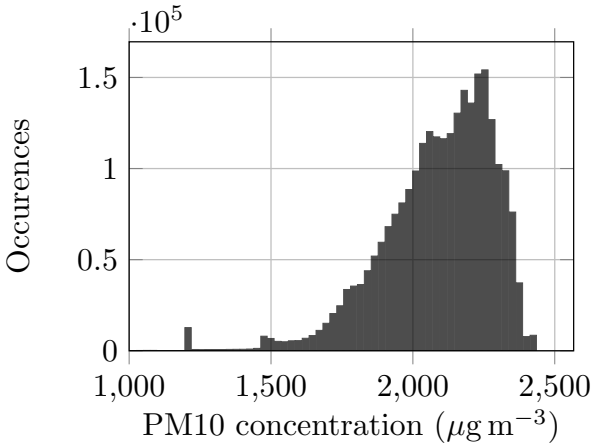

Figure 5.5.8: Cells occurrences histogram of the PM10 concentration at $t = 1500\,\mathrm{s}$ for the simulation using a linear PM10 filling of the system at the inlet faces.

Filling the stadium through a particle matter source term at the inlet faces leads to a PM10 concentration field heterogeneous at $t = 1500\,\mathrm{s}$, illustrated in Figure 5.5.8. Note that the low concentration occurrences (about $1250\,\mu\mathrm{g\,m^{-3}}$) can be explained by the start of the emptying of the stadium (the inlet scalar source term is set to 0).
Figure 5.5.9, left shows a comparison between the different transient initialisations performance regarding the PM10 concentration evolution. Very few differences can be observed between the two simulations, even if the system concentration field at $1500\,\mathrm{s}$ is different for each of them. However, when performing the simulation longer (Figure 5.5.9, right, corresponding to a linear PM10 source term), one can observe that the PM10 numerical evolution gets closer to the experimental data. Note that at around $3000\,\mathrm{s}$, the numerical curve underestimates the real PM10 evolution. This can be explained by either new sources terms that were not accounted for in the present simulations or a variation of the ventilation flux; both phenomena can not be confirmed given the available information.
The 0-D evolution evacuates faster the particles and is further away from the experimental data than the CFD simulation. Indeed, it is likely that the initial concentration and air circulation were not homogeneous in the stadium, as shown in this study first simulations, which is the case in 0-D. Note that no thermal stratification was considered in this validation case. This could possibly lead to a variation of the numerical results.
Two main elements should be kept in mind. The first is the validation of the entering mass flux of 60% of the maximum AHU power, which is in agreement with the information given by the stadium monitoring team. This will be the inlet flux from now on.

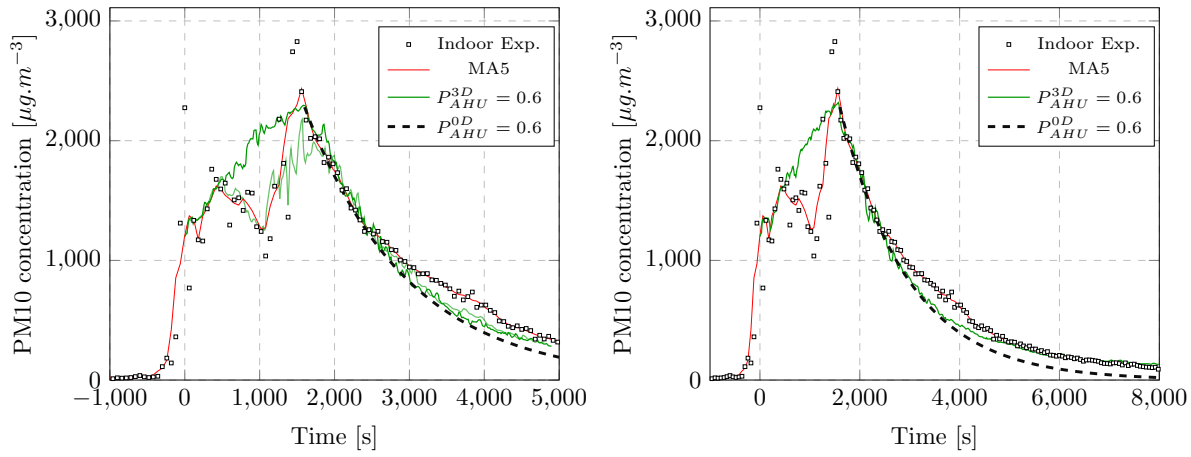

Figure 5.5.9: Numerical PM10 concentration over time compared to the experimental measurements and to the 0-D model. (Left) Comparison of the transient inlet source conditions. (Right) Longer simulation.

Moreover, this test proved that reproducing numerical results close to the reality relies importantly on accurate boundary conditions. Thus, in the 2023 experimental campaign, important attention should be given to correctly collect enough useful information regarding the ambient and boundary conditions, including the outdoor ones.
To conclude this section, studying the propagation of a given specie (smoke, PM) could be an interesting experiment to do, if the campaign conditions allow it. Qualitative and quantitative data could be acquired and, if well combined with real-based boundary conditions, could be a good set of validation for turbulent transient schemes. Also, the numerical results were closed to the experimental, complementing the CPC scheme validation.

5.6 Experimental protocol

From both first simulations and validation related to Pierre de Coubertin stadium, interesting information was kept to design an experimental protocol to be performed in 2023. Indeed, zones of interest were identified by $k - \varepsilon$ isothermal and anisothermal simulations. Additionally, from the validation case the idea of reproducing the dispersion of a gas inside the system was highlighted. An additional attention should be given to correctly measure as accurately as possible the system information relative to the boundary conditions.
To perform the experimental measurements, anemometers are at our disposal to measure velocities, five pressure sensors and thermocouples to measure the temperature. Figure 5.6.1 presents two sketches with the main experimental strategy related to the dynamical and thermal measurements.
Concerning the velocity measurements, five anemometers are used to measure the instantaneous flow. Two anemometers are set respectively on the stands of the main stadium field, where the velocity was shown to be more important. Another anemometer will be installed in the center of the field. Finally, the two last anemometers are set in the corridors, behind the main field, as shown in Figure 5.6.1. This is done to measure a possible flow caused by the difference of pressure and temperature between the in and outdoor environments. These corridors are directly connected to external doors. To better quantify the pressure differential between the indoor environment and outside of the stadium (very important for free inlet/outlet conditions), several pressure sensors will be installed in both indoor and outdoor locations, notably in the front of the ventilation blows presented at the field height, represented in Figure 5.6.1, bottom, by a green circle. Two complementary hot wire anemometers are set in the other field side, to quantity the mass flow blown under the teams benches (represented by the red segments in the figure).

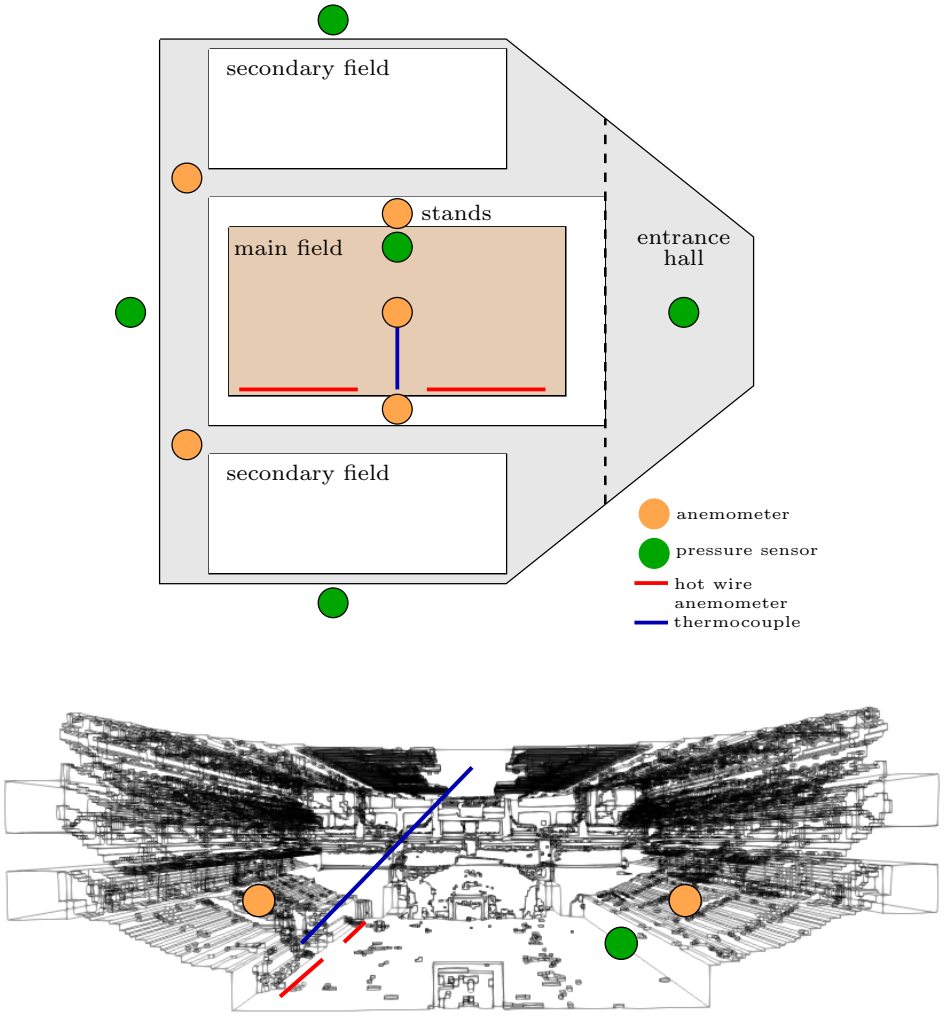

Figure 5.6.1: Sketch of the experimental protocol concerning the dynamical and thermal quantities. (Top) Location of the different sensors with a simplified stadium representation. (Bottom) Zoom on the stadium main field.

Finally the figure blue segment represents a thermocouple profile to catch the thermal stratification during the experimental campaign.
To these measurements could be added the study of a specie injected in the AHU system ducts, leading to an interesting validation database for turbulent transient problems (for instance, the dispersion of Helium).

5.7 Schemes and model comparison

This section compares, for the same configuration setup, three turbulence approaches and the IPC and CPC scheme. Note that since there is no dynamical or thermal experimental data available for the Coubertin stadium, this study has no goal of determining which approach or scheme performs better, but rather analyse if they present differences, and if it is the case, if they are in agreement with their theory.
More precisely, the temperature field and the time of computation are studied for a $k-\varepsilon$, $R_{ij}-\varepsilon$ and LES simulations using respectively the IPC and CPC schemes. To do so, the hot jet case, with $T_{in} = 298\,\mathrm{K}$

is ran during five minutes. The boundary conditions are identical to those presented for the anisothermal case in Section 5.4.

The time step is set to $0.03\,\mathrm{s}$ so the maximum CFL number reached during the simulation is equal to 0.9. The threshold error related to the inner iterations ε_{piso_0}, presented in Chapter 3.3, is set to 10^{-8}.

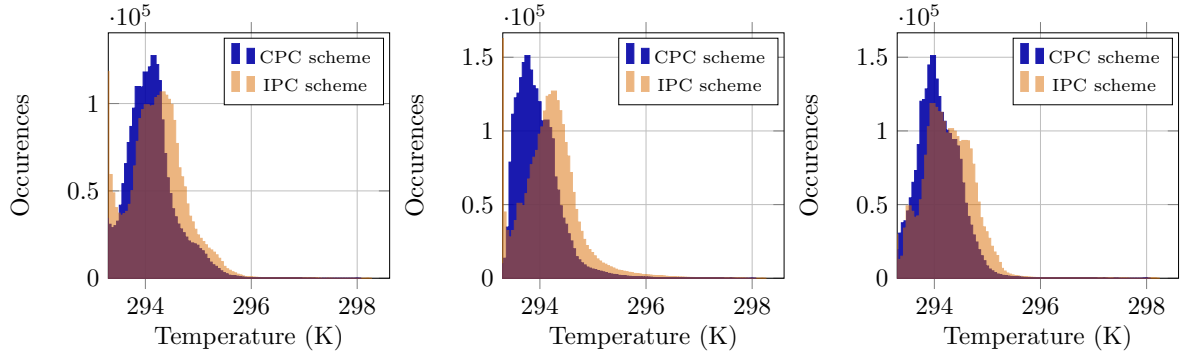

(a) $k-\varepsilon$ **(b)** $R_{ij}-\varepsilon$ **(c)** LES

Figure 5.7.1: Histogram of the cells temperature values for the three different turbulent simulations at $t = 300\,\mathrm{s}$.

When comparing the temperature distribution between the incompresssible and compressible pressure correction schemes (Figure 5.7.1), it is noticeable that the IPC scheme leads to a more important jet diffusion, for all turbulent simulations. Indeed, the orange temperature histograms are flatter compared to the blue ones, whose peak is at lower temperatures. Another difference between both schemes is the total computation time to perform the 5 minutes simulation.
Figure 5.7.2 shows, for each turbulent simulation, the time of computation per single iteration using both schemes. It is observed that for all simulations, the CPC presents performs faster. More precisely, the CPC scheme is equal to respectively 22%, 30% and 60% of the IPC scheme time of simulation. These important values are in agreement with the timer results presented in the Minibat validation case (Section 3.8.8). This difference can be explained by two major points. The first is a faster solver of the pressure equation and the second is the gradient computation time. Note that the time peaks for some iterations correspond to the post-processing visualisation outputs.
The turbulent approaches can be compared as well using Figure 5.7.3 results. The most flattened temperature histogram is the $R_{ij}-\varepsilon$ one. The hot jet seems to be the most diffused for this simulation. The LES simulation presents a higher peak of temperature, but with a relatively less flat shape. The $k-\varepsilon$ simulation led to a diffused jet, but with slightly more occurrence for low temperatures compared to the R_{ij} simulation. This can be confirmed looking at the air age histogram (Figure 5.7.3, (b)), where there are more cells with an important field value for the LES simulation, represented in green. Again, the air age confirms a better jet diffusion when using the $k-\varepsilon$ and R_{ij} approaches, with a less important age peak and a flattened shape. A complementary qualitative analysis can be made by looking at the final temperature field at a given slice of the stadium (Figure 5.7.4). As shown in the histograms, both $k-\varepsilon$ and R_{ij} simulations diffuse better the hot jet.
Finally, the time of simulation of the different turbulence approaches using the CPC scheme are presented in Figure 5.7.2, (d). As expected, the $k-\varepsilon$ simulation is the fastest, followed by the R_{ij} and then, the LES simulation. Again, due to the lack of validation results concerning thermal transients problems for this configuration, the conclusion of this section is the following: first, the numerical results confirmed those presented in the Minibat test case, where the $k-\varepsilon$ was the most diffusive turbulent approach, and the LES the less diffusive. Also, the LES simulation time of computation was almost equal to three times the $k-\varepsilon$ one, which is not negligible. Finally, the CPC scheme allowed, for the same simulation mesh, boundary and initial conditions, to perform faster iterations for all turbulent approaches. This is an important point to highlight while CFD simulations are often criticised to be computationally expensive for indoor systems design.

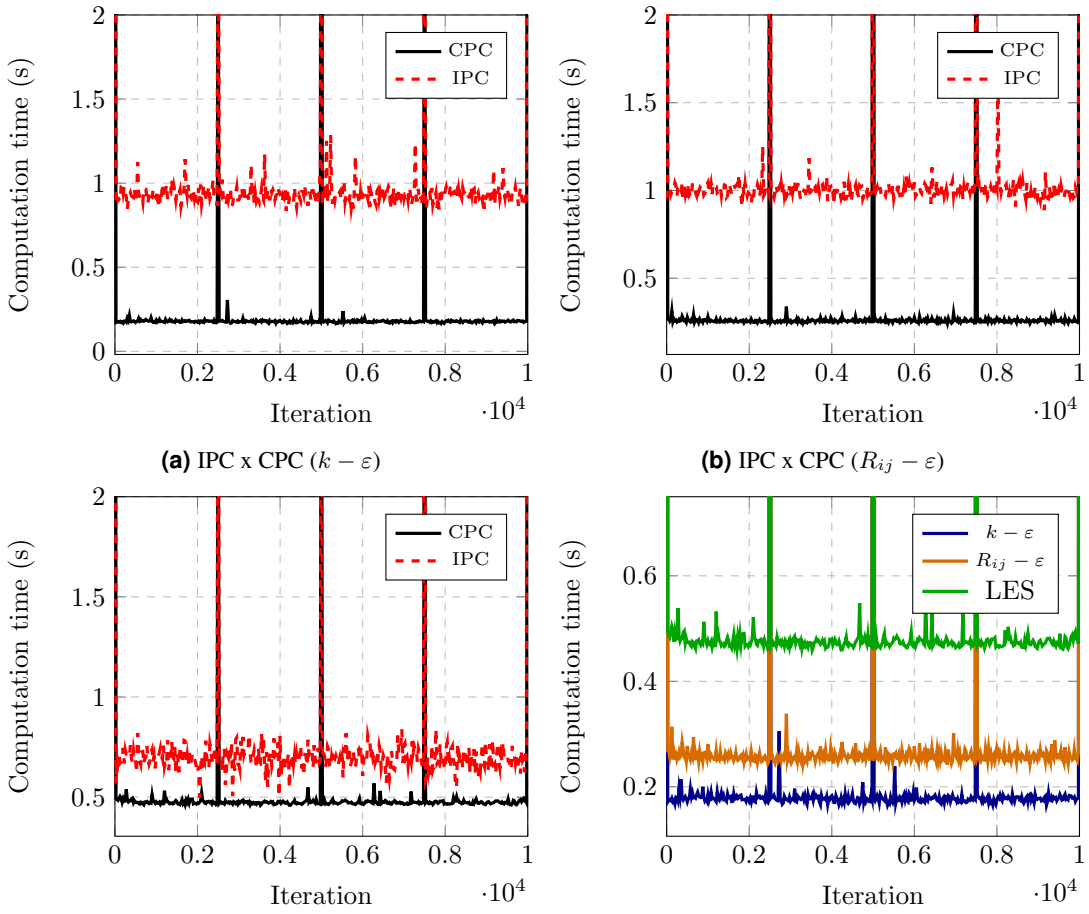

(a) IPC x CPC ($k-\varepsilon$)

(b) IPC x CPC ($R_{ij}-\varepsilon$)

(c) IPC x CPC (LES)

(d) CPC ($k-\varepsilon$ x $R_{ij}-\varepsilon$ x LES)

Figure 5.7.2: Computation time for the different simulations per iteration. Figures (a) (b) and (c) compares the time between the IPC and CPC schemes for each turbulent simulation. Figure (d) shows the three turbulent simulation timers for the CPC scheme.

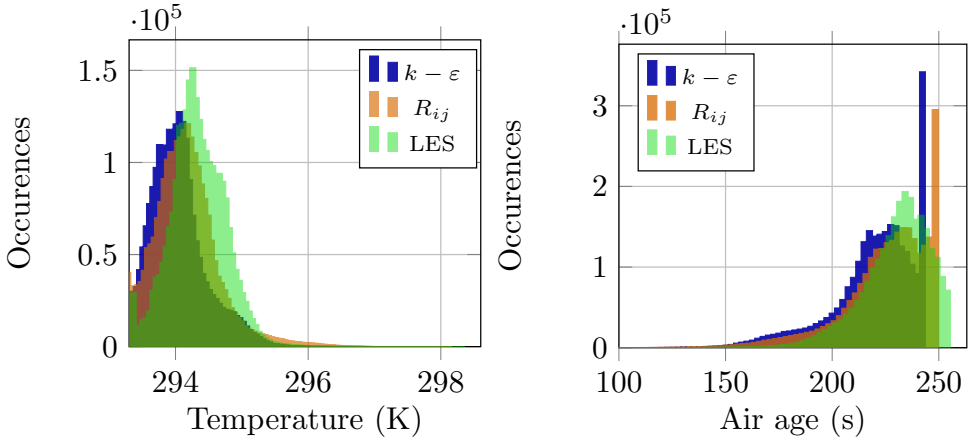

(a) CPC scheme - temperature histogram

(b) CPC scheme - air age histogram

Figure 5.7.3: Results using the CPC scheme at $t = 300\,\mathrm{s}$. (Left) Cells temperature histogram for the three turbulent simulations. (Right) Cells air age histogram for the three turbulent simulations.

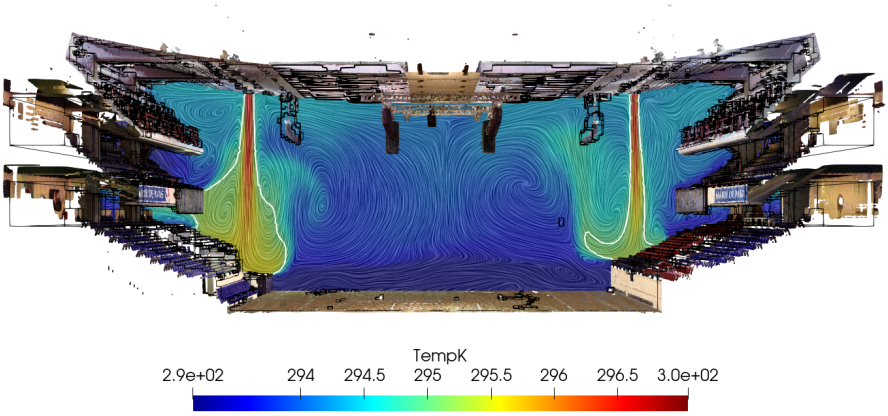

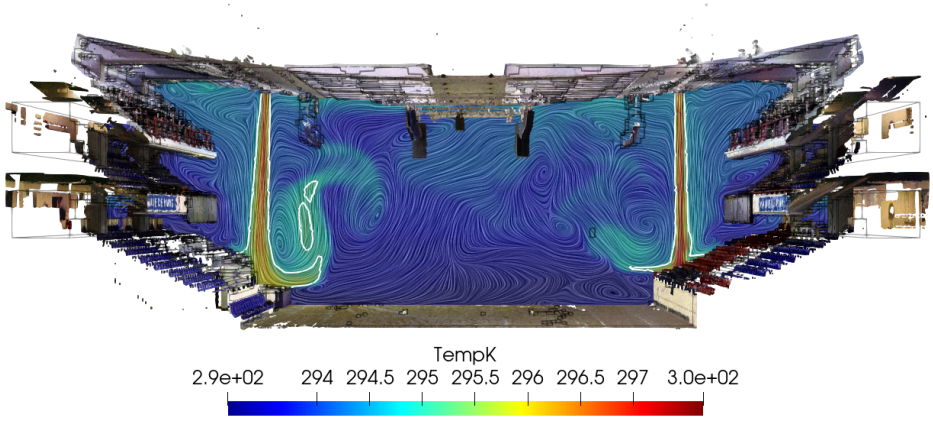

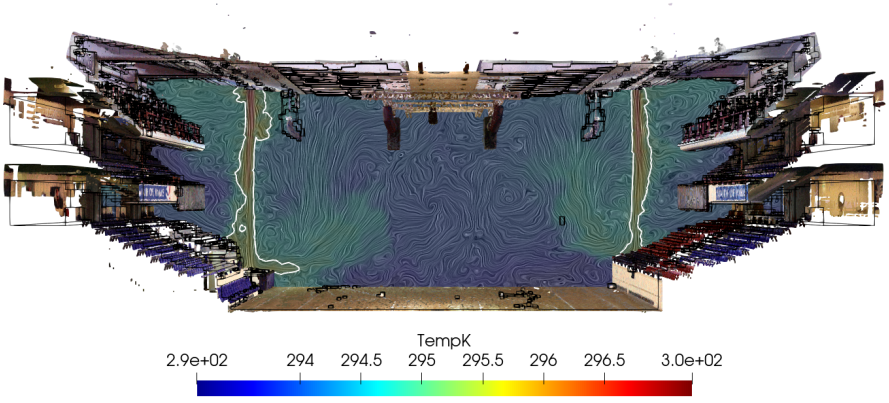

Figure 5.7.4: Slice of the temperature field (in colour) at the stadium mid width, with the isocontour $T = 295\,\mathrm{K}$ at $t = 300\,\mathrm{s}$ for the three turbulent simulations. (Top) $k - \varepsilon$. (Center) $R_{ij} - \varepsilon$. (Bottom) LES.

5.8 Impact of the modification of the stadium ceiling

In this section an example of application of the indoor air scheme is given, where the main stadium ceiling design is studied. Renovation works are actually in process regarding some stadium zones. Among them, it is planned to install acoustic absorbing panels close to the roof. The objective of this section is to evaluate if this type of change would impact its ventilation efficiency, and thus its energy consumption. To do so, the only experimental data available, presented in Section 5.5 is used and the same study is performed, but with a change in the numerical mesh.
The acoustic panels are modeled as six 3-D boxes of $[8.0, 10.0, 0.3]\mathrm{m}$ placed at $z = 13\,\mathrm{m}$ (height of the boxes centre) as shown in Figure 5.8.1. At first, the expected results would be a slower PM10 concentration emptying compared to the CFD simulation presented before. As mentioned, the simulation performed aims to reproduce the PM10 concentration measured during the French handball final match. The final strategy of Section 5.5 is retained: a constant source term is imposed in the stadium inlet faces for $t \in [0, 1500]\mathrm{s}$. Then, this source is set to 0 and the emptying of the system particles field is studied. The system inlet velocity is constant during all the simulation ($P_{AHU} = 0.6$).

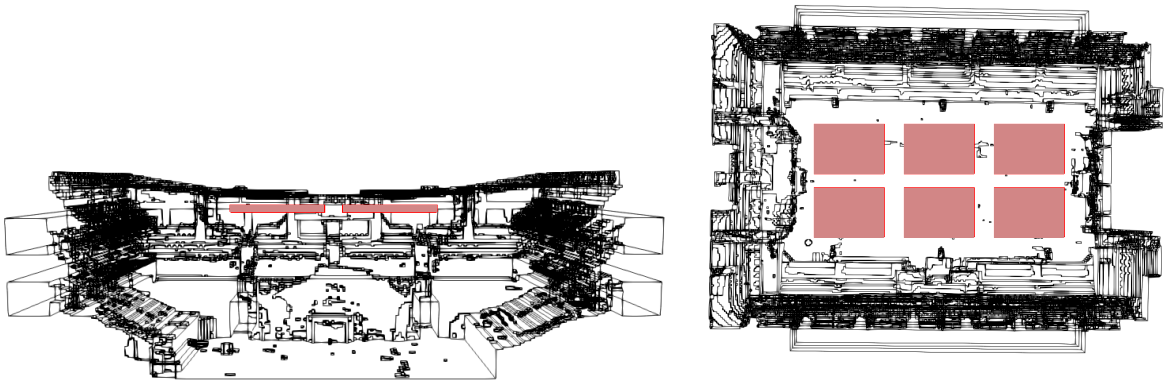

Figure 5.8.1: Sketch of a side and top view of the stadium with the mesh modification related to the acoustic absorbing panels.

The time step is set so the simulation maximum CFL number is equal to 0.8. The error threshold related to inner iterations is equal to $\varepsilon_{piso_0} = 10^{-8}$. The numerical results for this new mesh ($P^{3D}_{AHU_2}$) are compared to the previous one using ($P^{3D}_{AHU} = 0.6$) and to the 0-D model of the stadium (P^{0D}_{AHU}). In addition to comparing the PM10 concentration in a particular spatial point, it is interesting to compare this concentration histogram to the previous one. This gives an insight of the field distribution in the system. Figure 5.8.2 presents the PM10 concentration cells histogram for both P^{3D}_{AHU} simulations at $t = 1500\,\mathrm{s}$ and $t = 8000\,\mathrm{s}$. Both histograms at the different times are clearly different, which already shows the impact of the acoustic panels in the stadium dynamics. At $t = 1500\,\mathrm{s}$ (left figure), the simulation with panels presents a higher peak of concentration and a less flattened shape. Note that the source term imposed at the inlet faces in the beginning of the simulation is exactly the same for both cases. Yet, even if the stadium overall PM10 concentration is higher in presence of panels, the studied point concentration at $1500\,\mathrm{s}$ (Figure 5.8.3, left, orange lines) for the simulation $P^{3D}_{AHU_2}$ is close to the previous one. The histograms at the final simulation time are distinct as well. The simulation with no panels present a less important peak of PM10 concentration, even if both histogram shapes are similar. This confirms a less important air emptying rate in the presence of panels, which would lead either to a more polluted space or a more important energy consumption. Figure 5.8.3 presents the locally studied PM10 concentration along time for the two simulations. Globally, the new mesh simulation leads to results close to the experimental ones, with an exponentially decreasing concentration curve. However,

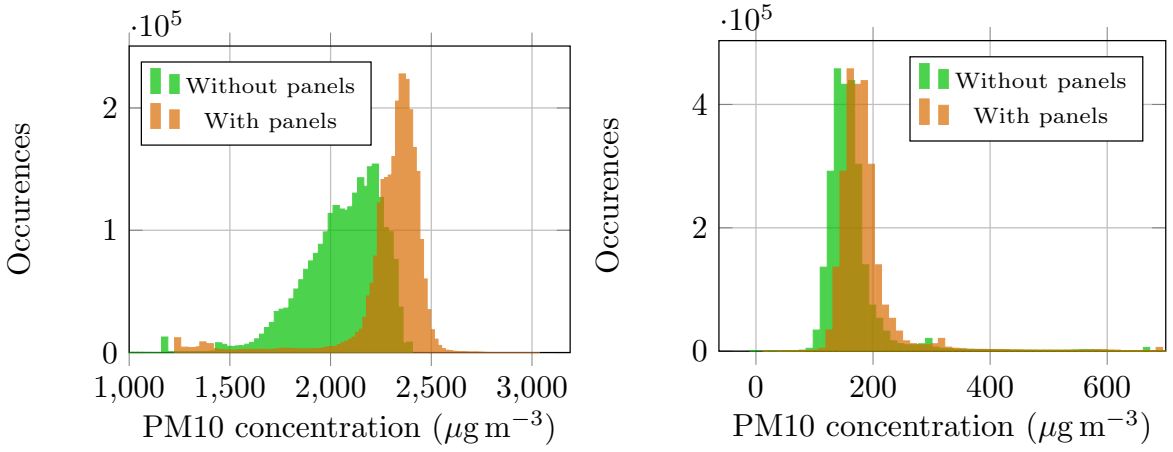

(a) $t = 1500$s **(b)** $t = 8000$s

Figure 5.8.2: Histogram of the cells PM10 concentration at two different times for both simulations with and without acoustic panels.

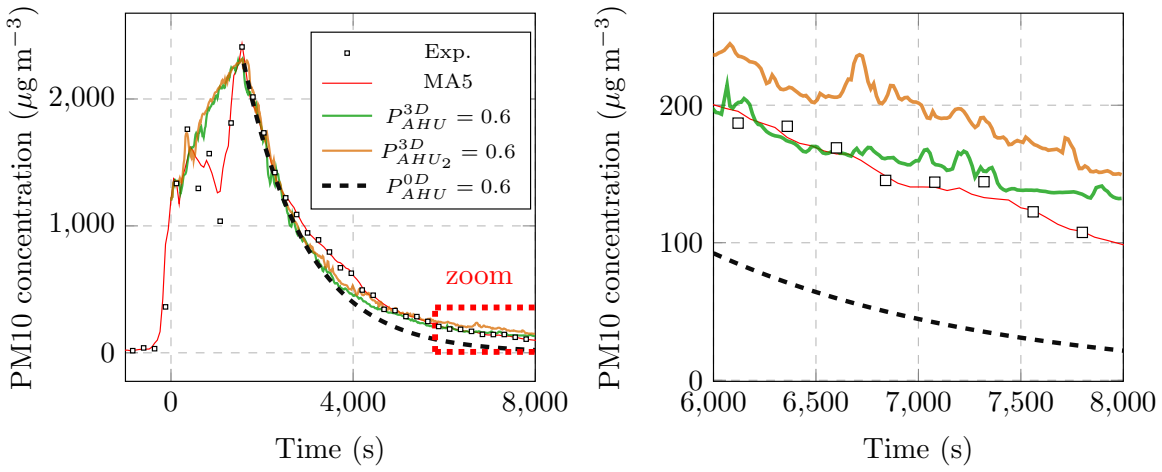

(a) $t \in [0, 8000]$s **(b)** $t \in [6000, 8000]$s)

Figure 5.8.3: PM10 concentration along time for simulations with and without acoustic panels for $P_{AHU} = 0.6$.

when zooming in the time interval $[6000, 8000]$s, some differences can be observed between the three different evolution (Figure 5.8.3, right). While the simulation with no panels (green lines) are the closest to the expected data, the curve related to the mesh with panels is higher, which goes with the histogram results presented in the paragraph above and with the expected results. Moreover, the difference between the 3-D and 0-D simulations is emphasised here with an important relative difference. At $t = 8000$ s, the 0-D PM10 concentration underestimates the experimental data by 80%. Thus, in case of the installation of new panels in the stadium ceiling, the CFD numerical results suggests that some ventilation efficiency is lost, which could be recovered by increasing the AHU power.

5.9 Summary

This chapter provides an example of an applied case using the CPC numerical scheme. Different numerical simulations were performed on the Pierre de Coubertin stadium system, leading to an experimental protocol, an additional validation case and a study on the stadium geometry.
All simulations are run on a three dimensional numerical mesh build from a cloud of points, obtained by laser scans. This mesh generation strategy was detailed. First computations provided useful information to determine interesting zones to place velocity sensors and to identify if the stadium can present a thermal stratification. Then, the scheme was validated using experimental data available through the reproduction of the PM10 concentration evolution during a handball competition. Numerical results were in agreement with the expected ones and performed better than a 0-D model. From this case and using the identified zones aforementioned, an experimental protocol was proposed. Different turbulence approaches were then compared related to a hot jet diffusion and computation time, for both the IPC and CPC schemes. Simulations carried out with the CPC schemes were run faster compared to the incompressible scheme. Such result emphasises the interest of using the proposed time scheme for indoor environment studies, were the computation time is an important numerical factor. Finally, the impact of installing acoustic panels in the stadium ceiling in the flow was shown and discussed. Their presence led to a less important stadium ventilation efficiency.
In the Coubertin stadium framework, further studies shall focus on three major points. The first is to produce a better representation of the system geometry. Indeed, some hypothesis were made in this chapter which led to a mesh accounting for only the main stadium field. Including some additional zones such as the entrance hall could lead to a better representation of the link between the in and outdoor environments, which is currently done by the numerical boundary conditions. The second point is to better represent the stadium flow using experimentally based boundary conditions. This can be done thanks to the future experimental data campaign and by defining more boundary zones (for instance, windows were not considered in the presented simulations). For that matter, the use of artificial intelligence methods could be of interest. For instance, by performing a classification on the available cloud of points information, such as the colours, one could automatically separate the given zones (walls, doors, windows), leading to a more precise mesh.

CHAPTER 6

Conclusion and perpectives

Achievements of this work

In this manuscript, a novel time scheme for indoor airflow CFD applications is introduced, implemented in code_saturne, analysed, verified and validated. The scheme is designed to take into account the different physical processes responsible for the flow in indoor environments. Among them, one may highlight the pressure variation, the conservation of the total energy, the compatibility with RANS and LES turbulence approaches and the moisture dynamics. The scheme development is divided into two main parts and a third one provides an example of the scheme application to a large-scale problem.
First, a second order conservative time scheme for variable density flow is introduced for dry air. The compressible Navier–Stokes equations supplemented with the ideal gas law are discretised in space and time using the finite volume method. Belonging to the pressure-correction class of schemes, the second time convergence order is reached through a staggered variables arrangement in time. A numerical parameter, denoted θ, allows a simulation to switch between the first and second order, allowing the scheme to be applied for both steady and unsteady applications. The pressure variation is considered through the linearisation of the equation of state, leading to an Helmholtz equation to be solved in the scheme correction step. The acoustic effects are implicited, avoiding stability constraints related to the speed of sound. Finally, the total energy is conserved by solving the internal energy equation with a source term related to the discrete kinetic energy equation. A numerical analysis related to the scheme thermodynamic variables positivity is performed and new Fourier and CFL conditions are defined.
Then, a verification and validation is made on a wide variety of test cases representing the physical stakes of the indoor environment and going from the incompressible to the compressible type of flow. For some cases, the numerical results are compared to other code_saturne time marching methods. The scheme properties are first successfully verified on analytic and academic cases: a pressure cooker like system is considered to insure its correct pressure variation and to verify its time convergence order, while the preservation of mass and momentum and its compatibility with different spatial schemes are tested in an one-dimensional convection tube case. Then, two Riemann problems are studied to check the consistency of the scheme with both smooth and singular solutions. Among them, the Sod (1978) case showed the importance of the source term implemented in the internal energy equation step to catch accurately shock solutions. Different reference and experimental test cases are used for the validation process. The scheme was shown to be accurate for natural convection, gravity flow and axisymmetric jets simulations. More importantly, in cases with thermal variation and in and outlets boundary conditions, the proposed scheme was shown to be faster than an incompressible solver. Such results from the verification and validation

processes suggest that the numerical scheme can be used for both incompressible and compressible problems, enlarging its domain of application.
The extension of the dry air scheme to moist air applications is then detailed and a specific treatment in case of phase change is presented. An homogeneous model is used and the mixture is assumed to have a small volume fraction of liquid compared to the gaseous ones. After writing the mixture governing equations, the discretisation and strategy of saturation treatment are introduced. A transport equation for the total water mass fraction is solved and the Newton method is used to compute the temperature from the internal energy, if needed. An important attention is given to keep the numerical properties presented for the dry air scheme. A numerical analysis is then made, leading to stability conditions similar to those presented for the dry air scheme. For verification purposes, the Riemann problem associated to the moist air system of equations is then introduced and its exact solution derived. Finally, the moist air scheme is verified first through a 0-D dimensional volume to test its ability to correctly reproduce water phase change and through two type of Riemann problems. Accounting for the moist dynamics and its effects on the flow completed the physical stakes identified to be simulated by the numerical solver.
Finally, the last chapter illustrates one example of application of the indoor air scheme on a more complex configuration. Preliminary studies on the Pierre de Coubertin stadium indoor airflow are performed and provide some useful insight and information. The numerical mesh used was built from a 3-D cloud of points. A new validation was performed for the numerical scheme, where the numerical results where in agreement with the experimental ones. The identification of dynamic and thermal zones of interest led to the design of an experimental protocol. Three different turbulence approaches were compared using the presented and an incompressible schemes; their differences concerning the numerical jet diffusion and their time of computation were compared. In this comparison, the LES simulation has been shown to be the less diffusive but the most computationally expensive approach. Lastly, some modifications are brought to the system and its impact on the flow are quantified and analysed, emphasising a type of application for the numerical scheme.
Regarding the main objective presented in the introduction, which was to develop a numerical tool in the local simulation scale for indoor applications, the proposed indoor air scheme provided correct and accurate numerical solutions related to the physics identified and chosen to be modelled. Its compatibility with different convective spatial schemes, turbulence approaches (RANS and LES simulations) and accuracy for both incompressible and compressible flow cases is promising for future applications and developments. Moreover, given its stability conditions, shown to be less constraining than the classical CFL condition and its simulation reduced time, the solver seems ready to be used and applied for indoor studies.
However some points are left for further investigations and developments. Those are detailed in the next section.

Perspectives

- **Extending the indoor scheme verification and validation process**
  Additional studies regarding the presented numerical scheme would extend its validation domain.

  - Concerning the dry air scheme, further validation can be made for compressible flows. Indeed, high Mach-number studies would complete the compressible verification cases of this manuscript (Woodward and Colella (1984); McCroskey (1987)). Moreover, most physical processes were verified and validated separately. Cases with the presence of various phenomena, such as mixed convection, would be of great interest. For that purpose, one may cite Lecocq et al. (2008); Sharma et al. (2015) for mixed convection and other test cases of interest not studied in this manuscript: Birman et al. (2005) for non-Boussinesq gravity flows, Hunt and Kaye (2005) for lazy plumes and Amielh et al. (1996); Van Hooff et al. (2012) for jets. Finally, larger scales simulations related to the urban environment would

emphasise the scheme utility for indoor studies, where insights of the outdoor flow could directly impact the indoor one. The outdoor part of the simulation can be compared as well to an atmospheric solver, such as code_saturne atmospheric module.

- Concerning the moist air scheme, more verification and validation cases need to be carried out to verify its accuracy related to phase change. Further investigation can be made concerning the exact solution for the Riemann problem of the system of equations with phase change. Moreover, validation cases with phase change in the indoor environment framework are still to be tested, which would complete this process and certify the applicability of the homogeneous model for thermo-aeraulic applications. Other validation cases such as the Minibat moist study (Teodosiu et al., 2003; Teodosiu, 2013), the Mistral configuration, cooling towers (Razafindrakoto et al., 1998; Blain et al., 2016) and orographic precipitation (Bouzereau, 2004) can be highlighted. Note that to achieve accurate results in some of the aforementioned cases may induce the use of one or more supplementary equations that are thus left for further investigation (for instance, in order to simulate orographic precipitation, a nucleation modelling may be necessary).

- **Physical phenomena to investigate**
  Besides the supplementary verification and validation proposed, some new numerical features to be implemented and analysed are of interest. Note that for each new implementation it is highly recommended to perform a verification and validation process.

  - This work did not focused particularly on the dynamical and thermal walls functions, even if they were used for some simulations. Some work related to other existing walls functions interesting for indoor flow's driving processes such as natural convection may be highlighted (Howard and Tully, 2012; Wald, 2016; Mangeon, 2020).
  - Moreover, the strategy adopted in the correction scheme step, which solves an Helmholtz equation, could be extended for other mixtures and equations of state. Intuitively, the easiest mixture to be generalised is the mixture of different ideal gases (except the air vapor mixture, studied in the fourth chapter). Such implementation is relatively feasible for linearly dependent equations of states related to the pressure.
  - The numerical scheme compatibility with other turbulent approaches that are more and more used in the academic and industrial fields can be tested or developed as well. Some approaches can be highlighted such as the hybrid RANS-LES or the unsteady RANS. These methods can be of high interest when simulating different flow phenomena scales at the same time.
  - Further investigation shall focus as well on the physical phenomena identified in Section 2.2 which were not accounted for in the scheme design. Radiation and the occupants thermal, dynamical and chemical impact on the flow would complement the scheme accuracy related to the indoor environment. One should keep in mind that chemical reactions are sensible to radiation and that its inclusion in the simulation would lead to source terms in the thermal equation . In that scope, La Gennusa et al. (2007) studied the radiation impact on the indoor thermal comfort. Concerning the occupants impact on the flow, one may cite Ai and Melikov (2018) and Srebric et al. (2008) for interesting studies on the boundary conditions related to an occupant and droplet dispersion.
  - Surface condensation laws would also complement the moist air scheme, which currently takes into account only the volume phase change. The implemented law could be validated for instance in the case presented in Teodosiu (2013).
  - Other physical phenomena that may not be neglected in some cases is the moisture dynamics related to fluid-solid interaction in the indoor environment. Existent hygrothermal models can be found in Busser et al. (2018)

- In the same scope, chemical reactions were not considered in this work but can be important to take into account for local scale IAQ studies. The coupling of the CPC numerical scheme to a chemistry module, such as the ssh aerosol module (Sartelet et al., 2020), can lead to interesting results and insights on a system IAQ. At first glance, this coupling should not be a problem, where a mixture of ideal gases and a small volume of aerosols could be transported. For instance, VOCs, that are responsible for the creation of ground-level ozone, can react with species such as nitrogen oxides. Yet, this point need to be treated carefully. Two major difficulties exist. The first is to identify the numerous primary and secondary reactions important in the indoor environment context (refer to Uhde and Salthammer (2007) and Fiorentino et al. (2021)). The second is to perform the coupling between them and the CFD solver. If too many reactions are considered, the computation time is very likely to be multiplied. From preliminary studies one may find that further developments are necessary to reach accurate chemical simulations, such as law walls for VOCs (Murakami et al., 2000a; Huang and Haghighat, 2002; Haghighat et al., 2005).
- The same numerical design can be used for reactive flow and combustion applications. However, the enthalpy equation is recommended in that case given the use of the species reaction enthalpy that are commonly referenced in the literature. Still, the kinetic energy based source term can be adapted to this equation. The pressure step would remain unchanged and the staggered variable arrangement can be kept. Yet, an additional attention for moist flow would be necessary and the mixture would change as well.

- **Applications**

  Some examples of application can be highlighted:

  - The design and optimisation of industrial and residential ventilation systems. This is applicable for desk offices, rooms with important thermal sources, such as server centres, the air ventilation in nuclear power-plants or hospital rooms.
  - Risk assessment studies. For instance, investigating combustion conditions for industrial systems such as hydrogen dispersion in enclosed environments.
  - Indoor air quality studies such as the dispersion of potentially dangerous chemical species in enclosed rooms with many occupants (classrooms, offices, stadiums).

- **Coupling to other numerical methods**

  - Coupling CFD and multi zones models is a promising perspective to perform faster and accurate simulations related to the indoor environment. On the one hand simulations using the CPC scheme can provide useful information to tune a larger scale model corresponding to a characteristic flow (jet, plume). This model can be in turn used for multi zones simulations or for detailed CFD ones. Even if its impact in the results accuracy needs to be quantified, one would be sure to accelerate the total computational time. Both simulation tools can be complementary in a simulation where two rooms are studied but with different complexity. The CFD could be used for the more complex one, whereas the other is studied through a multi zone model. Again, a particular attention should be given on the boundary conditions coupling.
  - Artificial intelligence (AI) methods can be of interest as well when trying to characterise complex flow. Such methods could be used to provide a model data, thus accelerating CFD simulations (turbulent quantities for instance). Yet, accurate training data is necessary. Given the difficulty to gather interesting data covering a wide enough range of flow information with experiences, CFD simulations may be the key to train, verify and validate such models. Other AI application could be to automatise the choice of a CFD sub-models (turbulence,

buoyancy, compressible or incompressible) during a simulation given its results thanks to a learning classification algorithm. The reader may refer to a review on neural networks applications related to CFD in the indoor framework (Calzolari and Liu, 2021).

- **Numerical study of complex configurations**

  Finally, some perspectives regarding the study of more complex geometries are provided.

  - As mentioned previously, accurate boundary conditions are crucial to achieve numerical results in agreement with reality. Beyond their type of value, the way one define the boundary faces groups is of great importance. In this manuscript, these groups were defined manually by defining geometrical criteria. Therefore, classification methods, based on points colours for instance, would be helpful to define more precise boundary groups. Various techniques exist and are left for further investigation. For instance, the reader may refer to Grilli et al. (2017).

  The numerous perspectives show that there are still several points to be studied and the potential of using the proposed numerical scheme for many applications in the indoor environment.

Bibliography

Aarts, M., Boxem, G., Costola, D., Diepens, J., Gousseau, P., Hensen, J., van Hoof, J., van Hooff, T., Hopfe, C., Loomans, M., et al., 2009. Healthy environments from a broad perspective: an overview of research performed at the unit building physics and systems of eindhoven university of technology, in: conference; Research Day International Conference on Perspectives on European Healthcare Design and Planning: Achieving Excellence in Diversity; 2009-05-26; 2009-05-26, TNO. p. 10. URL: https://www.researchgate.net/publication/266049841_Healthy_environments_from_a_broad_perspective_-_an_overview_of_research_performed_at_the_Unit_Building_Physics_and_Systems_of_Eindhoven_University_of_Technology.

ADEME, 2018. Climat, air et energies, chiffres clés URL: https://librairie.ademe.fr/cadic/1731/2018-climat-air-energie_chiffres-cles-010354.pdf.

Ai, Z.T., Melikov, A.K., 2018. Airborne spread of expiratory droplet nuclei between the occupants of indoor environments: A review. Indoor air 28, 500–524. doi:https://doi.org/10.1111/ina.12465.

Allard, F., Inard, C., 1992. Natural and mixed convection in rooms: prediction of thermal stratification and heat transfer by zonal models, in: Proceedings of International Symposium of Room Air Convection and Ventilation Effectiveness, pp. 335–342. URL: https://www.aivc.org/sites/default/files/airbase_6063.pdf.

Alsaad, H., Voelker, C., . CFD analysis of indoor air quality in office rooms equipped with desk fans. 16th IBPSA International Conference and Exibition URL: http://www.ibpsa.org/proceedings/BS2019/BS2019_210162.pdf.

Ambrosini, W., Forgione, N., Oriolo, F., Dannöhl, C., Konle, H.J., 2005. Experiments and cfd analyses on condensation heat transfer in a square cross section channel URL: https://www.osti.gov/etdeweb/biblio/20622075.

Amielh, M., Djeridane, T., Anselmet, F., Fulachier, L., 1996. Velocity near-field of variable density turbulent jets. International Journal of Heat and mass transfer 39, 2149–2164. doi:https://doi.org/10.1016/0017-9310(95)00294-4.

Amino, H., Flageul, C., Benhamadouche, S., Tiselj, I., Carissimo, B., Ferrand, M., 2022. A time-staggered second order conservative time scheme for variable density flow. International Journal for Numerical Methods in Fluids doi:http://dx.doi.org/10.1002/fld.5116.

Antoine, C., 1888. Vapor pressure: a new relationship between pressure and temperature. CR Acad. Sci 107, 681–685.

Archambeau, F., Hérard, J.M., Laviéville, J., 2009. Comparative study of pressure-correction and godunov-type schemes on unsteady compressible cases. Computers & Fluids 38, 1495–1509. doi:10.1016/j.compfluid.2008.12.005.

Archambeau, F., Méchitoua, N., Sakiz, M., 2004. Code saturne: A finite volume code for the computation of turbulent incompressible flows-industrial applications. International Journal on Finite Volumes 1. doi:10.1016/j.compfluid.2008.12.005.

Arens, E., Baughman, A., 1996. Indoor humidity and human health: Part ii - buildings and their systems. ASHRAE Transactions 102, 212–221. URL: https://www.researchgate.net/publication/279573028_Indoor_humidity_and_human_health_Part_II_-_Buildings_and_their_systems.

Ascher, U.M., Ruuth, S.J., Spiteri, R.J., 1997. Implicit-explicit runge-kutta methods for time-dependent partial differential equations. Applied Numerical Mathematics 25, 151–167.

Assemblée Nationale Française, a.a.S., 2018. Loi : Evolution du logement, de laménagement et du numérique URL: https://www.ecologie.gouv.fr/loi-portant-evolution-du-logement-lamenagement-et-du-numerique-elan.

Axley, J., 2007. Multizone airflow modeling in buildings: History and theory. HVAC&R Research 13, 907–928. doi:10.1080/10789669.2007.10391462.

Baldwin, B., Barth, T., 1991. A one-equation turbulence transport model for high reynolds number wall-bounded flows, in: 29th aerospace sciences meeting, p. 610. doi:https://doi.org/10.2514/6.1991-610.

Baldwin, B., Lomax, H., 1978. Thin-layer approximation and algebraic model for separated turbulentflows, in: 16th aerospace sciences meeting, p. 257. doi:https://doi.org/10.2514/6.1978-257.

Banat, F.A., 1994. Membrane distillation for desalination and removal of volatile organic compounds from water doi:https://escholarship.mcgill.ca/concern/theses/6682x584f.

Barton, I.E., 1998. Comparison of simple-and piso-type algorithms for transient flows. International Journal for numerical methods in fluids 26, 459–483. doi:https://doi.org/10.1002/(SICI)1097-0363(19980228)26:4\%3C459::AID-FLD645\%3E3.0.CO;2-U.

Becker, R., Braack, M., Rannacher, R., 1999. Numerical simulation of laminar flames at low mach number by adaptive finite elements. Combustion Theory and Modelling 3, 503–534. doi:10.1088/1364-7830/3/3/305.

Bellivier, A., 2004. Modélisation numérique de la thermoaéraulique du bâtiment: des modèles CFD à une approche hybride volumes finis/zonale. Ph.D. thesis. Université de la Rochelle. URL: https://www.theses.fr/2004LAROS114.

Benacchio, T., Klein, R., 2019. A semi-implicit compressible model for atmospheric flows with seamless access to soundproof and hydrostatic dynamics. Monthly Weather Review 147, 4221–4240. doi:10.1175/MWR-D-19-0073.1.

Bhagat, R.K., Wykes, M.D., Dalziel, S.B., Linden, P., 2020. Effects of ventilation on the indoor spread of covid-19. Journal of Fluid Mechanics 903. doi:https://doi.org/10.1017/jfm.2020.720.

Birman, V., Martin, J., Meiburg, E., 2005. The non-boussinesq lock-exchange problem. part 2. high-resolution simulations. Journal of Fluid Mechanics 537, 125–144. doi:https://doi.org/10.1017/S0022112005005033.

Bispen, G., Lukáčová-Medvid'ová, M., Yelash, L., 2017. Asymptotic preserving imex finite volume schemes for low mach number euler equations with gravitation. Journal of Computational Physics 335, 222–248. doi:https://doi.org/10.1016/j.jcp.2017.01.020.

Blain, N., Belaud, A., Miolane, M., 2016. Development and validation of a cfd model for numerical simulation of a large natural draft wet cooling tower. Applied Thermal Engineering 105, 953–960. doi:https://doi.org/10.1016/j.applthermaleng.2016.03.020.

Blaise, J., 2008. Influence de la géométrie d'une source thermique sur le développement du panache. Ph.D. thesis. Université Henri Poincaré-Nancy 1. URL: https://hal.univ-lorraine.fr/tel-01748346.

Blocken, B., 2018. Les over rans in building simulation for outdoor and indoor applications: A foregone conclusion?, in: Building Simulation, Springer. pp. 821–870. doi:https://doi.org/10.1007/s12273-018-0459-3.

Boscheri, W., Dimarco, G., Loubère, R., Tavelli, M., Vignal, M.H., 2020. A second order all mach number imex finite volume solver for the three dimensional euler equations. Journal of Computational Physics 415, 109486. doi:https://doi.org/10.1016/j.jcp.2020.109486.

Boscheri, W., Pareschi, L., 2021. High order pressure-based semi-implicit imex schemes for the 3d navier-stokes equations at all mach numbers. Journal of Computational Physics 434, 110206. doi:https://doi.org/10.48550/arXiv.2008.01789.

Boussinesq, J., 1903. Théorie analytique de la chaleur. Gauthier Villars 2 .

Bouzereau, E., 2004. Implementation of a micro-physical scheme for warm clouds in the meteorological model'mercure': Application to cooling tower plumes and to orographic precipitation; representation des nuages chauds dans le modele meteorologique'mercure': Application aux panaches d'aerorefrigerants et aux precipitations orographiques URL: https://www.theses.fr/2004PA066381.

Bouzinaoui, A., Devienne, R., Fontaine, J.R., 2007. An experimental study of the thermal plume developed above a finite cylindrical heat source to validate the point source model. Experimental thermal and fluid science 31, 649–659. doi:https://doi.org/10.1016/j.expthermflusci.2006.06.010.

Bridgeman, O., Aldrich, E., 1964. Vapor pressure tables for water .

Buettner, T., 2020. Perspectives de population mondiale–une vision sur le long terme/world population prospects–a long view. Economie et Statistique 520, 9–29. URL: https://librairie.ademe.fr/changement-climatique-et-energie/1725-climat-air-et-energie-9791029712005.html.

Busser, T., Berger, J., Piot, A., Pailha, M., Woloszyn, M., 2018. Experimental validation of hygrothermal models for building materials and walls: an analysis of recent trends URL: Experimentalvalidationofhygrothermalmodelsforbuildingmaterialsandwalls:ananalysisofrecenttrends.

Bustamante, E., García-Diego, F.J., Calvet, S., Estellés, F., Beltrán, P., Hospitaler, A., Torres, A.G., 2013. Exploring ventilation efficiency in poultry buildings: the validation of computational fluid dynamics (CFD) in a cross-mechanically ventilated broiler farm. Energies 6, 2605–2623. doi:http://dx.doi.org/10.3390/en6052605.

Calzolari, G., Liu, W., 2021. Deep learning to replace, improve, or aid cfd analysis in built environment applications: A review. Building and Environment 206, 108315. doi:https://doi.org/10.1016/j.buildenv.2021.108315.

Catalina, T., Virgone, J., Kuznik, F., 2009. Evaluation of thermal comfort using combined cfd and experimentation study in a test room equipped with a cooling ceiling. Building and environment 44, 1740–1750. doi:https://doi.org/10.1016/j.buildenv.2008.11.015.

Chang, T., Hsieh, Y., Kao, H., 2006. Numerical investigation of airflow pattern and particulate matter transport in naturally ventilated multi-room buildings. Indoor air 16, 136–152. doi:https://doi.org/10.1111/j.1600-0668.2005.00410.x.

Chassaing, P., Antonia, R., Anselmet, F., Joly, L., Sarkar, S., 2002. Variable density fluid turbulence. volume 69. Springer Science & Business Media. doi:https://doi.org/10.1007/978-94-017-0075-7.

Chen, Q., 1995. Comparison of different k-ε models for indoor air flow computations. Numerical Heat Transfer, Part B Fundamentals 28, 353–369. doi:https://doi.org/10.1080/10407799508928838.

Chen, Q., 2009. Ventilation performance prediction for buildings: A method overview and recent applications. Building and environment 44, 848–858. doi:https://doi.org/10.1016/j.buildenv.2008.05.025.

Chen, Q., Srebric, J., 2002. A procedure for verification, validation, and reporting of indoor environment CFD analyses. Hvac&R Research 8, 201–216. doi:10.1080/10789669.2002.10391437.

Choi, S.K., Kim, S.O., 2012. Turbulence modeling of natural convection in enclosures: A review. Journal of Mechanical Science and Technology 26, 283–297. doi:https://doi.org/10.1007/s12206-011-1037-0.

Chorin, A.J., 1968. Numerical solution of the navier-stokes equations. Mathematics of computation 22, 745–762. doi:10.2307/2004575.

Clerc, S., 2000. Journal of Computational Physics 161, 354–375.

Colas, C., Ferrand, M., Hérard, J.M., Latché, J.C., Le Coupanec, E., 2019. An implicit integral formulation to model inviscid fluid flows in obstructed media. Computers & Fluids 188, 136–163. doi:10.1016/j.compfluid.2019.05.014.

Colella, P., Pao, K., 1999. A projection method for low speed flows. Journal of Computational Physics 149, 245–269. doi:10.1006/jcph.1998.6152.

Cook, M., Ji, Y., Hunt, G., 2003. Cfd modelling of natural ventilation: combined wind and buoyancy forces. International Journal of Ventilation 1, 169–179. doi:http://dx.doi.org/10.1080/14733315.2003.11683632.

Cook, M.J., Lomas, K.J., 1997. Guidance on the use of computational fluid dynamics for modelling buoyancy driven flows. Proceedings of the IBPSA Building Simulation 97 , 57–72URL: https://www.researchgate.net/publication/237588799_GUIDANCE_ON_THE_USE_OF_COMPUTATIONAL_FLUID_DYNAMICS_FOR_MODELLING_BUOYANCY_DRIVEN_FLOWS.

Cordier, F., Degond, P., Kumbaro, A., 2012. An asymptotic-preserving all-speed scheme for the euler and navier–stokes equations. Journal of Computational Physics 231, 5685–5704. doi:https://doi.org/10.48550/arXiv.1108.2876.

Crank, J., Nicolson, P., 1947. A practical method for numerical evaluation of solutions of partial differential equations of the heat-conduction type, in: Mathematical Proceedings of the Cambridge Philosophical Society, Cambridge University Press. pp. 50–67. doi:10.1017/S0305004100023197.

Cuce, E., Sher, F., Sadiq, H., Cuce, P.M., Guclu, T., Besir, A.B., 2019. Sustainable ventilation strategies in buildings: CFD research. Sustainable Energy Technologies and Assessments 36, 100540. doi:https://doi.org/10.1016/j.seta.2019.100540.

D'Agostino, D., Congedo, P.M., 2014. Cfd modeling and moisture dynamics implications of ventilation scenarios in historical buildings. Building and Environment 79, 181–193. doi:https://doi.org/10.1016/j.buildenv.2014.05.007.

D'Agostino, D., Congedo, P.M., Cataldo, R., 2014. Computational fluid dynamics (cfd) modeling of microclimate for salts crystallization control and artworks conservation. Journal of cultural heritage 15, 448–457. doi:https://doi.org/10.1016/j.culher.2013.10.002.

Dalton, J., 1802. Experimental essays on the constitution of mixed gases. Manchester Literary and Philosophical Society Memo 5, 535–602. doi:https://www.biodiversitylibrary.org/part/308525.

Daly, B.J., Harlow, F.H., 1970. Transport equations in turbulence. The physics of fluids 13, 2634–2649. doi:https://doi.org/10.1063/1.1692845.

Darbandi, M., Hosseinizadeh, S.F., 2006. Numerical simulation of thermobuoyant flow with large temperature variation. Journal of thermophysics and heat transfer 20, 285–296. doi:10.2514/1.15804.

Defforge, C.L., Carissimo, B., Bocquet, M., Bresson, R., Armand, P., 2021. Improving numerical dispersion modelling in built environments with data assimilation using the iterative ensemble kalman smoother. Boundary Layer Meteorology 179, 209–240. doi:10.1007/s10546-020-00588-9.

Degond, P., Tang, M., 2011. All speed scheme for the low mach number limit of the isentropic euler equations. Communications in Computational Physics 10, 1–31. doi:https://doi.org/10.4208/cicp.210709.210610a.

Dehoux, F., 2012. Modélisation statistique des écoulements turbulents en convection forcée, mixte et naturelle. Ph.D. thesis. Poitiers. URL: https://www.theses.fr/2012POIT2276.

Demirdžić, I., Lilek, Ž., Perić, M., 1993. A collocated finite volume method for predicting flows at all speeds. International Journal for Numerical Methods in Fluids 16, 1029–1050. doi:10.1002/fld.1650161202.

Desjardins, O., Blanquart, G., Balarac, G., Pitsch, H., 2008. High order conservative finite difference scheme for variable density low mach number turbulent flows. Journal of Computational Physics 227, 7125–7159. doi:10.1016/j.jcp.2008.03.027.

Douce, A., Delalondre, C., Biausser, H., Guillot, J.B., 2003. Numerical modelling of an anodic metal bath heated with an argon transferred arc. ISIJ international 43, 1128–1135. doi:10.2355/isijinternational.43.1128.

Downar-Zapolski, P., Bilicki, Z., Bolle, L., Franco, J., 1996. The non-equilibrium relaxation model for one-dimensional flashing liquid flow. International journal of multiphase flow 22, 473–483. doi:https://doi.org/10.1016/0301-9322(95)00078-X.

Du Vachat, R., 1977. Realizability inequalities in turbulent flows. The Physics of Fluids 20, 551–556. doi:https://doi.org/10.1063/1.861911.

Duffal, V., 2020. Développement dun modèle hybride RANS-LES pour létude des efforts instationnaires en paroi. Ph.D. thesis. Université de Pau et des Pays de l'Adour. URL: https://www.theses.fr/2020PAUU3015.

Echekki, T., 2009. Multiscale methods in turbulent combustion: strategies and computational challenges. Computational Science & Discovery 2, 013001. doi:https://doi.org/10.1088/1749-4699/2/1/013001.

Eymard, R., Gallouët, T., Guichard, C., Herbin, R., Masson, R., 2014. Tp or not tp, that is the question. Computational Geosciences 18, 285–296. doi:10.1007/s10596-013-9392-9.

Fanger, P., 1984. Moderate thermal environments determination of the pmv and ppd indices and specification of the conditions for thermal comfort. ISO 7730 URL: https://www.iso.org/standard/14567.html.

Fanger, P.O., et al., 1970. Thermal comfort. analysis and applications in environmental engineering. Thermal comfort. Analysis and applications in environmental engineering. doi:https://doi.org/10.1177/146642407209200337.

Ferrand, M., Fontaine, J., Angelini, O., 2014. An anisotropic diffusion finite volume algorithm using a small stencil, in: Finite Volumes for Complex Applications VII-Elliptic, Parabolic and Hyperbolic Problems. Springer, pp. 577–585. doi:10.1007/978-3-319-05591-6_57.

Ferrand, M., Harris, J.C., 2021. Finite volume arbitrary lagrangian-eulerian schemes using dual meshes for ocean wave applications. Computers & Fluids 219, 104–860. doi:10.1016/j.compfluid.2021.104860.

Ferziger, J.H., Perić, M., Street, R.L., 2002. Computational methods for fluid dynamics. volume 3. Springer. doi:https://doi.org/10.1007/978-3-642-56026-2.

Feustel, H.E., 1999. Comisan international multizone air-flow and contaminant transport model. Energy and Buildings 30, 3–18. doi:https://doi.org/10.1016/S0378-7788(98)00043-7.

Fiorentino, E.A., Wortham, H., Sartelet, K., 2021. Combining homogeneous and heterogeneous chemistry to model inorganic compound concentrations in indoor environments: the h 2 i model (v1. 0). Geoscientific Model Development 14, 2747–2780. doi:https://doi.org/10.5194/gmd-14-2747-2021.

Flageul, C., Tiselj, I., Benhamadouche, S., Ferrand, M., 2019. A correlation for the discontinuity of the temperature variance dissipation rate at the fluid-solid interface in turbulent channel flows. Flow, Turbulence and Combustion 103, 175–201. doi:https://link.springer.com/article/10.1007/s10494-019-00008-0.

Foucquier, A., Robert, S., Suard, F., Stéphan, L., Jay, A., 2013. State of the art in building modelling and energy performances prediction: A review. Renewable and Sustainable Energy Reviews 23, 272–288. doi:https://doi.org/10.1016/j.rser.2013.03.004.

Fountain, M., Arens, E., Xu, T., Bauman, F., Oguro, M., 1999. An investigation of thermal comfort at high humidities. ASHRAE Transactions 105. URL: https://escholarship.org/content/qt94m840fb/qt94m840fb.pdf.

Fourier, J.B.J., Darboux, G., et al., 1822. Théorie analytique de la chaleur. volume 504. Didot Paris. doi:https://doi.org/10.1017/CBO9780511693229.

Fromm, J.E., 1968. A method for reducing dispersion in convective difference schemes. Journal of Computational Physics 3, 176–189. doi:https://doi.org/10.1016/0021-9991(68)90015-6.

Gagge, A.P., Fobelets, A., Berglund, L., et al., 1986. A standard predictive index of human response to the thermal environment. ASHRAE trans 92, 709–731. URL: https://www.aivc.org/sites/default/files/airbase_2522.pdf.

Gallouët, T., Gastaldo, L., Herbin, R., Latché, J.C., 2008. An unconditionally stable pressure correction scheme for the compressible barotropic navier-stokes equations. ESAIM: Mathematical Modelling and Numerical Analysis 42, 303–331. doi:https://doi.org/10.1051/m2an:2008005.

Gallouët, T., Hérard, J.M., Seguin, N., 2002. Some recent finite volume schemes to compute euler equations using real gas eos. International journal for numerical methods in fluids 39, 1073–1138. doi:https://doi.org/10.1002/fld.346.

Gan, G., Awbi, H.B., 1994. Numerical simulation of the indoor environment. Building and Environment 29, 449–459. doi:https://doi.org/10.1016/0360-1323(94)90004-3.

Gao, N., Niu, J., 2005. CFD study of the thermal environment around a human body: a review. Indoor and built environment 14, 5–16. doi:https://doi.org/10.1177/1420326X05050.

Gauffre, M.C., Benhamadouche, S., Badel, P.B., 2020. Wall-modeled large eddy simulation of the flow through pwr fuel assemblies at re h= 66 000validation on califs experimental setup. Nuclear Technology 206, 255–265. doi:10.1080/00295450.2019.1642684.

Gavrilyuk, S., Hérard, J.M., Hurisse, O., Toufaili, A., 2022. Theoretical and numerical analysis of a simple model derived from compressible turbulence. Journal of Mathematical Fluid Mechanics 24, 1–34. URL: https://hal.inria.fr/IUSTI/hal-03079453v2.

Germano, M., 1992. Turbulence: the filtering approach. Journal of Fluid Mechanics 238, 325336. doi:10.1017/S0022112092001733.

Greenspan, L., 1976. Functional equations for the enhancement factors for co2-free moist air. Journal of Research of the National Bureau of Standards. Section A, Physics and Chemistry 80, 41. doi:https://doi.org/10.6028\%2Fjres.080A.007.

Gresse, T., Merlier, L., Kuznik, F., 2020. Detailed airflow dynamics and temperature data of axisymmetric and anisothermal jets developing in a room. Data in brief 29, 105382. doi:10.1016/j.dib.2020.105382.

Grilli, E., Menna, F., Remondino, F., 2017. A review of point clouds segmentation and classification algorithms. The International Archives of Photogrammetry, Remote Sensing and Spatial Information Sciences 42, 339.

Guermond, J.L., Minev, P., Shen, J., 2006. An overview of projection methods for incompressible flows. Computer methods in applied mechanics and engineering 195, 6011–6045. doi:10.1016/j.cma.2005.10.010.

Guillard, H., Viozat, C., 1999. On the behaviour of upwind schemes in the low mach number limit. Computers & fluids 28, 63–86. doi:https://doi.org/10.1016/S0045-7930(98)00017-6.

Guimet, V., Laurence, D., 2002. A linearised turbulent production in the k-ε model for engineering applications, in: Engineering Turbulence Modelling and Experiments 5. Elsevier, pp. 157–166. doi:http://dx.doi.org/10.1016/B978-008044114-6/50014-4.

Guo, W., Liang, S., He, Y., Li, W., Xiong, B., Wen, H., 2022. Combining energyplus and cfd to predict and optimize the passive ventilation mode of medium-sized gymnasium in subtropical regions. Building and Environment 207, 108420. doi:https://doi.org/10.1016/j.buildenv.2021.108420.

Gupta, J.K., Lin, C.H., Chen, Q., 2011. Transport of expiratory droplets in an aircraft cabin. Indoor air 21, 3–11. doi:https://doi.org/10.1111/j.1600-0668.2010.00676.x.

Haack, J., Jin, S., Liu, J.G., 2012. An all-speed asymptotic-preserving method for the isentropic euler and navier-stokes equations. Communications in Computational Physics 12, 955–980. doi:http://dx.doi.org/10.4208/cicp.250910.131011a.

Hager, W.W., Zhang, H., 2006. A survey of nonlinear conjugate gradient methods. Pacific journal of Optimization 2, 35–58.

Haghighat, F., Huang, H., Lee, C.S., 2005. Modeling approaches for indoor air voc emissions from dry building materials–a review. ASHRAE Transactions 111. URL: https://www.researchgate.net/publication/287716478_Modeling_approaches_for_indoor_air_VOC_emissions_from_dry_building_materials_-_A_review.

Han, X., Morgans, A.S., 2015. Simulation of the flame describing function of a turbulent premixed flame using an open-source les solver. Combustion and Flame 162, 1778–1792. doi:10.1016/j.combustflame.2014.11.039.

Harlow, F.H., Amsden, A.A., 1968. Numerical calculation of almost incompressible flow. Journal of Computational Physics 3, 80–93. doi:10.1016/0021-9991(68)90007-7.

Harlow, F.H., Amsden, A.A., 1971. A numerical fluid dynamics calculation method for all flow speeds. Journal of Computational Physics 8, 197–213. doi:10.1016/0021-9991(71)90002-7.

Harlow, F.H., Welch, J.E., 1965. Numerical calculation of time-dependent viscous incompressible flow of fluid with free surface. The physics of fluids 8, 2182–2189. doi:10.1063/1.1761178.

Härtel, C., Meiburg, E., Necker, F., 2000. Analysis and direct numerical simulation of the flow at a gravity-current head. part 1. flow topology and front speed for slip and no-slip boundaries. Journal of Fluid Mechanics 418, 189–212. doi:10.1017/S0022112000001221.

Hassan, N., Khan, M.M.K., Rasul, M., 2013. Temperature monitoring and CFD analysis of data centre. Procedia Engineering 56, 551–559. doi:https://doi.org/10.1016/j.proeng.2013.03.159.

Hérard, J.M., Hurisse, O., 2012. A fractional step method to compute a class of compressible gas–liquid flows. Computers & Fluids 55, 57–69. doi:http://dx.doi.org/10.1016/j.compfluid.2011.11.001.

Herbin, R., Kheriji, W., Latche, J.C., 2012. Staggered schemes for all speed flows, in: ESAIM: Proceedings, EDP Sciences. pp. 122–150. doi:https://doi.org/10.1051/proc/201235008.

Herbin, R., Latché, J.C., Zaza, C., 2020. A cell-centred pressure-correction scheme for the compressible euler equations. IMA Journal of Numerical Analysis 40, 1792–1837. doi:10.1093/imanum/drz024.

Heseltine, E., Rosen, J., 2009. Who guidelines for indoor air quality: dampness and mould URL: https://apps.who.int/iris/handle/10665/164348.

van der Heul, D.R., Vuik, C., Wesseling, P., 2003. A conservative pressure-correction method for flow at all speeds. Computers & Fluids 32, 1113–1132. doi:10.1016/S0045-7930(02)00086-5.

van Hooff, T., Blocken, B., 2013. Cfd evaluation of natural ventilation of indoor environments by the concentration decay method: Co2 gas dispersion from a semi-enclosed stadium. Building and Environment 61, 1–17. doi:https://doi.org/10.1016/j.buildenv.2012.11.021.

Howard, R.J., Tully, B., 2012. A wall heat transfer function for equilibrium flows-a combination of reichardt and kader profiles with wang type scaling, in: THMT-12. Proceedings of the Seventh International Symposium On Turbulence Heat and Mass Transfer, Begel House Inc. doi:http://dx.doi.org/10.1615/ICHMT.2012.ProcSevIntSympTurbHeatTransfPal.90.

Hoyes, J., Ivings, M., 2016. CFD modelling of hydrogen stratification in enclosures: Model validation and application to par performance. Nuclear Engineering and Design 310, 142–153. doi:https://doi.org/10.1016/j.nucengdes.2016.08.036.

Huang, H., Haghighat, F., 2002. Modelling of volatile organic compounds emission from dry building materials. Building and Environment 37, 1127–1138. doi:http://dx.doi.org/10.5194/isprs-archives-XLII-2-W3-339-2017.

Huang, X., Zhang, Q., Tanaka, I., 2021. Optimization of architectural form for thermal comfort in naturally ventilated gymnasium at hot and humid climate by orthogonal experiment. Energies 14, 3228. doi:http://dx.doi.org/10.3390/en14113228.

Huang, Y., Sung, H.G., Hsieh, S.Y., Yang, V., 2003. Large-eddy simulation of combustion dynamics of lean-premixed swirl-stabilized combustor. Journal of Propulsion and Power 19, 782–794. doi:10.2514/2.6194.

Hunt, G., Kaye, N., 2005. Lazy plumes. Journal of Fluid Mechanics 533, 329–338. doi:https://doi.org/10.1017/S002211200500457X.

Hunt, G., Linden, P., 1999. The fluid mechanics of natural ventilationdisplacement ventilation by buoyancy-driven flows assisted by wind. Building and environment 34, 707–720. doi:https://doi.org/10.1016/S0360-1323(98)00053-5.

Hurisse, O., 2017. Numerical simulations of steady and unsteady two-phase flows using a homogeneous model. Computers & Fluids 152, 88–103. doi:http://dx.doi.org/10.1016/j.compfluid.2017.04.007.

Inard, C., Bouia, H., Dalicieux, P., 1996. Prediction of air temperature distribution in buildings with a zonal model. Energy and buildings 24, 125–132. doi:https://doi.org/10.1016/0378-7788(95)00969-8.

Isaacson, E., Keller, H.B., 2012. Analysis of numerical methods. Courier Corporation.

Ishii, M., Hibiki, T., 2010. Thermo-fluid dynamics of two-phase flow. Springer Science & Business Media. doi:https://doi.org/10.1007/978-1-4419-7985-8.

Issa, R.I., 1986a. The computation of compressible and incompressible recirculating flows by a non-iterative implicit scheme. Journal of Computational Physics 62, 66–82. doi:10.1016/0021-9991(86)90100-2.

Issa, R.I., 1986b. Solution of the implicitly discretised fluid flow equations by operator-splitting. Journal of computational physics 62, 40–65. doi:10.1016/0021-9991(86)90099-9.

Jarrin, N., Benhamadouche, S., Laurence, D., Prosser, R., 2006. A synthetic-eddy-method for generating inflow conditions for large-eddy simulations. International Journal of Heat and Fluid Flow 27, 585–593. doi:https://doi.org/10.1016/j.ijheatfluidflow.2006.02.006.

Jasak, H., 2009. Openfoam: open source CFD in research and industry. International Journal of Naval Architecture and Ocean Engineering 1, 89–94. doi:https://doi.org/10.2478/IJNAOE-2013-0011.

Jiang, Y., Beghein, C., Chen, Q., 2002. Study of particle dispersion in buildings with large eddy simulation, in: Indoor Air 2002, 9th International Conference on Indoor Air Quality and Climate, p. na. URL: https://hal.archives-ouvertes.fr/hal-00312486.

Karki, K., Patankar, S., 1989. Pressure based calculation procedure for viscous flows at all speeds in arbitrary configurations. AIAA journal 27, 1167–1174. doi:10.2514/3.10242.

Kassomenos, P., Karayannis, A., Panagopoulos, I., Karakitsios, S., Petrakis, M., 2008. Modelling the dispersion of a toxic substance at a workplace. Environmental modelling & software 23, 82–89. doi:https://doi.org/10.1016/j.envsoft.2007.05.003.

Kaushik, M., Kumar, R., Humrutha, G., 2015. Review of computational fluid dynamics studies on jets. American Journal of Fluid Dynamics 5, 1–11. doi:10.5923/s.ajfd.201501.01.

Kestin, J., Whitelaw, J., 1964. The viscosity of dry and humid air. International Journal of Heat and Mass Transfer 7, 1245–1255. doi:https://doi.org/10.1016/0017-9310(64)90066-3.

Kheriji, W., Herbin, R., Latché, J.C., 2013. Pressure correction staggered schemes for barotropic one-phase and two-phase flows. Computers & Fluids 88, 524–542. doi:https://doi.org/10.1016/j.compfluid.2013.09.022.

Kilic, M., Sevilgen, G., 2008. Modelling airflow, heat transfer and moisture transport around a standing human body by computational fluid dynamics. International Communications in Heat and Mass Transfer 35, 1159–1164. doi:https://doi.org/10.1016/j.icheatmasstransfer.2008.05.006.

Klainerman, S., Majda, A., 1981. Singular limits of quasilinear hyperbolic systems with large parameters and the incompressible limit of compressible fluids. Communications on pure and applied Mathematics 34, 481–524. doi:10.1002/cpa.3160340405.

Kofoed, P., 1991. Thermal plumes in ventilated rooms URL: https://www.aivc.org/sites/default/files/airbase_4254.pdf.

Kolmogorov, A.N., 1941a. Equations of turbulent motion in an incompressible fluid, in: Dokl. Akad. Nauk SSSR, pp. 299–303. URL: https://www.semanticscholar.org/paper/Equations-of-turbulent-motion-in-an-incompressible-Kolmogorov/990bd16cb8a65404276ad3b9b9f3489efadf3dbb.

Kolmogorov, A.N., 1941b. The local structure of turbulence in incompressible viscous fluid for very large reynolds numbers. Cr Acad. Sci. URSS 30, 301–305. doi:https://doi.org/10.1098/rspa.1991.0075.

Kovasznay, L.S., 1953. Turbulence in supersonic flow. Journal of the Aeronautical Sciences 20, 657–674. doi:https://doi.org/10.2514/8.2793.

Kraus, A., Merzari, E., Norddine, T., Marin, O., Benhamadouche, S., 2021. Direct numerical simulation of fluid flow in a 5x5 square rod bundle. International Journal of Heat and Fluid Flow 90, 108833. doi:https://doi.org/10.1016/j.ijheatfluidflow.2021.108833.

Kusuda, T., 1976. NBSLD, the computer program for heating and cooling loads in buildings. volume 69. The Bureau. URL: https://nvlpubs.nist.gov/nistpubs/Legacy/IR/nbsir74-574.pdf.

Kuznik, F., 2005. Etude expérimentale des jets axisymétriques anisothermes horizontaux se développant près dune paroi. application à la modélisation numérique des cavités ventilées. INSA, Lyon URL: http://theses.insa-lyon.fr/publication/2005ISAL0108/these.pdf.

Kuznik, F., Rusaouën, G., Brau, J., 2007. Experimental and numerical study of a full scale ventilated enclosure: Comparison of four two equations closure turbulence models. Building and Environment 42, 1043–1053. doi:10.1016/j.buildenv.2005.11.024.

Kuznik, F., Rusaouën, G., Hohotă, R., 2006. Experimental and numerical study of a mechanically ventilated enclosure with thermal effects. Energy and buildings 38, 931–938. doi:10.1016/j.enbuild.2005.08.016.

Kwong, Q.J., Adam, N.M., Sahari, B., 2014. Thermal comfort assessment and potential for energy efficiency enhancement in modern tropical buildings: A review. Energy and buildings 68, 547–557. doi:https://doi.org/10.1016/j.enbuild.2013.09.034.

La Gennusa, M., Nucara, A., Pietrafesa, M., Rizzo, G., 2007. A model for managing and evaluating solar radiation for indoor thermal comfort. Solar Energy 81, 594–606. doi:https://doi.org/10.1016/j.solener.2006.09.005.

Launder, B., Sharma, B., 1974a. Application of the energy-dissipation model of turbulence to the calculation of flow near a spinning disc. Letters in Heat and Mass Transfer 1, 131 – 137. URL: http://www.sciencedirect.com/science/article/pii/0094454874901507, doi:https://doi.org/10.1016/0094-4548(74)90150-7.

Launder, B.E., Sharma, B.I., 1974b. Application of the energy-dissipation model of turbulence to the calculation of flow near a spinning disc. Letters in heat and mass transfer 1, 131–137. doi:10.1016/0094-4548(74)90150-7.

Lawrance, A., 2020. Learning from the ovhcloud data center fire. Data Center Dynamics Newsletter URL: https://www.datacenterdynamics.com/en/opinions/learning-ovhcloud-data-center-fire/.

Le Quéré, P., Masson, R., Perrot, P., 1992. A chebyshev collocation algorithm for 2d non-boussinesq convection. Journal of computational physics 103, 320–335. doi:10.1016/0021-9991(92)90404-M.

Le Quéré, P., Weisman, C., Paillère, H., Vierendeels, J., Dick, E., Becker, R., Braack, M., Locke, J., 2005. Modelling of natural convection flows with large temperature differences: a benchmark problem for low mach number solvers. part 1. reference solutions. ESAIM: Mathematical Modelling and Numerical Analysis 39, 609–616. doi:10.1051/m2an:2005027.

Le Quéré, P., Weisman, C., Paillere, H., Vierendeels, J., Dick, E., Becker, R., Braack, M., Locke, J., 2005. Modelling of natural convection flows with large temperature differences: A benchmark problem for low mach number solvers. part 1. reference solutions. http://dx.doi.org/10.1051/m2an:2005027 39. doi:10.1051/m2an:2005027.

Lecocq, Y., Bournaud, S., Manceau, R., Duret, B., Brizzi, L., 2008. U-rans simulation of mixed-convection around a finite wall-mounted heated cylinder cooled by cross-flow, in: Fluids Engineering Division Summer Meeting, pp. 713–723. URL: https://hal.archives-ouvertes.fr/hal-00406124.

Lee, J.H.w., Chu, V., Chu, V.H., 2003. Turbulent jets and plumes: A Lagrangian approach. volume 1. Springer Science & Business Media. doi:https://doi.org/10.1007/978-1-4615-0407-8.

Lilly, D.K., 1992. A proposed modification of the germano subgridscale closure method. Physics of Fluids A: Fluid Dynamics 4, 633–635. URL: https://doi.org/10.1063/1.858280, doi:10.1063/1.858280, arXiv:https://doi.org/10.1063/1.858280.

Linden, P.F., 1999. The fluid mechanics of natural ventilation. Annual review of fluid mechanics 31, 201–238. doi:https://doi.org/10.1146/annurev.fluid.31.1.201.

Liu, J., Aizawa, H., Yoshino, H., 2004. Cfd prediction of surface condensation on walls and its experimental validation. Building and Environment 39, 905–911. doi:https://doi.org/10.1016/j.buildenv.2004.01.015.

Liu, J., Zhu, S., Kim, M.K., Srebric, J., 2019. A review of CFD analysis methods for personalized ventilation (pv) in indoor built environments. Sustainability 11, 4166. doi:https://doi.org/10.3390/su11154166.

Liu, Y., Liu, Z., Luo, J., 2015. Numerical investigation of the unsteady thermal plume around human body in closed space. Procedia Engineering 121, 1919–1926. doi:https://doi.org/10.1016/j.proeng.2015.09.176.

Lu, T., Viljanen, M., 2009. Prediction of indoor temperature and relative humidity using neural network models: model comparison. Neural Computing and Applications 18, 345–357. doi:http://dx.doi.org/10.1007/s00521-008-0185-3.

Lü, X., 2002a. Modelling of heat and moisture transfer in buildings: I. model program. Energy and buildings 34, 1033–1043. doi:https://doi.org/10.1016/S0378-7788(02)00021-X.

Lü, X., 2002b. Modelling of heat and moisture transfer in buildings: Ii. applications to indoor thermal and moisture control. Energy and buildings 34, 1045–1054. doi:https://doi.org/10.1016/S0378-7788(02)00022-1.

Lumley, J.L., 1979. Computational modeling of turbulent flows. Advances in applied mechanics 18, 123–176. doi:https://doi.org/10.1016/S0065-2156(08)70266-7.

Ma, L., Nmira, F., Consalvi, J.L., 2019. Verification and validation of a variable–density solver for fire safety applications. Numerical Heat Transfer, Part B: Fundamentals 76, 107–129. doi:10.1080/10407790.2019.1647721.

Malys, L., Musy, M., Inard, C., 2015. Microclimate and building energy consumption: Study of different coupling methods. Advances in Building Energy Research 9, 151–174.

Mangeon, G., 2020. Modélisation au second ordre des transferts thermiques turbulents pour tous types de conditions aux limites thermiques à la paroi. Ph.D. thesis. Pau. URL: https://tel.archives-ouvertes.fr/tel-02923253/document.

McCroskey, W., 1987. A critical assessment of wind tunnel results for the NACA 0012 airfoil. Technical Report. URL: https://apps.dtic.mil/sti/pdfs/ADA193182.pdf.

Meng, L., Qiu, H., Wan, L., Ai, Y., Xue, Z., Guo, Q., Deshpande, R., Zhang, L., Meng, J., Tong, C., et al., 2020. Intubation and ventilation amid the covid-19 outbreak: Wuhans experience. Anesthesiology 132, 1317–1332. doi:https://doi.org/10.1097/aln.0000000000003296.

Menter, F.R., 1994. Two-equation eddy-viscosity turbulence models for engineering applications. AIAA journal 32, 1598–1605. doi:https://doi.org/10.2514/3.12149.

De Laage de Meux, B., Audebert, B., Manceau, R., Perrin, R., 2015. Anisotropic linear forcing for synthetic turbulence generation in large eddy simulation and hybrid rans/les modeling. Physics of Fluids 27, 035115. doi:http://dx.doi.org/10.1063/1.4916019.

Milliez, M., Carissimo, B., 2007. Numerical simulations of pollutant dispersion in an idealized urban area, for different meteorological conditions. Boundary-Layer Meteorology 122, 321–342. doi:10.1007/s10546-006-9110-4.

Mora, L., 2003. Prédiction des performances thermo-aérauliques des bâtiments par association de modèles de différents niveaux de finesse au sein d'un environnement orienté objet. Ph.D. thesis. Université de la Rochelle. URL: https://www.theses.fr/2003LAROS097.

Moukalled, F., Darwish, M., 2001. A high-resolution pressure-based algorithm for fluid flow at all speeds. Journal of Computational Physics 168, 101–130. doi:10.1006/jcph.2000.6683.

Moureau, V., Bérat, C., Pitsch, H., 2007. An efficient semi-implicit compressible solver for large-eddy simulations. Journal of Computational Physics 226, 1256–1270. doi:10.1016/j.jcp.2007.05.035.

Murakami, S., Kato, S., Kondo, Y., Ito, K., Yamamoto, A., 2000a. Voc distribution in a room based on cfd simulation coupled with emission/sorption analysis, in: Proceedings of the Seventh International Conference on Air Distribution in Rooms, Citeseer. pp. 473–478. URL: https://citeseerx.ist.psu.edu/viewdoc/download?doi=10.1.1.540.9353&rep=rep1&type=pdf.

Murakami, S., Kato, S., Zeng, J., 2000b. Combined simulation of airflow, radiation and moisture transport for heat release from a human body. Building and environment 35, 489–500. doi:https://doi.org/10.1016/S0360-1323(99)00033-5.

Musy, M., Winkelmann, F., Wurtz, E., Sergent, A., 2002. Automatically generated zonal models for building air flow simulation: principles and applications. Building and Environment 37, 873–881. doi:https://doi.org/10.1016/S0360-1323(02)00050-1.

Nielsen, P.V., 2015. Fifty years of CFD for room air distribution. Building and Environment 91, 78–90. doi:https://doi.org/10.1016/j.buildenv.2015.02.035.

Norddine, T., 2020. Towards realizability of second order closure turbulence models and numerical methods for atmospheric flows. Technical Report. Centre dEnseignement et de Recherche en Environnement Atmosphérique, Ecole des Ponts Paris Tech.

Comité Européen de Normalisation, C., 2007. Indoor environmental input parameters for design and assessment of energy performance of buildings addressing indoor air quality, thermal environment, lighting and acoustics. EN 15251 URL: http://www.cres.gr/greenbuilding/PDF/prend/set4/WI_31_Pre-FV_version_prEN_15251_Indoor_Environment.pdf.

Norton, T., Grant, J., Fallon, R., Sun, D.W., 2010. Optimising the ventilation configuration of naturally ventilated livestock buildings for improved indoor environmental homogeneity. Building and Environment 45, 983–995. doi:https://doi.org/10.1016/j.buildenv.2009.10.005.

Ogura, Y., Phillips, N.A., 1962. Scale analysis of deep and shallow convection in the atmosphere. Journal of Atmospheric Sciences 19, 173 – 179. URL: https://journals.ametsoc.org/view/journals/atsc/19/2/1520-0469_1962_019_0173_saodas_2_0_co_2.xml, doi:10.1175/1520-0469(1962)019<0173:SAODAS>2.0.CO;2.

Ooi, S.K., Constantinescu, G., Weber, L.J., 2007. 2d large-eddy simulation of lock-exchange gravity current flows at high grashof numbers. Journal of Hydraulic Engineering 133, 1037–1047. doi:https://doi.org/10.1061.

Pareschi, L., Russo, G., 2005. Implicit–explicit runge–kutta schemes and applications to hyperbolic systems with relaxation. Journal of Scientific computing 25, 129–155. doi:http://dx.doi.org/10.1007/s10915-004-4636-4.

Park, J., Munz, C.D., 2005. Multiple pressure variables methods for fluid flow at all mach numbers. International journal for numerical methods in fluids 49, 905–931. doi:https://doi.org/10.1002/fld.1032.

Pierce, C.D., Moin, P., 2004. Progress-variable approach for large-eddy simulation of non-premixed turbulent combustion. Journal of fluid Mechanics 504, 73. doi:10.1017/S0022112004008213.

Plessis, G., Kaemmerlen, A., Lindsay, A., 2014. Buildsyspro: a modelica library for modelling buildings and energy systems, in: Proceedings of the 10 th International Modelica Conference; March 10-12; 2014; Lund; Sweden, Linköping University Electronic Press. pp. 1161–1169. doi:http://dx.doi.org/10.3384/ecp140961161.

Politis, E., Giannakoglou, K., 1997. A pressure-based algorithm for high-speed turbo-machinery flows. International journal for numerical methods in fluids 25, 63–80. doi:10.1002/(SICI)1097-0363(19970715)25.

Pope, S.B., 2000. Turbulent flows. Cambridge university press. doi:https://doi.org/10.1017/CBO9780511840531.

Popinet, S., 2003. Gerris: a tree-based adaptive solver for the incompressible euler equations in complex geometries. Journal of computational physics 190, 572–600. doi:https://doi.org/10.1016/S0021-9991(03)00298-5.

Posner, J., Buchanan, C., Dunn-Rankin, D., 2003. Measurement and prediction of indoor air flow in a model room. Energy and buildings 35, 515–526. doi:https://doi.org/10.1016/S0378-7788(02)00163-9.

Prandtl, L., 1925. Applications of modern hydrodynamics to aeronautics. US Government Printing Office. URL: https://ntrs.nasa.gov/citations/19930091180.

Qian, F., Yang, L., 2016. The numerical simulation and study on gymnasium indoor thermal environment of airpak, in: 2016 International Conference on Energy, Power and Electrical Engineering, Atlantis Press. pp. 24–29. doi:https://dx.doi.org/10.2991/epee-16.2016.6.

Qin, T., Guo, Y., Chan, C., Lin, W., 2006. Numerical investigation of smoke exhaust mechanism in a gymnasium under fire scenarios. Building and environment 41, 1203–1213. doi:https://doi.org/10.1016/j.buildenv.2005.05.009.

Ramalho, O., Kirchner, S., 2007. Indoor air quality in french dwellings, national survey 2003-2005, in: Monitoring Ambient Air 2007: The Importance of Indoor Air, Automation and Analytical Management Group, Royal Society of Chemistry. URL: https://hal.archives-ouvertes.fr/hal-00701705.

Razafindrakoto, E., Denis, C., Balestre, L., 1998. N3S-AERO. A multidimensional model for numerical simulation of flows in cooling towers. Technical Report. Electricite de France. URL: https://inis.iaea.org/search/searchsinglerecord.aspx?recordsFor=SingleRecord&RN=32004165.

RH, P., Chilton, C., 1973. Chemical engineers handbook. McG r aw URL: https://www.accessengineeringlibrary.com/content/book/9780071422949.

Rhie, C., Chow, W.L., 1983. Numerical study of the turbulent flow past an airfoil with trailing edge separation. AIAA journal 21, 1525–1532. doi:10.2514/3.8284.

Richardson, L.F., 1922. Weather prediction by numerical process. University Press. doi:https://doi.org/10.1017/CBO9780511618291.

Riffelli, S., 2021. Global comfort indices in indoor environments: A survey. Sustainability 13, 12784. doi:http://dx.doi.org/10.3390/su132212784.

Rui, Z., Guangbei, T., Jihong, L., 2008. Study on biological contaminant control strategies under different ventilation models in hospital operating room. Building and environment 43, 793–803. doi:https://doi.org/10.1016/j.buildenv.2007.01.018.

Sadrizadeh, S., Holmberg, S., 2015. How safe is it to neglect thermal radiation in indoor environment modeling with high ventilation rates?, in: Proceedings of the 36th AIVC, 5th TightVent & 3rd venticool Conference. doi:https://www.aivc.org/sites/default/files/44_0.pdf.

Sagaut, P., Terracol, M., Deck, S., 2013. Multiscale and multiresolution approaches in turbulence-LES, DES and Hybrid RANS/LES Methods: Applications and Guidelines. World Scientific. doi:https://doi.org/10.1142/p878.

Sajjadi, H., Salmanzadeh, M., Ahmadi, G., Jafari, S., 2017. Turbulent indoor airflow simulation using hybrid les/rans model utilizing lattice boltzmann method. Computers & Fluids 150, 66–73. doi:https://doi.org/10.1016/j.compfluid.2017.03.028.

Sakai, K., Murata, Y., Kubo, R., Kajiya, R., Ishihara, O., 2007. Measurement and cfd analysis of unsteady thermal environment in gymnasium adopted displacement air condition system, in: Proc. of the 6th Int. conference on Indoor Air Quality, Ventilation & Energy Conservation in Buildings, Citeseer. pp. 352–359. URL: https://www.researchgate.net/publication/241724755_MEASUREMENT_AND_CFD_ANALYSIS_OF_UNSTEADY_THERMAL_ENVIRONMENT_IN_GYMNASIUM_ADOPTED_DISPLACEMENT_AIR_CONDITION_SYSTEM.

Salat, J., Xin, S., Joubert, P., Sergent, A., Penot, F., Le Quere, P., 2004. Experimental and numerical investigation of turbulent natural convection in a large air-filled cavity. International journal of heat and fluid flow 25, 824–832. doi:https://doi.org/10.1016/j.ijheatfluidflow.2004.04.003.

Sartelet, K., Couvidat, F., Wang, Z., Flageul, C., Kim, Y., 2020. Ssh-aerosol v1. 1: A modular box model to simulate the evolution of primary and secondary aerosols. Atmosphere 11, 525. doi:https://doi.org/10.3390/atmos11050525.

Satoh, M., 2013. Atmospheric circulation dynamics and general circulation models. Springer Science & Business Media. doi:https://doi.org/10.1007/978-3-642-13574-3.

Saturne, C., 2019. 7.0. theory guide, edf r&d, 2021 URL: https://www.code-saturne.org/documentation/7.0/theory.pdf.

Schneider, N., 2015. Vorticité et mélange dans les écoulements de Rayleigh-Taylor turbulents, en approximation anélastique et de Boussinesq. Ph.D. thesis. Paris 6. URL: https://tel.archives-ouvertes.fr/tel-01293020/.

Schumann, U., 1977. Realizability of reynolds-stress turbulence models. The Physics of Fluids 20, 721–725. doi:https://doi.org/10.1063/1.861942.

Sharma, A.K., Mahapatra, P.S., Manna, N.K., Ghosh, K., 2015. Mixed convection in a baffled grooved channel. Sadhana 40, 835–849. doi:http://dx.doi.org/10.1007/s12046-014-0328-4.

Shen, C., Gao, N., Wang, T., 2013. CFD study on the transmission of indoor pollutants under personalized ventilation. Building and Environment 63, 69–78. doi:https://doi.org/10.1016/j.buildenv.2013.02.003.

Shi, L., An, R., 2017. An optimization design approach of football stadium canopy forms based on field wind environment simulation. Energy Procedia 134, 757–767. doi:https://doi.org/10.1016/j.egypro.2017.09.575.

Shir, C.C., 1973. A preliminary numerical study of atmospheric turbulent flows in the idealized planetary boundary layer. Journal of Atmospheric Sciences 30, 1327 – 1339. URL: https://journals.ametsoc.org/view/journals/atsc/30/7/1520-0469_1973_030_1327_apnsoa_2_0_co_2.xml, doi:10.1175/1520-0469(1973)030<1327:APNSOA>2.0.CO;2.

Shree, V., Marwaha, B.M., Awasthi, P., 2019. Assessment of indoor air quality in buildings using CFD: A brief review. International Journal of Mathematical, Engineering and Management Sciences 4, 1154. doi:http://dx.doi.org/10.33889/IJMEMS.2019.4.5-091.

Skillen, A., Revell, A., Craft, T., 2016. Accuracy and efficiency improvements in synthetic eddy methods. International Journal of Heat and Fluid Flow 62, 386–394. doi:https://doi.org/10.1016/j.ijheatfluidflow.2016.09.008.

Smagorinsky, J., 1963. General circulation experiments with the primitive equations: I. the basic experiment. Monthly Weather Review 91, 99 – 164. URL: https://journals.ametsoc.org/view/journals/mwre/91/3/1520-0493_1963_091_0099_gcewtp_2_3_co_2.xml, doi:10.1175/1520-0493(1963)091<0099:GCEWTP>2.3.CO;2.

Smith, A., Cebeci, T., 1967. Numerical solution of the turbulent-boundary-layer equations. Technical Report. DOUGLAS AIRCRAFT CO LONG BEACH CA AIRCRAFT DIV. URL: https://apps.dtic.mil/sti/citations/AD0656430.

Smoller, J., 2012. Shock waves and reactiondiffusion equations. volume 258. Springer Science & Business Media. doi:https://doi.org/10.1007/978-1-4612-0873-0.

Sod, G.A., 1978. A survey of several finite difference methods for systems of nonlinear hyperbolic conservation laws. Journal of computational physics 27, 1–31. doi:10.1016/0021-9991.

Sofotasiou, P., Hughes, B., Ghani, S.A., 2017. Cfd optimisation of a stadium roof geometry: a qualitative study to improve the wind microenvironment. Sustainable Buildings 2, 8. doi:https://doi.org/10.1051/sbuild/2017006.

Ministère de la Transition Ecologique et Solidaire, M.d.l.C.d.T., 2018. Plan renovation energétique des bâtiments .

Sørensen, D.N., Voigt, L.K., 2003. Modelling flow and heat transfer around a seated human body by computational fluid dynamics. Building and environment 38, 753–762. doi:https://doi.org/10.1016/S0360-1323(03)00027-1.

Spalart, P., Allmaras, S., 1992. A one-equation turbulence model for aerodynamic flows, in: 30th aerospace sciences meeting and exhibit, p. 439. doi:https://doi.org/10.2514/6.1992-439.

Spengler, J.D., Chen, Q., 2000. Indoor air quality factors in designing a healthy building. Annual Review of Energy and the Environment 25, 567–600. doi:https://doi.org/10.1146/annurev.energy.25.1.567.

Speziale, C.G., Sarkar, S., Gatski, T.B., 1991. Modelling the pressurestrain correlation of turbulence: an invariant dynamical systems approach. Journal of Fluid Mechanics 227, 245272. doi:10.1017/S0022112091000101.

Srebric, J., Vukovic, V., He, G., Yang, X., 2008. Cfd boundary conditions for contaminant dispersion, heat transfer and airflow simulations around human occupants in indoor environments. Building and Environment 43, 294–303. doi:https://doi.org/10.1016/j.buildenv.2006.03.023.

Steele, J.M., 2004. The Cauchy-Schwarz master class: an introduction to the art of mathematical inequalities. Cambridge University Press. doi:https://doi.org/10.1017/CBO9780511817106.

Steeman, H.J., Janssens, A., Carmeliet, J., De Paepe, M., 2009. Modelling indoor air and hygrothermal wall interaction in building simulation: Comparison between cfd and a well-mixed zonal model. Building and environment 44, 572–583. doi:https://doi.org/10.1016/j.buildenv.2008.05.002.

Studnikov, E., 1970. The viscosity of moist air. Journal of engineering physics 19, 1036–1037. doi:http://dx.doi.org/10.1080/19443994.2012.714925.

Sun, C., Zhai, Z., 2020. The efficacy of social distance and ventilation effectiveness in preventing covid-19 transmission. Sustainable cities and society 62, 102390. doi:https://doi.org/10.1016/j.scs.2020.102390.

Sutherland, W., 1895. Xxxvii. the viscosity of mixed gases. The London, Edinburgh, and Dublin Philosophical Magazine and Journal of Science 40, 421–431. doi:https://doi.org/10.1080/14786449508620789.

Temam, R., 1969. Sur l'approximation de la solution des équations de navier-stokes par la méthode des pas fractionnaires (i). Archive for Rational Mechanics and Analysis 32, 135–153. doi:10.1007/BF00247678.

Teodosiu, C., Hohota, R., Rusaouën, G., Woloszyn, M., 2003. Numerical prediction of indoor air humidity and its effect on indoor environment. Building and Environment 38, 655–664. doi:https://doi.org/10.1016/S0360-1323(02)00211-1.

Teodosiu, C., Kuznik, F., Teodosiu, R., 2014. Cfd modeling of buoyancy driven cavities with internal heat sourceapplication to heated rooms. Energy and Buildings 68, 403–411. doi:https://doi.org/10.1016/j.enbuild.2013.09.041.

Teodosiu, R., 2013. Integrated moisture (including condensation)–energy–airflow model within enclosures. experimental validation. Building and Environment 61, 197–209. doi:https://doi.org/10.1016/j.buildenv.2012.12.011.

Teshome, E., F. Haghighat, F., 2004. Zonal models for indoor air flow-a critical review. International journal of ventilation 3, 119–129. doi:https://doi.org/10.1080/14733315.2004.11683908.

Toftum, J., Jørgensen, A.S., Fanger, P.O., 1998. Upper limits for indoor air humidity to avoid uncomfortably humid skin. Energy and Buildings 28, 1–13. doi:https://doi.org/10.1016/S0378-7788\%2897\%2900017-0.

Tonello, N., Fournier, Y, F.M., 2017. Implementation of a drift flux multiphase model for 3d draft cooling tower simulations in code saturne, in: 18th IAHR International Conference on Cooling Tower and Air Cooled Heat Exchanger, Lyon, France.

Tong, Z., Chen, Y., Malkawi, A., Adamkiewicz, G., Spengler, J.D., 2016. Quantifying the impact of traffic-related air pollution on the indoor air quality of a naturally ventilated building. Environment international 89, 138–146. doi:https://doi.org/10.1016/j.envint.2016.01.016.

Toro, E.F., 2013. Riemann solvers and numerical methods for fluid dynamics: a practical introduction. Springer Science & Business Media. doi:https://doi.org/10.1007/b79761.

Touloukian, Y., Saxena, S., Hestermans, P., 1975. Thermophysical properties of matter, vol. 11: Viscosity. IFI/Plenum URL: https://apps.dtic.mil/sti/citations/ADA129114.

Tsilingiris, P., 2018. Review and critical comparative evaluation of moist air thermophysical properties at the temperature range between 0 and 100 c for engineering calculations. Renewable and Sustainable Energy Reviews 83, 50–63. doi:https://doi.org/10.1016/j.rser.2017.10.072.

Uhde, E., Salthammer, T., 2007. Impact of reaction products from building materials and furnishings on indoor air qualitya review of recent advances in indoor chemistry. Atmospheric Environment 41, 3111–3128. doi:https://doi.org/10.1016/j.atmosenv.2006.05.082.

UNO, 2018. 2018 revision of world urbanization prospects URL: https://www.un.org/development/desa/publications/2018-revision-of-world-urbanization-prospects.html.

Van Doormaal, J., Raithby, G., McDonald, B., 1987. The segregated approach to predicting viscous compressible fluid flows doi:10.1115/1.3262097.

Van Hooff, T., Blocken, B., Defraeye, T., Carmeliet, J.v., Van Heijst, G., 2012. Piv measurements and analysis of transitional flow in a reduced-scale model: ventilation by a free plane jet with coanda effect. Building and Environment 56, 301–313. doi:https://doi.org/10.1016/j.buildenv.2012.03.020.

Versteeg, H.K., Malalasekera, W., 2007. An introduction to computational fluid dynamics: the finite volume method. Pearson education. URL: https://www.pearson.com/en-us/subject-catalog/p/introduction-to-computational-fluid-dynamics-an-the-finite-volume-method/P200000005670/9780131274983.

Vierendeels, J., Riemslagh, K., Dick, E., 1999a. A multigrid semi-implicit line-method for viscous incompressible and low-mach-number flows on high aspect ratio grids. Journal of Computational Physics 154, 310–341. doi:10.1006/jcph.1999.6315.

Vierendeels, J., Riemslagh, K., Dick, E., 1999b. A multigrid semi-implicit line-method for viscous incompressible and low-mach-number flows on high aspect ratio grids. Journal of Computational Physics 154, 310 – 341. URL: http://www.sciencedirect.com/science/article/pii/S0021999199963155, doi:https://doi.org/10.1006/jcph.1999.6315.

Wald, J.F., 2016. Lois de paroi adaptatives pour un modèle de fermeture du second ordre dans un contexte industriel. Ph.D. thesis. Université de Pau et des Pays de l'Adour. URL: https://hal.inria.fr/tel-01415106/file/These_VersionFinaleDeposee.pdf.

Wall, C., Pierce, C., Moin, P., 2003. A method for large eddy simulation of acoustic combustion instabilities URL: https://www.researchgate.net/publication/253613907_Large_Eddy_Simulation_of_Acoustic_Combustion_Instabilities.

Wall, C., Pierce, C.D., Moin, P., 2002. A semi-implicit method for resolution of acoustic waves in low mach number flows. Journal of Computational Physics 181, 545–563. doi:10.1006/jcph.2002.7141.

Walton, G., Dols, W.S., et al., 2006. Contam 2.4 user guide and program documentation URL: https://nvlpubs.nist.gov/nistpubs/Legacy/IR/nistir7251.pdf.

Wang, L., Chen, Q., 2007. Validation of a coupled multizone-CFD program for building airflow and contaminant transport simulations. HVAC&R Research 13, 267–281. URL: https://www.ecologie.gouv.fr/plan-renovation-energetique-des-batiments.

Wang, L.L., Chen, Q., 2008. Evaluation of some assumptions used in multizone airflow network models. Building and Environment 43, 1671–1677. doi:https://doi.org/10.1016/j.buildenv.2007.10.010.

WHO, 2021. Pollution de lair à lintérieur des habitations et santé URL: https://www.who.int/fr/news-room/fact-sheets/detail/household-air-pollution-and-health.

Wilke, C., 1950. A viscosity equation for gas mixtures. The journal of chemical physics 18, 517–519. doi:https://doi.org/10.1063/1.1747673.

Wolkoff, P., 2018. Indoor air humidity, air quality, and health–an overview. International journal of hygiene and environmental health 221, 376–390. doi:https://doi.org/10.1016/j.ijheh.2018.01.015.

Woodward, P., Colella, P., 1984. The numerical simulation of two-dimensional fluid flow with strong shocks. Journal of computational physics 54, 115–173. doi:https://doi.org/10.1016/0021-9991(84)90142-6.

Yakhot, V., Orszag, S., Thangam, S., Gatski, T., Speziale, C., 1992. Development of turbulence models for shear flows by a double expansion technique. Physics of Fluids A: Fluid Dynamics 4, 1510–1520. doi:https://doi.org/10.1063/1.858424.

Yang, L., Ye, M., et al., 2014. CFD simulation research on residential indoor air quality. Science of the Total Environment 472, 1137–1144. doi:https://doi.org/10.1016/j.scitotenv.2013.11.118.

Yasuda, T., Vassilicos, J.C., 2018. Spatio-temporal intermittency of the turbulent energy cascade. Journal of Fluid Mechanics 853, 235–252. doi:https://doi.org/10.1017/jfm.2018.584.

You, S., Li, W., Ye, T., Hu, F., Zheng, W., 2017. Study on moisture condensation on the interior surface of buildings in high humidity climate. Building and Environment 125, 39–48. doi:https://doi.org/10.1016/j.buildenv.2017.08.041.

Zhai, Z., 2006. Application of computational fluid dynamics in building design: aspects and trends. Indoor and built environment 15, 305–313. doi:https://doi.org/10.1177/1420326X06067336.

Zhai, Z., Chen, Q., Scanlon, P.W., 2002. Design of a ventilation system for an indoor auto-racing complex/discussion. ASHRAE Transactions 108, 989. URL: https://engineering.purdue.edu/~yanchen/paper/2002-3.pdf.

Zhai, Z., Srebric, J., Chen, Q., 2003. Application of CFD to predict and control chemical and biological agent dispersion in buildings. International Journal of Ventilation 2, 251–264. doi:https://doi.org/10.1080/14733315.2003.11683669.

Zhai, Z.J., Zhang, Z., Zhang, W., Chen, Q.Y., 2007. Evaluation of various turbulence models in predicting airflow and turbulence in enclosed environments by cfd: Part 1summary of prevalent turbulence models. Hvac&R Research 13, 853–870. URL: https://engineering.purdue.edu/~yanchen/paper/2007-8.pdf.

Zhang, T., Chen, Q.Y., 2007. Novel air distribution systems for commercial aircraft cabins. Building and Environment 42, 1675–1684. doi:https://doi.org/10.1016/j.buildenv.2006.02.014.

Zschaeck, G., Frank, T., Burns, A., 2014. Cfd modelling and validation of wall condensation in the presence of non-condensable gases. Nuclear Engineering and Design 279, 137–146. doi:https://doi.org/10.1016/j.nucengdes.2014.03.007.

Zukowska, D., Melikov, A., Popiolek, Z., 2007. Thermal plume above a simulated sitting person with different complexity of body geometry, in: Proceedings of the 10th International Conference on Air Distribution in RoomsRoomvent, Technical University of Denmark. pp. 191–198. URL: http://homes.civil.aau.dk/pvn/cfd-benchmarks/csp_literature/Roomvent_2007/Zukowska_D_Melikov_and_Popiolek_2007b.pdf.

Zukowska, D., Melikov, A., Popiolek, Z., 2012. Impact of personal factors and furniture arrangement on the thermal plume above a sitting occupant. Building and Environment 49, 104–116. doi:https://doi.org/10.1016/j.buildenv.2011.09.015.